CENTRO DE INVESTIGACIÓN Y DE ESTUDIOS AVANZADOS DEL INSTITUTO POLITÉCNICO NACIONAL

UNIDAD ZACATENCO

PROGRAMA DE DOCTORADO

NANOCIENCIAS Y NANOTECNOLOGÍA

"Diseño y evaluación de nanopartículas núcleo-envoltura de Au-MFe_2O_4 (M-Fe/Co/Mn) plasmónicas/magnéticas funcionalizadas con Doxorrubicina para la terapéutica del cáncer"

TESIS

Que presenta

RAVICHANDRAN MANISEKARAN

Para obtener el grado de

DOCTOR EN CIENCIAS

EN LA ESPECIALIDAD DE

Nanociencias y Nanotecnología

Directores de la Tesis:

Dr. VELUMANI SUBRAMANIAM

(Departamento de ingeniería eléctrica - Sección electrónica del estado sólido)

Dr. JOSE TAPIA RAMIREZ

(Departamento de Genética y Biología Molecular)

Ciudad de México Marzo, 2017

Design and evaluation of plasmonic/magnetic Au-MFe_2O_4 (M-Fe/Co/Mn) core-shell nanoparticles functionalized with Doxorubicin for cancer therapeutics

Examination committee:

Supervisor

Dr. Velumani Subramaniam (Department of Electrical Engineering - SEES)

Co-supervisor

Dr. Jose Tapia Ramirez (Department of Genetics and Molecular Biology)

Committee members:

Dr. Miguel Garcia Rocha (Department of Physics)

Dr. Jaime Santoyo Salazar (Department of Physics)

Dr. Arturo Vera Hernandez (Department of Electrical Engineering - Section of Bioelectronics)

Dr. Mauricio Ortega López (Department of Electrical Engineering - SEES)

External Examiner:

Dr. J. Enrique Chong Quero (Mechatronics Department at ITESM - CEM)

Declaration

I hereby declare that the work presented in this thesis entitled "**Design and evaluation of plasmonic/magnetic Au-MFe_2O_4 (M-Fe/Co/Mn) core-shell nanoparticles functionalized with Doxorubicin for cancer therapeutics**" is submitted for the degree of *Doctor of Philosophy in Science (Specialized in Nanoscience and Nanotechnology)* has been carried out by me at Center for Research and Advanced Studies of the National Polytechnic Institute (*CINVESTAV-IPN*), Zacatenco, Mexico city under the joint supervision of Dr. S.Velumani and Dr. Jose Tapia Ramirez. The work is original and has not been submitted in part or full by me for award of any other degree or diploma in any other University.

RAVICHANDRAN MANISEKARAN

8th Marzo 2017

To my family, friends, professors and especially to my brother

"It doesn't matter how beautiful your theory is, it doesn't matter how smart you are. If it doesn't agree with experiment, it's wrong"

- **Richard Feynman**

"It ain't about how hard you hit. It's about how hard you can get hit and keep moving forward!"

- **Sylvester Stallone**

"The world is your oyster. It's up to you to find the pearls"

- **Chris Gardner**

Table of Contents

Abstract

Medical scientists in the field of nanomedicine are exploring novel hybrid nanomaterials for efficient designing of multifunctional nanoflotillas. Over the past few years, the combination of magnetic and plasmonic nanoparticles have drawn major interest due to their unique characteristics. Undoubtedly, iron oxide nanoparticles were considered as an efficient flotilla and the engineering of such a biomedical platform with a biocompatible surface coating usually gold shell provides stabilization under various physiological conditions. This modular design enables these nanoparticles to perform multiple functions simultaneously, such as in multimodal imaging, drug delivery and real-time monitoring, as well as combined therapeutic approaches which serve as one of the most promising candidate for various biological applications.

So, in this thesis we have developed a multifunctional magneto-plasmonic core-shell nanoparticles by iterative seeding based method. This nanocargo consists of an iron oxide nanokernel (Fe_3O_4, $CoFe_2O_4$, $MnFe_2O_4$) as a core and multiple layers of gold as a functionalizable active stratum. Gold coated iron oxide nanokernel helps in augmenting the physiological stability and enhancing surface plasmon resonance property. We have also proposed a novel aspect of site-specific targeting of Doxorubicin using iterative core-shell nanoparticles as a nanopayload and folic acid as a targeting agent for cancerous cells. The multiple gold iterations and difference in shell size and shapes have been well explained using XRD and HRTEM. HAADF-STEM and line mapping confirms the formation of core-shell structure. One single layer of Au on nanokernel offers the capability of binding drugs, but multiple coating further augments the physiological stability and tunes surface plasmon resonance as well as dielectrics for proficient loading of drugs as well as pH-dependent release in specific microenvironment. The functionalization of folic acid and Doxorubicin was confirmed by UV-Visible spectroscopy, FTIR and TGA which confirmed the formation of non-covalent interactions. SQUID explained the efficacy of iterative method by confirming that even after multiple Au iterations, the core-shell nanoparticles was highly superparamagnetic. The stability of nanoparticles was scrutinized by measuring the zeta potential measurements, which was found to be in the range of -5 to -40 at different pH. The nanoparticle complex was found to be non-toxic for normal cells and considerably toxic for Hep2 cells detected by confocal microscopy and MTT assay. The drug loading capacity was

found to be more than 80%. The targeted delivery of Doxorubicin using gold coated iron oxide nanokernel as a nanopayload is demonstrated in this thesis. Drug-release was carried out at 3 different pH like 5.4, 6.8 & 7.4 and found that at pH 5.4 the release is maximum which is favourable for cancer cell treatment. Doxorubicin release kinetics profile has been fit based on Zero-order, First Order, Higuchi and Hixson-Crowell model. MRI showed that the core-shell possess enhanced T_2 contrast for imaging both normal and cancer cells. Microwave based magnetic hyperthermia studies exhibited an augmentation in the temperature due to the transformation of radiation energy into heat at 2.45 GHz. There was an enhancement in cancer cell cytotoxicity when hyperthermia combined with chemotherapy. Hence, this single nanoplatform can deliver 3-pronged theranostic applications viz., targeted drug-delivery, MR imaging and hyperthermia. This drug delivery system can act as an efficient nanocarrier in the cancer micromilieu for synaphic targeting, diagnosing and assassinating of the cancer cells, thus rescuing the life of patients.

Keywords: *Iron oxide, Gold, Core-shell nanoparticles, Folic acid, Doxorubicin*

Resumen

Los científicos médicos en el campo de la nanomedicina están explorando nuevos nanomateriales híbridos para el diseño eficiente de nanoflotillas multifuncionales. En los últimos años, la combinación de nanopartículas magnéticas y plasmónicas han dibujado un gran interés debido a sus características únicas. Sin lugar a dudas, las nanopartículas de óxido de hierro se consideraron como una flotilla eficiente y la ingeniería de una plataforma de este tipo biomédico con un revestimiento de la superficie biocompatible generalmente concha de oro proporciona estabilización en diversas condiciones fisiológicas. Este diseño modular permite que estas nanopartículas para realizar múltiples funciones simultáneamente, como en formación de imágenes multimodal, administración de fármacos y monitorización en tiempo real, así como enfoques terapéuticos combinados que sirven como uno de los candidatos más prometedores para diversas aplicaciones biológicas.

Por lo tanto, en esta tesis se ha desarrollado un magneto-plasmónica multifuncionales nanopartículas core-shell por método basado en la siembra iterativo. Este nanocargo consiste en un nanokernel óxido de hierro (Fe_3O_4, $CoFe_2O_4$, $MnFe_2O_4$) como un núcleo y múltiples capas de oro como un estrato activo funcionalizable. recubierto de oro nanokernel óxido de hierro ayuda en el aumento de la estabilidad fisiológica y la mejora de la propiedad de resonancia de plasmón de superficie. También hemos propuesto un nuevo aspecto de la orientación específica de sitio de doxorrubicina utilizando nanopartículas core-shell iterativos como nanopayload y ácido fólico como agente de dirección para las células cancerosas. Las múltiples iteraciones de oro y diferencia en el tamaño de la carcasa y formas han sido bien explicada mediante DRX y HRTEM. HAADF-STEM y asignación de las líneas confirma la formación de la estructura de núcleo-corteza. Una sola capa de Au en nanokernel ofrece la capacidad de unión a las drogas, pero recubrimiento múltiple aumenta aún más la estabilidad fisiológica y melodías de resonancia de plasmones, así como dieléctricos para la carga competentes de las drogas, así como la liberación dependiente del pH en el microambiente específico de la superficie. La funcionalización de ácido fólico y doxorrubicina se confirmó por espectroscopía UV-Visible, FTIR y TGA que confirmó la formación de interacciones no covalentes. SQUID explica la eficacia del método iterativo mediante la confirmación de que, incluso después de múltiples iteraciones Au, las nanopartículas core-shell fue altamente superparamagnético. La estabilidad de las nanopartículas fue analizado mediante la medición

de las mediciones de potencial zeta, que se encontró a estar en el intervalo de -5 a -40 a diferentes pH. Se encontró que el complejo de nanopartículas para ser no tóxicos para las células normales y considerablemente tóxica para las células Hep2 detectados por microscopía confocal y el ensayo de MTT. Se encontró que la capacidad de carga de fármaco para ser más de 80%. La distribución selectiva de doxorrubicina utilizando nanokernel óxido de hierro recubierto de oro como nanopayload se demuestra en esta tesis. De liberación de fármaco se llevó a cabo en 3 pH diferente, como 5,4, 6,8 y 7,4 y se encontró que a pH 5,4 la liberación es máximo, que es favorable para el tratamiento de células de cáncer. Doxorrubicina perfil cinética de liberación ha sido adaptarse sobre la base de orden cero, de primer orden, Higuchi y el modelo Hixson-Crowell. Resonancia magnética mostró que el core-shell posee contraste T2 mejorada para las células de imágenes normales y cancerosas. estudios de hipertermia magnética basados microondas exhibieron un aumento en la temperatura debido a la transformación de energía de radiación en calor a 2,45 GHz. Hubo una mejora en la citotoxicidad de células de cáncer cuando la hipertermia se combina con la quimioterapia. Por lo tanto, este único nanoplataforma puede ofrecer aplicaciones teranósticos de 3 puntas a saber., Dirigida administración de fármacos, la RM y la hipertermia. Este sistema de administración de fármaco puede actuar como un nanotransportador eficiente en el micromilieu cáncer para la orientación synaphic, diagnosticar y asesinar de las células cancerosas, rescatando así la vida de los pacientes.

Palabras clave: *óxido de hierro, oro, las nanopartículas core-shell, ácido fólico, doxorrubicina*

Compilation thesis

This thesis is a compilation of one book chapter and three research articles. The contribution of the candidate and co-authors includes chapters 1 & 2, 4, 5, and 6 are hereby set forth.

Chapter 1 & 2: based on published book chapter.

Goldie Oza, M. Ravichandran, Pravin Jagadale, S. Velumani, Engineering of Nanobiomaterials, Chapter 14: Inorganic nanoflotillas as engineered particles for drug and gene delivery, 1st Edition, Volume 2, Applications of Nanobiomaterials, Edited by A. Grumezescu, pages 429-483; 01/2016, Elsevier, ISBN: 9780323415323. Doi: http://dx.doi.org/10.1016/B978-0-323-41532-3.00014-2

Chapter 4: based on research article which is under communication.

M.Ravichandran, Goldie Oza, S. Velumani, Jose Tapia Ramirez, A. Vera, L. Leija, Designing a versatile nanocargo as a tri-pronged kunai for cancer therapy

Chapter 5: based of published research article.

Ravichandran, M. et al. Plasmonic/Magnetic Multifunctional nanoplatform for Cancer Theranostics, Sci. Rep. 6, 34874; Doi: 10.1038/srep34874 (2016)

Chapter 6: based on research article in preparation for communication.

Nano-Flotillas $MnFe_2O_4$@Au core-shell nanoparticles: An efficient MRI contrast agent, magneto-hyperthermal and drug-delivery armada for cancer

Acknowledgements

"The more I study science, the more I believe in God"

-Albert Einstein

Performing a doctorate research was been a phenomenal experience. This journey made me to expand my skills and learning process of different aspects which will be very helpful for my life and also for the future research. The two most important skills I developed for life long was patience and emotions ranging from thrilling excitement to disappointment happened during the last four years.

"If a country is to be corruption free and become a nation of beautiful minds, I strongly feel there are three key societal members who can make a difference. They are the father, the mother and the teacher"

-Abdul Kalam

I extend my sincere gratitude towards all the people who made this research work described in this thesis possible. First and foremost reverent and hearty thanks to my research supervisors Dr. S. Velumani and Dr. Jose Tapia Ramirez for their constant support, valuable suggestions, encouragement, and advices. I will be always thankful for teaching me many lessons of life directly or indirectly apart from research. It is my privilege for me to work under their guidance. I am really thankful to them for always giving me a motivation and freedom to work in the various departments and interdisciplinary field of cancer theranostics.

"A good teacher can inspire hope, ignite the imagination, and instill a love of learning"

-Brad Henry

Thanks to the examination committee members and external examiner: Prof. Miguel Garcia Rocha (Physics department), Prof. Jaime Santoyo Salazar (Physics department), Prof. Arturo Vera Hernandez (Electrical engineering - Bioelectronics section), Prof. Mauricio Ortega López (Electrical Engineering department - SEES), and Prof. J. Enrique Chong Quero [Mechatronics Department at Instituto Tecnológico y de Estudios Superiores de Monterrey (ITESM) – Campus Estado de México (CEM)] for critical reading of the thesis and giving me valuable suggestions & comments which improved the quality of the thesis. And also appreciate the contributions of all the co-authors in the various manuscripts for their continuous support technically and interpreting the results for publishing and finally, thank

Nanoscience and Nanotechnology program coordinator Dr. Jose Gerardo Cabanas Moreno for his complete support throughout the PhD program.

"Collaborate with people you can learn from"

-Pharrell Williams

Collaborations from various departments (Physics, Cell biology, Electrical engineering – SEES, Bioelectronics, Chemistry, Molecular Pathogenesis and infectómica, Toxicology, LANE, LANSE,) of CINVESTAV-IPN, Universidad Autónoma de Nuevo León (UANL) - Nuevo León, Centro Nacional de Investigación en Imagenología e Instrumentación Médica (CI^3M), Universidad Autónoma Metropolitana - Iztapalapa (UAM-I), Instituto de Investigaciones en Materiales (IIM), Universidad Nacional Autónoma de México (UNAM), Mexico. Thank you all.

"We rise by lifting others"

-Robert Ingersoll

I convey my sincere thanks to all department secretaries especially Alma Mercedes Zamudio Martínez, Jessica Marquez Duenas, María Ofelia Muñoz Ramírez from Nanoscience program for their continuous help in many things and Oscar Ivan Buendia Montano Department of Becas y Estímulos (Scholarship dept.) for his valuable aid in processing the scholarship and conference commission documents which made me comfortable to carry out my various documentation works. Appreciation will be essential for auxiliaries, technicians and some of the professors from various departments and institutes for their collaboration for characterizing the samples. I would like to thank Dr. Daniel Bahena Uribe, M. en I. Alvaro Ángeles Pascual (LANE, HRTEM analysis), Q.F.B. Sirenia González Posos (LANSE, TEM analysis), Dr. Jorge Roque De La Puente (LANE, FESEM analysis), Prof. Sergio Tomas (Physics department, XPS analysis), M. en C. Miguel Galván Arellano (SEES, Raman spec), Ing. Angela Gabriela López Fabián (SEES, UV-Vis spec), M. en C. Adolfo Tavira Fuentes (SEES, XRD analysis), Adolfo Tavira Fuentes, Ing. Marcela Guerrero (Physics department, XRD and FTIR analysis), Dr. L. Leija, Jaime E Lara, M. en C. José Hugo Zepeda Peralta (Bioelectronics department, Hyperthermia studies), Dr. Francisco Garcia-Sierra, Norma Barragán Andrade (Cell Biology department, MTT assay, confocal studies etc.), Dr. Rodríguez Mario Alberto (CryoEM microsocpy), Q.B.P. Carlos Vazquez Calzada (Molecular Pathogenesis and infectómica, Confocal microscopy), Dra. Andrea De Vizcaya Ruiz (Zeta potential measurements, Toxicology department), Dr. Marco A.Garza-Navarro, Dr. Domingo

I.Garcia-Gutierrez (Mechanical and electrical engineering Department, SQUID analysis, UANL), Ing. Rafael Lara-Estrada, Dr. Emilio Sacristán-Rock (Electrical Engineering department, MR imaging, CI^{3}M, UAM), Dr. Francisco Manuel Sánchez Arévalo and Dr. Aarón Rojas Aguilar (TGA analysis, IIM, UNAM & Department of Chemistry, CINVESTAV-IPN) for their technical assistance in various characterizations without whom it would have not been possible to complete my research studies.

"We are a studying nation. Scholarship from science is important to the whole world and those people need to be able to be safe and secure in what they do"

-Malcolm Wallop

I would like to acknowledge for the PhD scholarship awarded by the Consejo Nacional De Ciencia Y Tecnología (CONACYT), Mexico and thank the CONACYT project No: 168577 for funding the four year research project. Finally, I also thank Sistema de Información Académica (SINAC) from CINVESTAV-IPN for financially supporting the conferences like IMRC, Cancun and Magnetic carrier conference, Canada.

"A friend is one that knows you as you are, understands where you have been, accepts what you have become, and still, gently allows you to grow"

-William Shakespeare

I express my cheerful thanks to my friends/brothers Dr. Sathish Balaji, Dr. Prashant Jawahar, Dr. Vignesh Natarajan, Dr. Mohamed Anjum, Dr. Atwar Hussain, and Dr. Raghavendran who gave their continuous support in many ways during my hard time of life. And also thank specially my friend Dr. Gayathri Devi Sivasankar, for being a good motivator.

"Colleagues should take care of each other, have fun, celebrate success, learn by failure, look for reasons to praise not to criticize, communicate freely and respect each other"

-Richard Branson

I want to thank my colleagues Dr. Goldie Oza for his guidance & motivation, Dr. Pablo Reyes Figuero, Dr. Rohini Neendoor Mohan, Dr. Victor Ishrayelu Merupo, M. en C. Latha Marasamy & M. en C. Aruna Devi Rasu Chettiar from whom i have learned some aspects of semiconductors, which will be helpful in the coming future. I also thank my other department friends for their discussions and good company.

"Rejoice with your family in the beautiful land of life!"

-Albert Einstein

Finally, I would take this rare opportunity to pay my high commendations to my lovable parents (Mr. G. Manisekaran & Mrs. Shanthi) for their unconditional love & support and making me to continue studies even during their tough times of life without them it would be impossible to achieve their dream. My special thanks to my brother (G.M.Ramkumar) for his help, moral support, guidance and keep boosting my confidence level to face any situation in the society. Lastly, I thank my sister (M. Manjula) being a second mother. So, without my family members backup i can't even imagine my doctoral research studies and also my academic journey. With their persistent love, and prayers, i am able to go through all the difficulties anytime.

"I can no other answer make but thanks, and thanks, and ever thanks..."

-William Shakespeare

Thank you all!

Best wishes & Regards,

Ravichandran Manisekaran

Contents

List of Figures

Chapter 1

Chapter 4

List of Tables

List of Abbreviations

AA	L-Ascorbic acid
AC	Alternating current
Ag	Silver
$AgNO_3$	Silver nitrate
Al	Aluminium
AMF	Alternating magnetic field
APCs	Antigen-presenting cells
Au	Gold
Ba	Barium
C	Carbon
CAR	Coxsackie and Adenovirus receptor
CARS	Coherent Anti-Stokes Raman scattering
CD	Cluster of Differentiation
CLSM	Confocal laser scanning microscopy
Co	Cobalt
CO_2	Carbon dioxide
CSNPs	Core-Shell Nanoparticles
CTAB	Hexadecyltrimethylammonium bromide
CT	Computed Tomography
Cu	Copper
3D	Three dimensional
Da	Daltons
D-Ala/L-Ala	D-Alanine/L-Alanine
DC	Dendritic cells
D-Glu	D-Glutamic acid
D-Lac	D-lactate
DCC	N, N'-Dicyclohexylcarbodiimide
DI	Deionized water
DM	Dextran magnetite
DMEM	Dulbecco's Modified Eagle Medium
DMSO	Dimethyl sulfoxide
DNA	Deoxyribonucleic acid
Dox	Doxorubicin hydrochloride
Dox-FA-CSNPs	Doxorubicin coated Folic Acid attached Core-Shell Nanoparticles
EDS	Energy Dispersive X-Ray Spectrometer
EGFR	Epidermal growth factor receptor
EM	Electromagnetic waves
EPR	Enhanced Permeability and Retention effect
Er	Erbium

f	Frequency
FA	Folic acid
FA-CSNPs	Folic Acid attached Core-Shell Nanoparticles
FBS	Fetal Bovine Serum
FDA	Food and Drug Administration
Fe	Iron
Fe_2O_3	Maghemite
Fe_3O_4	Magnetite
FOV	Field of Vision
FR	Folate receptors
FTIR	Fourier Transform Infrared Spectroscopy
FWHM	Full width at half maximum
Gd	Gadolinium
H	Hydrogen
H	Applied magnetic field
H_2O_2	Hydrogen peroxide
Hb	Hemoglobin
HC	Coercivity
HAADF-STEM	High-Angle Annular Dark-Field Scanning Transmission Electron Microscopy
$HAuCl_4$	Chloroauric acid
He-Ne	Helium-Neon
HPG	Hydrostatic pressure gradient
HRTEM	High Resolution Transmission Electron Microscopy
HSP70	Heat shock protein 70
Hz	Hertz
IFP	Interstitial fluid pressure
IONPs	Iron oxide nanoparticles
IV	Intravenously
JCPDS	Joint Committee on Powder Diffraction Standards
L-Lys	L-lysine
LNA	Locked nucleic acids
LSCM	Laser Scanning Confocal Microscopy
M	Magnetization
Mb	Myoglobin
MCL	Magnetite cationic liposomes
Mf	Manganese Ferrite nanoparticles
Mf@A	Gold coated manganese ferrite nanoparticles
MGCE	Magnetic glassy carbon electrode
MIC	Minimal inhibitory concentration
Mn	Manganese

$MnFe_2O_4$	Manganese Ferrite
MNPs@Au	Gold coated magnetic nanoparticles
Mr	Remanence
MR	Magnetic Resonance
MRS	Magnetic resonance spectroscopy
MRSA	Methicillin-resistant Staphylococcus aureus
MS	Magnetic saturation
MTT	3-(4,5-dimethylthiazol-2-yl) 2,5-diphenyltetrazolium bromide
Mw	Microwave
MwA	Microwave Ablation
MW	Molecular Weight
N_2	Nitrogen
$NaBH_4$	Sodium borohydride
NaOH	Sodium hydroxide
NaCl	Sodium chloride
NdFeB	Neodymium Iron Boron
NHS	N-Hydroxysuccinimide
NIR	Near-Infrared
Nk@A	Gold coated cobalt iron oxide nanokernels
NPs	Nanoparticles
O	Oxygen
OD	Optical density
ODNs	Oligodioxynucleotides
PBS	Phosphate buffer saline
Pd	Palladium
PD	Pharmacodynamics
PDDA	Poly(diallyldimethylammonium chloride)
PECA	Poly(ethyl-2-cyanoacrylate)
PEG	Polyethylene glycol
pH	Potential of Hydrogen
PK	Pharmacokinetics
PL	Photoluminescence
PPTT	Plasmonic Photothermal therapy
PTT	Photothermal therapy
PZS	Poly(cyclotriphosphazene-*co*-4,4'-sulfonyldiphenol)
QDs	Quantum dots
R^2	Regression coefficient
RES	Reticuloendothelial system
RF	Radio Frequency
RGB	Red-Green-Blue
RNA	Ribonucleic acid

ROS	Reactive oxygen species
S	Thiol functional group
SAR	Specific absorption rate
SAED	Surface analysis of electron diffraction
SEM	Scanning electron microscopy
SERS	Surface enhanced Raman spectroscopy
SiO_2	Silicon dioxide
siRNA	small interfering RNA
SLP	Specific loss power
SPIONs	Superparamagnetic Iron Oxide Nanoparticles
SPR	Surface Plasmon Resonance
SQUID	Superconducting Quantum Interference Device
SWR	Standing Wave Ratio
T_1	Spin-lattice relaxation
T_2	Spin-spin relaxation
TB	Blocking temperature
TBO	Toluidine blue O
TE	Echo time
TEA	Triethylamine
TEOS	Tetraethyl orthosilicate
TGA	Thermogravimetric Analysis
Tm	Thulium
TNF	Tumor necrosis factor
TR	Repetition time
USD	United States Dollar
UV-Vis	Ultra Violet-Visible
VRE	Vancomycin-resistant Enterococci
WHO	World Health Organization
XPS	X-ray Photoelectron Spectroscopy
XRD	X-Ray Diffraction
Yb	Ytterbium
Z	Atomic number

List of Symbols

α	Alpha
C	Celcius
cm	Centimetre
emu	Electromagnetic unit
eV	Electron-Volt
γ	Gamma
GHz	GigaHertz
gm	Gram
h	Hour
J	Joule
K	Kelvin
kcal	kilocalories
kDa	KiloDalton
kOe	KiloOersted
M/mol	Molarity
mg	Milligram
min	Minutes
ml	Millilitre
mm	Millimetre
mM	Millimolar
msec	Millisecond
mW	MilliWatt
mV	MilliVolt
nm	Nanometre
χ	Magnetic susceptibility
%	Percentage
r_2	Transverse relaxivity
sec	Seconds
U	Units
Θ	Theta
µg	Microgram
µl	Microlitre
W	Watt
ζ	Zeta

CHAPTER 1

Introduction to Nanomedicine & Cancer therapy

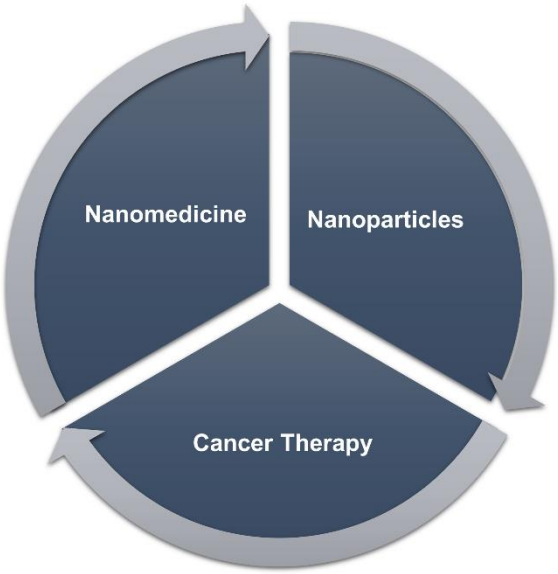

Table of Contents

1. Introduction

1.1 Nanomedicine

Nanomedicine, the application of different nanostructures in the field of medicine which is aiming to revolutionize the health of humankind by a new developmental sector of nanopharmaceuticals[1]. The rapid evolution of nanomedicines has the huge probability to give many benefits when correlated to conventional medicines[2]. The major advantage of nanomedicine is to create a multifunctional platform using one nanostructure. Therefore, the various properties of nanostructures/NPs are exploited as tools in all aspect of medicine starting from diagnosis to treatment even at a molecular or cellular level for very rare and irremediable diseases[3]. Some of the application of nanomedicine are as follows: drug delivery, therapies, *in vivo* imaging, *in vitro* diagnostics, biomaterials, active implants, bone substitute materials, dental restoratives and antibiotic materials[4–6]. In the last two decades, significant progress has been made in the field of nanomedicine and nanobiotechnology, resulting in an enormous number of products. So, by the end of 2020, one-third of research patents and many start-up companies in the nanomedicine sector will engage in the biomedical applications[7]. To be specific, as of 2013-1265 molecules are registered for clinical trials in which 789 were for nanomedicine applications or products[8]. **Figure 1.1** represents the list of some of the important nanomedicine-related search terms in ClinicalTrials.gov[9]. Therefore this proves the field of nanomedicine is booming at a faster rate. The global nanomedicine market was $1 trillion by 2015 but expected to be 100 fold in just 7 years[10].

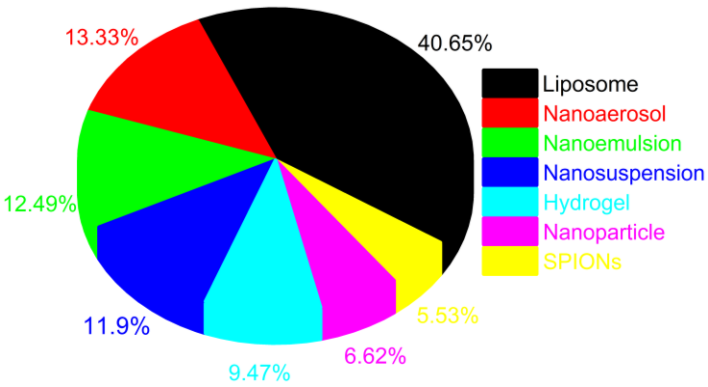

Figure 1.1. ClinicalTrials.gov search terms with the number of results (*Adapted with the permission from*[11])

From the growth of nanopharmaceuticals field[12] it is expected that the drug nanocrystals will majorly contribute in the market by the year 2021, generating ≈ $81.921

million USD[13], which is of 60:40 split in the market between nanocrystals and classic drug delivery systems[10]. It also contributes equally to diagnostics devices based on NPs[11] (**Figure 1.2**).

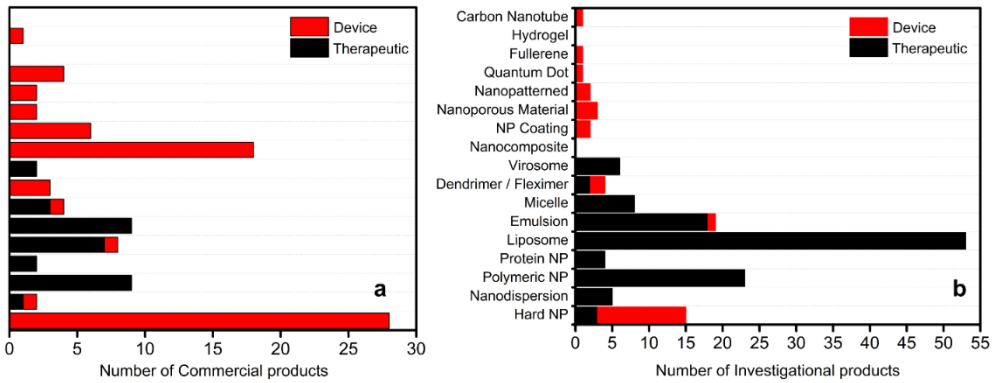

Figure 1.2. Graph representing the number of nanostructure based device and therapeutics in investigation and commercial product (*Adapted with the permission from*[11])

But the application of nanomedicine products will have to pass through different developmental stages, from basic research to a commercialized product in the market[8] (**Figure 1.3**). Most of the nanomedicine which is anticipated in the research will take more years from clinical use.

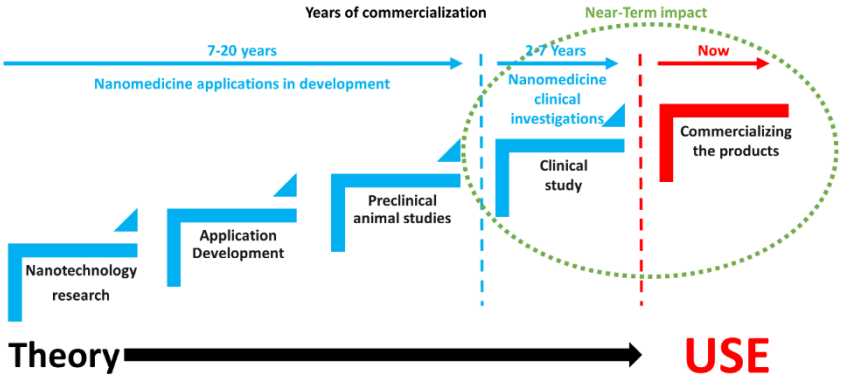

Figure 1.3. Five general stages of nanomedicine development (*Adapted with the permission from*[11])

Foresight and assessments represent a very bright future for both therapeutic and diagnostic uses in nanomedicine. As a matter of fact, nanomedicines sector may excel other nanotechnologies because it is one of the few that has a distinct market in healthcare. To prove the above statement, **Table 1.1, 1.2 & 1.3** represents some of the nano based drugs, devices, and implants which are approved by FDA and currently available for clinical use in many countries.

Table 1.1. Some of the FDA-Approved Agents utilizing Nanomedicine (*The table is reproduced with permission from reference*[11])

Trade Name	Active Ingredient	Indication	Approval
Abelcet	Liposomal amphotericin B	Invasive fungal infections	1995
Abraxane	Albumin protein-bound paclitaxel	Metastatic breast cancer	2005
Adagen	Pegylated adenosine deaminase enzyme	Severe combined immunodeficiency disease	1990
Alimta	Pemetrexed	Nonsquamous NSCLC, malignant pleural mesothelioma	2004
AmBisome	Liposomal amphotericin B	Fungal infections, leishmaniasis	1997
Cimzia	Pegylated Fab´ fragment of a humanized anti–TNF-alpha antibody	Crohn's disease, rheumatoid arthritis	2008
Copaxone	Glatiramer acetate	Multiple sclerosis	1996
DaunoXome	Liposomal daunorubicin citrate	HIV-associated Kaposi's sarcoma	1996
Depocyt(e)	Liposomal cytosine arabinoside	Lymphomatous meningitis	1999
Doxil	Pegylated-stabilized liposomal doxorubicin	AIDS-related Kaposi's sarcoma, refractory ovarian cancer, multiple myeloma	1995
Emend	Aprepitant nanocrystal particles	Chemotherapy-related nausea and vomiting	2003
Macugen	Pegaptanib	Wet age related macular degeneration	2004
Neulasta	Pegfilgrastim	Chemotherapy-associated neutropenia	2002
Oncaspar	PEG-asparaginase	Acute lymphocytic leukemia	1994
Ontak	Interleukin-2 diphtheria toxin fusion protein	Cutaneous T-cell lymphoma	1999
Pegasys	Peginterferon alpha-2a	Hepatitis B and C	2002
Renagel	Amine-loaded polymer	Serum phosphorus control in patients with CKD on dialysis	2000
Tricor	Fenofibrate	Hypercholesterolemia, mixed dyslipidemia, hypertriglyceridemia	2004

Table 1.2. Examples of applications of nanomaterials in implants (*The table is reproduced with permission from reference*[11])

Medical area	Nanomaterials used	Commercial name
Implants and prosthetics	Nano-hydroxyapatite	BoneSource (Lebinger)
Orthopaedic	Silver NP solution	Silvagard (AcryMed, 2005)
Wound management	Nano-hydroxyapatite	UltraDEX Recalcifying
Dental/dental care products	Nanoporous hydroxyapatite	(Periproducts)
Cardiac implants	Ultraporous beta-tricalcium	Vestasync (MIV Therapeutics)
Bone replacement scaffold	phosphate NPs	Vitoss (Orthovita, 2000)

Table 1.3. Medical Devices and Diagnostics utilizing Nanomedicine (*The table is reproduced with permission from reference*[14])

Name	Device/Diagnostic Type	Application	Manufacturer	Year Approved
FDA-Approved				
CellSearch	Antibodies bound to IO NPs	CTC detection	Veridex	2004
DNAarray	Lab-on-a-chip	DNA-based tests	CombiMatrix	2005
Gastromark	Silicone-coated ferumoxsil SPIOs	MRI contrast agent	AMAG Pharmaceuticals	1996
MultiHance	Gadolinium-based NPs	MRI contrast agent	Bracco Group	2004
Optimark	Gadolinium-based NPs	MRI contrast agent	Mallinckrodt	1999
Omniscan	Gadolinium-based NPs	MRI contrast agent	General Electric	1993
Silvagard	Silver NP solution	Anti-infective coating	AcryMed, Inc.	2005
Verigene	Functionalized gold NPs	Diagnostic tests	Nanosphere	2007
Vitoss	Ultraporous beta-TCP NPs	Bone-replacement scaffold	Orthovita	2000
Investigational				**Status (U.S.)**
Combidex	Dextran-coated ferumoxtran-10 USPIOs	MRI contrast agent	Advanced Magnetics	Phase 1, 2, 4
MagProbe	CD34 antibody-linked NPs/magnetic biopsy needle	Leukemia diagnosis	Senior Scientific	Phase 1
NanoTherm therapy	Aminosaline-coated IO NPs	Thermal ablation/hyperthermia therapy for liver, pancreatic cancer	MagForce AG	Preclinical

Finally, the unique properties of nanomedicines can effectively provide innovative solutions for treating many diseases. And a number of FDA-approved products and devices containing nanomaterials have already become available which is advancing the medicine and improving health care with a big hit. Even though there are various barriers that interfere the designing and availability of nano based medical products, it is expected that various scientific research in this operation will continue at a rapid pace, making these products become an essential segment of regular medicine in the coming future[14].

1.2 Cancer therapy

Currently, cancer is a second leading disease which causes major death in the world next to cardiac diseases[15]. Cancer causing factors include genetic factors; lifestyle factors, some types of infections and exposures to types of certain chemicals and radiation. According to the expert's prediction, there will be 22 million new cases each year[16] (**Figure 1.4)**.

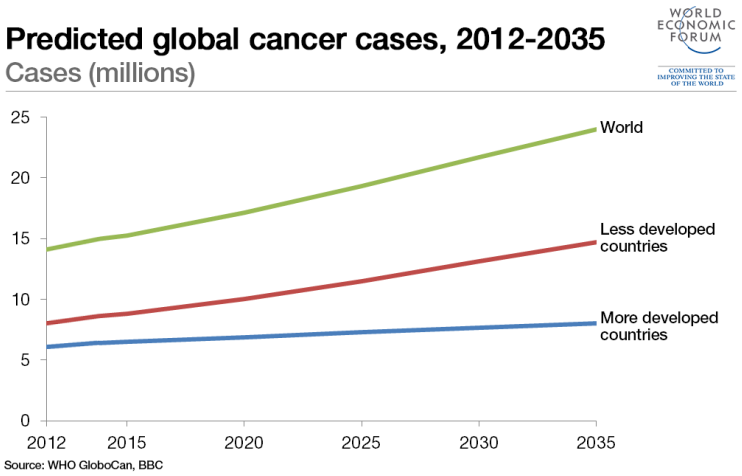

Figure 1.4. Predicted global cancer cases from 2012 to 2035 by WHO

In the present scenario, the treatment for common types of cancer is surgery, chemotherapy, radiation therapy, etc[17]. Even though these treatments have undoubtedly improved the survival of the cancer patients but they are certain drawbacks. For example, in case of prevailing cancer chemotherapy, the drugs distribute nonspecifically in the patient body, thus affecting both cancerous and normal cells[18]. Thus causing serious side-effects to normal tissues, cells, and organs, leading to a low quality of life for cancer patients[19]. Cancer treatments represent to be the largest therapeutic area for approved many nanomedicines, as well as for patents and research publications[20]. Therefore, many research attempts are made worldwide to attack only cancer cells specifically by sparing normal cells. So to accomplish the above goals, scientists are now focused to design new and better drugs to treat the cancer cells at the molecular level by employing the field of nanomedicine or nanopharmaceuticals[13]. These fields are selected appropriately by considering some of the inevitable characteristics such as

- biodegradability,
- biocompatibility,
- conjugation,
- Complexation or encapsulation[21].

Some of the important strategies for designing multifunctional nanostructures for cancer theranostics involve:

(1) Encapsulation and/or

(2) Covalent or noncovalent binding of components

which allows to recognize the cancer; allow tumor imaging, deliver a drug and kill the tumor cells[22]. The nanopharmaceuticals also aims to achieve a drugs with better advantages including,

- enhancing solubility of drugs,
- increasing the circulation time,
- decreasing non-specific uptake,
- avoiding side effects,
- intracellular penetration,
- ultimately aiming for specific cancer cell targeting,
- designing multifunctional NPs,

are developed and used for cancer theranostics to overcome the classical cancer treatments[23–28]. By achieving these goals there are already more than 20% of the therapeutic nanoparticulate systems already in the market for anticancer applications.

In cancer treatments, multifunctional nanosystems are completely dependent on the enhanced permeability and retention effect (EPR) caused by leaky vasculatures for the better accumulation of drug at the tumor sites[29,30]. But the NP size should be in the range of 20-100 nm to exploit the EPR effect[31]. These effect has given a pathway for various therapeutic NPs as a promising candidate to take over the traditional chemotherapy by killing or targeting only the cancer target site leaving the normal cells with negligible side-effects.

Currently, several NP-based chemotherapeutics have emerged in the market, while many of them are undergoing various stages of clinical or preclinical development (**Table 1.4**). Some notable examples are Doxil and Abraxane, both are administered as a first-line treatments in several types of cancer[32–35].

Table 1.4 Some of the examples of investigational agents for various types of cancers in U.S.

(*The table is reproduced with permission from reference*[14])

Name	Active Ingredient	Condition	Status in U.S.
Aurimune	Recombinant human TNF conjugated to gold NPs	Solid tumors	Phase 1
AuroShell	Gold-coated silica nanoshells	Head and neck cancer, solid tumors	Phase 1
BikDD NP	Liposomal pro-apoptotic Bik gene (BikDD)	Pancreatic cancer	Phase 1
BIND-014	Targeted multifunctional polymeric NP complex containing docetaxel	Advanced or metastatic cancer, solid tumors	Phase 1
CALAA-01	Anti-R2 siRNA/cyclodextran-containing polymer (CAL 101) and targeting agent (AD-PEG-Tf)	Solid tumors refractory to standard-of-care agents	Phase 1
Docetaxel-PNP	Docetaxel polymeric NPs	Advanced solid malignancies	Phase 1
Genexol-PM	Methoxy PEG–PLA paclitaxel	Breast and lung cancer	Phase 2
Myocet	Liposomal doxorubicin	Metastatic breast cancer	Phase 3
Rexin-G	Dominant-negative cyclin G1 construct pathotropic NP	Recurrent or metastatic breast cancer, pancreatic cancer, sarcoma	Phase 1, 2

Therefore, several NPs are designed in various ways with surface modifications, encapsulations etc., which have been widely investigated from diagnosis to therapy for cancer applications. This concept is becoming more and more common to many chemotherapies, gene therapies including optical, ultrasound, computed tomography (CT), MR imaging and nuclear imaging. These nanoparticle based systems are highly efficient to deliver the payload to a specific region by which not only treated but also to diagnose using imaging techniques with minor side-effects which are the main motto of nanomedicine based therapy for cancer treatment. This is achieved even with nanomole and picomole concentration of high sensitivity. With these promising advantageous method/techniques, it plays an important role for future cancer medicine.

1.3 Essential properties of nanoparticles for Therapeutic purpose and their applications in cancer

1.3.1 Essential properties of nanoparticles for Therapeutic purpose

The prevalent use of NPs for various biomedical applications continues to grow rapidly with high significance because of its unique properties[36,37]. Some of the basic properties plays an important role to make NPs unique which are as follows[38]:

- NP as scaffolds,
- Surface area of NPs,
- Size matters!,
- Optical properties,
- Magnetic properties,
- NPs platform.

1.3.1.1 Nanoparticle as scaffolds

Metallic NPs act as a platform or scaffold for the assemblage of multifunctional structures. They are colloidal suspensions, soluble in complex environments such as blood and tissues. They can be efficiently utilized for a plethora of applications such as sensing, imaging, and targeting of NPs inside the physiological system. This proficiency is enhanced by surface orchestration, ligand binding and slight alterations in the composition of the NP assembly[39,40]. Surface orchestrations such as polymers, lipids, peptides, DNA on the inorganic NPs help them to be stable due to electrostatic and steric effects, both. Ligands such as antibodies, enzymes bound to the NPs can tether surface receptors or substrates on the cellular exterior. Inorganic NPs can be doped by different metals so that there is physiologically desirable change in their properties, which helps them to maintain stability, biocompatibility, effective biodistribution and clearance capabilities. When the stability of NPs are ensured, then they are used for functionalization with drug/genes, fluorescent dyes, targeting ligands, so that they act as an efficient theranostic agent[41,42].

1.3.1.2 Surface area of nanoparticles

The surface to volume ratio is considered to be one of the important criteria for the properties of NPs. For example, the stability and versatility of NPs are completely depend on the large surface to volume ratio. This property can be tuned by controlling the size of the materials which plays a vital role in optimizing drug payloads and other NP based interactions.

And this makes the nanomaterials different from the bulk[43]. **Figure. 1.5** illustrates the high surface to volume ratio of the material.

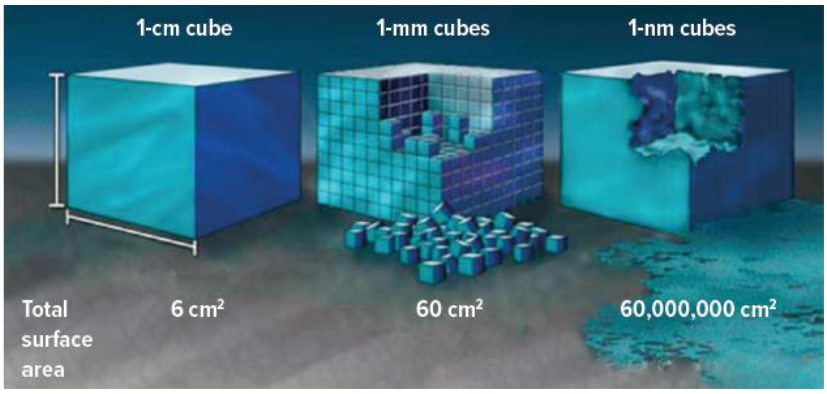

Figure 1.5. Illustration depicting the exponential increase in surface area (*Adapted from the National Technology Initiative*[44])

The large surface area of NPs is a critical factor which allows different surface orchestrations such as drug/gene, peptides, DNA leading to its multifaceted functions of biosensing, imaging and synaphic delivery of the drug/genes and gene. Moreover surface modification by lipids, polymeric coatings act like a stealth carrier circumventing the problem of reticuloendothelial clearance. But the basic requirement is to have a staunch and solid inorganic core which can give support for functionalization as well as allows biomolecules to interact along with the synaphic ligand. Such a paradigm scaffold helps in eliminating major problems arising due to the unfolding and rearrangements taking place when present in biological systems, thus leading to enhanced control of the physical chemistry of the surface.

1.3.1.2 Size matters!

Nanoparticles *en route* to their target in biological systems have to confront many barriers such as host immune system, hemodynamic shear force, Oxygen tension, interstitial fluid pressure, extracellular matrix. The transportation of a circulating nanoparticle is possible due to main reasons

1) Applied convective forces,

2) Brownian motion[45],

The extravasation of NPs is the resultant of the rate of fluid flow as well as filtration through the capillary, which completely depends on the hydrostatic pressure gradient (HPG). HPG is nothing but the vascular pressure and interstitial fluid pressure (IFP) difference. In the case of solid tumors, IFP is very high as compared to normal tumors due to the leaky

vasculature and diminished lymphatic drainage. Reduced blood flow and enhanced IFP leads to inhibition of transendothelial migration of NPs. Hence, increased NP size requires higher hemodynamic shear force to circumvent the higher IFP in tumors. This can be possible either by increasing the blood pressure transiently for enhanced drug/gene-delivery or induce hyperthermia for increased blood flow. Moreover, the most important step even before transvascular transport is their margination, i.e. the radial drift which dictates the transportation of a moving NP towards the blood vessel walls. The size of the NP is important enough when they have to interact with the vascular bed and have meaningful interactions with them. Margination is especially not favored when the NPs are transported in the tumor vasculature via convective means[46–48]. Moreover, the transportation of larger spherical nanoparticles is purely driven by convection, resulting in a greater difficulty in breaking away and moving towards the vessel wall. In contrast, smaller NPs show relatively higher diffusion rate, thus allowing them to travel laterally in the blood vessel easily. This has been reported by a study performed on liposomes which showed that liposomes of size 65 nm possess 3.4 times more margination rate as compared to a 130 nm liposome[49].

1.3.1.3 Shape of a nanoparticle

Shape plays a pivotal role in margination of the NPs towards the blood vessel walls. In contrast to spherical NPs, oblate-shaped particles experience torques which cause tumbling and rotations, which leads to lateral drift of NPs towards the blood vessel walls[48,50]. The cellular membranous interface interacting with NPs is dominated by its shape. Moreover, the reticuloendothelial clearance of the NPs is also dictated by the shape. There are reports which say that oblate shaped NPs are more favorable for circulation due to their lower uptake by macrophages[51,52]. This leads to increment in the blood residence time of NPs, thus increasing the probability of NPs to reach their destination without being cleared by the immune system. Immune system itself acts as a major obstacle which needs to be circumvented either by capping the NPs using stealth carriers or altering the shape. Moreover, entry of NPs inside normal and cancerous cells is also dominated by its geometry and strongly depends on the avidity of the NPs. Geometrically enhanced targeting is essential which can efficiently counterbalance hemodynamic forces, thus shedding off the NPs from the endothelium[53].

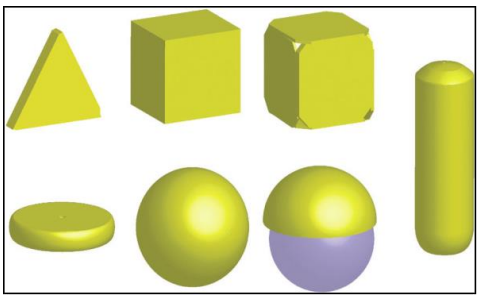

Figure 1.6. Different shapes available for NPs: triangle prisms, cubes, truncated cages, plates, spheres, shells, and nanorods (*Reproduced with permission from*[38])

Evasion of NPs especially by the macrophages is possible by two most critical parameters, size, and its shape. Spherical shaped NPs are responsible for enhanced rate of macrophage uptake. When 6 distinct classes of NPs of different shapes were evaluated, based on contact angle parameter, particle internalization velocity can also be deduced. Particles which possess high aspect ratios (~20) and if they are aligned with the long axis parallel to the cell membrane, it will internalize very slowly as compared to the particles which are aligned with its short axis parallel to the cell membrane. There is a discrepancy between the high rate of attachment of NPs and their internalization rate, in the sense that it's not necessary that those particles which possess a high rate of attachment will have very high internalization too. Previous reports have found that prolate ellipsoids having a major axis of 0.35-2 μm and minor axis of 0.2-2 μm had both highest attachment rate and slow internalization rate as compared to spherical particles of radius 0.26-1.8 μm and oblate ellipsoidal NPs having a major axis of 0.35-2.5 μm and a minor axis of 0.2-2 μm[54]. Moreover, the rate of phagocytosis of NPs depends on a particular geometry as well as it is purely organ-dependent. Once this process of phagocytosis is evaded by the NPs, the next most important task is to escape the blood vessel and traverse it, once it reaches the target site. The margination of NPs is dominated by their translational and rotational motion as well as buoyancy, viscous drag, Reynold`s number, gravity, Van der Waals forces of interactions, electrostatic double layer, and steric repulsive interactions. Spherical NPs follow streamline flow during their travel to balance these forces[47,55]. In contrast to spherical NPs, rod-shaped particles, based on their angle of orientation face lateral drift in the blood circulation. This drift occurs due to variable drag forces and torques experienced by the rods under blood flow. These dominant forces are responsible for their ability to marginate[47,56]. Furthermore, discoidal shapes (AR=0.5), hemispheres and ellipsoidal NPs (AR=0.5) also possess higher drift velocities as compared to

spheres[46]. But out of ellipsoids, hemispheres, and discs, only discoidal particles distinctly move in a highly oscillatory trajectories leading to enhanced interaction with the vessel wall. As the hemodynamic shear forces are decreased, the spherical NPs marginate almost two-fold. Shape readily enhances the process of margination; nanorods of AR~2 exhibited seven-fold more accumulation than nano-spheres under the same shear forces. Discs marginate more readily as compared to rods. High hemodynamic shear forces are also involved in lower adhesion rates of NPs since high shear rates dislodge the adhered particles and prevent any particle margination since it is really difficult for NPs to circumvent the problem of rapid flows.

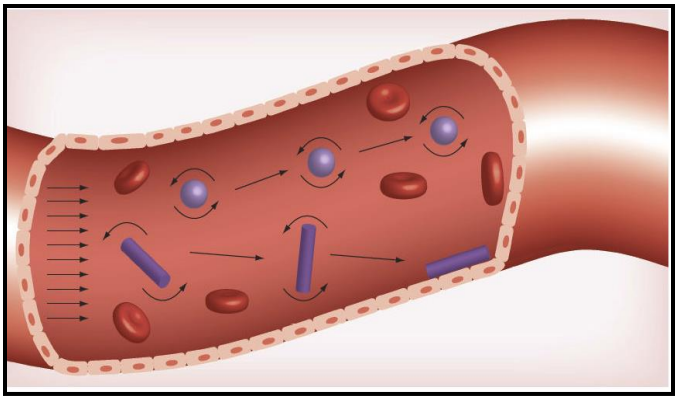

Figure 1.7. Effect of shape on NP margination Spherical NPs tend to remain in the center of the flow. Variable forces and torques exerted on rods underflow allow them to marginate and drift towards the vessel wall, where they are able to bind to wall receptors or extravagate through gaps between cells of the endothelium.

(Reproduced with permission from [57])

The geometry of the vessel is also an important criterion to evaluate margination of NPs (**Figure.1.7**). At bifurcation point, particles are more prone to get deposited rather than straight vessel[58]. The shape of the NP further enhances the deposition rate at the vessel junction, for instance, spheres display a lower ratio of bifurcation to straight vessel wall attachment than the ellipsoidal discs. Moreover, oblate shapes exhibit more advantages towards complex vessel geometries.

1.3.1.4 Optical properties

Biomedical Scientists working on inorganic NPs exploit their optical properties for sensing[59–61] and imaging purposes[62,63]. There is a very narrow window of light which allows penetration through the tissue. But often this narrow window is responsible for the effective excitation of organic fluorophores, the use of NPs poses a dynamic opportunity for the

exploitation of this spectral regime. Both semiconductors and metallic NPs exhibit optical properties. In the case of semiconductors, the physical confinement of the material at the nanoscale leads to specific optical properties. This concept of treating excitation of electrons as a "particle in a box" is known as quantum confinement effect[64]. Any alteration in the size or shape of a NP leads to changes in its electronic excitation behavior. This change in the absorption correspondingly causes a shift in its photoluminescence (PL), thus these nanoparticles can be tuned based on their desired applications.

Figure 1.8 CdTe/CdSe QD photoluminescence under UV excitation. The size of the QDs increases from left to right, modulating the emission from 520 nm to the NIR. *(Reproduced with permission from* [38])

Figure.1.8 shows CdSe QDs series which exhibits different emission wavelengths due to alterations in size. They can be exploited in biomedical applications since quantum confinement is material specific[65].

Metallic NPs exhibit a unique phenomenon of SPR[66]. SPR is defined as collective oscillation of conduction electrons at the surface of the metal NPs due to the excitation by the corresponding resonant wavelength of light. Hence this consequently causes a strong absorption of 10^9 $M^{-1}cm^{-1}$ OD for a 40 nm GNPs and ultrafast electronic relaxation. The SPR shift towards longer wavelengths is purely dependent on size and shape of the metal NPs. As the size of the NP increases, the amount of scattered light also increases as per Mie's theory. Furthermore, variations in shape such as nanorods, nanocages and nanoplates also result in unique scattering properties. This marriage between unique SPR phenomenon and scattering results in the enhancement of scattering properties, which makes them a proficient candidate for biomedical imaging applications.

1.3.1.5 Magnetic Properties

An electron is considered to be a point charge which orbits around the nucleus, thus rendering it orbital angular momentum and producing a magnetic field. Thus an electron

possesses orbital magnetic moment. Another fact that electron has a spin also adds up to the total magnetic moment of the electron. The total magnetic moment of the atom, in turn, is the vectorial addition of the moments of individual electron of the atom. The net magnetic moment of electrons is zero for energy levels filled with even numbered electrons. Hence, most of the solids do not possess net magnetic moment. But, there are certain transition metals such as iron, manganese, and cobalt, that have partially filled d-orbitals. Hence they have a net magnetic moment.

Faraday classified different substances to fall into three categories according to their behavior in a nonuniform magnetic field viz., diamagnetic, paramagnetic and ferromagnetic substances. In diamagnetic substances, the magnetic moments of the electrons in an atom cancel out each other. Hence the resultant magnetic moment of the atom is zero. In paramagnetic substances, all the magnetic moments of the electrons in an atom do not cancel out, so that the atom, as a whole, has a magnetic moment. Suppose that a specimen of a paramagnetic substance is placed in a magnetic field. Then each atomic magnet tends to rotate and align itself with the direction of the field. Perfect alignment is hindered by thermal vibrations of the atoms. If the temperature is kept constant, and the strength of the applied magnetic field is increased, then a stage is reached when almost all the elementary dipoles align themselves with the direction of the field. However, when the specimen is removed from the magnetic field, the alignment is disturbed by thermal vibrations and the specimen gets demagnetized. In ferromagnetic substances, individual atoms of ferromagnetic substance also behave like magnetic dipoles. A solid specimen of a ferromagnetic substance like iron is composed of many microscopic crystals; in each crystal, there are one or more regions, called domains within each of which there is an essentially perfect alignment of elementary magnetic dipoles. This is due to the special form of interaction, called exchange coupling between adjacent atoms. Thus ferromagnetism results not only from a property of an individual atom but also from an interaction between neighboring atoms. Now suppose that a specimen of a ferromagnetic substance is placed in a magnetic field. Then the domains which are already aligned in the direction of the magnetic field grow at the expense of the adjacent domains which are not so aligned. The atomic dipoles within some domains suddenly swing around to line up with the direction of the external field. As the field grows stronger, more and more domains flip around to line up with the direction of the external field, while those already aligned continue to grow. Finally, a stage reaches, when all the magnetic moments of all the

domains get aligned itself in the direction of the magnetic field. The specimen now becomes a permanent magnet and does not lose its magnetic property in spite of the magnetic field removal from the vicinity of the specimen[67,68].

Based on the net magnetic moment ferromagnetism can be distinguished from ferrimagnetism and anti-ferromagnetism. Ferrimagnetic materials always possess weak magnetic dipoles that are aligned in an antiparallel direction to the proximal strong dipoles in the absence of the external magnetic field. In the case of antiferromagnetic material, both the proximal dipoles are antiparallel in the absence of the external magnetic field and they are responsible for canceling each other[69] (**Figure 1.9**).

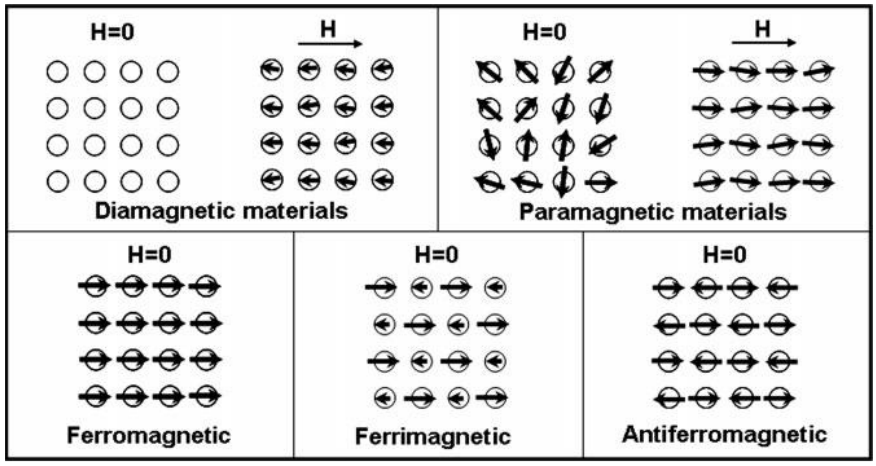

Figure 1.9. Schematic illustrating the arrangements of magnetic dipoles for five different types of materials in the absence or presence of *H* (*Reproduced with the permission from reference*[69]).

1.3.1.6 Nanoparticles platform

The main strategy for NP use in biomedical applications depends on its versatile modifications. Therefore, various nanoparticles act as well-defined multifunctional structures. This is achieved by slight variations in composition, surface coating, etc., which can lead enormous possibilities for sensing, imaging, and targeting of nanoparticles in biological systems[39,70,71].

1.3.2 Applications of nanomaterials in cancer

The tremendous advancement in the field of nanotechnology for over two decades resulted in a variety of nanostructures with novel properties. Almost all kinds of nanostructures are exploited for cancer diagnosis and treatment than any other medicine field. Some of the nanomaterials are as follows (**Figure 1.10.**):

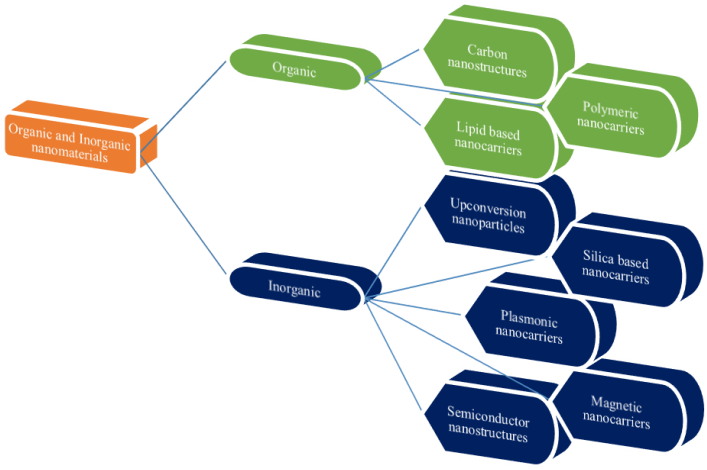

Figure 1.10. Classes of nanomaterials for cancer treatment and diagnosing

Each NPs have their own functions, so often used to fabricate multifunctional NPs. For example,

- Plasmonic NPs with different size and shape, have greater application in cancer for photothermal therapy (PTT)[72],
- Quantum dots (QDs) are useful in labeling and detection[73],
- MNPs are used for MR imaging, drug delivery and hyperthermia therapy[74],
- Polymeric NPs are used for encapsulation of therapeutic agents to increase half-life in the biological system[75].

Some of the applications of nanomaterials in the cancer therapy and detection are as follows:

1.3.2.1 Cancer detection

The invention of different imaging procedures gives the ability of detecting and visualizing tumor which is important before the treatment. Imaging techniques have become an important sector for early detection of cancers field. Because with these techniques, the early stage of cancer detection is made possible and sometimes even before the appearance of symptoms. And also important for evaluating the various stage and the exact locations of cancer which is very helpful pre and post-surgery, treatments.

1.3.2.1.1 MR Imaging

MR imaging is a non-invasive imaging procedure which produces three-dimensional (3D) detailed images without the use of any damaging radiation[76]. All the living objects and materials surrounded by us are mainly composed of atoms. Atoms consist of 3 particles that

are positively charged - protons, negatively charged - electrons, and neutrons with a neutral charge. The protons and neutrons are located inside the nucleus and electrons are present outside the nucleus as shown in **Figure 1.11**. These positively charged protons with a spin behaves like a mini bar magnet with its own magnetization. The billions of small magnets when placed within a large magnetic field, these magnetic vectors start interacting with the strong magnetic field and start rotating at a certain speed which is employed for recording the image from the scanner. For example, a hydrogen proton can be either parallel or antiparallel to the direction of magnetic. Different energy levels of protons determine whether they are parallel or antiparallel to the magnetic field. When protons are placed in a strong magnetic field it starts rotating around their axis at a frequency which can be determined by a constant number and magnetic field strength. This rotational motion is called magnetic resonance and defined by Larmor equation, which is as follows:

$$w_0 = \gamma \times B_0 \ldots\ldots\ldots\ldots\ldots (1)$$

γ - proton-specific constant called gyromagnetic ratio for hydrogen proton, B_0 - Applied main static field in the unit of Tesla, w_0 - rotational speed or frequency of the protons placed in the magnetic field in the unit of MHz[77].

The MRI scanner is comprised of 3 main components are (**Figure 1.12.**) superconducting primary magnet, 3 magnetic field gradient coils, RF transmitter and receiver.

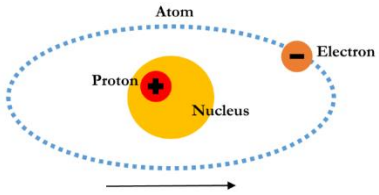

Figure 1.11. Composition of an atom

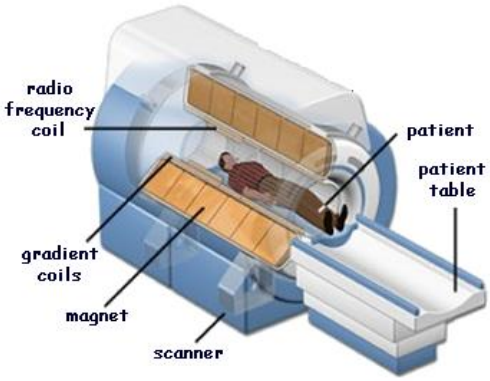

Figure 1.12. MRI Scanner cutaway[78]

It is widely used in medicine and biology due to its various advantages over other imaging methods:

- ✓ versatile contrasts,
- ✓ speed,
- ✓ the best spatial resolution,
- ✓ the possibility of multidimensional imaging,
- ✓ structural information
- ✓ functional information.

It is widely employed for

- Detection of diseases,
- Diagnosis,
- Treatment monitoring.

This technology is based on the direction of the rotational axis of protons found in the water in the living tissues[79].

Working principle of MRI

MR imaging employs strong magnets which are capable of producing a magnetic field which forces protons in the human body to align with that field. When an RF current is pulsed through the body, the protons are stimulated and spin out of equilibrium, attracted towards the pull of the produced magnetic field. When the RF field is off, the sensors in the MRI scanner can detect the energy released by the protons which realigned with the magnetic field. The time taken for the realignment of protons with the magnetic field, as well as the energy released, is purely depend on the changes due to the environment and also chemical nature of the molecules. By this measurements, physicians are able to find the difference between various tissue types based on the magnetic properties.

MR Imaging Parameters

To obtain an MR image, a patient is placed inside MR scanner and must remain very still during the imaging process to avoid blurring of the image. Contrast agents are injected to a patient *IV* either before or during the MRI procedure in order to increase the speed of protons to realign with the magnetic field. As the protons realign faster, the resulted image will be brighter.

Relaxations

The two main concepts in MRI are T_1 and T_2 relaxation[80] which can be defined as follows:

T_1 relaxation (spin-lattice relaxation) - interaction of protons with their environment (**Figure 1.13.**)

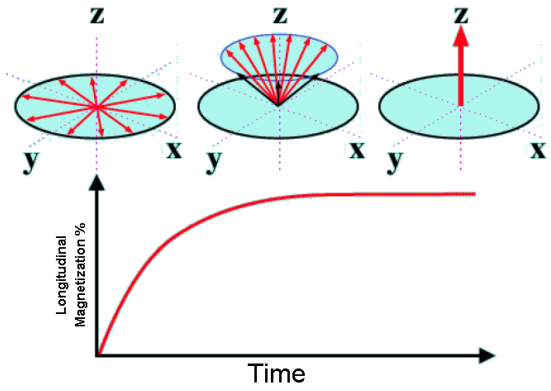

Figure 1.13. Mechanism of T_1 relaxation

T_2 relaxation (spin-spin relaxation) - interactions of protons among them (**Figure 1.14.**)

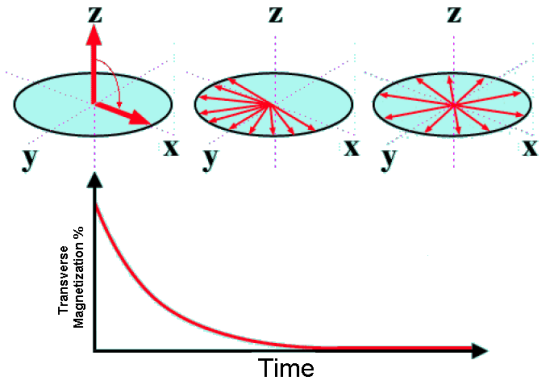

Figure 1.14. Mechanism of T_2 relaxation

MR imaging basically depends on the T_1 or T_2 times of protons present in various microstructures of organs to form a contrast image[3]. It provides perfect spatial resolution both morphologically and functional imaging in order to diagnose and assess the stages of a disease. But this is mainly due to the contrast agent which distinguish the normal and cancer cells. Nanomaterials with magnetic properties are usually employed either as T_1 or T_2 contrast agents, depending on the change in relaxation times of proton. Magnetic property can be given by paramagnetic ions, such as

- manganese[81],
- iron[82],

- gadolinium[83].

So, these ions are incorporated as a dopant within a magnetic or nonmagnetic matrix, or attached to the surface of a NP.

The most commonly used T_1 contrast agent is Gd and T_2 contrast agent is SPIONs. SPIONs usually reduce the spin-spin relaxation time thus decreasing the MRI signal and produces negative contrast[84]. These NPs can also be attached or encapsulated with imaging probes like QDs for dual purpose[85–88]. Recently, novel contrast agents have been designed which is based on GNPs for MR imaging[89]. Because the GNPs increases the MR imaging sensitivity which is used for clinical diagnosis[90].

1.3.2.1.2 Computed Tomography (CT)

CT is one of the imaging technique which uses computer processed X-ray scans to produce tomographic images of a specific site of the body[91]. These produced images are used for diagnostic and therapeutic purposes in medicine. For this technique, it is necessary that the contrast agent is specifically injected into the target site to produce effective images. So, usually, high atomic weight elements are employed for high X-ray absorption. Some of the commonly used contrast agents are iodine, gold, platinum, bismuth and tantalum[3]. The limitations for these agents are their short half-life in the body.

Therefore, NPs based contrast agents are developed which can be particularly targeted to the site of interest for better imaging. Among them, GNPs are exploited more because of high X-ray attenuation coefficient, synthesis, and biocompatibility. These NPs shows 5 times X-ray attenuation coefficient in the targeted cells. For example, 30 nm antibody-conjugated GNPs were injected intravenously *in vivo* for tumor targeting and CT imaging[92–94]. Recently, PEG encapsulated GNPs are employed for blood pool and tumor imaging which has prolonged half-decay circulation time of 11 h in rats[95]. Currently, NPs with more than one CT contrast elements have also been designed to provide sufficient contrast enhancement. For example, $BaYbF_5$ NPs containing two contrast elements have been developed[96].

1.3.2.1.3 Optical Imaging

Optical bioimaging employs an optical contrast provided by a change in the optical properties, such as light scattering, absorption, and luminescence between the region of the interest and the background region. This method enables diagnosis even at cellular or molecular level[97] and also provides guidance for intraoperative surgical removal of tumors[98,99].

NPs are used to create luminescence contrast for molecular imaging of cells and tissues, e.g., in coherent anti-Stokes Raman scattering (CARS) imaging for label-free detection[100].

The quantitative nature of the method becomes an additional advantage for tumor diagnosis and staging and also to quantify the cancer cells. QDs and GNPs are considered as the best agent for this procedure from the commonly used fluorophores[101]. Because they are excellent probes for confocal microscopy and two-photon confocal microscopy[102].

1.3.2.2 Nanopharmacotherapy

Nanopharmacotherapy (**Figure 1.15.**) has an advantage of evaluating significant improvements in the pharmacokinetics (PK)/(PD) pharmacodynamics profile of various drug moieties.

Figure 1.15. Benefits of nanopharmacotherapy

Some of the advantages of nanopharmacotherapy is as follows:

1.3.2.2.1 Targeted therapy

A drug-NP formulation can increase the concentration of drug at a target-specific to diseased sites. This depends on the extent of drug localization and targeting is divided into

(a) 1st order - particular tissue,

(b) 2nd order - particular cell type,

(c) 3rd order - particular organelle within a cell.

This can be achieved by EPR effect in the tumor tissues based on the formulation size[32]. But, this way of targeting is possible to cancer and inflammatory sites. Another way of targeting is usually by surface modified NPs to target cells/tissues[103].

1.3.2.2.2 Controlled Release

NPs offers a unique way to release the drugs in a controlled manner[104]. The types of release include as illustrated in **Figure 1.16.**

- Sustained release - it is a time-dependent release of drugs into the surroundings with an extended time period,
- Internal stimuli-sensitive release - the release depends on physiological/biochemical processes[105],
- Externally activated release - the release involves a two-step process,
  - ❖ Drug bio-distribute and accumulates at the target site,
  - ❖ And activated by external stimuli, to release drug[106,107].

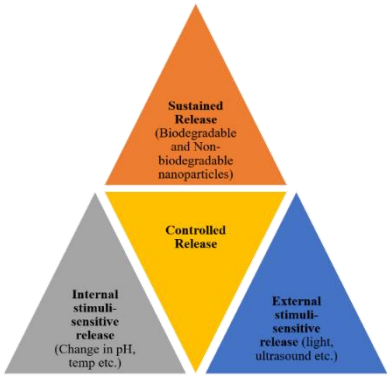

Figure 1.16. Types of Controlled release

1.3.2.3 Nanotherapies

NPs offers various types of therapies which are shown in **Figure 1.17.** Some of them are explained are as follows:

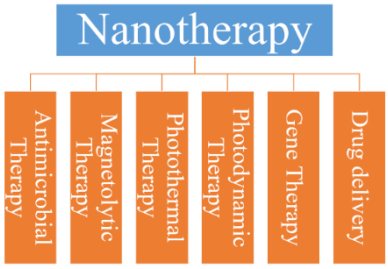

Figure 1.17. Types of nanotherapies

1.3.2.3.1 Drug Delivery

The drug delivery approach is a fusion of drug molecules with NPs via encapsulation, absorption or conjugation for administration in the body for treatment. Nano based drug delivery system provides a platform for attaching cocktail of drugs which can be targeted for complex diseases as a combination therapy. Usually for drug delivery systems either lipid or polymer based nanosystems are used. But recently, carbon and porous structures have been used[108]. Apart from this, other nanoparticles such as semiconductor NPs[109], GNPs and iron

oxide NPs[110] etc are also used. These nanostructures can be used to co-incorporate many therapeutic or diagnostic agents for combination therapy as multifunctional agents.

1.3.2.3.2 Photothermal therapy (PTT)

In PTT therapy, the NP itself serves as a drug for treating cancer cells[1]. Mostly, in this therapy metallic NPs with plasmonic absorption associated has been exploited. These plasmonic nanostructures can generate local heating up to 113°F. So, these NPs are targeted specifically to cancerous areas and subsequent light irradiation using near-infrared (NIR) laser results in cell death by the process of necrosis. This technique is also known as plasmonic photothermal therapy (PPTT), this therapy was tried initially by using a core-shell nanostructure consisting of a silica core and gold shell[72]. Furthermore, the gold nanoshells and nanorods with tunable SPR are used to treat thick tumor[111].

1.3.2.3.3 Hyperthermia/Magnetocytolytic Therapy

Hyperthermia is a technique of heat generation the tumor site[112]. In cancer treatment, hyperthermia is employed as one of the many clinical protocols as a co-adjuvant therapy. The raising the temperature in the cancerous environment results in changing the physiology of cancer cells leading to apoptosis[113]. This procedure complements with other available treatments like chemotherapy, radiation therapy, surgery, and gene therapy for cancer[114]. This therapy is classified into 3 different types based on the degree of temperature rise in the tumor region,

- Thermoablation – uses higher temperatures of heat >46°C which cause cells to undergo directly to tissue necrosis or coagulation,
- Moderate hyperthermia - <41°C to <46°C is used which effects cellular and tissue levels,
- Diathermia - temperatures above <41°C is employed usually in the treatment of rheumatic diseases.

During this heat treatment, the cancer cell undergoes irreversible protein damage which results in protein aggregation or inhibition affecting all the cellular functions[115]. The hyperthermia treatment purely depends on the

- Heat generation in the targeted site,
- Exposure time,
- Characteristics of cancer cells[116].

Depending on the diseased location, hyperthermia is also categorized as follows:

- Local hyperthermia involves small area of interest (tumor),
- Regional hyperthermia involves larger areas (whole tissue/organ),
- Whole body hyperthermia to treat metastatic cancer.

The main challenge in this therapy is producing heat to kill tumor cells without affecting the healthy cells. Because of this reason, local hyperthermia is considered to gain more attention than other types of hyperthermia[117,118]. Hyperthermia treatment was carried out by using external devices for transferring energy to tissues usually by light irradiation or electromagnetic waves. Some available techniques are ultrasound, RF, Mw, IR radiation, etc. Oncologists use hyperthermia combining with radiotherapy or chemotherapy or sometimes both. This approach results in eradicating cancer cells even though they are more vulnerable to other treatments.

The possibility of converting magnetic into thermal energy made the use of magnetic materials for hyperthermia treatment in 1957[119]. In this therapy, only MNPs are employed which can be controlled by magnetic field[120]. For example, at first, MNPs are injected into the body and using an external magnetic field the NPs are guided to the target site and using magnetic field the nanoparticles tend to produce heat which can release the drug and also the excess local heat (43-45°C) can kill the cancer cells. It is known as magnetically induced hyperthermia or magnetocytolysis[121]. The terms specific absorption rate (SAR) or specific loss power (SLP) is usually measured to evaluate the absorption efficiency of material (MNPs) to produce heat when exposed to AMF which defines the conversion of magnetic into heat energy[122]. For this applications, MNPs are proving to be a potential candidate because of their efficiency of converting magnetic energy into heat even at very less concentrations[123]. The heat generation by MNPs is mainly due to two processes (**Figure 1.18.**),

- Néel relaxation (internal) - the magnetic moment rotates within each particle,
- Brownian relaxation (external) - the particle rotates as a whole[124],

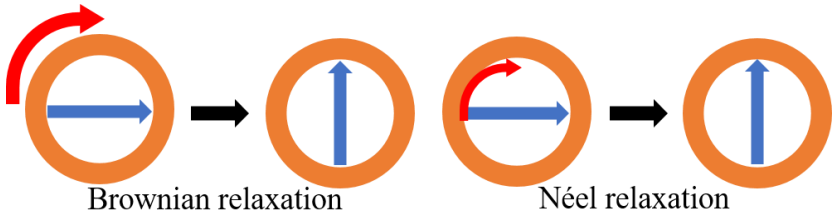

Figure 1.18. Two relaxations for heat generation

Brownian τ_B and Néel relaxation τ_N times[125,126] are calculated using the following equations,

$$\tau_B = \frac{3\eta V_H}{k_T} \ldots\ldots\ldots\ldots\ldots\ldots \quad (2)$$

where η is the viscosity coefficient of the matrix fluid, k the Boltzmann constant (1.38×10^{-23} J K^{-1}), and T the absolute temperature. V_H is taken as the hydrodynamic volume of the particle which is larger than the magnetic volume for a particle of radius.

$$\tau_N = \tau_0 \exp\left(\frac{KV}{K_B T}\right) \ldots\ldots\ldots \quad (3)$$

where $\tau_0 = 10^{-9}$ sec, K is the anisotropy constant, V is the volume of the magnetic particle, K_B is the Boltzmann constant and T is the temperature.

Combining above two equations, overall effective relaxation time τ of the particles can be obtained,

$$\tau = \frac{\tau_B \tau_N}{\tau_B + \tau_N} \ldots\ldots\ldots\ldots\ldots\ldots \quad (4)$$

The friction source from Néel and Brownian relaxation leads to a phase lag between H and the direction of the magnetic moments tends to produce thermal losses. So, by using the model of linear response times, it is easy to calculate MNPs SPL values[127]. SPL values are measured in terms of temperature rise per unit time and per gram of MNPs, multiplied by the calorific capacity of a sample. Usually, SPL values depend on following parameters:

- MNPs structure,
- Magnetic properties,
- Amplitude,
- AMF Frequency (f)[128–131].

A number of factors play a major role in MNPs designing for optimizing their hyperthermic effect have been reported which are as follows,

  - Size and size-distribution,
  - Carrier Viscosity,
  - Magnetic Anisotropy,
  - Stabilizing Ligand,

- Ability for tumor size reduction,
- Self-regulated hyperthermia,
- Multi-functionality.

Using MNPs and alternating current (AC) magnetic field, the magnetocytolysis therapy was carried out[132]. Some of the NPs employed in hyperthermia therapy, such as Mn, Fe, Co, Mg, and their oxides have been investigated. Generally, MNPs based hyperthermia controlled drug delivery, it is two types of mechanisms.

- *Type I – Hyperthermia based controlled drug delivery through bond breaking:* MNPs are attached with drug molecule through a linker and when AMF is applied, the drug molecule is released from the MNPs surface due to heating of the linker molecule[133].
- *Type II - Hyperthermia-based controlled drug delivery through enhanced permeability:* Drug is released from a polymeric matrix encapsulated with MNPs on the application of AMF/EMF[134,135] due to cracks formation of nm scale within a polymer due to heat generated by the MNPs.

As this thesis is majorly is concentrated on thermal ablation particularly Mw ablation, we are giving a brief explanation of the technique and advantages for the treatment of cancer.

1.3.2.3.3* Thermal ablation therapy

The treatment of a tumor by thermal or energy-based ablation is a method of applying extreme temperatures, either it can very high or low, to induce irreversible cell injury leading to tumor apoptosis and necrosis. Energy-based ablation has been employed for treating many tumor types which include liver, kidney, lung, bone as well as breast, adrenal glands especially for the patients who are very poor for surgery[136]. This therapy has several advantages over surgical methods:

- lower morbidity,
- surrounding tissues are preserved,
- extremely low cost,
- less hospitalization times[137],

as well as the therapy can be visually monitored.

Currently, the commonly used thermal ablation techniques are

- high-temperature-based:
  - radiofrequency ablation,

- microwave ablation (Mw),

➢ low-temperature-based:

- cryoablation.

Cell death mechanism by thermal ablation: In this therapy, the cancer cells or tumor region is majorly focused which affects the microenvironment of tumor and damages cellular membrane and also subcellular organelles either by direct or indirect mechanisms[138] (**Figure 1.19.**). Usually, the lesions caused by heat ablations are of 3 zones[139]:

i. central zone - immediately beyond the application tip which causes necrosis by ablation;

ii. peripheral zone - the region from thermal conduction of the central zone undergoes apoptosis;

iii. surrounding tissue - which is unaffected by ablation.

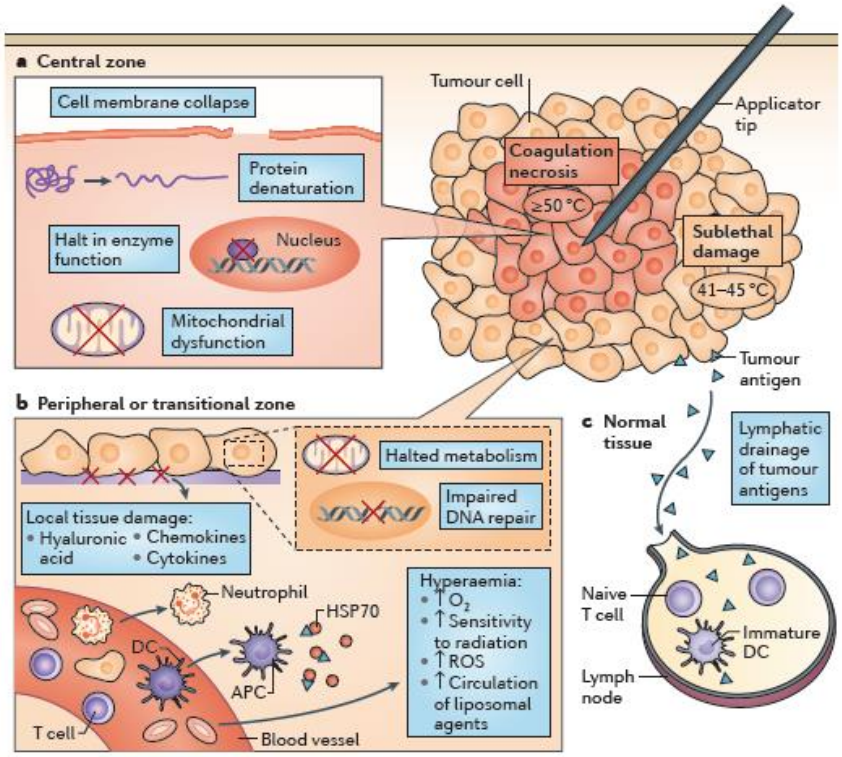

Figure 1.19. The zones of hyperthermic ablation: The applicator tip is surrounded by three zones, a) The central zone undergoes coagulative necrosis at temperatures ≥50 °C. Cell membrane collapse, protein denaturation, a halt in enzyme activity and DNA polymerase function, and mitochondrial dysfunction all occur[138], b) The peripheral or transitional zone has a steep negative temperature-gradient. At

temperatures between 41 °C and 45 °C there is still a heat-induced injury, but it is sublethal and reversible. Metabolic functions might be deranged or halted, and cells in this zone are vulnerable to further injury; for example, radiation-induced inhibition of DNA repair and cell recovery can eliminate already susceptible cells. The peripheral zone has increased blood flow, and this results in increased oxygenation that sensitizes the tumor tissue to radiation and may increase the formation of reactive oxygen species (ROS). Increased blood flow in this area facilitates the accumulation of liposomally-delivered chemotherapeutic agents. Damaged local tissue exposes hyaluronic acid and markers of endothelial injury, which stimulates the expression of vascular adhesion molecules and chemokines that attract immune cells. This zone contains the most inflammatory infiltrates, including neutrophils, macrophages, natural killer cells, dendritic cells (DCs), as well as $CD4^+$ and $CD8^+$ T lymphocytes. Intracellular necrotic debris stimulates phagocytosis, and tumor cells are engulfed by antigen-presenting cells (APCs). Heat shock protein 70 (HSP70) can chaperone antigens to APCs, c) In the normal surrounding tissues, blood vessels cause a heat-sink effect, which dissipates the elevated temperature and decreases the ablation efficacy. Tumor antigens that are released after necrosis drain to nearby lymph nodes, where they can stimulate immature DCs and naive T cells[140] (*Reproduced with the permission from reference*[136]).

Microwave ablation (MwA):

MwA employs electromagnetic (EM) waves to produce maximum heat to kills cancer cells by hyperthermic injury. An EM field usually used is in between 900–2500 MHz, is created by using an antenna intratumourally. This EM field forces the polar molecules predominantly water within the tumor tissue to realign continuously with that of oscillating electric field[141]. This mechanism is known as rotating dipoles or dielectric hysteresis. The rotation of water molecules increases their kinetic energy causing temperature increment in the tissues which can be more than 75-80°C without the concern of disrupting therapeutic delivery. MwA is more appropriate for tissues with higher impedance like lung and bone, and for tissues especially with a high water content like solid tumours[141]. MwA has several advantages when compared to other ablation therapies,

- ability to heat large tumor volumes,

- lower susceptibility to heat-sink effects because Mw systems are more faster and efficient[142],
- certain Mw frequencies can heat the cancer tissue up to 2 cm from the antenna[139],
- ability to use multiple antennas to increase the ablative effect, so larger tumors can be ablated simultaneously.

1.4 Motivation and Outline of the thesis

1.4.1 Motivation

The field of nanomedicine is rapidly growing and increasing the market demand to improve the public health by providing solutions to various unsolved diseases for many decades[8]. Therefore, this creates a huge demand for designing various nanomaterials for biomedical applications. But, the designing of new nanomaterial should meet the below criteria. Such as,

- Preparation of nanomaterials by facile method,
- Excellent physical property and performances,
- High stability in physiological environment,
- To have high biocompatibility and minimal toxicity,
- Long half-life in the case of *in-vivo* applications.

Even though a range of NPs are exploited with a variety of properties have been introduced to the biomedical field, MNPs and GNPs are always accepted to be a potential candidate because of their balance between unique properties, stability, and biocompatibility[143–145].

The significant importance of gold-magnetic nanocomposite initiated the main interest of the present study. To be very specific, this NPs are useful for numerous applications in enhanced computed tomography contrast, targeted drug delivery, contrast agents for MRI, diagnostic, treatment, bio-detection of DNA, RNA etc[146–148]. The main reason for the selection of noble metal gold is to achieve colloidal stability and well preserved physical property[149]. The primary criteria to consider a material is chosen for coating is based on its biocompatibility and cytotoxicity. This is because this outermost layer has a direct impact on the biological environment. As a result, gold becomes a suitable candidate because of its inertness, biocompatible, water solubility, and low toxic inorganic materials[143].

Gold nanoshell can dramatically prevent aggregation between the NPs by both electrostatic and steric repulsion. And also significantly protect the core NPs from the physiological environment by providing a compact armor. The gold versatile surface provides a platform for bio-conjugation of various functional groups or surface modifications, therefore provides a prominent opportunity to develop multifunctional nanocomposites[150]. The challenging part of gold coating is controlling the shell thickness[151], but it can be fine-tuned to control the size, shape, structure, stability, bio compatibility and molecules attached to the NPs.

To synthesize gold-magnetic composite NPs[150], there are various chemical methods. Therefore the main motivation of the work in this thesis is to develop a seed mediated based technique for the synthesis of gold-magnetic CSNPs with subsequent surface modifications with certain biological moieties and finally designing a multifunctional nanovehicle for cancer theranostics. The great importance of synthesized NPs is achieved to have the following characteristics:

- Tunable size and homogeneous size distribution,
- Stable for longer self-life,
- Less affected by physical environment leading to oxidation and corrosion,
- Biocompatible and low toxic,
- Surface functionalizable for any biomolecules.

1.4.2 Outline of the thesis

This thesis is mainly focused on designing a multifunctional CSNPs by seed mediated approach, employing superparamagnetic (magnetite, cobalt ferrite and manganese ferrite) NPs as a core with high magnetization synthesized by co-precipitation method and biocompatible monodispersed GNPs as a shell by citrate reduction method with tunable shell thickness. Surface modifications using FA and Dox has been carried out. To enhance the specificity of the CSNPs to cancer cells the surface has been modified with FA and Dox has been used as a chemotherapeutic agent because it acts against a range of tumor types either a single or multi-agent therapy (**Figure 1.20.**).

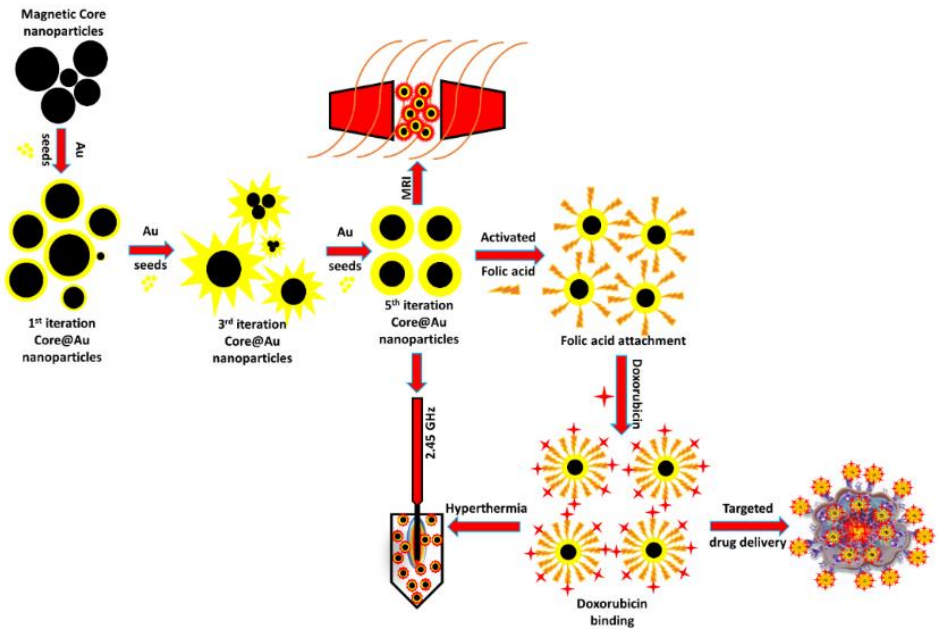

Figure 1.20. Schematic representation of core synthesis and Au iterations from 1-5 to enhance the SPR property. The surface is modified by attaching activated folic acid for specific targeting of cancer cells and also binding with anti-cancer drug doxorubicin for efficient chemotherapy. Finally, the whole complex is employed as MRI contrast agent and microwave based hyperthermal cargo at 2.45 GHz to track and treat cancer cells with high localization.

Subsequent characterization of their physical properties (structural, optical, magnetic) and evaluating their cytotoxicity, these NPs are finally exploited for various objectives in the field of cancer nanotheranostics as tripronged applications from tracking, diagnosing to therapeutics. Therefore this study can provide a much useful platform for future studies on the synthesis, surface modifications and nanomedicine especially in the cancer therapy field. Therefore, based on the objectives thesis is composed of 7 chapters and the chapter wise brief description is provided as follows:

First chapter: Provides a brief introduction to nanomedicine and cancer therapy with some important properties and its biomedical applications.

Second chapter: In this part of thesis, a literature survey of important concepts behind the whole work will be discussed in detail,

- Synthesis techniques, properties, various surface modifications and the importance of magnetic nanoparticles, gold nanoparticles. Finally, this part is

concluded with demand, various forms and multifunctional applications of core-shell nanoparticles in nanomedicine.

Third chapter: This chapter describes different characterization techniques, the experimental setup used for various application studies, materials and methods employed for nanoparticles synthesis, surface modification techniques and finally cell cultivation techniques for *in-vitro* studies.

Fourth chapter: Describes the background, characterizations, and applications of multifunctional magnetite coated gold core-shell nanoparticles.

Fifth chapter: Describes the background, doping of cobalt to magnetite nanoparticles, characterizations and applications of multifunctional cobalt ferrite coated gold core-shell nanoparticles.

Sixth chapter: Describes the background, doping of manganese to magnetite nanoparticles, characterizations, and applications of multifunctional manganese ferrite coated gold core-shell nanoparticles.

Seventh chapter: Finally, summary of the whole work and its output will be discussed in this chapter.

1.5 References

1. Paras N. Prasad. *Introduction to Nanomedicine and Nanobioengineering*. *Wiley* (John Wiley & Sons, 2012).
2. Bharali, D. J. & Mousa, S. A. Emerging nanomedicines for early cancer detection and improved treatment: Current perspective and future promise. *Pharmacol. Ther.* **128,** 324–335 (2010).
3. Chen, G., Roy, I., Yang, C. & Prasad, P. N. Nanochemistry and Nanomedicine for Nanoparticle-based Diagnostics and Therapy. *Chem. Rev.* **116,** 2826–2885 (2016).
4. Huber, F. X. *et al.* Evaluation of a novel nanocrystalline hydroxyapatite paste Ostim in comparison to Alpha-BSM more bone ingrowth inside the implanted material with Ostim compared to Alpha BSM. *BMC Musculoskelet. Disord.* **10,** 164 (2009).
5. Wagner, V., Husing, B., Gaisser, S. & Bock, A. K. Nanomedicine : Drivers for development and possible impacts. *Eur. Comm. Jt. Res. Cent.* 45–53 (2006).
6. Webster, T. J. Projections for nanomedicine into the next decade: But is it all about pharmaceuticals? *Int. J. Nanomedicine* **3,** (2008).
7. Lee Ventola, C. The Nanomedicine Revolution: Part 3: Regulatory and Safety Challenges. *Pharm. Ther.* **37,** 631–639 (2012).
8. Etheridge, M. L. *et al.* The big picture on nanomedicine: The state of investigational and approved nanomedicine products. *Nanomedicine Nanotechnology, Biol. Med.* **9,** 1–14 (2013).
9. ClinicalTrials.gov Background - ClinicalTrials.gov. Available at: https://clinicaltrials.gov/ct2/about-site/background.
10. Alexander, A. A. & Jotterand, F. Market Considerations for Nanomedicines and

Theranostic Nanomedicines. *Cancer Theranostics* 471–491 (2014). doi:10.1016/B978-0-12-407722-5.00025-6

11. Etheridge, M. L. *et al.* The big picture on nanomedicine: the state of investigational and approved nanomedicine products. (2013). doi:10.1016/j.nano.2012.05.013
12. Weissig, V., Pettinger, T. K. & Murdock, N. Nanopharmaceuticals (part 1): products on the market. *Int. J. Nanomedicine* **9,** 4357–4373 (2014).
13. Bawa, R. Nanopharmaceuticals: Nanopharmaceuticals. *Eur. J. Nanomedicine* **3,** (2010).
14. Ventola, C. L. The nanomedicine revolution: part 2: current and future clinical applications. *P T* **37,** 582–91 (2012).
15. Who. WHO | Cancer. *WHO* (2016).
16. Did we just get a small step closer to curing cancer?, World Economic Forum. Available at: https://www.weforum.org/agenda/2016/02/did-we-just-get-a-step-closer-to-curing-cancer/.
17. Med, I. J. & Res, N. ClinMed. **3,** 1–5 (2016).
18. Wicki, A., Witzigmann, D., Balasubramanian, V. & Huwyler, J. Nanomedicine in cancer therapy: Challenges, opportunities, and clinical applications. *J. Control. Release* **200,** 138–157 (2015).
19. Koo, H. *et al.* In vivo targeted delivery of nanoparticles for theranosis. *Acc. Chem. Res.* **44,** 1018–1028 (2011).
20. Morigi, V. *et al.* Nanotechnology in Medicine: From Inception to Market Domination. *J. Drug Deliv.* **2012,** 1–7 (2012).
21. Bawa, R. Nanoparticle-based therapeutics in humans: A survey. *Nanotechnol. Law Bus.* **5,** 135–155 (2008).
22. Kalash, R. *et al.* Differences in irradiated lung gene transcription between fibrosis-prone C57BL/6NHsd and fibrosis-resistant C3H/HeNHsd mice. *In Vivo* **28,** 147–171 (2014).
23. Liu, Y., Miyoshi, H. & Nakamura, M. Nanomedicine for drug delivery and imaging: A promising avenue for cancer therapy and diagnosis using targeted functional nanoparticles. *Int. J. Cancer* **120,** 2527–2537 (2007).
24. Torchilin, V. P. Targeted pharmaceutical nanocarriers for cancer therapy and imaging. *AAPS J.* **9,** E128–E147 (2007).
25. Ali, I. *et al.* Advances in nano drugs for cancer chemotherapy. *Curr. Cancer Drug Targets* **11,** 135–146 (2011).
26. Heidel, J. D. & Davis, M. E. Clinical developments in nanotechnology for cancer therapy. *Pharm. Res.* **28,** 187–199 (2011).
27. Davis, M. E., Chen, Z. G. & Shin, D. M. Nanoparticle therapeutics: an emerging treatment modality for cancer. *Nat. Rev. Drug Discov.* **7,** 771–782 (2008).
28. Heath, J. R., Heath, J. R., Davis, M. E. & Davis, M. E. Nanotechnology and cancer. *Annu. Rev. Med.* **59,** 251–65 (2008).
29. Greish, K. Enhanced permeability and retention (EPR) effect for anticancer nanomedicine drug targeting. *Methods Mol. Biol.* **624,** 25–37 (2010).
30. Kobayashi, H., Watanabe, R. & Choyke, P. L. Improving conventional enhanced permeability and retention (EPR) effects; What is the appropriate target? *Theranostics* **4,** 81–89 (2014).
31. Maeda, H. The enhanced permeability and retention (EPR) effect in tumor vasculature: The key role of tumor-selective macromolecular drug targeting. *Adv. Enzyme Regul.* **41,** 189–207 (2001).
32. Maeda, H. Tumor-selective delivery of macromolecular drugs via the EPR effect: Background and future prospects. *Bioconjug. Chem.* **21,** 797–802 (2010).

33. Brannon-Peppas, L. & Blanchette, J. O. Nanoparticle and targeted systems for cancer therapy. *Adv. Drug Deliv. Rev.* **64,** 206–212 (2012).
34. Northfelt, D. W. *et al.* Pegylated-liposomal doxorubicin versus doxorubicin, bleomycin, and vincristine in the treatment of AIDS-related Kaposi's sarcoma: Results of a randomized phase III clinical trial. *J. Clin. Oncol.* **16,** 2445–2451 (1998).
35. Schleich, N. *et al.* Comparison of active, passive and magnetic targeting to tumors of multifunctional paclitaxel/SPIO-loaded nanoparticles for tumor imaging and therapy. *J. Control. Release* **194,** 82–91 (2014).
36. Jain, K. K. Advances in the field of nanooncology. *BMC Med.* **8,** 83 (2010).
37. Kim, B. Y. S., Rutka, J. T. & Chan, W. C. W. Nanomedicine. *N. Engl. J. Med.* **363,** 2434–2443 (2010).
38. Doane, T. L. & Burda, C. The unique role of nanoparticles in nanomedicine: imaging, drug delivery and therapy. *Chem. Soc. Rev.* **41,** 2885–911 (2012).
39. Shenhar, R. & Rotello, V. M. Nanoparticles: Scaffolds and building blocks. *Acc. Chem. Res.* **36,** 549–561 (2003).
40. Salata, O. Applications of nanoparticles in biology and medicine. *J. Nanobiotechnology* **2,** 3 (2004).
41. Boal, A. K. & Rotello, V. M. Fabrication and Self-Optimization of Multivalent Receptors on Nanoparticle Scaffolds. *J. Am. Chem. Soc.* **122,** 734–735 (2000).
42. Ghosh, P. S., Han, G., Erdogan, B., Rosado, O. & Rotello, V. M. Binding of nanoparticle receptors to peptide α-helices using amino acid-functionalized nanoparticles. *J. Pept. Sci.* **14,** 134–138 (2008).
43. Bawa, R. Regulating nanomedicine. *Nat. Mater.* **6,** 249 (2007).
44. Brian Profitt. Hadoop: What It Is And How It Works. (2013). Available at: http://readwrite.com/2013/05/23/hadoop-what-it-is-and-how-it-works.
45. Decuzzi, P., Causa, F., Ferrari, M. & Netti, P. A. The effective dispersion of nanovectors within the tumor microvasculature. *Ann. Biomed. Eng.* **34,** 633–41 (2006).
46. Lee, S. Y., Ferrari, M. & Decuzzi, P. Shaping nano/micro-particles for enhanced vascular interaction in laminar flows. *Nanotechnology* **20,** 495101 (2009).
47. Gavze, E. & Shapiro, M. Particles in a shear flow near a solid wall: Effect of nonsphericity on forces and velocities. *Int. J. Multiph. Flow* **23,** 155–182 (1997).
48. Gentile, F. *et al.* The effect of shape on the margination dynamics of non-neutrally buoyant particles in two-dimensional shear flows. *J. Biomech.* **41,** 2312–8 (2008).
49. Toy, R., Hayden, E., Shoup, C., Baskaran, H. & Karathanasis, E. The effects of particle size, density and shape on margination of nanoparticles in microcirculation. *Nanotechnology* **22,** 115101 (2011).
50. Gavze, E. & Shapiro, M. Motion of inertial spheroidal particles in a shear flow near a solid wall with special application to aerosol transport in microgravity. *J. Fluid Mech.* **371,** S0022112098002109 (1998).
51. Geng, Y. *et al.* Shape effects of filaments versus spherical particles in flow and drug delivery. *Nat. Nanotechnol.* **2,** 249–255 (2007).
52. Champion, J. A. & Mitragotri, S. Role of target geometry in phagocytosis. *Proc. Natl. Acad. Sci. U. S. A.* **103,** 4930–4 (2006).
53. Decuzzi, P. & Ferrari, M. The adhesive strength of non-spherical particles mediated by specific interactions. *Biomaterials* **27,** 5307–5314 (2006).
54. Sharma, G. *et al.* Polymer particle shape independently influences binding and internalization by macrophages. *J. Control. Release* **147,** 408–12 (2010).
55. Decuzzi, P., Lee, S., Bhushan, B. & Ferrari, M. A theoretical model for the margination

of particles within blood vessels. *Ann. Biomed. Eng.* **33,** 179–90 (2005).
56. Park, J. & Butler, J. E. Analysis of the Migration of Rigid Polymers and Nanorods in a Rotating Viscometric Flow. *Macromolecules* **43,** 2535–2543 (2010).
57. Toy, R., Peiris, P. M., Ghaghada, K. B. & Karathanasis, E. Shaping cancer nanomedicine: the effect of particle shape on the in vivo journey of nanoparticles. *Nanomedicine (Lond).* **9,** 121–34 (2014).
58. Doshi, N. *et al.* Flow and adhesion of drug carriers in blood vessels depend on their shape: A study using model synthetic microvascular networks. *J. Control. Release* **146,** 196–200 (2010).
59. Murphy, C. J. Peer Reviewed: Optical Sensing with Quantum Dots. *Anal. Chem.* **74,** 520 A-526 A (2002).
60. Barone, P. W., Baik, S., Heller, D. A. & Strano, M. S. Near-infrared optical sensors based on single-walled carbon nanotubes. *Nat. Mater.* **4,** 86–92 (2004).
61. Jain, P. K., Huang, X., El-Sayed, I. H. & El-Sayed, M. A. Noble Metals on the Nanoscale: Optical and Photothermal Properties and Some Applications in Imaging, Sensing, Biology, and Medicine. *Acc. Chem. Res.* **41,** 1578–1586 (2008).
62. Jana, N. R. *et al.* Design and development of quantum dots and other nanoparticles based cellular imaging probe. *Phys. Chem. Chem. Phys.* **13,** 385–396 (2011).
63. Huang, X., El-Sayed, I. H. & El-Sayed, M. A. Applications of gold nanorods for cancer imaging and photothermal therapy. *Methods Mol. Biol.* **624,** 343–57 (2010).
64. Alivisatos, A. P. Semiconductor Clusters, Nanocrystals, and Quantum Dots. *Science (80).* **271,** (1996).
65. Michalet, X. *et al.* Quantum dots for live cells, in vivo imaging, and diagnostics. *Science* **307,** 538–44 (2005).
66. Huang, X., Neretina, S. & El-Sayed, M. A. Gold Nanorods: From Synthesis and Properties to Biological and Biomedical Applications. *Adv. Mater.* **21,** 4880–4910 (2009).
67. *Handbook of Nanophase and Nanostructured Materials*. (Kluwer Academic Publishers, 2003). doi:10.1007/0-387-23814-X
68. Lue, J. T. A review of characterization and physical property studies of metallic nanoparticles. *J. Phys. Chem. Solids* **62,** 1599–1612 (2001).
69. Jeong, U., Teng, X., Wang, Y., Yang, H. & Xia, Y. Superparamagnetic colloids: Controlled synthesis and niche applications. *Adv. Mater.* **19,** 33–60 (2007).
70. De, M., Ghosh, P. S. & Rotello, V. M. Applications of Nanoparticles in Biology. *Adv. Mater.* **1003,** 4225–4241 (2008).
71. Saha, K., Bajaj, A., Duncan, B. & Rotello, V. M. Beauty is skin deep: A surface monolayer perspective on nanoparticle interactions with cells and bio-macromolecules. *Small* **7,** 1903–1918 (2011).
72. Hirsch, L. R. *et al.* Metal nanoshells. *Ann. Biomed. Eng.* **34,** 15–22 (2006).
73. Law, W. C. *et al.* Aqueous-phase synthesis of highly luminescent CdTe/ZnTe core/shell quantum dots optimized for targeted bioimaging. *Small* **5,** 1302–1310 (2009).
74. Pankhurst, Q. A., Thanh, N. T. K., Jones, S. K. & Dobson, J. Progress in applications of magnetic nanoparticles in biomedicine. *J. Phys. D. Appl. Phys.* **42,** 224001 (2009).
75. Kamaly, N., Xiao, Z., Valencia, P. M., Radovic-Moreno, A. F. & Farokhzad, O. C. Targeted polymeric therapeutic nanoparticles: design, development and clinical translation. *Chem. Soc. Rev.* **41,** 2971–3010 (2012).
76. Lauterbur, P. C. C. Image formation by induced local interactions: Examples employing nuclear magnetic resonance. *Nature* **242,** 190–191 (1973).

77. Elmaoğlu, M. & Çelik, A. in *MRI Handbook* 7–23 (Springer US, 2011).
78. MRI. Available at: http://www.cyberphysics.co.uk/topics/medical/MRI.htm.
79. Magnetic Resonance Imaging (MRI) | National Institute of Biomedical Imaging and Bioengineering. Available at: https://www.nibib.nih.gov/science-education/science-topics/magnetic-resonance-imaging-mri.
80. Elmaoğlu, M. & Çelik, A. in *MRI Handbook* 25–46 (Springer US, 2011).
81. Zhang, Y., Lin, J. D., Vijayaragavan, V., Bhakoo, K. K. & Tan, T. T. Y. Tuning sub-10 nm single-phase $NaMnF_3$ nanocrystals as ultrasensitive hosts for pure intense fluorescence and excellent T1 magnetic resonance imaging. *Chem. Commun.* **48,** 10322–10324 (2012).
82. Cheng, K. *et al.* Magnetic nanoparticles: synthesis, functionalization, and applications in bioimaging and magnetic energy storage. *Chem. Soc. Rev.* **38,** 2532–2542 (2009).
83. Klasson, A. *et al.* Positive MRI contrast enhancement in THP-1 cells with Gd_2O_3 nanoparticles. *Contrast Media Mol. Imaging* **3,** 106–111 (2008).
84. Wang, Y. X. J. Superparamagnetic iron oxide based MRI contrast agents: Current status of clinical application. *Quant. Imaging Med. Surg.* **1,** 35–40 (2011).
85. Law, W. C. *et al.* Optically and magnetically doped organically modified silica nanoparticles as efficient magnetically guided biomarkers for two-photon imaging of live cancer cells. *J. Phys. Chem. C* **112,** 7972–7977 (2008).
86. Erogbogbo, F. *et al.* Biocompatible magnetofluorescent probes: Luminescent silicon quantum dots coupled with superparamagnetic iron(III) oxide. *ACS Nano* **4,** 5131–5138 (2010).
87. Lai, C. W. *et al.* Iridium-complex-functionalized Fe_3O_4/SiO_2 core/shell nanoparticles: A facile three-in-one system in magnetic resonance imaging, luminescence imaging, and photodynamic therapy. *Small* **4,** 218–224 (2008).
88. Mi, C. *et al.* Doped nanostructures. *Nanoscale* **2,** 1057 (2010).
89. Ma, Y. *et al.* Gold nanoshell nanomicelles for potential magnetic resonance imaging, light-triggered drug release, and photothermal therapy. *Adv. Funct. Mater.* **23,** 815–822 (2013).
90. Alric, C. *et al.* Gadolinium chelate coated gold nanoparticles as contrast agents for both X-ray computed tomography and magnetic resonance imaging. *J. Am. Chem. Soc.* **130,** 5908–5915 (2008).
91. Kalender, W. A. X-ray computed tomography. *Phys. Med. Biol.* **51,** R29–R43 (2006).
92. Popovtzer, R. Targeted gold nanoparticles enable molecular CT imaging of cancer: an *in vivo* study. *Int. J. Nanomedicine* **6,** 2859 (2011).
93. Hainfeld, J. F., Slatkin, D. N., Focella, T. M. & Smilowitz, H. M. Gold nanoparticles: A new X-ray contrast agent. *Br. J. Radiol.* **79,** 248–253 (2006).
94. Xu, C. *et al.* Au–Fe_3O_4 Dumbbell Nanoparticles as Dual-Functional Probes. *Angew. Chemie Int. Ed.* **47,** 173–176 (2008).
95. Zhou, B. *et al.* Synthesis and characterization of PEGylated polyethylenimine-entrapped gold nanoparticles for blood pool and tumor CT imaging. *ACS Appl. Mater. Interfaces* **6,** 17190–17199 (2014).
96. Liu, Y. *et al.* Hybrid $BaYbF_5$ nanoparticles: novel binary contrast agent for high-resolution in vivo X-ray computed tomography angiography. *Adv. Healthc. mater.* **1,** 461–6 (2012).
97. Ingvaldsen, J. E. & Gulla, J. A. *Context-aware user-driven news recommendation*. *CEUR Workshop Proceedings* **1542,** (John Wiley & Sons, Inc., 2015).
98. Orringer, D. a *et al.* Small solutions for big problems: the application of nanoparticles

to brain tumor diagnosis and therapy. *Clin. Pharmacol. Ther.* **85,** 531–534 (2009).
99. Orringer, D. A. *et al.* The brain tumor window model: A combined cranial window and implanted glioma model for evaluating iIntraoperative contrast agents. *Neurosurgery* **66,** 736–743 (2010).
100. Pezacki, J. P. *et al.* Chemical contrast for imaging living systems: molecular vibrations drive CARS microscopy. *Nat. Chem. Biol.* **7,** 137–145 (2011).
101. Koole, R. *et al.* Magnetic quantum dots for multimodal imaging. *Wiley Interdiscip. Rev. Nanomedicine Nanobiotechnology* **1,** 475–491 (2009).
102. Michalet, X. & Pinaud, F. F. Quantum Dots for Live Cells, in Vivo Imaging, and Diagnostics. *Science (80).* **307,** 538–545 (2005).
103. Swami, A. *et al.* in *Drug Delivery* 9–30 (Springer US, 2012). doi:10.1007/978-1-4614-2305-8
104. Pridgen, E. M., Langer, R. & Farokhzad, O. C. Biodegradable, polymeric nanoparticle delivery systems for cancer therapy. *Nanomedicine (Lond).* **2,** 669–680 (2007).
105. Torchilin, V. Multifunctional and stimuli-sensitive pharmaceutical nanocarriers. *Eur. J. Pharm. Biopharm.* **71,** 431–444 (2009).
106. Medeiros, S. F., Santos, A. M., Fessi, H. & Elaissari, A. Stimuli-responsive magnetic particles for biomedical applications. *Int. J. Pharm.* **403,** 139–161 (2011).
107. Katz, J. S. & Burdick, J. A. Light-responsive biomaterials: Development and applications. *Macromol. Biosci.* **10,** 339–348 (2010).
108. De Jong, W. H. & Borm, P. J. A. Drug delivery and nanoparticles: Applications and hazards. *Int. J. Nanomedicine* **3,** 133–149 (2008).
109. Probst, C. E., Zrazhevskiy, P., Bagalkot, V. & Gao, X. Quantum dots as a platform for nanoparticle drug delivery vehicle design. *Adv. Drug Deliv. Rev.* **65,** 703–718 (2013).
110. Cheng, Z. *et al.* Gelatin-encapsulated iron oxide nanoparticles for platinum (IV) prodrug delivery, enzyme-stimulated release and MRI. *Biomaterials* **35,** 6359–6368 (2014).
111. Hirsch, L. R. *et al.* Nanoshell-mediated near-infrared thermal therapy of tumors under magnetic resonance guidance. *Proc. Natl. Acad. Sci. U. S. A.* **100,** 13549–54 (2003).
112. Heat-Related Illness: Symptoms, Types, and First Aid. Available at: http://www.medicinenet.com/hyperthermia/article.html.
113. Van Loo, G. *et al.* The role of mitochondrial factors in apoptosis: A Russian roulette with more than one bullet. *Cell Death Differ.* **9,** 1031–42 (2002).
114. Kumar, C. S. S. R. & Mohammad, F. Magnetic nanomaterials for hyperthermia-based therapy and controlled drug delivery. *Adv. Drug Deliv. Rev.* **63,** 789–808 (2011).
115. Goldstein, L. S., Dewhirst, M. W., Repacholi, M. & Kheifets, L. Summary, conclusions and recommendations: adverse temperature levels in the human body. *Int. J. Hyperth.* **19,** 373–384 (2003).
116. Raaphorst, G. P., Freeman, M. L. & Dewey, W. C. Radiosensitivity and Recovery from Radiation Damage in Cultured CHO Cells Exposed to Hyperthermia at 42.5 or 45.5°C. *Radiat. Res.* **79,** 390 (1979).
117. Habash, R. W. Y., Bansal, R., Krewski, D. & Alhafid, H. T. Thermal therapy, Part 2: Hyperthermia techniques. *Crit. Rev. Biomed. Eng.* **34,** 491–542 (2006).
118. Cabuy, E. Hyperthermia in cancer treatment Hyperthermia in Cancer Treatment. *Neoplasma* **41,** 269–276 (2016).
119. GILCHRIST, R. K. *et al.* Selective inductive heating of lymph nodes. **146,** 596–606 (1957).
120. McCarthy, J. R. & Weissleder, R. Multifunctional magnetic nanoparticles for targeted

imaging and therapy. *Adv. Drug Deliv. Rev.* **60,** 1241–1251 (2008).
121. Dutz, S. & Hergt, R. Magnetic particle hyperthermia-A promising tumour therapy? *Nanotechnology* **25,** 452001 (2014).
122. Bornstein, B. A. *et al.* Local hyperthermia, radiation therapy, and chemotherapy in patients with local-regional recurrence of breast carcinoma. *Int. J. Radiat. Oncol.* **25,** 79–85 (1993).
123. Jordan, A. *et al.* Inductive heating of ferrimagnetic particles and magnetic fluids: Physical evaluation of their potential for hyperthermia. *Int. J. Hyperth.* **9,** 51–68 (1993).
124. Jeyadevan, B. Present status and prospects of magnetite nanoparticles-based hyperthermia. *J. Ceram. Soc. Japan* **118,** 391–401 (2010).
125. Suto, M. *et al.* Heat dissipation mechanism of magnetite nanoparticles in magnetic fluid hyperthermia. *J. Magn. Magn. Mater.* **321,** 1493–1496 (2009).
126. Kötitz, R., Weitschies, W., Trahms, L. & Semmler, W. Investigation of Brownian and Néel relaxation in magnetic fluids. *J. Magn. Magn. Mater.* **201,** 102–104 (1999).
127. Rosensweig, R. E. Heating magnetic fluid with alternating magnetic field. *J. Magn. Magn. Mater.* **252,** 370–374 (2002).
128. Hergt, R. *et al.* Physical limits of hyperthermia using magnetite fine particles. *IEEE Trans. Magn.* **34,** 3745–3754 (1998).
129. Jean-Paul Fortin, *et al.* Size-Sorted Anionic Iron Oxide Nanomagnets as Colloidal Mediators for Magnetic Hyperthermia. *J. Am. Chem. Soc.*, ***129*** **(9)**, 2628–2635 (2007).
130. Fortin, J. P., Gazeau, F. & Wilhelm, C. Intracellular heating of living cells through Néel relaxation of magnetic nanoparticles. *Eur. Biophys. J.* **37,** 223–228 (2008).
131. Gupta, A. K. & Gupta, M. Synthesis and surface engineering of iron oxide nanoparticles for biomedical applications. *Biomaterials* **26,** 3995–4021 (2005).
132. Schütt, W. *et al.* Applications of Magnetic Targeting in Diagnosis and Therapy-Possibilities and Limitations: A Mini-Review. *Hybridoma* **16,** 109–117 (1997).
133. Derfus, A. M. *et al.* Remotely triggered release from magnetic nanoparticles. *Adv. Mater.* **19,** 3932–3936 (2007).
134. Kost, J., Wolfrum, J. & Langer, R. Magnetically enhanced insulin release in diabetic rats. *J. Biomed. Mater. Res.* **21,** 1367–1373 (1987).
135. Zonghuan Lu, *et al.* Magnetic Switch of Permeability for Polyelectrolyte Microcapsules Embedded with Co@Au Nanoparticles. *Langmuir*, ***21*** **(5)**, 2042–2050 (2005).
136. Chu, K. F. & Dupuy, D. E. Thermal ablation of tumours: biological mechanisms and advances in therapy. *Nat. Rev. Cancer* **14,** 199–208 (2014).
137. Pereira, P. L. Actual role of radiofrequency ablation of liver metastases. *Eur. Radiol.* **17,** 2062–70 (2007).
138. Nikfarjam, M., Muralidharan, V. & Christophi, C. Mechanisms of Focal Heat Destruction of Liver Tumors. *J. Surg. Res.* **127,** 208–223 (2005).
139. Ahmed, M., Brace, C. L., Lee, F. T. & Goldberg, S. N. Principles of and advances in percutaneous ablation. *Radiology* **258,** 351–69 (2011).
140. Den Brok, *et al.* Efficient loading of dendritic cells following cryo and radiofrequency ablation in combination with immune modulation induces anti-tumour immunity. *Br. J. Cancer* **95,** 896–905 (2006).
141. Lubner, M. G., Brace, C. L., Hinshaw, J. L. & Lee, F. T. Microwave tumor ablation: mechanism of action, clinical results, and devices. *J. Vasc. Interv. Radiol.* **21,** S192-203 (2010).
142. Wright, A. S., Lee, F. T. & Mahvi, D. M. Hepatic microwave ablation with multiple antennae results in synergistically larger zones of coagulation necrosis. *Ann. Surg. Oncol.*

10, 275–83 (2003).
143. Yeh, Y. C., Creran, B. & Rotello, V. M. Gold nanoparticles: preparation, properties, and applications in bionanotechnology. *Nanoscale* **4,** 1871–80 (2012).
144. Wang, C. *et al.* Morphology and electronic structure of the oxide shell on the surface of iron nanoparticles. *J. Am. Chem. Soc.* **131,** 8824–8832 (2009).
145. Lyon, J. L., Fleming, D. A., Stone, M. B., Schiffer, P. & Williams, M. E. Synthesis of Fe oxide Core/Au shell nanoparticles by iterative hydroxylamine seeding. *Nano Lett.* **4,** 719–723 (2004).
146. Xu, C., Wang, B. & Sun, S. Dumbbell-like Au-Fe_3O_4 nanoparticles for target-specific platin delivery. *J. Am. Chem. Soc.* **131,** 4216–4217 (2009).
147. Kim, D., Kim, J. W., Jeong, Y. Y. & Jon, S. Antibiofouling Polymer Coated Gold@Iron Oxide Nanoparticle (GION) as a Dual Contrast Agent for CT and MRI. *Bull. Korean Chem. Soc.* **30,** 1855–1857 (2009).
148. Lim, J. K., Majetich, S. A. & Tilton, R. D. Stabilization of superparamagnetic iron oxide core-gold shell nanoparticles in high ionic strength media. *Langmuir* **25,** 13384–13393 (2009).
149. Wang, L. *et al.* Monodispersed core-shell Fe_3O_4@Au nanoparticles. *J. Phys. Chem. B* **109,** 21593–21601 (2005).
150. Lim, J. & Majetich, S. A. Composite magnetic-plasmonic nanoparticles for biomedicine: Manipulation and imaging. *Nano Today* **8,** 98–113 (2013).
151. Jin, X. *et al.* Facile deposition of continuous gold shells on Tween-20 modified Fe_3O_4 superparticles. *J. Mater. Chem. B* **1,** 1921–1925 (2013).

CHAPTER 2

Literature survey on Magnetic, Gold and Core-shell Nanoparticles

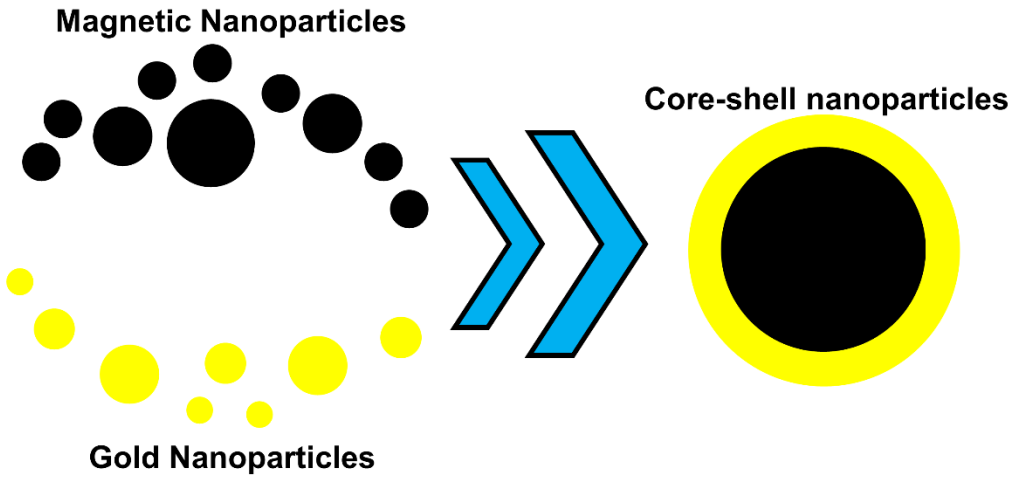

Table of Contents

2.1 Synthesis, Properties, Surface functionalization and applications of Nanoparticles

2.1.1 Magnetic nanoparticles (MNPs)

2.1.1.1 Synthesis and properties

Magnetic materials at nanoscale possess various biomedical applications due to their unique physical properties at the cellular and molecular levels of the biological interface. They are an efficient theranostic agent since they are considered to be good for therapeutic purposes, as well as for MR contrast imaging[1,2]. They have been exploited for the diagnosis and treatment of cancer[3], cardiovascular diseases[4] and neurological diseases[5]. The size, shape, surface charge, surface chemistries, and composition can be tailored for such NPs so that their magnetic properties are improved and hence can be used proficiently for the theranostic purpose, both *in vivo* as well as *in vitro*[6].

As a contrast agent, such MNPs have been commercially used since they enhance the proton relaxation of specific tissues, serving as MR contrast imaging agents. The commercially available materials are Lumiren® and Gastromark® for bowel contrast imaging, Endorem® and Ferridex IV® for liver/spleen imaging, etc[7]. As a treatment agent, these NPs have been utilized as a magnetic drug-targeting agent[8] as well as an active targeting agent[9,10]. Other NPs possess the defect of lack of targeting strategies, hence, when they are biodistributed systemically after conjugating with drugs, they are intrinsically inefficient to reach towards their target. But MNPs can be targeted towards cancer cells due to the external magnetic field. This reduces the deleterious side-effects and drug dosage due to the synaphic delivery of drugs.

Magnetic nanomaterials possess the ability to penetrate the magnetic field through human tissue and manipulate in such a way that they can be exploited for medicinal purposes[11]. The material's magnetic property is symbolized by its magnetic susceptibility (χ) that is the ratio of induced magnetization (M) to the applied magnetic field (H). At a nanoscale of the order of tens of nanometers, ferri or ferromagnetic materials possess a large single magnetic domain having a large magnetic moment. In the presence of an external magnetic field, this single magnetic domain having a magnetic moment is aligned parallel to H. But at high temperatures (blocking temperature TB) (37°C) and in the absence of an external magnetic

field, thermal fluctuations can stimulate free rotation of the particles, thus leading to a loss in net magnetization. Hence this superparamagnetic property, which renders NPs without any remnant magnetization after the removal of external fields, helps them to maintain their colloidal stability and prevents any agglomeration with the vascular proteins. Moreover, these superparamagnetic particles possess individual magnetic domains and their coupling interactions lead to higher magnetic susceptibilities.

Superparamagnetism is a favorable property but the reduction of size also comes with a disadvantage, that as the size of the particle decreases, the surface-to-volume ratio increases leading to manifestations of surface effects, that is, spin canting, noncollinear spins, that affect the overall magnetic properties[12]. Recently, there have been reports in which magnetization of iron oxide NPs (Fe_3O_4 and Fe_2O_3) have been increased by doping them with ions such as cobalt, manganese, zinc, nickel, and iron itself. $MnFe_2O_4$ is nontoxic *in vitro* and has higher magnetic susceptibility than iron oxide NPs. Both cobalt and nickel ferrites, though they possess *in vivo* toxicities, possess unique MR imaging properties. Furthermore, iron oxide NPs are also coated with Fe, where iron oxide acts as a core and Fe as a shell so that the magnetization value increases from 30 to 50 emu/g for plain iron oxide NPs to Fe/Fe_3O_4 CSNPs having 102 emu/g. In another instance, Pt, Au, and Ag have been used for coating the surface of iron oxide NPs. FePt has been used to bind DNA and protein on its surface[13,14], while Au/Fe_3O_4 CSNPs have been utilized to improve the biocompatibility of iron oxide NPs and bind anticancer drugs for delivery inside cancer cells[15] (**Figure 2.1**).

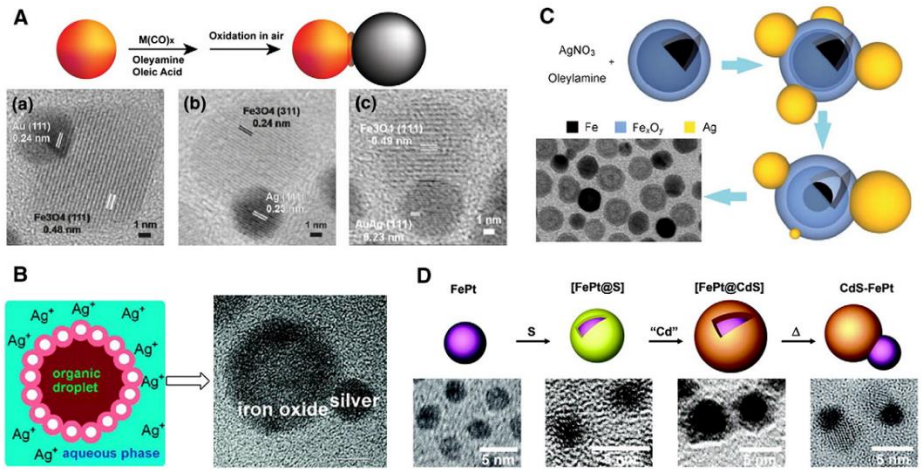

Figure 2.1. A) Schematic illustration of the growth of metal-oxides dumbbell MNPs on pre-made noble metal NPs and HRTEM) images of a) Au-Fe_3O_4, b) Ag-Fe_3O_4, and c) Au, Ag-Fe_3O_4 MNPs. *(Reproduced with permission from*[16] *Copyright 2010 American Chemical Society)* B)

Schematic illustration of the growth of Ag-hollow Fe_3O_4 dumbbell MNPs in the aqueous phase. *(Reproduced with permission from*[17] *Copyright 2010 American Chemical Society)* C) Schematic illustration of the growth of Ag-hollow Fe_3O_4 dumbbell MNPs in organic phase *(Reproduced with permission from*[18]*)* D) Schematic illustration of the growth of FePt–CdS dumbbell MNPs *(Reproduced with permission from*[19] *Copyright 2004 American Chemical Society).*

2.1.1.2 Surface functionalization

MNPs need to be functionalized by surface ligands such as polymeric coatings, metallic coats such as silica or gold, liposomes, and micelles since individually they are toxic and tend to be easily recognized and cleared out by the reticuloendothelial system (RES) before reaching their target. The effectiveness of MNPs is increased by improving their steathiness by surface functionalization, thus increasing their retention time in blood circulation, so that there is the maximum probability of MNPs reaching their target[20–22].

2.1.1.3 Applications

2.1.1.3.1 Delivery of siRNA/DNA

The delivery of genes is unfavorable due to inefficiencies in their transfection, short half-life in blood, being nonspecific, as well as deprived diffusion through cell membranes[23,24]. This can be overcome by conjugating MNPs with antisense oligodioxynucleotides (ODNs), which is also known as magnetofection. This has been successfully optimized for *in vitro* applications and now is being tested for *in vivo* applications[25,26]. A dendrimer-tethered MNPs has been used to transport antisense surviving ODNs to breast and liver cancer cells[27]. Researchers have demonstrated that positively charged polyamide amine-coated MNPs, when complexed with ODNs, can downregulate the surviving gene, as well as protein, in 15 min. This consequently led to the inhibition of cellular growth.

MNPs after surface functionalization act as an important vehicle for delivery of small interfering RNA (siRNA)[28]. There are a plethora of cationic polymers which are coated onto the surfaces of MNPs, along with polyethyleneimine-coated MNPs which have been utilized for the delivery of siRNA. There are reports on NIFR-labeled MNPs, which are covalently bound with siRNA, that can silent GFP production in a GFP-expressed xenograft in a tumor mouse model. The report confirms the *in vivo* tumor uptake of such MNPs conjugates due to EPR effect, which can be used for MR imaging purposes. The future endeavor is to exploit such conjugates for therapeutic purposes[29,30].

2.1.1.3.2 Delivery of drugs

Chemotherapeutic agents possess the most disadvantageous effects of nonspecificity and augmented side-effects to healthy tissues. This can be circumvented by utilizing MNPs due to magnetic targeting and site-specific delivery of therapeutic cargoes[31–33]. To make it simple, the process involves attachment of an anticancer drug on to prefunctionalized MNPs. This conjugate on intravenous injection was followed by application of an external magnetic field gradient to target the NPs on the pathological site. Due to a hyperthermal effect, the drugs are released onto the desired site. But the execution of such a simple process has been complicated by physicochemical parameters such as field strength and geometry, hemodynamic shear force, depth of the tumor tissue, which play a pivotal role in drug delivery[34]. MNPs attached to epirubicin have reached early clinical trials which have been targeted to tumors. Patients tolerate such conjugates, but the most challenging task is the occurrence of embolization of blood vessels, due to limited field penetration into tissues, such conjugates cannot be used *in vivo*. There is no proper control of drug diffusion after release and toxicity of MNPs. For the comprehension of the effects of MNPs, there is a creation of a mathematical model, which takes care of the hydrodynamics of the blood vessels, particle volumes, magnetic field strength, etc. This model proves that magnetic drug targeting could be useful only on the targets which are close to the surface of the body[35–37]. This study inspired attachment of mitoxantrone on the surface of starch-coated MNPs in VX2 squamous cell carcinomas on the hind limbs of New Zealand White rabbits. It was demonstrated that such conjugates could completely eradicate tumors after 35 days of treatment[38,39]. In other instances, traditional drugs such as etoposide, doxorubicin, methotrexate, and cisplatin have been either attached to MNPs or encapsulated inside polymer functionalized MNPs for the treatment of malignant prostate and breast tumors[40–42]. Moreover, there are reports in which poly(ethyl-2-cyanoacrylate) (PECA)-coated MNPs are attached to two different types of drugs, that is, hydrophobic cisplatin and hydrophilic gemcitabine. This helps in controlled release of cisplatin due to its hydrophobicity and rapid release of gemcitabine due to its hydrophilicity[43].

2.1.1.3.3 MR imaging

MR imaging is a significant technique which employs contrast agents like SPIONs to clearly distinguish between healthy and pathologically different tissues/cells. Recently the various developments in MR imaging have implemented *in vivo* scanning even at a very high resolution[44]. To visualize and track cells by MR imaging, it is vital to magnetically tag cells.

Recently, Tat protein-derived peptide sequences have been used for internalizing a various marked proteins into cells[45]. The tagging of MNPs with cells does not affect its normal mechanisms like viability, differentiation, or even the proliferation of $CD34^+$ cells. The research evidence shows that the transgene expression can be envisaged by MRI *in vivo*[46]. The researchers have attached human holo-transferrin to MNPs and demonstrated the receptor level increment on the surface of the cell which causes noticeable changes in MR imaging signals. These SPIONs are almost non-toxic when administered *IV*, which is confirmed from various clinical use[47], and as the MNPs has highly biodegradable, which allows multiple imaging of transgene expression for a prolonged time. Therefore, this new field in MR imaging opens a provocative area for establishing additional and innovative strategies for imaging the different gene expressions in deep organs[48].

MNPs have been widely employed to reveal apoptosis by MR imaging[49]. The post-treatment of tumor cells *in vivo* shows changes in MR image contrast which reflect the cell morphological appearance due to apoptosis[50]. The C2 domain - synaptotagmin I, binds to cell membranes (especially to anionic phospholipids), which binds to the apoptotic cells plasma membrane this can be evaluated by both confocal microscopy and flow cytometry. Therefore, the administration of C2-SPIONs can significantly increase the image contrast of a tumor where apoptotic cells are high in number. This method paved the way for both *in vitro* and *in vivo* detection of apoptotic cells after the chemotherapy[51].

Thus, this MR imaging technique can detect apoptosis at an early stage after the post-treatment which is advantageous over other methods like magnetic resonance spectroscopy (MRS) and radionuclide method with high spatial resolution. Due to various advantages over other contrast agents, recently SPIONs has been clinically approved by FDA as a MR imaging blood pool agent[52].

2.1.1.3.4 Hyperthermia

Magnetic hyperthermia is one of the currently employed therapy for treatment of cancer by exposing cancer cells/tissues under alternating magnetic field (AMF). It is due to the production of heat caused due to magnetic hysteresis loss by MNPs when subjected to AMF. The heat generation completely depends on the MNPs nature and AMF parameters. MNPs are injected in the tumor region and placed within an AMF which will heat up to a certain temperature depending on the various parameters like magnetization of MNPs and AMF strength. Cancer cells are prone to die/damage when the temperature is as high as 43°C,

but the normal cells can survive even at higher temperatures. The size of the MNPs plays an important role in producing heat inside the cancer cells[53].

Many research work using MNPs for hyperthermia has already been carried out as a therapeutic agent for various types of cancers by evaluating with animal models[54] or using *in vitro* cancer cell lines[55]. Choosing optimum AMF and MNPs size even very small quantity is enough to produce required amount (order of a tenth of milligram) of heat in a specific site which leads up to cell necrosis/apoptosis. The research has shown that hyperthermia augments cell cytotoxicity by chemotherapy and chemo hyperthermia with brain tumor cell lines, which were confirmed by various hyperthermia studies with multimodel rat, rabbits, and dogs[56]. Using interstitial microwave antennas, it is evaluated that a maximum tolerable dose for dog's normal brain is around 44°C for 30 min.

Modified aminosilan MNPs showed increased differential endocytosis specifically into glioblastoma cells *in vitro*[57]. This study shows a 10-fold increased uptake by glioblastoma cells. And these modified aminosilan-type NPs were also taken up by cancer cells lines like prostate carcinoma cells *in vitro*. This shows that the MNPs size and surface is very important for the endocytosis process into the cancer cells. And also dextran coated magnetite (DM) are employed for hyperthermia of oral cancer hyperthermia. This NPs suspension was injected into the tumor and heated upto 43-45°C by an AMF of 500 kHz. The results suggested that the growth inhibition of tongue carcinoma in the 4 time heating group when compared to the control group. And also, the survival rate was higher in the heated groups than in the control[58].

Furthermore, combined therapies of hyperthermia and gene may be possible in the near future. For example, using magnetite cationic liposomes (MCLs) combined with TNF-α gene therapy driven by the stress-inducible promoter was employed for hyperthermia for the first time. In nude mice, MCLs induced cell necrosis in the tumor area on heating under an AMF. The produced heat stress resulted in an increase of TNF-α gene expression when compared with that of the non-heated tumor. This combinational treatment completely arrested the growth of tumor in an animal model over a month period, proving it to be a potential candidate for future cancer treatment[59].

2.1.2 Gold nanoparticles (GNPs)

2.1.2.1 Synthesis and properties

GNPs have been exploited as a theranostic agent as they possess unique capability of binding amine (-NH_2) as well as thiol (-SH) functional groups[60–63]. They act as a paradigm for

drug or gene delivery vehicles since they can synaphically interact with miscreant cells and possess decreased systemic toxicity, improved efficacy, effective biodistribution and clearance of therapeutics[64]. They have attracted biomedical scientists for synthesizing different sizes (in the range of 1-100 nm) and shapes (including spherical, rods, cuboids, CSNPs, and much more)[65–67] of GNPs. The biomedical applications of such NPs are size as well as shape-dependent as gold nanorods, gold nanoshells, and other gold nanostructures, when injected into the body, can absorb NIR light since the body tissues possess high transparency towards NIR light. Gold nanostructures aid in drug/gene release as well as PTT when exposed to NIR. There are different strategies for binding drugs or genes to drug-delivery vehicles, but GNPs efficiently tether via covalent linking. This is possible either by amino linkage or thiol linkage between GNPs and therapeutic agents. Smaller-sized GNPs (5 nm) exhibit large optical absorption due to SPR, while larger NPs (10-100 nm) scatter exorbitantly, but they can absorb light only in the visible region. The biological tissues are less transparent to visible light as compared to near-infrared light, hence gold nanorods and nanoshells are synthesized which possess strong SPR in the near IR region. Gold nanorods are synthesized using a surfactant known as CTAB as a capping agent. But due to the inherent toxicity of CTAB, several groups are exchanging it with controlled surface chemistries. Gold nanoshells possess a spherical dielectric core having a thin gold layer acting like a shell[68].

2.1.2.2 Surface functionalization

GNPs are functionalized via thiol moiety, but this proves to be conditionally advantageous. Thiol groups have the tendency to be exchanged with the solution, which is a limitation, but in certain cases when inside the cells due to high levels of glutathione in the cytoplasm it can also be useful for drug release by means of exchange reaction[69]. Glutathione partially displaces the thiol group on the surface of NPs, thus causing the release of covalently bound drugs. The stability of NPs can be enhanced if the system is made more complex, in the sense that multiple thiols can be grafted onto the single NP, making it more stable[70,71]. A cyclical disulfide can also be used for multiple binding points in a multidentate fashion with GNPs increasing the binding energies. Hence exploiting 1,2-dithiane end group, thioctic acid, and in situ dithiocarbamate has shown an efficient way of grafting onto a GNPs surface[72,73]. This refers to thiol groups which are considered to be covalently stronger as compared to amine groups. In cases where weaker binding forces are needed, such as noncovalent ones especially for drug release purposes, NPs can attach or trap molecules via amine groups. If

efficient drug release is the desire of a biomedical scientist, then only GNPs tethered to amines can accomplish this role since bond strength between gold and the amino group is B6 kcal/mol as compared to 47 kcal/mol for thiols[74]. GNPs are proficient vehicles for delivery of DNA/RNA or drugs for traversing through the cell membrane. The entry of nucleotide inside the cell is restricted due to its negative charge, hence through thiol linkage, they can interact with GNPs and traverse through the membrane via the above-explained mechanisms. There are certain drugs which are toxic to normal cells and cannot enter the miscreant culprits, such as bacteria or cancer cells, due to resistance against them. GNPs, nanorods, or nanoshells can tether such drugs and then via a targeted mechanism using antibodies or certain molecules, they can enter inside the cells synaphically.

2.1.2.3 Applications

2.1.2.3.1 Delivery of siRNA/DNA

GNPs are considered to be an efficient system for delivery of either DNA or RNA for gene silencing and consequently for therapeutic purposes. Mirkin et al[75] demonstrated that a dense layer of ssDNA molecules can coat the surface of citrate stabilized spherical NPs via thiol linkers and hence can be exploited for gene silencing. Though ssDNA possess high negative charge density, the NP-ssDNA conjugate could not prevent the internalization into the cells. Moreover, the conjugates are protease and nuclease-resistant. The tethering of complementary DNA to the ssDNA immobilized NPs becomes stronger since there is a staunch dense packing of DNA around the NPs leading to increased efficiency for gene silencing applications[70]. In another instance, instead of regular DNA, chemically modified nucleic acids, known as locked nucleic acids (LNA), were used which have the advantage of being more stable and enhanced complementary DNA binding capacities. They also efficiently tether GNPs. Hence, tailor-made DNA for desirable functions is the requirement so that we can apprehend and predict the NP conjugate structures and their functions[76]. The stability of such DNA functionalized GNPs can be correlated to the salt concentration and curvature of the NP surface[77]. DNA packing density decreases as the size of the NPs increases to 60 nm, reaching a plateau near the packing density of ssDNA on a flat substrate. Spherical NPs acted like a paradigm based on which ssDNA attachment on rod-shaped NPs was possible with complete accuracy.

Furthermore, similar to ssDNA, even RNA attachment was possible and was then demonstrated by Mirkin et al[78]. Anti-firefly luciferase siRNA was conjugated to GNPs and

their gene knockout potential was noted and compared with the regularly used cationic lipid transfection agents[79]. Nuclease-free synthesis of GNPs was possible through diethyl pyro-carbonate treatment and autoclaving since RNA is highly susceptible to nucleases. This treatment is possible only for the citrate-capped spherical GNPs and not for gold nanorods since at high temperatures they tend to reshape into spherical ones. This kind of coupling between GNPs and siRNA is considered to enhance the stability of such conjugates in serum eight-fold as compared to bare siRNA. Such conjugates are resistant to degradation from many physiological RNA cleavers.

2.1.2.3.2 Delivery of drugs

Controlled release of drugs is an important criterion for designing a good drug delivery system. Other parameters, such as high surface area, tunability, and decreased physiological side-effects, are playing a critical role in deciding whether the delivery system can be used for delivering the drugs. There are many antibiotics which have gained resistance against microorganisms and are sometimes toxic to host cells. GNPs have come to the rescue of such drugs and have been conjugated with them for transforming resistant bacterial cells to sensitive ones. Moreover, this conjugation has also led to a reduction in the toxicity of host cells. Notably, vancomycin is the antibiotic to which Enterococci and Gram-negative bacteria such as Escherichia coli have become resistant (**Figure 2.2.**). Such strains have been tested after conjugating vancomycin with GNPs via thiol linkage which showed very good activity against both bacterial strains. The modus operandi of such particles is due to multivalency since multiple drug molecules on a single NP led to the increased binding to the D-Ala-D-Ala moieties at the terminal position[80–82].

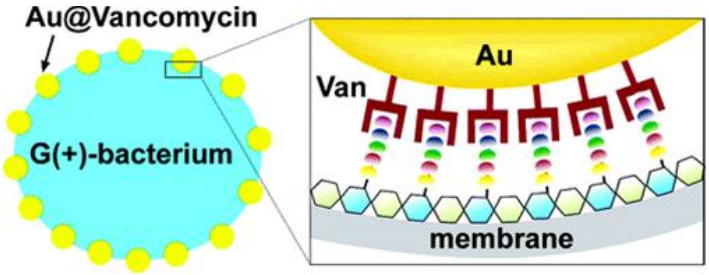

Figure 2.2. Illustration of a possible multivalent interaction between a Van-capped Au nanoparticle (2) and a VanA genotype VRE strain (hexagons: glycosides; ellipses represent the amino acid residues of the glycanpeptidyl precursor with different colors: L-Ala (yellow), D-Glu (orange), L-Lys (green), D-Ala (blue), and D-Lac (purple) *(Reprinted with permission from*[82] *Copyright 2003 American Chemical Society*).

The orientation of vancomycin is very critical for enhancing the binding with bacteria. Hence covalent tethering between GNPs and vancomycin is an important method to be exploited. Moreover, bis(vancomycin) cystamide has been exploited to surface functionalize NPs since they can absorb near-IR wavelengths of light maximally[83,84]. GNPs can also be utilized for binding a variety of bacterial types such as vancomycin-resistant Enterococci (VRE) and meticillin-resistant staphylococcus aureus (MRSA) strains. Once such NPs are bound to resistant strains, they can cause photothermal destruction with maximal efficiency. This method is even nontoxic for nonbacterial cells, which was determined by the MTT assays with human epidermoid carcinoma epithelial cells. Instead of antibiotics, photosensitizers such as toluidine blue O (TBO) were also covalently attached to tiopronin-functionalized GNPs, that were highly stable[85]. There was a four-fold decrease in the minimal inhibitory concentration (MIC) when irradiated with white light or laser light when TBO-functionalized GNPs are used in comparison with free TBO. In another instance, many anticancer drugs have been utilized for their attachment with GNPs, since they tend to exhibit systemic side-effects and are nonspecific, affecting normal cells too. The chemotherapeutic drugs such as cisplatin, paclitaxel, tamoxifen and doxorubicin are a few examples of this class. GNPs have proved to be advantageous in the sense that after their attachment with anticancer drugs, the conjugate is less toxic with increased specificity towards cancer cells as compared to free drug. **Table 2.1** summarizes GNP-drug conjugates for bactericidal applications.

Table 2.1. Summary of gold nanoparticle–drug conjugates for bactericidal applications showing the drugs which have been studied, any extra treatment which is required, the attachment chemistry to the gold surface, the type of bacteria tested, and the corresponding references *(Adapted from the reference[86])*

Drug/treatment	Attachment	Tested against	Reference
Vancomycin	Thiol	VRE, gram-negative	(Gu et al, 2003)
Vancomycin/photothermal	Thiol	Gram-positive, gram-negative, VRE, MRSA, PDRAB	(Huang et al, 2007)
Ampicillin, streptomycin, kanamycin	Amine	Gram-positive, gram-negative	(Saha, et al.,2007)
Cefaclor	Amine	Gram-positive, gram-negative	(Rai, Prabhune, & Perry, 2010)
Toluidine blue O /photosensizitization	Thiol	Gram-positive	(Gil-Tomas, et al., 2007)

2.1.2.3.3 Plasmonic photothermal therapy (PPTT)

Currently, the most widely employed technique to treat cancer and some infectious disease are Photothermal therapy (PTT) which can damage the cells[87]. The main principle behind this method is as follows: GNPs have a capability of maximum absorption in the visible or near-IR region, so when it is excited with the corresponding light source which causes vibrations of atoms in GNPs and produces enough heat. So, when GNPs are injected into the human body to treat cancer cells the NPs produce heat which kills or damage the cells. This thermal treatment can be produced both local heating (with Mw, ultrasonic) and general hyperthermia[88]. Therefore, both local and general hyperthermia leads to irreversible damage to the cells. The thermal cancer treatment is a big revolution, which enabled controlled injury to tumor region to be achieved.

GNPs were started for PTT use in 2003[89,90]. Afterward, it was called as plasmonic photothermal therapy (PPTT)[88]. In the beginning for selective damage to target cells researcher employed 20 and 30 nm GNPs irradiated with a laser pulse to produce local heating[91]. The unique GNPs are able to hold their optical properties inside the cells for quite a long time under certain conditions. So, successive irradiation with pulsed laser controls the cell inactivation by means of non-traumatic mode. Specifically, a cluster of small 30 nm GNPs produces more heat at low laser power than the free individual particles[92]. Usually, the gold nanoshell and nanorod are best suited for PPTT[93]. In the recent years, the number of research publications dealing with the application in PPTT is increasing especially of gold nanorods[94–96]; nanoshells[97–100].

But to avoid GNPs toxicity in the liver, spleen and its side-effects in other organs, the surface functionalization is carried out. Usually, there are two delivery strategies,

- conjugation of GNPs to polymer coating,
- conjugation with antibodies to target only cancer cells

The commonly used polymer for drug delivery is PEG, this is because it acts to increase the bioavailability, NPs stability and prolonging the circulation time in the bloodstream by less accessible to the immune system. This method is called passive and in the active version where antibodies are used[101,102]. The active delivery method is more reliable and effective, because of employing antibodies to a specific tumor, most commonly used antibodies are epidermal growth factor receptor (EGFR) and its types[103,104] as well as tumor necrosis factor (TNF)[105]. Because of this multifunctionality, the GNP conjugated with antibody can be used for both

diagnosis and PPTT[106,107]. For example, liposomes functionalized GNPs labeled with anti-Her2[108] and transferrin[109], shows increased penetration of NPs into cancer cells. Finally, GNPs with SPR property shows a promising candidate for PPTT of cancer and other diseases.

2.1.2.3.4 Photodynamic therapy (PDT)

To treat cancer using photosensitizers at a specific wavelength of visible light is known PDT method[110]. Usually, photosensitizers are injected into the human body intravenously, but sometimes contact and oral administration are also done which will accumulate in tumors regions. Then the tumor region is irradiated using laser light at a specific wavelength of which dye can absorb. Therefore, the substance produces highly active radicals which will induce necrosis and apoptise the tumor cells or tissues[111]. The major drawbacks of using photosensitizer in PDT is that they remain in the human body for a longer time, thus leaving the patient tissues highly sensitive to light. It is notable[112] that some of the metallic NPs can be employed as an effective fluorescence quenchers. Recently[113,114] it is shown that the plasmonic particle can enhance the fluorescence intensity by placing at an optimal distance from the metal. This concept improved the efficiency of PDT. Therefore, several investigations have been carried out for drug delivery by coating GNPs with a layer of polymer[115–118]. And to improve the entry of photoactive material, the surface of GNPs have been modified using peptides and proteins[119,120]. Recently, composite NPs made of MNPs with gold nanoshell (CSNPs) with PEG coating along with impregnation of photodynamic dye and antibodies has been employed for effective PDT[121]. Finally, GNPs attached with photodynamic dyes can also be used as an antimicrobial effect has been reported[122–124].

2.1.3 Core-shell nanoparticles (CSNPs)

Core-shell nanoparticles are captivating huge attention than other NPs because it comprises more than one material which exhibited new and improved properties (**Figure. 2.4.**)[125–127]. Since these NPs have emerged at the verge between materials chemistry and other fields, such as biomedical, pharmaceutical, optics and catalysis[128]. CSNPs are highly functional materials with modified properties. The fascinating properties arising either from core or shell can be ultimately different. The properties can also be modified by altering the constituting materials of core and shell or their ratios[129]. These CSNPs are widely explored especially because it can be manipulated easily to meet the requirements of different application[130,131]. The true goal of designing CSNPs is for following possibilities,

- Surface modification,

- Increase the functionality,
- Stability.

CSNPs are widely used in different fields like biomedical[132,133] and pharmaceutical applications[131]. In case of biomedical field, CSNPs are majorly used for

- bioimaging[134,135],
- controlled drug release[136,137],
- targeted drug delivery[6,136,138],
- cell labeling[139,140],
- tissue engineering applications[141].

The CSNPs are classified into three types (**Figure 2.3.**), such as:

(a) core–shell,

(b) hollow core–shell,

(c) rattle core–shell nanostructures.

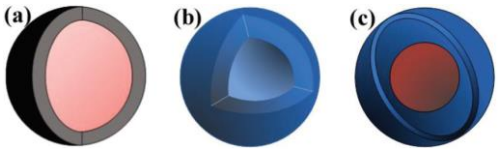

Figure 2.3. Types of Multifunctional nanomaterials (*Reproduced with permission from reference*[142])

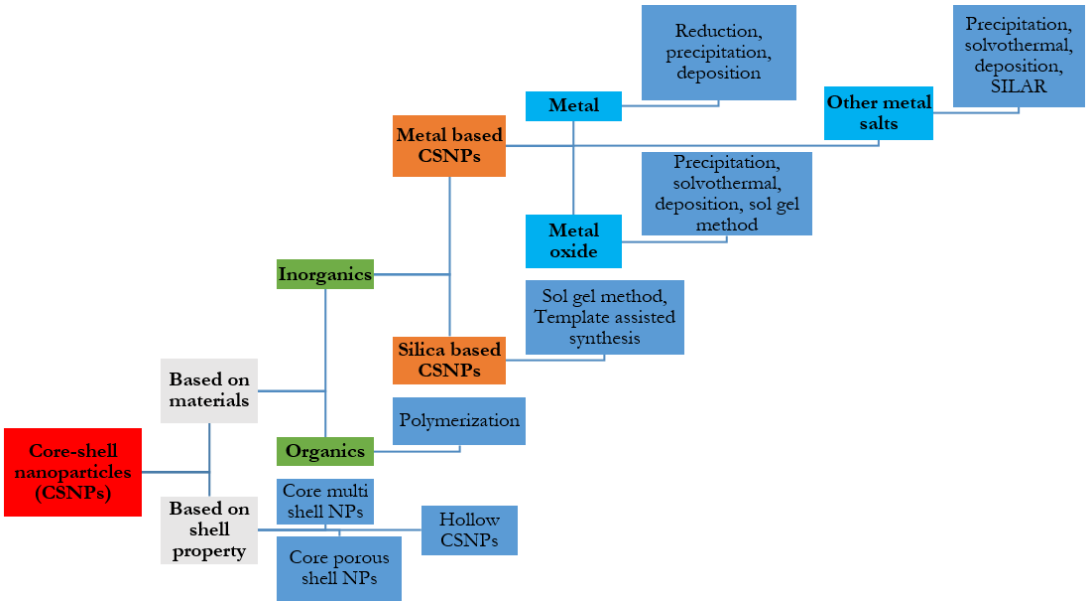

Figure. 2.4. General classification of CSNPs based on material-type and properties of their shells

But, as this thesis is purely concentrated only on CSNPs. So, the various synthesis methods, characterization techniques, and applications will be discussed in detail below.

2.1.3.1 Design of Core-shell nanomaterials

The CSNPs are a class of nanocomposite which contains an inner core shielded with one or more shells of different other materials. Therefore, CSNPs can exist in different amalgamations[128]. The properties of CSNPs are mainly correlated with the materials used for the synthesis of core, shell, and also related to the interface layer. Thus, it offers potential opportunities and capabilities for manipulating properties by controlling the chemical compositions and sizes of the core and shell[144,145].

The synthesis and selection of the material for CSNPs are completely depended on the application type. Therefore, designing CSNPs are generally depended on the final application. For example in the case of drug delivery application, the core material could possess magnetic property, and the shell can be made of either polymer or porous silica[146]. Similarly, for nanocatalysts, the core is comprised of Fe_3O_4 or Fe_2O_3, while the shell is a metal nanocluster[147]. The morphology, size etc. of a core material predicts the architecture of CSNPs. For designing a multifunctional system for performing various therapies and imaging of cancer cells[148], the magnetic core with a porous silica shell can be encapsulated. Finally, GNPs can be formed as a subsequent shell around the silica shell, which can be employed as a multifunctional structure for imaging, drug delivery, and photothermal therapy.

As a matter of fact, the design of CSNPs is merely depend on the type of core and its size. For example, a multifunctional CSNPs were MNPs are used as core for MR imaging in which the core size is a deciding factor because when the magnetic core size is lesser than 50 nm it will possess weak magnetic forces in the scanner and MNPs larger than 300 nm will obviously get trapped in the lungs and liver causing side-effects or toxicity[149]. Therefore, in most of the cases, functionalization are considered to be a crucial process for designing the shell. Commonly, the gold shell is fabricated around the magnetic cores using thiol groups as functional linkers which aid for attaching gold nanoclusters for the formation of shell[150]. Thus using above strategies various CSNPs architectures are constructed using the nature of the core and shell materials (**Figure. 2.5.**)[151].

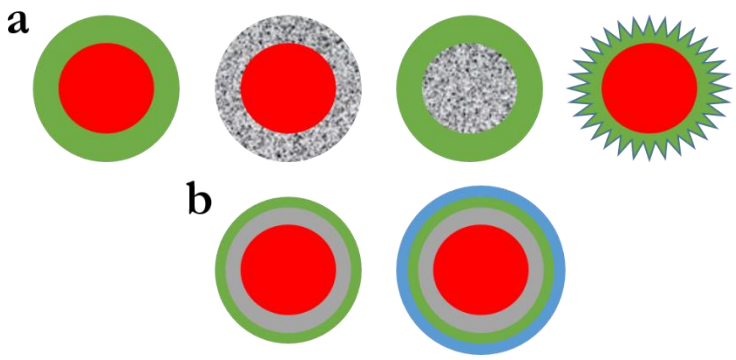

Figure 2.5. Different CSNPs structures with (a) porous core and shell, (b) different core-multiple shell structures

2.1.3.2 Fabrication techniques of Core-shell nanomaterials

2.1.3.2.1 Core materials

The applications of CSNPs is dependent on the material selection of core and shell. Usually, the core is composed of metals, metal oxides, QDs, and polymer. Many types of research have been carried out for synthesizing CSNPs using metal oxides[152], Au[153], Ag[154], Co[155], Fe, and polymer cores[156] for various applications. For example, metal oxide NPs used for photocatalytic, drug control release and delivery applications. Additionally, Au noble metal nanocores have been used for nanocatalysis and PTT. QDs for bio-imaging and diagnostics. Iron, cobalt, manganese, and gadolinium[157] core NPs play important roles in MR imaging[158]. Furthermore, Fe-based MNPs exhibiting as a potential candidate as a multifunctional nanosystem for therapy, imaging, and diagnosing[159].

2.1.3.2.2 Shell fabrication

There are several synthesis approaches for forming nanoshell on the core NPs. Mostly, core NPs are synthesized first and then shell NPs are made. This is because the core NPs (substrate/matrix) surfaces provide nucleation sites for the shell atoms to nucleate on it. Various techniques for coating different types of shell materials are as follows:

2.1.3.2.2.1 Metal-oxide shell

Formation of metal-oxide shell on the core materials lead to produce a wide spectrum of properties. For example, metal-oxide shell on MNPs generates interesting semiconducting and magneto-optical properties. Although the various types of metal-oxides are used for shell formation, silicon dioxide (SiO_2) is still widely employed for shell formation using sol–gel approach, which involves hydrolysis and condensation of the tetraethyl orthosilicate (TEOS).

Some of the examples are Au@SiO_2[160], Ag@SiO_2[161] (**Figure. 2.6.**), and Pd@SiO_2. However, a much understanding of the shell formation process is necessary for controlling the size or thickness of metal-oxides on to the cores NPs[162].

Figure. 2.6. Scheme of the proposed formation process and TEM images of a SiO_2 shell around a Ag nanocore (*Reprinted with permission from reference[161] Copyright 2013, American Chemical Society*)

2.1.3.2.2.2 Noble metal shells

Noble metal shells coating onto NPs has gained its strong place in the research topic as it results in peculiar characteristics and versatile applications. Currently, the most important synthesis methods for coating noble metal is the reverse micelle technique which is usually carried out by varying the metal salt ratio to the amount of reducing agent. This method has been widely used to form metal shells around MNPs such as Co and Fe NPs[163–165]. Another method is the thermal decomposition method at high temperatures[166]. For example, Pd shell coating onto Ni Core using oleylamine at an elevated temperature[167]. In the case of Au coated MNPs by thermal decomposition, MNPs were synthesized first in the presence of oleic acid and oleylamine mixture. After that, Au shell was introduced by chloroauric acid ($HAuCl_4$) reduction. Additionally, silver (Ag) shell was constructed around the CSNPs by adding silver nitrate ($AgNO_3$) in the presence of reducing agent. Au coated MNPs not only provide the dual functionality of the magnetic and plasmonic properties but also long-term stability. So, it possesses great platform for both therapeutic and diagnostic applications[168].

2.1.3.2.2.3 Dense shells

The shell formation on the core is usually dense or solid. This type of dense shell is usually made of silica or alumina, and sometimes with carbon. The silica or alumina shell will show a hydrophilic character and carbon shows a hydrophobic character. These dense shells are widely used for coating MNPs which can be utilized for biological applications. However, in the recent years, polymer shells are coated homogeneously on the core NPs which provides stealth mechanism to the core and found to be more suitable candidates.

2.1.3.2.2.4 Mesoporous shells

The formation of dense shells around NPs provides protecting, insulating and multi-functionality. But, the novel opportunities can be obtained using the mesoporous shell as because it can hold different moieties and dissipates it in and out from the core. This mesoporous shell diameter ranges from 2 to 15 nm, depending on the surfactant used. CTAB has been widely employed to form mesoporous silica shells around different types of cores. For instance, amino functionalized Si shell has been fabricated around silica cores[169], and MNPs[170] using anionic surfactants. Mesoporous shells with a pore size of 7 nm have also been fabricated using a Pluronic P123 surfactant[171].

2.1.3.3 Characterization techniques for core-shell nanoparticles[143]

Here, some of the important characterization techniques employed for CSNPs are discussed in brief: In the case of CSNPs, the combination of the core, shell, surface functionalization plays crucial effects on their properties and applications. So, in order to describe the properties of CSNPs, it is mandatory to elucidate, i.e., the size, shape, surface characteristics and existence of dopants.

XRD is a method used for evaluating the crystal phases of various materials, including CSNPs. Particularly for CSNPs, it is an important tool which can shed light on the presence of CSNPs. This can even detect the separated phases of core and shell simultaneously.

Scanning electron microscopy (SEM) and transmission electron microscopy (TEM) analysis were usually carried out to determine the size, shape, and homogeneity of the CSNPs. But, in the case of SEM, it uses only secondary electrons so it generates only a surface image, which is very difficult to distinguish the CSNPs structure with SEM analysis.

HRTEM aids in the simultaneous analysis of both lattice fringes and interplanar atomic spacings of CSNPs which clearly distinguish the core and shell. Additionally, EDS (accessory to TEM instruments), can serve as a powerful technique for determining the elemental distribution in a specified region. In the case of HAADF-STEM, which in one of the most important analytical method to confirm the formation of CSNPs were regions with a larger atomic number are determined by brighter contrast in images. Therefore, using this Z-contrast images one can analyze the element distribution visually.

The unique optical properties are exploited which is exhibited by noble metals. So, plasmonic, and absorption properties of various NPs used to synthesize CSNPs are characterized directly or indirectly by several spectroscopic methods. UV-Vis spectroscopy is

the most widely used spectroscopic methods for the analysis of different NP types. In the case of, organic type CSNPs, IR spectroscopy was used for the identification of the various organic moieties present in the CSNPs.

Another most important technique for studying the CSNPs surface characteristics is Raman spectroscopy. And also, surface enhanced Raman spectroscopy (SERS) is used for investigating CSNPs incorporated with SERS active metals like Cu, Au, and Ag.

2.1.3.4 Applications of core-shell nanoparticles

CSNPs have major advantages in the field of biomedical and electronics. Some of the different applications are as follows:

2.1.3.4.1. Biomedical applications

CSNPs has got a variety of exciting applications in the field of biomedicine which have been developed by researchers over the past few decades. Some of them are mentioned below:

2.1.3.4.1.1. Drug targeting and delivery

For drug delivery and targeting, CSNPs are designed with exceptional properties,

- At first, the drug is encapsulated with the help of surface functionalization along with a linker for specific targeting to cancer cell,
- Then these CSNPs will reach the target cell site and disintegrate the drugs which are attached on to the surface acting like a drug cargo.

The drug release from the CSNPs will be triggered heat, light, pH or ion concentration. By further attaching the fluorescent material, these CSNPs, which can be considered either as sensors or to track the drug delivery to a specific site. Generally, MNPs made of superparamagnetic Fe, Ni, Co are often used to design the core with suitable shell coatings for *in vivo* drug release and sensor applications[172,173]. Presently, MNPs with polymer CSNPs are typically employed for drug delivery, cell labeling, separation[174,175], and tumor delineation[176]. This is due to their biocompatibility with living cells, so, MNPs@polymer and MNPs@SiO_2 are often used over bare MNPs for drug delivery applications[177,178].

2.1.3.4.1.2. Bioimaging

There are different types of molecular bioimaging techniques used for both *in vivo* and *in vitro* specimens. But, CSNPs comprising of both QDs and MNPs are synthesized for dual-mode of optical and MR imaging simultaneously[176,179,180]. These CSNPs use either QDs or dye-doped QDs. However, QDs shows a high level of toxicity which can be minimized by coating

them with appropriate materials to form a CSNPs for utilizing *in vivo* optical imaging applications[181,182].

For bioimaging, both fluorescence and photoluminescence properties are also used by incorporating lanthanide metal group. Usually, lanthanide metals show good luminescence, so with well-designed biocompatible shell, these materials can be possibly utilized for the imaging and detection. By choosing right lanthanide dopants such as Er, Yb or Tm, the emission spectra can be shifted to green, blue or red wavelengths with increased intensity[183–185].

2.1.3.4.1.3. Sensors

Sensors are compact devices which assess and quantify a physical property and transfer it into a signal, which can be interpreted by a different instrument. The biomacromolecules like DNA, RNA, glucose, cholesterol, etc., can be detected using NPs based sensors for *in vivo* applications. Currently, MNPs coated with metal, silica, polymers, are used for bioanalytical sensors[186–188]. One of the big research breakthroughs is the detection of tumor cells in *in vivo* using Au/Ag CSNPs[189]. And damaged DNA can be detected using MNPs based sensors such as Fe/Fe_2O_3 CSNPs[190], where the MNPs surface is functionalized with cytochrome P450, myoglobin (Mb) and hemoglobin (Hb) to mimic *in vivo* toxicity[191].

2.1.3.4.2. Catalytic applications

The MNPs properties are greatly influenced by surface coating with functional materials like noble metals, semiconductors, etc[192,193]. For example, MNPs based catalyst has been fabricated Fe_3O_4@SiO_2-Au@m-SiO_2 double CSNPs considered as integrated catalysts for the catalytic reduction of 4-nitrophenol and styrene epoxidation (**Figure 2.7.**). Furthermore, Au@Fe_2O_3 with SiO_2 was employed for the catalytic conversion of CO to CO_2 whose conversion is more efficient when compared to uncoated Au@SiO_2[194]. This proves that MNPs incorporation plays a vital role in conversion efficiency in catalysis. And bimetallic CSNPs[195], such as Au/Pd[196] and Au/Ag[197], are currently employed majorly in catalytic reactions.

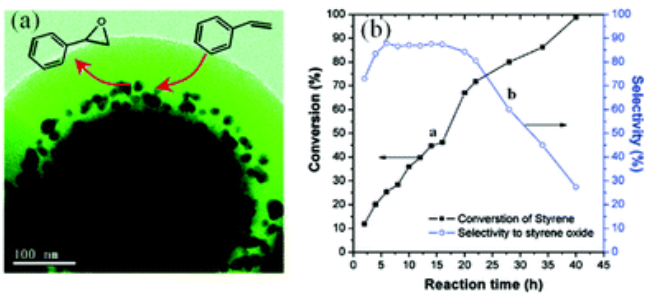

Figure. 2.7. (a) TEM image and (b) the conversion of styrene and selectivity of styrene oxide over multifunctional Fe_3O_4@SiO_2-Au@mSiO_2 double CSNPs as a highly integrated catalyst system (*Reprinted with permission from reference[147] Copyright 2010, American Chemical Society*)

2.1.3* Gold coated magnetic nanoparticles (MNPs@Au)

Gold coated magnetic nanoparticles (MNPs@Au) have been highly recognized by material scientists and efficiently used in various fields. To be specific, effectively employed in biomedicine, including MR imaging[198], targeted drug-delivery[199], etc. The main reason behind the usage of MNPs@Au in many sectors is because these CSNPs are highly versatile; both magnetic and plasmonic properties can be highly tuned/tailored depending on the applications by modifying CSNPs size, shell, morphology, and surface functionalization. This thesis is completely devoted to MNPs@Au so it is necessary for us to discuss various synthesis methods, surface modification, and finally some of the biomedical applications which are represented as follows:

Synthesis of MNPs@Au

As discussed earlier, the MNPs@Au synthesis involves two main processes,

1. Iron/iron oxide core is synthesized first,
2. then subsequent of Au shell coating is done

The previous sections explain the various methods and surface functionalization of MNPs and GNPs. So, we have discussed some of the major challenges involved in the synthesis of MNPs@Au below.

Challenges in Au shell formation

Some of the challenges faced by researchers in the formation of Au shell around the iron oxide core are as follows[200]:

- when MNPs are coated with Au layer it is necessary to ensure that the NPs are completely protected without exposing the core NPs,
- to accurately control the thickness of the Au shell,
- to characterize the synthesized MNPs@Au morphologically.

Formation mechanism of MNP@Au

The formation of MNP@Au using Au shell can be of 2 types (**Figure 2.8.**), which is as follows:

Direct coating - Au shell is formed directly on the MNP surface

Indirect coating - glue material is used onto MNP surface and then Au shell is formed

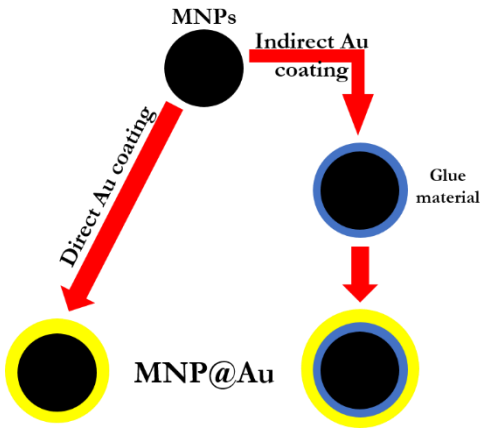

Figure 2.8. Illustration representing direct and indirect routes for gold shell coating

Direct Au coating

In the case of direct Au coating, sodium citrate method is widely used technique for the synthesis of Au shell onto the surface of MNP core. In this technique, the Au seeds are prepared by using $HAuCl_4$ precursor solution in the presence of sodium citrate, by mixing with MNPs under vigorous stirring[201,202]. Here, sodium citrate acts as a both reducing agent and also as a capping agent, so it provides NPs stability by preventing MNPs aggregation. The formation MNP@Au is confirmed by a change of reaction solution color from faint brown to burgundy[203,204].

For instance, when the MNPs are synthesized using thermal decomposition at high temperatures using organic compounds such as oleic acid and oleylamine, the gold shell is formed by reduction of $HAuCl_4$ in the presence of chloroform. This technique produces thick Au shell and to make it water-soluble, sodium citrate and CTAB is employed. To increase the Au shell size, gold precursor along with ascorbic acid and CTAB is used. This direct coating provides a fine control of both shell thickness and smoothness[205,206].

Indirect Au coating

MNP@Au CSNPs can be obtained by indirect Au coating by employing a glue layer in between the MNPs core and the outer GNPs shell which provides enough stability during the formation of CSNPs and also for other biomolecule functionalization.

Researchers developed poly-L-histidine as the glue material for CSNPs synthesis. The MNPs were synthesized using oleic acid capping and were dispersed in chloroform. So, to make MNPs water-soluble their surface was modified using an amphiphilic polymer with a carboxylic acid. The pol-L-histidine was added to the reaction mixture which adsorbs onto the

amphiphilic polymer *via* electrostatic interactions. Finally, $HAuCl_4$ is reduced onto the chelating agent with hydroxylamine forming the Au shell[207].

In a different study, a polymer poly(cyclotriphosphazene-*co*-4,4'-sulfonyldiphenol) (PZS) was used as the glue material. The MNPs were coated with PZS layer and then Au seeds were added which get adsorbs on the PZS surface by reduction of $HAuCl_4$ by sodium borohydride ($NaBH_4$)[208].

Silica has been widely used as a glue material for CSNPs synthesis[209]. Firstly, the MNPs were synthesized by co-precipitation method, then it is coated with a silica shell through the sol–gel technique. Secondly, Si coated MNPs were formed with three layers of positively charged polyelectrolytes, to ensure a smooth and uniform NPs surface. Later, negatively charged Au seeds using $HAuCl_4$ and ascorbic acid as the reducing agent was formed. The finally formed Au shell was about 30 nm thick by this process[210].

Surface functionalization of MNPs@Au

The surface modification/functionalization of MNPs@Au is a crucial step which plays an important for their use in various fields like analytical chemistry and biomedicine. The functionalized MNPs@Au has the ability to express very high sensitivity, specificity, and biocompatibility *in vitro* or *in vivo*. For example, in the biosensor, drug delivery nanocargo development of where the functionalized MNPs@Au act as an active element. The process of functionalization on the surface of Au nanoshell behaves as a bridge between the molecules for targeting or delivery in the specific site. The great advantage of nanoshell is its versatility, so any kind of biomolecules can be attached to enzymes, proteins, DNA, RNA, drugs etc. Additionally, the Au shell coating results in protecting the inner core from various environmental factors and also in the case of MNPs it prevents the aggregation which is the major drawbacks by means of electrostatic charge usually causing repulsion between MNPs.

Applications of MNPs@Au

Some of the potential applications of MNPs@Au ranging from biosensing to medical imaging and therapies are discussed.

Imaging

Some of the investigations compare MRI contrast agents like as-synthesized Au@MNPs, Feridex, dextran-MNPs which revealed similar r_2 values which confirm that the Au shell has no detrimental effect on the internal magnetic properties of the MNPs. But, Au@MNPs increase biocompatibility and long blood circulation time[16]. Other combination

diagnostic techniques like MRI-CT, MRI-ultrasound imaging, and MRI-photoacoustic imaging employs Au@MNPs probes.

CT relies on the attenuation of X-rays[211]. MRI-CT-ultrasound imaging probe was designed based on 6.1 nm Au@MNPs with a sugar-coating. The results showed that the Au shell enhances CT contrast, MNP core showed high T_2-weighted MR imaging and also allowed the imaging extravascular regions using ultrasound, which was not achievable with the microbubbles which are currently in clinical use[212].

Photoacoustic imaging where contrast is dependent on the absorption of light with the presence of contrast agents[191]. Au@MNPs nanoroses was synthesized which was found to possess a high r_2 relaxivity of 219 $mM^{-1}s^{-1}$ when compared to commercially available Feridex. Therefore, Au@MNPs offers a solid platform to be used in imaging technologies as a diagnostic tool adding several benefits to patients[213].

Hyperthermia

Hyperthermia therapy is used to treat superficial tumors by heat. This therapy offers an advantage of treating in a specific region or a whole body. MNPs and GNPs are commonly used candidates for hyperthermia to generate a cytotoxic environment to attack cancer cells[214].

For the MNPs based hyperthermia, the AMF with the frequencies of kHz - MHz is applied. Heat would be produced by MNPs due to the Brownian and the Neél modes. For GNPs based hyperthermia, the characteristic plasmon absorption in the NIR region which convert 100% absorbed NIR light into heat. But, the photo-induced hyperthermia can only treat shallow cancer but not in deeper tissues[215].

The Au-Fe_xO_y CSNPs possess both magnetic and photo induced hyperthermia properties with many advantages:

(1) this CSNPs can be used both for therapy and also for imaging at once,

(2) as it is a combination of two different kinds of NPs, it can enhance tumor cell killing even at very small concentrations in the body.

Magnetic-induced hyperthermia

The magnetic-induced hyperthermia for Au-Fe_3O_4 CSNPs can be achieved even with the smaller oscillating magnetic field frequencies with 44 Hz - 430 Hz. The heat generated by CSNPs are much higher when compared to MNPs alone under the same condition. This high heat generation purely depends on the higher magnetic anisotropy with the Au shell. Even though both Au-Fe_xO_y CSNPs and MNPs can be used for magnetic-induced hyperthermia for

cancer therapy, but Au-Fe_xO_y CSNPs will drastically reduce the aggregation of MNPs under magnetic field[216].

Photo-induced hyperthermia

Au-Fe_3O_4 CSNPs are widely employed for combination therapy in photo-induced hyperthermia using Au NPs and for MR imaging using MNPs in several literatures[217–219]. The CSNPs are immobilized with an antibody which could specifically target cancer cells, and when NIR laser is applied which could cause the cancer cell death. Au-Fe_3O_4 NPs can absorb in the NIR region, through which photo-induced hyperthermia can be achieved. Core/cluster/shell: Au@Fe_3O_4@SiO_2 NPs with anti-HER2 was designed. These NPs binds only to the HER2+ to target SKBR3 cells. Then, NIR laser is applied which will initiate cell death. The fluorescence images observed that the cells upon NIR laser irradiation were dead[220].

Drug delivery

Functionalized Au-Fe_3O_4 dumbbell shaped NPs with herceptin attached on MNPs and the cisplatin attached on the GNPs were used as a drug nanocargo. This multifunctional nanocargo can do multi-tasking work during therapy without disturbing each other. It is due to the difference in length, size and ligand thickness is quite large which may interfere with the each other's performance. The drug release profile was studied using dialysis tube at pH 7, in comparison to cisplatin release. There is a very low percentage of cisplatin is released in just 2 hours. But the release has been increased when the pH is lowered which is close to endosomal pH. The viability of cells was evaluated with control and cisplatin, which indicated that the viability of the nanocomplexes was negligible for its therapeutic effect[221].

Gene delivery

Gene therapy has become one of the great potential therapy for treating many diseases including cancer. But due to the low efficiencies of nonviral gene vectors, currently, this therapy is still limited[26]. MNPs based 'Magnetofection' has been used to overcome this drawback by associating gene vectors with the aid of a magnetic field[222]. Several research reports prove that MNPs improves the efficiency of viral and nonviral gene vectors up to several folds under the influence of magnetic field.

Usually, adenovirus and its linked viruses are the most efficiently tested for cancer gene therapy[223]. This vector is efficacy is highly dependent upon the coxsackie and adenovirus receptor (CAR) expression level of the target/cancer cell. If CAR level is low then it leads to poor gene transduction occurs. To overcome this, γ-Fe_2O_3@Au CSNPs is conjugated with

adenovirus and introduced into the cells which increased the adenovirus gene expression over 1000 times. Furthermore, these CSNPs entered the cell directly, independent of any pathways. Thus, the γ-Fe_2O_3@Au CSNPs have a huge potential to increase adenovirus tropism and also enhances gene transduction efficiency[224].

DNA-based biosensors

Functionalized Au NPs are effectively employed for various DNA based sensors. Au NPs are functionalized with thiolated oligonucleotides to recognize complementary DNA targets[225]. A 3-layer sandwich nanocomposite structure was designed based on SiO_2@Fe_3O_4@Au core/cluster/shell particles for sensing DNA[226]. These NPs were functionalized with 3' and 5' thiol-modified DNA strands, which were responsible for complementary hybridization with a target oligonucleotide of base pair mismatch. Usual aptamers are either DNA or RNA with specific identification of target biomolecules. But recently, due to the convenience of oligonucleotide functionalization *via* Au–S bonds an ultrasensitive aptasensor for thrombin was designed using Fe_3O_4@Au cluster/shell NPs[227].

Enzyme-based biosensors

The enzyme-based sensor combines the enzyme specificity and electrochemical techniques to be potentially used in diagnostics and monitoring. Au NPs have been extensively employed in modified electrodes because of their

- electrical conductivity,
- biocompatibility,
- enzyme immobilization on Au NPs surface *via* Au-S bonds.

Currently, Au@Fe_xO_y NPs were used to design enzyme-based sensors. Au@Fe_xO_y NPs can easily be immobilized onto the electrode surface under magnetic field. The Fe_3O_4@Au CSNPs is attached to the surface of a magnetic glassy carbon electrode (MGCE). Horse heart Mb was immobilized on CSNPs using cysteine. This modified electrode Mb-Fe_3O_4@Au-MGCE showed a good reduction performance of H_2O_2[191].

And also, when Au NPs are attached with a fluorescence marker, the light emitted from dye will be quenched by Au NPs. So, this property is utilized for developing enzyme. For instance, flower-shaped Au@Fe_3O_4 CSNPs used as a template to design an optical probe containing a fluorescent dye Cy5.5-GPLGVRG-TDOPA on the MNPs surface and SH-PEG_{5000} onto Au NPs surface. This complex is quite efficient for *in vivo* tumor imaging[213].

Cell sorting and separation

MNPs based separation has become the most widely employed techniques for biomarker purification, separation, and sorting. The usage of Au@MNPs efficiently improve the separation. For example, two hybrid Fe_3O_4@Au@Fe_3O_4 nanodumbbells and Fe_3O_4@Au necklace-like structures proved improved sorting and separation with tunable properties of both magnetic and optical[228]. Fe_3O_4@Au CSNPs are used for the purification of $CD4^+$ lymphocytes from the spleen of mice[229]. Another investigation also used poly(diallyldimethylammonium chloride) coated Fe_3O_4 (PDDA@Fe_3O_4) NPs by the coprecipitation method for cell purification[230]. The 4-mercaptophenylboronic acid-modified Fe_3O_4@C@Au CSNPs were synthesized and used for selective enrichment and separation of glycoproteins and glycopeptides[231].

Catalysis

Au NPs plays an important role in several catalytic processes[232–234]. Recently, Au@MNPs CSNPs were popularized to successfully demonstrate many catalytic effects for carbon-monoxide oxidation[235], hydrogen peroxide (H_2O_2)[236], reduction of nitrophenols[237] and H_2O_2[238]. The Au@Fe_xO_y NPs enables good separation for recycling the nanocatalysts from the reaction mixture using an external magnet. Also, the Au@Fe_3O_4 nanocatalysts can be easily recycled and reused with a conversion efficiency of around 100%.

2.2 References

1. Tartaj, P., del Puerto Morales, M., Veintemillas-Vergaguer, S., Gonzalez-Carreño, T. & Serna, C. J. Progress in the preparation of magnetic nanoparticles for applications in biomedicine. *J. Phys. D. Appl. Phys.* **42,** 182–197 (2009).
2. Corot, C., Robert, P., & Port, M. Recent advances in iron oxide nanocrystal technology for medical imaging. *Adv. Drug Deliv. Rev.* **58,** 1471–1504 (2006).
3. Ferrari, M. Cancer nanotechnology: opportunities and challenges. *Nat. Rev. Cancer* **5,** 161–171 (2005).
4. Wickline, S. A., Neubauer, A. M., Winter, P. M., Caruthers, S. D. & Lanza, G. M. Molecular imaging and therapy of atherosclerosis with targeted nanoparticles. *J. Magn. Reson. Imaging* **25,** 667–680 (2007).
5. Corot, C. *et al.* Macrophage imaging in central nervous system and in carotid atherosclerotic plaque using ultrasmall superparamagnetic iron oxide in magnetic resonance imaging. *Invest. Radiol.* **39,** 619–625 (2004).
6. Gupta, A. K. & Gupta, M. Synthesis and surface engineering of iron oxide nanoparticles for biomedical applications. *Biomaterials* **26,** 3995–4021 (2005).
7. Bonnemain, B. Superparamagnetic Agents in Magnetic Resonance Imaging: Physicochemical Characteristics and Clinical Applications A Review. *J. Drug Target.* **6,**

167–174 (1998).
8. Senyei, A., Widder, K. & Czerlinski, G. Magnetic guidance of drug-carrying microspheres. *J. Appl. Phys.* **49,** 3578–3583 (1978).
9. Veiseh, O. *et al.* Optical and MRI multifunctional nanoprobe for targeting gliomas. *Nano Lett.* **5,** 1003–1008 (2005).
10. Torchilin, V. P. Multifunctional nanocarriers. *Adv. Drug Deliv. Rev.* **64,** 302–315 (2012).
11. Mourino, M. R. From Thales to Lauterbur, or from the lodestone to MR imaging: magnetism and medicine. *Radiology* **180,** 593–612 (1991).
12. Lu, A. H., Salabas, E. L. Magnetic nanoparticles: Synthesis, protection, functionalization, and application. *Angew. Chemie - Int. Ed.* **46,** 1222–1244 (2007).
13. Gao, J. *et al.* FePt@CoS_2 yolk-shell nanocrystals as a potent agent to kill HeLa cells. *J. Am. Chem. Soc.* **129,** 1428–1433 (2007).
14. Jinhao Gao, *et al.* Fluorescent Magnetic Nanocrystals by Sequential Addition of Reagents in a One-Pot Reaction: A Simple Preparation for Multifunctional Nanostructures. *J. Am. Chem. Soc.*, **129 (39),** pp 11928–11935 (2007).
15. De la Presa, P. *et al.* Synthesis and characterization of FePt/Au core-shell nanoparticles. *J. Magn. Magn. Mater.* **316,** e753–e755 (2007).
16. Wang, C., Yin, H., Dai, S. & Sun, S. A General Approach to Noble Metal−Metal Oxide Dumbbell Nanoparticles and Their Catalytic Application for CO Oxidation. *Chem. Mater.* **22,** 3277–3282 (2010).
17. Pan, Y., Gao, J., Zhang, B., Zhang, X. & Xu, B. Colloidosome-based Synthesis of a Multifunctional Nanostructure of Silver and Hollow Iron Oxide Nanoparticles. *Langmuir* **26,** 4184–4187 (2010).
18. Peng, S., Lei, C., Ren, Y., Cook, R. E. & Sun, Y. Plasmonic/Magnetic Bifunctional Nanoparticles. *Angew. Chemie Int. Ed.* **50,** 3158–3163 (2011).
19. Hongwei Gu, Rongkun Zheng, XiXiang Zhang, and & Bing Xu. Facile One-Pot Synthesis of Bifunctional Heterodimers of Nanoparticles: A Conjugate of Quantum Dot and Magnetic Nanoparticles. (2004). doi:10.1021/JA0496423
20. Chouly, C., Pouliquen, D., Lucet, I., Jeune, J. J. & Jallet, P. Development of superparamagnetic nanoparticles for MRI: effect of particle size, charge and surface nature on biodistribution. *J. Microencapsul.* **13,** 245–255 (1996).
21. Gref, R. *et al.* 'Stealth' corona-core nanoparticles surface modified by polyethylene glycol (PEG): Influences of the corona (PEG chain length and surface density) and of the core composition on phagocytic uptake and plasma protein adsorption. *Colloids Surfaces B Biointerfaces* **18,** 301–313 (2000).
22. Moghimi, S. M., Hunter, a C. & Murray, J. C. Long-circulating and target-specific nanoparticles: theory to practice. *Pharmacol. Rev.* **53,** 283–318 (2001).
23. Juliano, R. L., Alahari, S., Yoo, H., Kole, R. & Cho, M. Antisense pharmacodynamics: Critical issues in the transport and delivery of antisense oligonucleotides. *Pharm. Res.* **16,** 494–502 (1999).
24. Brigger, I., Dubernet, C. & Couvreur, P. Nanoparticles in cancer therapy and diagnosis. *Adv. Drug Deliv. Rev.* **54,** 631–651 (2002).
25. Krotz, F. *et al.* Magnetofection-A highly efficient tool for antisense oligonucleotide delivery in vitro and in vivo. *Mol Ther* **7,** 700–710 (2003).
26. Plank, C., Scherer, F., Schillinger, U., Anton, M. & Bergemann, C. Magnetofection: Enhancing and targeting gene delivery by magnetic force. *Eur. Cells Mater.* **3,** 79–80 (2002).

27. Pan, B. *et al.* Dendrimer-modified magnetic nanoparticles enhance efficiency of gene delivery system. *Cancer Res.* **67,** 8156–8163 (2007).
28. Schillinger, U. *et al.* Advances in magnetofection - Magnetically guided nucleic acid delivery. *J. Magn. Magn. Mater.* **293,** 501–508 (2005).
29. Medarova, Z., Pham, W., Farrar, C., Petkova, V. & Moore, A. *In vivo* imaging of siRNA delivery and silencing in tumors. *Nat. Med.* **13,** 372–7 (2007).
30. Mykhaylyk, O. *et al.* Magnetic nanoparticle formulations for DNA and siRNA delivery. *J. Magn. Magn. Mater.* **311,** 275–281 (2007).
31. Pankhurst, Q. A., Connolly, J., Jones, S. K. & Dobson, J. Applications of magnetic nanoparticles in biomedicine. *J. Phys. D. Appl. Phys.* **36,** 167–181 (2003).
32. Dobson, J. Gene therapy progress and prospects: magnetic nanoparticle-based gene delivery. *Gene Ther.* **13,** 283–287 (2006).
33. Chomoucka, J. *et al.* Magnetic nanoparticles and targeted drug delivering. *Pharmacol. Res.* **62,** 144–149 (2010).
34. Neuberger, T., Hofmann, H., Hofmann, M. & Von Rechenberg, B. Superparamagnetic nanoparticles for biomedical applications: Possibilities and limitations of a new drug delivery system. *J. Magn. Magn. Mater.* **293,** 483–496 (2005).
35. Grief, A. D. & Richardson, G. Mathematical modelling of magnetically targeted drug delivery. *J. Magn. Magn. Mater.* **293,** 455–463 (2005).
36. Lübbe, A. S. *et al.* Clinical experiences with magnetic drug targeting: a phase I study with 4'-epidoxorubicin in 14 patients with advanced solid tumors. *Cancer Res.* **56,** 4686–4693 (1996).
37. Lübbe, A. S., Alexiou, C. & Bergemann, C. Clinical applications of magnetic drug targeting. *J. Surg. Res.* **95,** 200–6 (2001).
38. Mornet, S., Vasseur, S., Grasset, F. & Duguet, E. Magnetic nanoparticle design for medical diagnosis and therapy. *J. Mater. Chem.* **14,** 2161–2175 (2004).
39. Alexiou, C. *et al.* Locoregional cancer treatment with magnetic drug targeting. *Cancer Res.* **60,** 6641–6648 (2000).
40. Schulze, K. *et al.* Intraarticular application of superparamagnetic nanoparticles and their uptake by synovial membrane - An experimental study in sheep. *J. Magn. Magn. Mater.* **293,** 419–432 (2005).
41. Kohler, N. *et al.* Methotrexate-immobilized poly(ethylene glycol) magnetic nanoparticles for MR imaging and drug delivery. *Small* **2,** 785–792 (2006).
42. Kohler, N., Sun, C., Wang, J. & Zhang, M. Methotrexate-modified superparamagnetic nanoparticles and their intracellular uptake into human cancer cells. *Langmuir* **21,** 8858–8864 (2005).
43. Yang, J., Lee, H., Hyung, W., Park, S.-B. & Haam, S. Magnetic PECA nanoparticles as drug carriers for targeted delivery: synthesis and release characteristics. *J. Microencapsul.* **23,** 203–212 (2006).
44. Johnson, G. A. *et al.* Histology by magnetic resonance microscopy. *Magn. Reson. Q.* **9,** 1–30 (1993).
45. Fawell, S. *et al.* Tat-mediated delivery of heterologous proteins into cells. *Proc. Natl. Acad. Sci. U. S. A.* **91,** 664–668 (1994).
46. Weissleder, R. *et al.* In vivo magnetic resonance imaging of transgene expression. *Nat. Med.* **6,** 351–355 (2000).
47. Enochs, W. S., Harsh, G., Hochberg, F. & Weissleder, R. Improved delineation of human brain tumors on MR images using a long-circulating, superparamagnetic iron oxide agent (Combidex). *J. Magn. Reson. Imaging* **9,** 228–232 (1999).

48. Contag, P. R., Olomu, I. N., Stevenson, D. K. & Contag, C. H. Bioluminescent indicators in living mammals. *Nat. Med.* **4,** 245–247 (1998).
49. Zhao, M., Beauregard, D. A. D. A. a, Loizou, L., Davletov, B. & Brindle, K. M. M. K. M. Non-invasive detection of apoptosis using magnetic resonance imaging and a targeted contrast agent. *Nat. Med.* **7,** 1241–1244 (2001).
50. Poptani, H. *et al.* Monitoring thymidine kinase and ganciclovir-induced changes in rat malignant glioma in vivo by nuclear magnetic resonance imaging. *Cancer gene therapy* **5,** 101–109 (1998).
51. Blankenberg, F. G. *et al.* Quantitative analysis of apoptotic cell death using proton nuclear magnetic resonance spectroscopy. *Blood* **89,** 3778–3786 (1997).
52. Nunn, A. V. W. *et al.* Characterisation of secondary metabolites associated with neutrophil apoptosis. *FEBS Lett.* **392,** 295–298 (1996).
53. Gupta, A. K. & Gupta, M. Synthesis and surface engineering of iron oxide nanoparticles for biomedical applications. *Biomaterials* **26,** 3995–4021 (2005).
54. Luderer, A. A. *et al.* Glass-Ceramic-Mediated, Magnetic-Field-Induced Localized Hyperthermia: Response of a Murine Mammary Carcinoma. *Radiat. Res.* **94,** 190 (1983).
55. C.F. Chan, D., B. Kirpotin, D. & A. Bunn Jr., P. Synthesis and evaluation of colloidal magnetic iron oxides for the site-specific radiofrequency-induced hyperthermia of cancer. *J. Magn. Magn. Mater.* **122,** 374–378 (1993).
56. Brady, L. W., Heilmann, H. P., Seegenschmiedt, M. H., Fessenden, P. & Vernon, C. C. *Thermoradiotherapy and Thermochemotherapy*. *Springer Berlin* **173,** (Springer Berlin Heidelberg, 2012).
57. Jordan, A. *et al.* Endocytosis of dextran and silan-coated magnetite nanoparticles and the effect of intracellular hyperthermia on human mammary carcinoma cells in vitro. *J. Magn. Magn. Mater.* **194,** 185–196 (1999).
58. Wada, S., Tazawa, K., Furuta, I. & Nagae, H. Antitumor effect of new local hyperthermia using dextran magnetite complex in hamster tongue carcinoma. *Oral Dis.* **9,** 218–223 (2003).
59. Ito, A., Shinkai, M., Honda, H. & Kobayashi, T. Heat-inducible TNF-α gene therapy combined with hyperthermia using magnetic nanoparticles as a novel tumor-targeted therapy. *Cancer Gene Ther.* **8,** 649–654 (2001).
60. Petros, R. a & DeSimone, J. M. Strategies in the design of nanoparticles for therapeutic applications. *Nat. Rev. Drug Discov.* **9,** 615–627 (2010).
61. Kudgus, R. A., Bhattacharya, R. & Mukherjee, P. Cancer nanotechnology: emerging role of gold nanoconjugates. *Anticancer. Agents Med. Chem.* **11,** 965–973 (2011).
62. Arvizo, R. R. *et al.* Intrinsic therapeutic applications of noble metal nanoparticles: past, present and future. *Chem Soc Rev* **41,** 2943–2970 (2012).
63. Doane, T. & Burda, C. Nanoparticle mediated non-covalent drug delivery. *Adv. Drug Deliv. Rev.* **65,** 607–621 (2013).
64. Li, S. D. & Huang, L. Pharmacokinetics and biodistribution of nanoparticles. *Mol. Pharm.* **5,** 496–504 (2008).
65. Tao, A. R., Habas, S. & Yang, P. Shape control of colloidal metal nanocrystals. *Small* **4,** 310–325 (2008).
66. Daniel, M.-C. & Astruc, D. Gold nanoparticles: assembly, supramolecular chemistry, quantum-size-related properties, and applications toward biology, catalysis, and nanotechnology. *Chem. Rev.* **104,** 293–346 (2004).
67. Jadzinsky, P. D., Calero, G., Ackerson, C. J., Bushnell, D. A. & Kornberg, R. D. Structure of a thiol monolayer-protected gold nanoparticle at 1.1 A resolution. *Science*

318, 430–3 (2007).
68. Alkilany, A. M., Thompson, L. B., Boulos, S. P., Sisco, P. N. & Murphy, C. J. Gold nanorods: Their potential for photothermal therapeutics and drug delivery, tempered by the complexity of their biological interactions. *Adv. Drug Deliv. Rev.* **64,** 190–199 (2012).
69. Hong, R. *et al.* Glutathione-mediated delivery and release using monolayer protected nanoparticle carriers. *J. Am. Chem. Soc.* **128,** 1078–1079 (2006).
70. Rosi, N. L. Oligonucleotide-Modified Gold Nanoparticles for Intracellular Gene Regulation. *Science (80-.).* **312,** 1027–1030 (2006).
71. Li, Z. Multiple thiol-anchor capped DNA-gold nanoparticle conjugates. *Nucleic Acids Res.* **30,** 1558–1562 (2002).
72. Huff, T. B., Hansen, M. N., Zhao, Y., Cheng, J. X. & Wei, A. Controlling the cellular uptake of gold nanorods. *Langmuir* **23,** 1596–1599 (2007).
73. Letsinger, R. L., Elghanian, R., Viswanadham, G. & Mirkin, C. A. Use of a steroid cyclic disulfide anchor in constructing gold nanoparticle-oligonucleotide conjugates. *Bioconjug. Chem.* **11,** 289–291 (2000).
74. Hoft, R. C., Ford, M. J., McDonagh, A. M. & Cortie, M. B. Adsorption of amine compounds on the Au(111) surface: A density functional study. *J. Phys. Chem. C* **111,** 13886–13891 (2007).
75. A. D. McFarland, C. L. Haynes, C. A. Mirkin, R. P. V. D. and H. A. G. Citrate Synthesis of Gold Nanoparticles, MRSEC Education, University of Wisconsin–Madison. (2004).
76. Seferos, D. S., Giljohann, D. A., Rosi, N. L. & Mirkin, C. A. Locked nucleic acid-nanoparticle conjugates. *ChemBioChem* **8,** 1230–1232 (2007).
77. Hill, H. D., Millstone, J. E., Banholzer, M. J. & Mirkin, C. A. The role radius of curvature plays in thiolated oligonucleotide loading on gold nanoparticles. *ACS Nano* **3,** 418–424 (2009).
78. Storhoff, J. J., Elghanian, R., Mirkin, C. A. & Letsinger, R. L. Sequence-dependent stability of DNA-modified gold nanoparticles. *Langmuir* **18,** 6666–6670 (2002).
79. Giljohann, D. A., Seferos, D. S., Prigodich, A. E., Patel, P. C. & Mirkin, C. A. Gene regulation with polyvalent siRNA-nanoparticle conjugates. *J. Am. Chem. Soc.* **131,** 2072–2073 (2009).
80. Xing, B. *et al.* Self-assembled multivalent vancomycin on cell surfaces against vancomycin-resistant enterococci (VRE). *Chem. Commun. (Camb).* 2224–2225 (2003).
81. Rao, J. A Trivalent System from Vancomycin·D-Ala-D-Ala with Higher Affinity Than Avidin·Biotin. *Science (80).* **280,** 708–711 (1998).
82. Gu, H., Ho, P. L., Tong, E., Wang, L. & Xu, B. Presenting vancomycin on nanoparticles to enhance antimicrobial activities. *Nano Lett.* **3,** 1261–1263 (2003).
83. Huang, W. C., Tsai, P. J. & Chen, Y. C. Functional gold nanoparticles as photothermal agents for selective-killing of pathogenic bacteria. *Nanomedicine (Lond).* **2,** 777–787 (2007).
84. Kell, A. J. *et al.* Vancomycin-modified nanoparticles for efficient targeting and preconcentration of gram-positive and gram-negative bacteria. *ACS Nano* **2,** 1777–1788 (2008).
85. Gil-Tomás, J. *et al.* Lethal photosensitisation of Staphylococcus aureus using a toluidine blue O–tiopronin–gold nanoparticle conjugate. *J. Mater. Chem.* **17,** 3739 (2007).
86. Vigderman, L. & Zubarev, E. R. Therapeutic platforms based on gold nanoparticles and their covalent conjugates with drug molecules. *Adv. Drug Deliv. Rev.* **65,** 663–676 (2013).

87. Kennedy, L. C. *et al.* A new era for cancer treatment: Gold-nanoparticle-mediated thermal therapies. *Small* **7,** 169–183 (2011).
88. Huang, X., Jain, P. K., El-Sayed, I. H. & El-Sayed, M. A. Plasmonic photothermal therapy (PPTT) using gold nanoparticles. *Lasers Med. Sci.* **23,** 217–228 (2008).
89. Hirsch, L. R. *et al.* Nanoshell-mediated near-infrared thermal therapy of tumors under magnetic resonance guidance. *Proc. Natl. Acad. Sci. U. S. A.* **100,** 13549–54 (2003).
90. Zharov, V. P., Galitovsky, V. & Viegas, M. Photothermal detection of local thermal effects during selective nanophotothermolysis. *Appl. Phys. Lett.* **83,** 4897–4899 (2003).
91. Pitsillides, C. M., Joe, E. K., Wei, X., Anderson, R. R. & Lin, C. P. Selective cell targeting with light-absorbing microparticles and nanoparticles. *Biophys. J.* **84,** 4023–4032 (2003).
92. Huang, X., Qian, W., El-Sayed, I. H. & El-Sayed, M. A. The potential use of the enhanced nonlinear properties of gold nanospheres in photothermal cancer therapy. *Lasers Surg. Med.* **39,** 747–753 (2007).
93. Harris, N., Ford, M. J. & Cortie, M. B. Optimization of plasmonic heating by gold nanospheres and nanoshells. *J. Phys. Chem. B* **110,** 10701–10707 (2006).
94. Takahashi, H., Niidome, T., Nariai, A., Niidome, Y. & Yamada, S. Gold Nanorod-sensitized Cell Death: Microscopic Observation of Single Living Cells Irradiated by Pulsed Near-infrared Laser Light in the Presence of Gold Nanorods. *Chem. Lett.* **35,** 500–501 (2006).
95. Huff, T. B. *et al.* Hyperthermic effects of gold nanorods on tumor cells. *Nanomedicine (Lond).* **2,** 125–32 (2007).
96. Pissuwan, D., Valenzuela, S. M., Killingsworth, M. C., Xu, X. & Cortie, M. B. Targeted destruction of murine macrophage cells with bioconjugated gold nanorods. *J. Nanoparticle Res.* **9,** 1109–1124 (2007).
97. Loo, C., Lowery, A., Halas, N., West, J. & Drezek, R. Immunotargeted nanoshells for integrated cancer imaging and therapy. *Nano Lett.* **5,** 709–711 (2005).
98. Stern, J. M. *et al.* Efficacy of Laser-Activated Gold Nanoshells in Ablating Prostate Cancer Cells in Vitro. *J. Endourol.* **21,** 939–943 (2007).
99. Diagaradjane, P. *et al.* Modulation of *in vivo* tumor radiation response via gold nanoshell-mediated vascular-focused hyperthermia: Characterizing an integrated antihypoxic and localized vascular disrupting targeting strategy. *Nano Lett.* **8,** 1492–1500 (2008).
100. Waldman, S. A. *et al.* Opportunities for near-infrared thermal ablation of colorectal metastases by guanylyl cyclase C-targeted gold nanoshells. *Future Oncol.* **2,** 705–716 (2006).
101. Phillips, M. A., Gran, M. L. & Peppas, N. A. Targeted nanodelivery of drugs and diagnostics. *Nano Today* **5,** 143–159 (2010).
102. Nie, S. Understanding and overcoming major barriers in cancer nanomedicine. *Nanomedicine (Lond).* **5,** 523–528 (2010).
103. El-Sayed, I. H., Huang, X. & El-Sayed, M. A. Selective laser photo-thermal therapy of epithelial carcinoma using anti-EGFR antibody conjugated gold nanoparticles. *Cancer Lett.* **239,** 129–135 (2006).
104. Melancon, M. P. *et al. In vitro* and *in vivo* targeting of hollow gold nanoshells directed at epidermal growth factor receptor for photothermal ablation therapy. *Mol. Cancer Ther.* **7,** 1730–1739 (2008).
105. Visaria, R. K. *et al.* Enhancement of tumor thermal therapy using gold nanoparticle-assisted tumor necrosis factor-α delivery. *Mol. Cancer Ther.* **5,** 1014–20 (2006).
106. Larson, T. a, Bankson, J., Aaron, J. & Sokolov, K. Hybrid plasmonic magnetic nanoparticles as molecular specific agents for MRI/optical imaging and photothermal

therapy of cancer cells. *Nanotechnology* **18,** 325101 (2007).
107. Ke, H. *et al.* Gold-nanoshelled microcapsules: A theranostic agent for ultrasound contrast imaging and photothermal therapy. *Angew. Chemie - Int. Ed.* **50,** 3017–3021 (2011).
108. Kirpotin, D. B. *et al.* Antibody targeting of long-circulating lipidic nanoparticles does not increase tumor localization but does increase internalization in animal models. *Cancer Res.* **66,** 6732–6740 (2006).
109. Choi, C. H. J., Alabi, C. A., Webster, P. & Davis, M. E. Mechanism of active targeting in solid tumors with transferrin-containing gold nanoparticles. *Proc. Natl. Acad. Sci. U. S. A.* **107,** 1235–40 (2010).
110. Tuchin, V. V. *Handbook of Photonics for Biomedical Science (Series in Medical Physics and Biomedical Engineering)*. (CRC Press, 2010).
111. Wilson, R. The use of gold nanoparticles in diagnostics and detection. *Chem. Soc. Rev.* **37,** 2028–2045 (2008).
112. Lakowicz, J. R. *et al.* Plasmon-controlled fluorescence: a new paradigm in fluorescence spectroscopy. *Analyst* **133,** 1308–1346 (2008).
113. Bardhan, R., Grady, N. K., Cole, J. R., Joshi, A. & Halas, N. J. Fluorescence enhancement by au nanostructures: Nanoshells and nanorods. *ACS Nano* **3,** 744–752 (2009).
114. Ming, T. *et al.* Experimental Evidence of Plasmophores: Plasmon-Directed Polarized Emission from Gold Nanorod–Fluorophore Hybrid Nanostructures. *Nano Lett.* **11,** 2296–2303 (2011).
115. Sershen, S. R., Westcott, S. L., Halas, N. J. & West, J. L. Temperature-sensitive polymer-nanoshell composites for photothermally modulated drug delivery. *J. Biomed. Mater. Res.* **51,** 293–298 (2000).
116. Radt, B., Smith, T. A. & Caruso, F. Optically addressable nanostructured capsules. *Adv. Mater.* **16,** 2184–2189 (2004).
117. Shiotani, A., Mori, T., Niidome, T., Niidome, Y. & Katayama, Y. Stable incorporation of gold nanorods into N-isopropylacrylamide hydrogels and their rapid shrinkage induced by near-infrared laser irradiation. *Langmuir* **23,** 4012–4018 (2007).
118. Nakamura, T. *et al.* Large payloads of gold nanoparticles into the polyamine network core of stimuli-responsive PEGylated nanogels for selective and noninvasive cancer photothermal therapy. *Nanoscale* **2,** 739–746 (2010).
119. Chithrani, B. D. & Chan, W. C. W. Elucidating the mechanism of cellular uptake and removal of protein-coated gold nanoparticles of different sizes and shapes. *Nano Lett.* **7,** 1542–1550 (2007).
120. Liu, S. Y., Liang, Z. S., Gao, F., Luo, S. F. & Lu, G. Q. In vitro photothermal study of gold nanoshells functionalized with small targeting peptides to liver cancer cells. *J. Mater. Sci. Mater. Med.* **21,** 665–674 (2010).
121. Bardhan, R. *et al.* Tracking of Multimodal Therapeutic Nanocomplexes Targeting Breast Cancer in Vivo. *Nano Lett.* **10,** 4920–4928 (2010).
122. Kuo, W. S. *et al.* Antimicrobial gold nanorods with dual-modality photodynamic inactivation and hyperthermia. *Chem. Commun.* **103,** 4853 (2009).
123. Kuo, W. S. *et al.* Gold Nanorods in Photodynamic Therapy, as Hyperthermia Agents, and in Near-Infrared Optical Imaging. *Angew. Chemie* **122,** 2771–2775 (2010).
124. Tuchina, E. S., Tuchin, V. V, Khlebtsov, B. N. & Khlebtsov, N. G. Phototoxic effect of conjugates of plasmon-resonance nanoparticles with indocyanine green dye on Staphylococcus aureus induced by IR laser radiation. *Quantum Electron.* **41,** 354–359

(2011).
125. Henglein, A. Small-particle research: physicochemical properties of extremely small colloidal metal and semiconductor particles. *Chem. Rev.* **89,** 1861–1873 (1989).
126. Spanhel, L., Weller, H. & Henglein, A. Photochemistry of semiconductor colloids. 22. Electron ejection from illuminated cadmium sulfide into attached titanium and zinc oxide particles. *J. Am. Chem. Soc.* **109,** 6632–6635 (1987).
127. Youn, H. C., Baral, S. & Fendler, J. H. Dihexadecyl phosphate, vesicle-stabilized and in situ generated mixed cadmium sulfide and zinc sulfide semiconductor particles: preparation and utilization for photosensitized charge separation and hydrogen generation. *J. Phys. Chem.* **92,** 6320–6327 (1988).
128. Ghosh Chaudhuri, R. & Paria, S. Core/shell nanoparticles: Classes, properties, synthesis mechanisms, characterization, and applications. *Chem. Rev.* **112,** 2373–2433 (2012).
129. Oldenburg, S., Averitt, R., Westcott, S. & Halas, N. Nanoengineering of optical resonances. *Chem. Phys. Lett.* **288,** 243–247 (1998).
130. Daniel, M. C. M. & Astruc, D. Gold Nanoparticles: Assembly, Supramolecular Chemistry, Quantum-Size Related Properties and Applications toward Biology, Catalysis and Nanotechnology,. *Chem. Rev.* **104,** 293–346 (2004).
131. Caruso, F. Nanoengineering of Particle Surfaces. *Adv. Mater.* **13,** 11–22 (2001).
132. Balakrishnan, S., Bonder, M. J. & Hadjipanayis, G. C. Particle size effect on phase and magnetic properties of polymer-coated magnetic nanoparticles. *J. Magn. Magn. Mater.* **321,** 117–122 (2009).
133. Salgueiriño-Maceira, V. & Correa-Duarte, M. A. Increasing the Complexity of Magnetic Core/Shell Structured Nanocomposites for Biological Applications. *Adv. Mater.* **19,** 4131–4144 (2007).
134. Babes, Denizot, Tanguy, Le Jeune & Jallet. Synthesis of Iron Oxide Nanoparticles Used as MRI Contrast Agents: A Parametric Study. *J. Colloid Interface Sci.* **212,** 474–482 (1999).
135. De Farias, P. M. A. *et al.* Highly fluorescent semiconductor core–shell CdTe–CdS nanocrystals for monitoring living yeast cells activity. *Appl. Phys. A* **89,** 957–961 (2007).
136. Dresco, P. A., Zaitsev, V. S., Gambino, R. J. & Chu, B. Preparation and Properties of Magnetite and Polymer Magnetite Nanoparticles. *Langmuir* **15,** 1945–1951 (1999).
137. Sounderya, N. & Zhang, Y. Use of Core/Shell Structured Nanoparticles for Biomedical Applications. *Recent Patents Biomed. Eng.* **1,** 34–42 (2008).
138. Laurent, S. *et al.* Magnetic Iron Oxide Nanoparticles: Synthesis, Stabilization, Vectorization, Physicochemical Characterizations, and Biological Applications. *Chem. Rev.* **108,** 2064–2110 (2008).
139. Jaiswal, J. K., Mattoussi, H., Mauro, J. M. & Simon, S. M. Long-term multiple color imaging of live cells using quantum dot bioconjugates. *Nat. Biotechnol.* **21,** 47–51 (2002).
140. Michalet, X. & Pinaud, F. F. Quantum Dots for Live Cells, in Vivo Imaging, and Diagnostics. *Science (80).* **307,** 538–545 (2005).
141. De, M., Ghosh, P. S. & Rotello, V. M. Applications of Nanoparticles in Biology. *Adv. Mater.* **1003,** 4225–4241 (2008).
142. El-toni, A. M., Habila, M. A. & Labis, P. Design, synthesis and applications of core–shell, hollow core, and nanorattle multifunctional nanostructures. *Nanoscale*, **8**, 2510–2531 (2016).
143. Gawande, M. B. *et al.* Core-shell nanoparticles: synthesis and applications in catalysis and electrocatalysis. *Chem. Soc. Rev.* **44,** 7540–7590 (2015).
144. Jun, Y. *et al.* Heterostructured magnetic nanoparticles: their versatility and high

performance capabilities. *Chem. Commun.* **35,** 1203–1214 (2007).
145. Niemeyer, C. M. Nanoparticles, Proteins, and Nucleic Acids: Biotechnology Meets Materials Science. *Angew. Chemie Int. Ed.* **40,** 4128–4158 (2001).
146. Zhang, X. F. *et al.* Fe_3O_4–silica core–shell nanoporous particles for high-capacity pH-triggered drug delivery. *J. Mater. Chem.* **22,** 14450 (2012).
147. Deng, Y. *et al.* Multifunctional Mesoporous Composite Microspheres with Well-Designed Nanostructure: A Highly Integrated Catalyst System. *J. Am. Chem. Soc.* **132,** 8466–8473 (2010).
148. Ma, M. *et al.* Au capped magnetic core/mesoporous silica shell nanoparticles for combined photothermo/chemo-therapy and multimodal imaging. *Biomaterials* **33,** 989–998 (2012).
149. Barbé, C. *et al.* Silica Particles: A Novel Drug-Delivery System. *Adv. Mater.* **16,** 1959–1966 (2004).
150. Mohammad-Beigi, H., Yaghmaei, S., Roostaazad, R. & Arpanaei, A. Comparison of different strategies for the assembly of gold colloids onto Fe_3O_4@SiO_2 nanocomposite particles. *Phys. E Low-dimensional Syst. Nanostructures* **49,** 30–38 (2013).
151. Srdic, V., Mojic, B., Nikolic, M. & Ognjanovic, S. Recent progress on synthesis of ceramics core/shell nanostructures. *Process. Appl. Ceram.* **7,** 45–62 (2013).
152. Khan, E. A., Hu, E. & Lai, Z. Preparation of metal oxide/zeolite core–shell nanostructures. *Microporous Mesoporous Mater.* **118,** 210–217 (2009).
153. Yang, Y. C. *et al.* Facet-dependent optical properties of polyhedral Au–Cu_2O core–shell nanocrystals. *Nanoscale* **6,** 4316 (2014).
154. Tian, J. *et al.* Ag@poly(m-phenylenediamine)-Ag core–shell nanoparticles: one-step preparation, characterization, and their application for H_2O_2 detection. *Catal. Sci. Technol.* **1,** 1393 (2011).
155. Zhang, L. *et al.* Controllable synthesis of core–shell Co@CoO nanocomposites with a superior performance as an anode material for lithium-ion batteries. *J. Mater. Chem.* **21,** 18279 (2011).
156. Tian, J., Jin, J., Zheng, F. & Zhao, H. Self-Assembly of Gold Nanoparticles and Polystyrene: A Highly Versatile Approach to the Preparation of Colloidal Particles with Polystyrene Cores and Gold Nanoparticle Coronae. *Langmuir* **26,** 8762–8768 (2010).
157. Xue, X. *et al.* Emerging functional nanomaterials for therapeutics. *J. Mater. Chem.* **21,** 13107 (2011).
158. Kim, J. *et al.* Multifunctional nanostructured materials for multimodal imaging, and simultaneous imaging and therapy. *Chem. Soc. Rev.* **38,** 372–390 (2009).
159. Jun, Y., Lee, J. & Cheon, J. Chemical Design of Nanoparticle Probes for High-Performance Magnetic Resonance Imaging. *Angew. Chemie Int. Ed.* **47,** 5122–5135 (2008).
160. Zhu, X. *et al.* Au@SiO_2 core–shell nanoparticles for laser desorption/ionization time of flight mass spectrometry. *Analyst* **137,** 2454 (2012).
161. Bai, Z. *et al.* Fluorescent pH Sensor Based on Ag@SiO_2 Core–Shell Nanoparticle. *ACS Appl. Mater. Interfaces* **5,** 5856–5860 (2013).
162. Li, G. *et al.* Noble metal nanoparticle@metal oxide core/yolk–shell nanostructures as catalysts: recent progress and perspective. *Nanoscale* **6,** 3995 (2014).
163. Lin, J. *et al.* Gold-Coated Iron (Fe@Au) Nanoparticles: Synthesis, Characterization, and Magnetic Field-Induced Self-Assembly. *J. Solid State Chem.* **159,** 26–31 (2001).
164. Carpenter, E. E., Sims, J. A., Wienmann, J. A., Zhou, W. L. & O'Connor, C. J. Magnetic

properties of iron and iron platinum alloys synthesized via microemulsion techniques. *J. Appl. Phys.* **87,** 5615 (2000).
165. Salazar-Alvarez, G. *et al.* Fabrication and Properties of Self-Assembled Nanosized Magnetic Particles. *MRS Proc.* **707,** W7.1.1 (2001).
166. Fleming, D. A. *et al.* Chemically Functional Alkanethiol Derivitized Magnetic Nanoparticles. *MRS Proc.* **746,** Q6.4 (2002).
167. Seung Uk Son, *et al.* Designed Synthesis of Atom-Economical Pd/Ni Bimetallic Nanoparticle-Based Catalysts for Sonogashira Coupling Reactions. *J. Am. Chem. Soc.*, **126 (16)**, 5026–5027 (2004).
168. Zhichuan Xu, Yanglong Hou, and & Sun, S. Magnetic Core/Shell Fe_3O_4/Au and Fe_3O_4/Au/Ag Nanoparticles with Tunable Plasmonic Properties. *J. Am. Chem. Soc.*, **129 (28)**, 8698–8699 (2007).
169. El-Toni, A. M. *et al.* Synthesis of double mesoporous core–shell silica nanospheres with radially oriented mesopores via one-templating step using anionic surfactant. *Chem. Commun.* **46,** 6482 (2010).
170. El-Toni, A., Ibrahim, M., Labis, J., Khan, A. & Alhoshan, M. Optimization of Synthesis Parameters for Mesoporous Shell Formation on Magnetic Nanocores and Their Application as Nanocarriers for Docetaxel Cancer Drug. *Int. J. Mol. Sci.* **14,** 11496–11509 (2013).
171. Qian, X. *et al.* Controllable fabrication of uniform core–shell structured zeolite@SBA-15 composites. *Chem. Sci.* **2,** 2006 (2011).
172. Wang, G. & Harrison, A. Preparation of Iron Particles Coated with Silica. *Journal of Colloid and Interface Science* **217,** 203–207 (1999).
173. Deng, S., Pingali, K. C. & Rockstraw, D. A. Synthesis of Ru-Ni Core-Shell Nanoparticles for Potential Sensor Applications. *IEEE Sens. J.* **8,** 730–734 (2008).
174. Chertok, B., David, A. E. & Yang, V. C. Polyethyleneimine-modified iron oxide nanoparticles for brain tumor drug delivery using magnetic targeting and intra-carotid administration. *Biomaterials* **31,** 6317–6324 (2010).
175. Pathak, C., Jaiswal, Y. K. & Vinayak, M. Queuine promotes antioxidant defence system by activating cellular antioxidant enzyme activities in cancer. *Biosci. Rep.* **28,** (2008).
176. Kircher, M. F. *et al.* A Multimodal Nanoparticle for Preoperative Magnetic Resonance Imaging and Intraoperative Optical Brain Tumor Delineation Advances in Brief A Multimodal Nanoparticle for Preoperative Magnetic Resonance Imaging and Intraoperative Optical Brain Tumor Delinea. *Cancer Res*, **63(23)**, 8122–8125 (2003).
177. Lien, Y. H. & Wu, T. M. Preparation and characterization of thermosensitive polymers grafted onto silica-coated iron oxide nanoparticles. *J. Colloid Interface Sci.* **326,** 517–521 (2008).
178. Woo-ram Lee, *et al.* Redox−Transmetalation Process as a Generalized Synthetic Strategy for Core−Shell Magnetic Nanoparticles. *J. Am. Chem. Soc.*, **127 (46)**, pp 16090–16097 (2005).
179. Tan, W. *et al.* Bionanotechnology based on silica nanoparticles. *Med. Res. Rev.* **24,** 621–638 (2004).
180. Eyk A. Schellenberger, David Sosnovik, Ralph Weissleder, and & Lee Josephson. Magneto/Optical Annexin V, a Multimodal Protein. *Bioconjugate Chem.*, **15 (5)**, 1062–1067 (2004).
181. Daneshvar, H. *et al.* Imaging characteristics of zinc sulfide shell, cadmium telluride core quantum dots. *Nanomedicine* **3,** 21–29 (2008).
182. SalmanOgli, A. & Rostami, A. Investigation of electronic and optical properties of

(CdSe/ZnS/CdSe/ZnS) quantum dot–quantum well heteronanocrystal. *J. Nanoparticle Res.* **13,** 1197–1205 (2011).

183. Ying Wang, *et al.* Mechanism of Strong Luminescence Photoactivation of Citrate-Stabilized Water-Soluble Nanoparticles with CdSe Cores. *J. Phys. Chem. B*, **108 (40)**, 15461–15469 (2004).
184. Wang, Y. *et al.* Upconversion Luminescence of β-$NaYF_4$: Yb^{3+}, Er^{3+}@β-$NaYF_4$ Core/Shell Nanoparticles: Excitation Power Density and Surface Dependence. *J. Phys. Chem. C* **113,** 7164–7169 (2009).
185. Qian, H. S. & Zhang, Y. Synthesis of Hexagonal-Phase Core−Shell $NaYF_4$ Nanocrystals with Tunable Upconversion Fluorescence. *Langmuir* **24,** 12123–12125 (2008).
186. Stanciu, L., Won, Y. H., Ganesana, M. & Andreescu, S. Magnetic Particle-Based Hybrid Platforms for Bioanalytical Sensors. *Sensors* **9,** 2976–2999 (2009).
187. Qiu, J. D., Cui, S. G., Deng, M. Q. & Liang, R. P. Direct electrochemistry of myoglobin immobilized in NiO/MWNTs hybrid nanocomposite for electrocatalytic detection of hydrogen peroxide. *J. Appl. Electrochem.* **40,** 1651–1657 (2010).
188. Qiu, J. D., Cui, S. G. & Liang, R. P. Hydrogen peroxide biosensor based on the direct electrochemistry of myoglobin immobilized on ceria nanoparticles coated with multiwalled carbon nanotubesby a hydrothermal synthetic method. *Microchim. Acta* **171,** 333–339 (2010).
189. Khlebtsov, N. *et al.* Analytical and Theranostic Applications of Gold Nanoparticles and Multifunctional Nanocomposites. *Theranostics* **3,** 167–180 (2013).
190. Wang, X., Yang, T. & Jiao, K. Electrochemical sensing the DNA damage in situ induced by a cathodic process based on Fe@Fe_2O_3 core–shell nanonecklace and Au nanoparticles mimicking metal toxicity pathways in vivo. *Biosens. Bioelectron.* **25,** 668–673 (2009).
191. Qiu, J. D., Peng, H. P., Liang, R. P. & Xia, X. H. Facile preparation of magnetic core–shell Fe_3O_4@Au nanoparticle/myoglobin biofilm for direct electrochemistry. *Biosens. Bioelectron.* **25,** 1447–1453 (2010).
192. Zhang, X. F. *et al.* Synthesis, structure and magnetic properties of SiO_2-coated Fe nanocapsules. *Mater. Sci. Eng. A* **454,** 211–215 (2007).
193. Xuan, S., Wang, Y. X. J., Yu, J. C. & Leung, K. C. F. Preparation, Characterization, and Catalytic Activity of Core/Shell Fe_3O_4@Polyaniline@Au Nanocomposites. *Langmuir* **25,** 11835–11843 (2009).
194. Yin, H., Ma, Z., Chi, M. & Dai, S. Heterostructured catalysts prepared by dispersing Au@Fe_2O_3 core–shell structures on supports and their performance in CO oxidation. *Catal. Today* **160,** 87–95 (2011).
195. Riccardo Ferrando, Julius Jellinek, and & Johnston, R. L. Nanoalloys: From Theory to Applications of Alloy Clusters and Nanoparticles. *Chem. Rev.*, ***108*** **(3)**, 845–910 (2008).
196. Wang, L. & Yamauchi, Y. Autoprogrammed Synthesis of Triple-Layered Au@Pd@Pt Core−Shell Nanoparticles Consisting of a Au@Pd Bimetallic Core and Nanoporous Pt Shell. *J. Am. Chem. Soc.* **132,** 13636–13638 (2010).
197. Fan, F. R. *et al.* Epitaxial Growth of Heterogeneous Metal Nanocrystals: From Gold Nano-octahedra to Palladium and Silver Nanocubes. *J. Am. Chem. Soc.* **130,** 6949–6951 (2008).
198. Kumagai, M. *et al.* Enhanced in vivo magnetic resonance imaging of tumors by PEGylated iron-oxide-gold core-shell nanoparticles with prolonged blood circulation

properties. *Macromol. Rapid Commun.* **31,** 1521–1528 (2010).
199. Kayal, S. & Ramanujan, R. V. Anti-Cancer Drug Loaded Iron–Gold Core–Shell Nanoparticles (Fe@Au) for Magnetic Drug Targeting. *J. Nanosci. Nanotechnol.* **10,** 5527–5539 (2010).
200. Silva, S. M., Tavallaie, R., Sandiford, L., Tilley, D. & Gooding, J. J. Gold coated magnetic nanoparticles : from preparation to surface modification for analytical and biomedical applications. *Chem. Commun.* **52,** 7528–7540 (2016).
201. Ghorbani, M., Hamishehkar, H., Arsalani, N. & Entezami, A. A. Preparation of thermo and pH-responsive polymer@Au/Fe_3O_4 core/shell nanoparticles as a carrier for delivery of anticancer agent. *J. Nanoparticle Res.* **17,** 305 (2015).
202. Lo, C. K. *et al.* Homocysteine-protected gold-coated magnetic nanoparticles: synthesis and characterisation. *J. Mater. Chem.* **17,** 2418 (2007).
203. Rudakovskaya, P. G., Beloglazkina, E. K., Majouga, A. G. & Zyk, N. V. Synthesis and characterization of terpyridine-type ligand-protected gold-coated Fe_3O_4 nanoparticles. *Mendeleev Commun.* **20,** 158–160 (2010).
204. Zhou, H. *et al.* Ultrasensitive DNA monitoring by Au–Fe_3O_4 nanocomplex. *Sensors Actuators B Chem.* **163,** 224–232 (2012).
205. Lingyan Wang, Lingyan Wang, *et al.* Monodispersed Core−Shell Fe_3O_4@Au Nanoparticles. *J. Phys. Chem. B*, ***109*** **(46)**, 21593–21601 (2005).
206. Zhichuan Xu, Yanglong Hou, and & Sun, S. Magnetic Core/Shell Fe_3O_4/Au and Fe_3O_4/Au/Ag Nanoparticles with Tunable Plasmonic Properties. *J. Am. Chem. Soc.*, ***129*** **(28)**, 8698–8699 (2007).
207. Jin, Y., Jia, C., Huang, S. W., O'Donnell, M. & Gao, X. Multifunctional nanoparticles as coupled contrast agents. *Nat. Commun.* **1,** 1–8 (2010).
208. Hu, Y., Meng, L., Niu, L. & Lu, Q. Facile Synthesis of Superparamagnetic Fe_3O_4 @polyphosphazene@Au Shells for Magnetic Resonance Imaging and Photothermal Therapy. *ACS Appl. Mater. Interfaces* **5,** 4586–4591 (2013).
209. Dong, W. *et al.* Facile Synthesis of Monodisperse Superparamagnetic Fe_3O_4 Core@hybrid@Au Shell Nanocomposite for Bimodal Imaging and Photothermal Therapy. *Adv. Mater.* **23,** 5392–5397 (2011).
210. Salgueiriño-Maceira, V. *et al.* Bifunctional gold-coated magnetic silica spheres. *Chem. Mater.* **18,** 2701–2706 (2006).
211. Taufika Islam Williams, *et al.* Epithelial Ovarian Cancer: Disease Etiology, Treatment, Detection, and Investigational Gene, Metabolite, and Protein Biomarkers. (2007). doi:10.1021/PR070041V
212. Zhuo, Y., Yuan, P. X., Yuan, R., Chai, Y. Q. & Hong, C. L. Bienzyme functionalized three-layer composite magnetic nanoparticles for electrochemical immunosensors. *Biomaterials* **30,** 2284–2290 (2009).
213. Xie, J. *et al.* Manipulating the Power of an Additional Phase: A Flower-like Au-Fe_3O_4 Optical Nanosensor for Imaging Protease Expressions *In vivo*. *ACS Nano* **5,** 3043–3051 (2011).
214. Cherukuri, P., Glazer, E. S. & Curley, S. A. Targeted hyperthermia using metal nanoparticles. *Adv. Drug Deliv. Rev.* **62,** 339–345 (2010).
215. Rai, P. *et al.* Development and applications of photo-triggered theranostic agents. *Adv. Drug Deliv. Rev.* **62,** 1094–1124 (2010).
216. Mohammad, F., Balaji, G., Weber, A., Uppu, R. M. & Kumar, C. S. S. R. Influence of Gold Nanoshell on Hyperthermia of Super Paramagnetic Iron Oxide Nanoparticles

(SPIONs). *J. Phys. Chem. C. Nanomater. Interfaces* **114,** 19194–19201 (2010).
217. Kim, J. *et al.* Designed Fabrication of Multifunctional Magnetic Gold Nanoshells and Their Application to Magnetic Resonance Imaging and Photothermal Therapy. *Angew. Chemie Int. Ed.* **45,** 7754–7758 (2006).
218. Xu, C. *et al.* Au-Fe_3O_4 Dumbbell Nanoparticles as Dual-Functional Probes. *Angew. Chemie Int. Ed.* **47,** 173–176 (2008).
219. García, I., Gallo, J., Genicio, N., Padro, D. & Penadés, S. Magnetic Glyconanoparticles as a Versatile Platform for Selective Immunolabeling and Imaging of Cells. *Bioconjug. Chem.* **22,** 264–273 (2011).
220. Bardhan, R. *et al.* Nanoshells with Targeted Simultaneous Enhancement of Magnetic and Optical Imaging and Photothermal Therapeutic Response. *Adv. Funct. Mater.* **19,** 3901–3909 (2009).
221. Xu, C., Wang, B. & Sun, S. Dumbbell-like Au-Fe_3O_4 Nanoparticles for Target-Specific Platin Delivery. *J. Am. Chem. Soc.* **131,** 4216–4217 (2009).
222. Plank, C., Scherer, F., Schillinger, U., Bergemann, C. & Anton, M. Magnetofection: Enhancing and Targeting Gene Delivery with Superparamagnetic Nanoparticles and Magnetic Fields. *J. Liposome Res.* **13,** 29–32 (2003).
223. Cho, K., Wang, X., Nie, S., Chen, Z. G. & Shin, D. M. Therapeutic nanoparticles for drug delivery in cancer. *Clin. Cancer Res.* **14,** 1310–6 (2008).
224. Kamei, K. *et al.* Direct cell entry of gold/iron-oxide magnetic nanoparticles in adenovirus mediated gene delivery. *Biomaterials* **30,** 1809–1814 (2009).
225. Thaxton, C. S., Georganopoulou, D. G. & Mirkin, C. A. Gold nanoparticle probes for the detection of nucleic acid targets. *Clin. Chim. Acta* **363,** 120–126 (2006).
226. Savka I. Stoeva, Fengwei Huo, Jae-Seung Lee, and & Mirkin, C. A. Three-Layer Composite Magnetic Nanoparticle Probes for DNA. *J. Am. Chem. Soc.*, ***127*** **(44)**, 15362–15363 (2005).
227. Zhao, J. *et al.* Ultrasensitive electrochemical aptasensor for thrombin based on the amplification of aptamer–AuNPs–HRP conjugates. *Biosens. Bioelectron.* **26,** 2297–2303 (2011).
228. Wang, C. & Irudayaraj, J. Multifunctional Magnetic-Optical Nanoparticle Probes for Simultaneous Detection, Separation, and Thermal Ablation of Multiple Pathogens. *Small* **6,** 283–289 (2010).
229. Liu, H. L., Sonn, C. H., Wu, J. H., Lee, K. M. & Kim, Y. K. Synthesis of streptavidin-FITC-conjugated core-shell Fe_3O_4-Au nanocrystals and their application for the purification of CD4+ lymphocytes. *Biomaterials* **29,** 4003–4011 (2008).
230. Yu, C. J., Lin, C. Y., Liu, C. H., Cheng, T. L. & Tseng, W. L. Synthesis of poly(diallyldimethylammonium chloride)-coated Fe_3O_4 nanoparticles for colorimetric sensing of glucose and selective extraction of thiol. *Biosensors and Bioelectronics* **26,** (2010).
231. Qi, D., Zhang, H., Tang, J., Deng, C. & Zhang, X. Facile synthesis of mercaptophenylboronic acid-functionalized core-shell structure Fe_3O_4@C@Au magnetic microspheres for selective enrichment of glycopeptides and glycoproteins. *J. Phys. Chem. C* **114,** 9221–9226 (2010).
232. Hashmi, A. S. K. & Hutchings, G. J. Gold Catalysis. *Angew. Chemie Int. Ed.* **45,** 7896–7936 (2006).
233. Arcadi, A. Alternative Synthetic Methods through New Developments in Catalysis by Gold. *Chem. Rev.* **108,** 3266–3325 (2008).
234. Corma, A. *et al.* Supported gold nanoparticles as catalysts for organic reactions. *Chem.*

Soc. Rev. **37,** 2096 (2008).
235. Yin, H. *et al.* Colloidal deposition synthesis of supported gold nanocatalysts based on Au–Fe_3O_4 dumbbell nanoparticles. *Chem. Commun.* **37,** 4357 (2008).
236. Edwards, J. K. *et al.* Direct synthesis of hydrogen peroxide from H_2 and O_2 using Au–Pd/Fe_2O_3 catalysts. *J. Mater. Chem.* **15,** 4595 (2005).
237. Ge, J., Huynh, T., Hu, Y. & Yin, Y. Hierarchical Magnetite/Silica Nanoassemblies as Magnetically Recoverable Catalyst–Supports. *Nano Lett.* **8,** 931–934 (2008).
238. Lee, Y., Garcia, M. A., Frey Huls, N. A. & Sun, S. Synthetic Tuning of the Catalytic Properties of Au-Fe_3O_4 Nanoparticles. *Angew. Chemie Int. Ed.* **49,** 1271–1274 (2010).

CHAPTER 3

Characterization Techniques, Experimental setup & Cell Cultivation

Table of Contents

3. Characterization Techniques

The as-prepared NPs samples were characterized by a series of instruments to investigate their structure, morphology, magnetic and optical properties.

3.1 Structural Characterization

Table 3.1 List of instruments used for various characterizations

Characterization	Model & Company
X-Ray Diffraction (XRD)	X'Pert PRO XRD spectrometer & PANalytical
Transmission Electron Microscopy (TEM)	JEM-ARM200F & JEOL
Electron Diffraction Spectroscopy (EDS)	XMax 80 & Oxford
Cryo Electron Microscopy (CryoEM)	Tecnai F20 & FEI
Fourier Transform Infrared Spectroscopy (FTIR)	Nicolet iS50 FTIR Spectrometer & Thermo Scientific
Zeta potential Analysis	Zetasizer Nano ZS90 & Malvern instruments
X-ray Photoelectron Spectroscopy (XPS)	K-Alpha XPS System & Thermo Scientific
Thermo Gravimetric Analysis (TGA)	TGA Q50 & TA Instruments
Superconducting Quantum Interference Device (SQUID)	MPMS & Quantum Design
UV-Visible Spectroscopy (UV-Vis)	UV-2401PC & Shimadzu

3.1.1 X-ray Diffraction (XRD)

XRD is a basic method for determining the atomic position within a crystal. This technique uses a beam of x-rays which interacts with the crystal powders and causes diffraction. From the angles and intensities of these diffracted beams, the atomic positions of the sample can be analyzed, as well as their chemical bonds, disorder, average size and various other information[1].

The obtained peaks are indicative of a particular phase and material which can be compared with the database of Joint Committee on Powder Diffraction Standards (JCPDS) to confirm the phase of the synthesized material.

XRD patterns of the NPs samples were obtained using a X'Pert PRO XRD spectrometer (PANalytical B.V., Holland) from 10 to 90° (2θ value) using Cu K-α radiation (0.15418 nm).

3.1.2 Transmission Electron Microscopy (TEM)

TEM is one of the widely used microscopy technique which is based on an electron beam transmitted through a sample. To make it simple, the transmitted electrons interact with the sample as they pass through it and an image is formed. Then the image is magnified and focused in an imaging device usually in a digital camera. TEMs are usually capable of imaging at a very high resolution than other microscopes. At smaller magnifications TEM image contrast is due to absorption of electrons by the material, depending on the thickness and constituents of the sample. At higher magnifications (HRTEM), complex wave interactions modulate the image intensity. And using the alternate modes of TEM, it allows identifying chemical elements, crystal orientation, and electronic structure as well as the imaging[2].

The high-angle annular dark field scanning transmission electron microscopy (HAADF-STEM) is one of the high-resolution microscopy techniques that benefits most from the most recent improvement of the aberration corrector[3]. Therefore, the HAADF-STEM technique has attracted enormous attention for its various applications such as tomography[4], size and thickness measurement usually at atomic scale, structure characterization[5] and composition measurement. This technique uses a sharply focused beam to scan across the sample and the annular dark field (ADF) detector collects only the scattered electrons from the sample. Thus the resulting image contrast is always referred as Z-contrast[6].

TEM images (**Figure 3.1**) were taken on a HRTEM (JEOL, JEM-ARM200F) equipped with HAADF-STEM detector and Oxford XMax 80 Energy Dispersive X-Ray Spectrometer (EDS). The sample was prepared in such a way that aggregation in the grid was avoided. Then, 10 µl of the sample were dispersed in 100 µl of isopropanol, which was sonicated for 30 mins; then a drop of sonicated NPs dispersion was placed onto the amorphous carbon-coated 200 mesh copper grid (Ted Pella, Inc.). Finally, the sample was allowed to dry at ambient temperature before it was loaded into the microscope.

Figure 3.1. TEM instrument for morphology analysis, EDS and HAADF-STEM techniques (*Laboratorio Avanzado de Nanoscopía Electrónica - LANE, CINVESTAV-IPN, Mexico city*)

3.1.3 Cryo Electron Microscopy (CryoEM)

CryoEM is a technique for studying a wide range of biologically interesting samples, ranging from the structure and dynamics to study cellular morphology[7]. In a typical analysis, samples are imaged in a hydrated, native state without the use of stains.

The internalization of NPs inside the cells was confirmed by CryoEM analysis. 5µl of CSNPs suspensions were made into a thin liquid film which was prepared on lacy carbon grid (Pelco, USA) and then quenched into liquid ethane to freeze the sample using a Leica EM-CPC chamber. Tecnai F20 (FEI) operated at 200kV to obtain the images which were recorded with a USC1000 slow scan CCD camera (Gatan) at 50000x.

3.1.4 Fourier Transform Infrared Spectroscopy (FTIR)

The main aim of infrared (IR) absorption spectroscopy is to measure the absorption of light at different wavelength by the samples. At specific frequencies, chemical bonds tend to vibrate corresponding to energy levels. Resonant frequencies can be related to the strength of the bond and the mass of the atoms. Thus the frequency of such vibrations can be associated with a particular bond type[8].

FTIR is a less intuitive way to obtain information. This technique is based on the impact of a beam containing different frequencies of light at once to the sample and measures how much of that beam is absorbed by it. Then, the beam is modified to contain a different combination of frequencies, giving a second data point. This process is repeated many times.

Afterward, a computer takes all these data and gives the absorption at each wavelength. The samples were measured in a Nicolet iS50 FTIR Spectrometer (Thermo Scientific). This system enables to collect data over a range of 4000 to 400 cm^{-1} with a resolution of 0.5 cm^{-1}.

3.1.5 Zeta (ζ) potential Analysis

Zeta potential is a measure of the electrostatic or charges repulsion/attraction between particles, to understand the fundamental parameters which affect NPs stability[9]. The zeta potential values were determined by using a Zetasizer Nano ZS90 (Malvern instruments) (**Figure 3.2**) at 25°C at a wavelength of He-Ne laser 633 nm, Max 4 mW at a scattering angle of 90° using a Universal 'dip' cell kit. Data were obtained using a monomodal acquisition according to the Smoluchowski theory. The measurements were repeated 3 times. Before the analysis, the samples were well sonicated for 1 h to avoid aggregation.

Figure 3.2. Zeta potential instrument setup (*Department of Toxicology, CINVESTAV-IPN, Mexico city*)

3.1.6 X-ray Photoelectron Spectroscopy (XPS)

XPS is used to study the composition and electronic state of the surface of a NPs by employing photon-ionization and energy-dispersive analysis of the emitted photoelectrons. And also it allows calculating the concentrations of different elements in the sample quantitatively by comparing the peak area of respective elements[10].

In this thesis, the XPS analysis was performed using a K-Alpha X-ray Photoelectron Spectrometer (XPS) System (Surface Analysis, Thermo Scientific). Monochromated, Micro-focused Al Kα was used as an X-ray source type. The binding energy of C1s carbon was used for calibration. The spectrum was obtained via collecting electrons ejected from core level by incident X-ray photons. This technique has been used to characterize the electron states of the various elements of CSNPs.

3.1.7 Thermogravimetric Analysis (TGA)

TGA is an analytical method which measures the amount and rate of weight change of a sample in a controlled atmosphere. It offers enough information about the weight change of a material due to dehydration, oxidation, and decomposition[11].

Thermal analysis was carried out for liquid samples using a TGA Q50 (TA Instruments) from 30 to 900°C under nitrogen flow with a heating rate of 10°C/min.

3.2 Magnetic Characterization

3.2.1 Superconducting Quantum Interference Device (SQUID)

Magnetization versus applied field was measured at a fixed temperature which provides the CSNPs response to a magnetic gradient. The magnetic measurement allows us to calculate the size of the particles when the temperature is increased and also to estimate the temperature above which the NPs becomes superparamagnetic[12].

The magnetic properties of NPs were determined with a superconducting quantum interference device SQUID magnetometer (MPMS, Quantum Design). The magnetization hysteresis of the samples was obtained by changing H between +70 to -70 kOe at 3 different temperatures like 5 K, 300 K and 312 K. The hysteresis of the samples was also obtained at 100 kOe using a temperature interval from 1.8 to 312 K. The measurements were performed on NPs in powder form. The NPs samples are dried in an oven at 90°C for 3 h and used to measure the magnetization of NPs.

3.3 Optical characterization

3.3.1 UV-Visible Spectroscopy

The absorption spectrum of a compound is one of its most useful and unique physical characteristics[13], which gives an advantage of both

i) Identification (qualitative analysis) and

ii) Estimation (quantitative analysis).

The surface plasmon resonance (SPR) of gold can be characterized by UV-Vis spectrometer. As for gold NPs, absorption in UV-Vis spectrum is a reflection of the resonant oscillation frequency of collective free electrons in gold nanocrystal[14].

UV-Vis spectra were performed by UV-Vis spectra was obtained using Shimadzu Corporation UV-2401PC UV-Vis spectrometer. The Samples were dispersed in a polar solvent such as DI water. Baseline was obtained using standard solution and measured in the range of

200-1000 nm at 1 nm sensitivity. This technique has been used to characterize the absorption spectra of NPs.

3.4 Experimental set-up for applications studies

3.4.1 *In-vitro* drug release studies

The process of drug release in which a drug molecule is converted into suitable product form when it is subjected to absorption, distribution, metabolism and excretion (ADME) for showing Pharmacological activity.

Drug release from CSNPs was studied using a dialysis method[15]. Dialysis bags were soaked before use in DI water at room temperature for 12 h to remove the preservative, followed by rinsing thoroughly with distilled water. *In-vitro* release of Dox from CSNPs was conducted by dialysis in a dialysis sac with 50 ml of PBS. Three sacs were prepared to contain Dox-FA-CSNPs for cumulative release (pH 5.3, 6.8 and 7.4) with continuous stirring to simulate the intercellular, intracellular and external environment of cancer cells[16]. To carry out this study, 2 ml of dialyzed Dox-FA-CSNPs complex was used. Two ends of the dialysis sac were tightly bound with threads. The sac was hung inside a beaker with the help of a glass rod so that the portion of the dialysis sac with the formulation dipped into the buffer solution. The flask was kept on a magnetic stirrer and stirring was maintained at 100 rpm at 37°C with a thermostatic control. Then, 1 ml of sample was withdrawn from the system at a known time period to determine the drug content. To compensate the PBS solution as soon as 1 ml was drawn, it was replaced with the same equivalent volume. The amount of Dox released was determined using UV-Vis spectrophotometer at 485 nm which was the signature absorbance of Dox. All the experiments were repeated thrice for all the samples. This drug release study was also explained with different drug kinetics models in order to explain the release mechanism.

3.4.2 Drug kinetics models

The mechanism of drug release from the optimized formulation of CSNPs was studied using various model dependent kinetics by correlating the cumulative i*n-vitro* release profiles at various pH. The various kinetic models are as follows:

i) **Zero order** (cumulative amount of drug released vs. time),

ii) **First order** (log cumulative percentage of drug remaining vs. time),

iii) **Higuchi model** (cumulative percentage of drug released vs. square root of time) &

iv) **Hixson-Crowell model** (cumulative percentage drug release vs. square root of time).

The use of above drug kinetic modeling turns out to be very useful as it predicts the release kinetics before the drug release systems are realized. Using cumulative i*n-vitro* release values in the below formulas we calculated the drug kinetics.

3.4.2.1 Zero-order

Zero order determines the drug delivery system where the release of the drug is completely independent of its drug concentration[17]. The equation is,

$$Q_t = Q_0 + K_0 t \quad \text{..... (1)}$$

Where Q_t is the amount of drug dissolved in time t, Q_0 is the initial amount of drug in the solution (mostly Q_0 =0) and K_0 is the zero order release constant expressed in units of concentration/time.

3.4.2.2 First order

This model describes the absorption and elimination of drugs, even though it is quite difficult to understand the mechanism[17,18] and it is completely dependent on drug concentration The equation can be expressed as,

$$\log Q_t = \log Q_0 + K_1 t \quad \text{..... (2)}$$

Where Q_t is the amount of drug dissolved in time$t$, Q_0 is the initial amount of drug in the solution (mostly Q_0 =0) and K_1 is the first-order release constant.

3.4.2.3 Higuchi model

This model is probably the most used mathematical equation which is purely based on the drug release from matrix system[18]. It is often applicable to the different geometrics and porous system. The equation is as follows:

$$Q_t = Q_0 = K_H t^{1/2} \quad \text{..... (3)}$$

Where Q_t is the amount of drug dissolved in time t, Q_0 is the initial amount of drug in the solution (mostly Q_0 =0) and K_H is the Higuchi release constant.

3.4.2.4 Hixson-Crowell model

This mathematical modelling describe the drug release based on the change in surface area and also diameter of particle[19,20]. The equation is,

$$\sqrt[3]{Q_0} - \sqrt[3]{Q_t} = K_{HC}t \quad \text{..... (4)}$$

Where Q_t is the amount of drug dissolved in time t, Q_0 is the initial amount of drug in the solution (mostly Q_0 =0) and K_{HC} is the Hixson Crowell constant.

Table 3.2 Applications of different kinetic mathematical modelling

Kinetic Model	Applications
Zero-order	Dissolution of drug from modified release pharmaceutical dosage form
First order	Drug dissolved in pharmaceutical dosage forms
Higuchi model	Dissolution of drug from modified release dosage forms
Hixson-Crowell model	Drug release from several modified release dosage forms

3.4.3 Magnetic Resonance (MR) Imaging experiments

MR imaging was performed with a 7 T clinical Signa HDxt scanner (Varian) (**Figure 3.3**). T_2-weighted images were acquired using the following parameters: 7 T, Repetition time TR=2000 msec, fast spin echo, FOV=3*3 cm, Echo time TE=15-250 msec, slice thickness=4 mm and resolution 256×256 points. For T_1 measurements, coronal spin-echo sequences with fixed echo time (TE)=24 msec and varying repetition time (TR) (25 msec to 4 sec) were used. CSNPs suspensions was taken at varying concentrations.

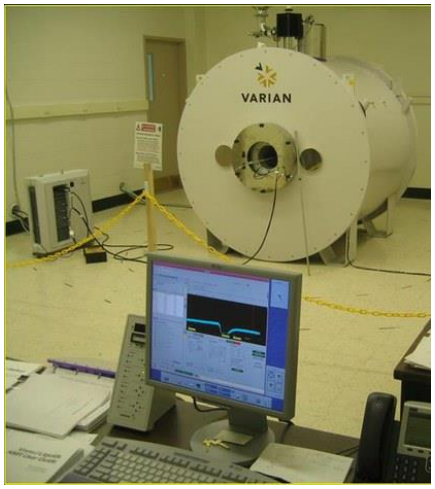

Figure 3.3 Varian 7 T MR Scanner used for the imaging study (*Centro nacional de investigación en imagenología e instrumentación médica – **ci³m,** Universidad Autónoma Metropolitana, Iztapalapa*)

3.4.3.1 Phantom preparation for MR Imaging

A pellet containing CSNPs labelled with L6 and Hep2 cells was mixed with 1.5 ml of preheated 0.5% agarose gel at 40°C. Then the labeled cells are incorporated with agar phantom which is cooled down to room temperature to solidify and stored at 4°C. The agar gel with the cells are considered as a control for phantom MR imaging studies.

3.4.4 Hyperthermia experiment setup

The setup (**Figure 3.4**) used to apply the Mw electromagnetic field to perform the experiments consisted of a generator (SML 03, Rhode & Schwarz, Germany) set to a frequency of 2.45 GHz. This signal was then amplified using an RF & Mw module power amplifier (1164-BBM3Q6AHM, Empower, USA). The output power was then monitored through the use of a dual direct coupler (DC7154M, Amplifier Research, USA) and a power meter (PM2002, Amplifier Research, USA) to ensure an output power of 6 W and to monitor the reflected power of the system. To adjust the standing wave ratio (SWR) to an optimal value, a coaxial stub tuner (1878C, Maury Microwave Corp., USA) was used along a network analyzer (E5071B, Agilent Technologies, USA) to measure and reduce the SWR to a minimum prior to each experiment[21].

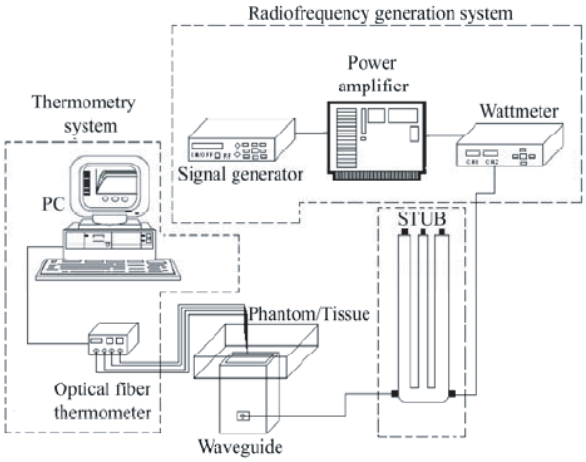

Figure 3.4. Experiment set-up used for Mw based hyperthermia studies (*Department of Electrical Engineering - Bioelectronics section, CINVESTAV-IPN, Mexico city*)

3.4.4.1 Temperature Measurements

Non electromagnetic interfering optical fiber probes temperature sensors (M3300, Luxtron, USA) were used to record temperature increment. The temperature was measured inside the PBS. Each test lasted 150 sec in order to study the temperature response as a function of time. The temperatures were recorded every sec during the experiments using True Temp software (Luxtron, USA).

3.4.4.2 Hyperthermia measurements

The heating effect of CSNPs was studied using Mw based hyperthermia at 2.45 GHz. The aqueous sample of various CSNPs concentrations was taken and well dispersed with PBS (volume is made upto 1 ml). Then the applicator was placed in the sample and the temperature is measured. The samples were exposed to Mw for 150 sec at 6 W.

3.5 Materials

Ferric (III) chloride hexahydrate ($FeCl_3$•$6H_2O$, 97%), Ferrous (II) chloride tetrahydrate ($FeCl_2$•$4H_2O$, ≥99%), Cobalt (II) nitrate hexahydrate (CoN_2O_6•$6H_2O$, 99.999%), Manganese (II) chloride tetrahydrate ($MnCl_2$•$4H_2O$, 99.99%), sodium hydroxide (NaOH, >98%), Gold (III) chloride trihydrate ($HAuCl_4$•$3H_2O$, ≥99.9%), L-Ascorbic acid (AA) ($C_6H_8O_6$, ≥99.0%), Dimethyl sulfoxide (DMSO) (CH_3SOCH_3, ≥99.9%), Sodium chloride (NaCl, ≥99.5%), Hexadecyltrimethylammonium bromide (CTAB) ($CH_3(CH_2)_{15}N(Br)(CH_3)_3$, ≥99.0%), Folic acid (FA) ($C_{19}H_{19}N_7O_6$, ≥97%), N-Hydroxysuccinimide (NHS) ($C_4H_5NO_3$, 98%), N,N'-Dicyclohexylcarbodiimide (DCC) ($C_6H_{11}N{=}C{=}NC_6H_{11}$, 99%), Triethylamine (TEA) ($(C_2H_5)_3N$, ≥99%), Doxorubicin hydrochloride (Dox) ($C_{27}H_{29}NO_{11}$•HCl), MTT [3-(4,5-dimethylthiazol-2-yl) 2,5-diphenyltetrazolium bromide], Hoechst Stain solution, Phalloidin–Tetramethylrhodamine B isothiocyanate, paraformaldehyde, ethanol (CH_3CH_2OH, ≥99.8%) and Dialysis sacks (MW 12,000 Da) were purchased from Sigma-Aldrich (Mexico). Dulbecco's Modified Eagle Medium (DMEM), fetal bovine serum (FBS), Phosphate buffer saline (PBS) and streptomycin were obtained from Gibco, Life Technologies. Agarose (UltraPure, Agarose) was purchased from Invitrogen, Thermo scientific. Deionized water (DI) was used for all experiments. All chemicals were used directly without any further purification.

3.6 Synthesis Methods

3.6.1 Synthesis of core nanoparticles

Magnetic core (Fe_3O_4, $CoFe_2O_4$ & $MnFe_2O_4$) NPs were synthesized using co-precipitation method. The precursors 0.5 M of ferric (III) chloride and 0.25 M of

i) Ferrous (II) chloride,

ii) Cobalt (II) nitrate,

iii) Manganese (II) chloride,

were taken in the ratio of 1:0.5 and in order to avoid the precipitation of the salts, they were initially dissolved separately in 10 ml of nitrogen (N_2) degassed DI water and mixed with 1.5 M solution of 40 ml NaOH, which was used as a reducing agent. The entire synthesis process was carried out under N_2 atmosphere for 1.5 h at 80°C (pH 12). The black resultant precipitate (**Figure 3.5**) was separated using an NdFeB strong magnet and it was washed 3 times with DI water. This pure NPs were further used for CSNPs formation. The reaction is as follows:

$$\mathbf{2Fe^{3+} + Fe^{2+}/Co^{2+}/Mn^{2+} + 8OH^{-} \longrightarrow Fe_3O_4/CoFe_2O_4/MnFe_2O_4 + 4H_2O} \text{ ..... (5)}$$

Figure 3.5. As-synthesized black core NPs separated using strong magnet

3.6.2 Core seed preparation

200 µl of as-synthesized NPs was centrifuged and dispersed in 1 ml of DI water (pH adjusted to 7). Then, 400 µl of DMSO was added and the mixture was stirred continuously under N_2 atmosphere at 75°C for 3 h to reduce the aggregation of NPs.

3.6.3 Synthesis of gold nanoshell

Au coating was carried out using gold seed solution which were prepared freshly by mixing 0.5 ml (1 M) of CTAB, 1 ml (50 mM) of ascorbic acid (AA) and 100 µl (1 M) of $HAuCl_4 \bullet 3H_2O$ solution. This solution complex mixture was sonicated for 30 mins. The golden yellow color immediately changed to a milky orange color and then to a milky white color (**Figure 3.6**).

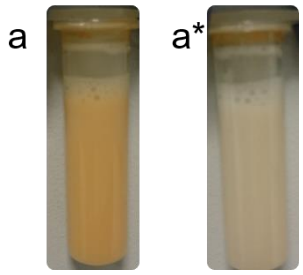

Figure 3.6. Gold seed solution from milky orange (a) to milky white colour (a*)

3.6.4 Synthesis of core-shell nanoparticles (CSNPs)

The seed solution of core (Fe_3O_4 & $MnFe_2O_4$) and gold were used to synthesize CSNPs. In this case, the ratio of 1:5 was taken. This was because we had already optimized the ratio with 1:5, 1:7, and 1:9 and found that 1:5 was appropriate for the CSNPs. Initially, 1 part of milky-white colored gold seed solution was added dropwise to the faint brown-colored core seed solution. This solution mixture was stirred for 4 h continuously until the brown colored solution turned into purple (**Figure 3.7**).

Au iterations

Then, with the above gold seed solution, the gold iteration was continued for 5 times for every 2 h with $CoFe_2O_4$ core. Finally, a dark purple color CSNPs solution was obtained.

Figure 3.7. Dark purple color CSNPs solution

Then, these CSNPs were magnetically separated by magnetic separation technique using NdFeB block magnet and they were washed twice with a mixture of hexane and ethanol (1:1 ratio) to obtain high purity NPs excluding excess gold NPs. The washed NPs were centrifuged again twice to remove excess CTAB from the solution which was confirmed using FTIR.

3.6.5 Folic acid activation and attachment onto CSNPs

Folic Acid (MW = 441 Da) (**Figure 3.8**) has been used as a targeting agent to actively target cancer cells. This is because, FA is a vitamin whose receptor is frequently overexpressed on the surface of human cancer cells[22] but it is highly restricted in normal tissues. In addition, the folate receptor is efficiently cell internalized after binding with its ligand[23,24]. The cell-surface receptor has a very high affinity for FA which makes it to move into the cell cytoplasm[25,26]. This provides a huge platform for efficient intracellular delivery of anticancer agents.

Activated FA was used for the attachment onto the surface of CSNPs. The reason behind the activation of FA was to activate the carboxylate group. This was carried out by dissolving FA (0.25 gm) into 20 ml of DMSO which was subjected for 1 h sonication to ensure complete dispersion. Later, carboxylate group present in FA was activated by mixing 0.125 gm of DCC and 0.225 gm of NHS. The complete reaction was carried out under N_2 atmosphere at 30°C for 12 h (FA/DCC/NHS molar ratio 2:1:2)[27]. The resultant product was filtered using Whatman filter paper; then it was further used for attach onto CSNPs.

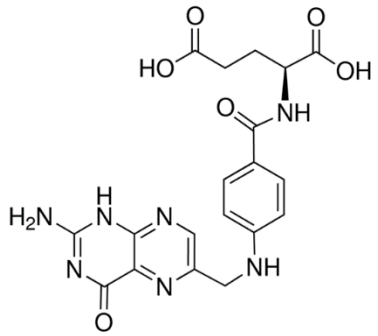

Figure 3.8. Structure of Folic acid

The attachment was carried out by mixing 1 ml of activated FA and 10 ml of CSNPs under N_2 atmosphere, stirring the mixture continuously for 5 h. Then, N_2 atmosphere was detached and the reaction was continuously stirred for 24 h. Finally, this reaction mixture was filtered using Whatman filter paper. Then the process of dialysis was carried out to eliminate unreacted FA using a 3000 kDa dialysis membrane in PBS (pH 7.4). After centrifugation, the pellet was again dialyzed in DI water for a period of 24 h. The activated FA binding onto the surface of CSNPs was studied using UV-Vis spectroscopy analysis.

3.6.6 Surface functionalization of doxorubicin

Anthracycline antibiotic Dox (**Figure 3.9**) has shown great treatment potential which has the ability to combat rapidly dividing cells leading to slow disease progression which made it to use as a one of the important chemotherapeutic agent for various cancer types. But showing a high toxicity on noncancerous cells in the human body[28]. It acts by binding to DNA-associated enzymes, it can intercalate the base pairs of the DNA's double helix[29] and also binds to multiple molecular targets like topoisomerase enzymes I and II causing various cytotoxic effects occur in conjunction leading to DNA damage[30].

Dox was used to kill cancerous cells using FA attached CSNPs. Activated FA functionalization on CSNPs acted as an anchor for the binding of Dox. To bind Dox, 5 ml FA-CSNPs was mixed with 1 ml of TEA and 5 ml of DMSO as a solvent; finally, 400 µl of 5 mM Dox solution were added. This mixture was purged using N_2 gas under continuous stirring at 60°C for 5 h. The final complex solution was dialyzed to remove the unbound or excess of Dox. The Dox binding was studied by characterization techniques like FTIR and UV-Vis spectroscopy.

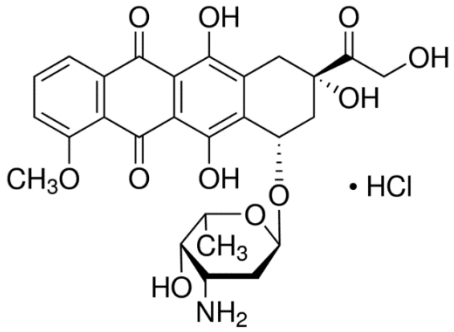

Figure 3.9. Structure of Doxorubicin hydrochloride

3.7 Doxorubicin loading and loading efficiency

Before initiating the drug release studies, it was very significant to determine the Dox loading to ensure the exact amount of Dox bound onto FA-CSNPs complex was so decisive to calculate the proper drug delivery study. It can be calculated using the below formula:

$$\textit{Concentration of drug loaded} = \textit{Concentration of drug initially loaded} - \textit{Concentration of drug of unbound drug} \quad \text{..... (6)}$$

Loading efficiency of drug is an important aspect, because this should be relatively higher to avoid loss of drugs during the production and also to minimize the use of high drug concentration. Thus the drug loading efficiency was determined by the following equation[31]:

$$\textbf{Drug loading efficieny}\ (\%) = \frac{\textbf{Concentration of drug finally loaded}}{\textbf{Concentration of drug initially loaded}} \times \mathbf{100} \ldots\ldots\ldots\ldots \textbf{(7)}$$

3.8 Cell studies

3.8.1 Cell Culture Preparation

L6 (skeletal muscle cell line) and Hep2 cells (laryngeal carcinoma cell line) were cultured in DMEM supplemented with 100 U/ml penicillin, 10% FBS and 100 μg/ml streptomycin with a 5% CO_2 atmosphere in a humidified incubator at 37°C.

3.8.2 Cytotoxicity Assay

The MTT tetrazolium assay has been widely used technique to evaluate the number of viable cells in multi-well culture plates. Viable cells with active metabolism convert MTT dye into a purple colored formazan product. But the dead cells lose the ability to convert MTT into formazan, thus color transformation serves as a useful marker to detect only the viable cells[32].

To carry out MTT assay, L6 and Hep2 cells were seeded into a 24-well plate with a cell density of 1×10^5 cells/plate and suspended in DMEM for 24 h at 37°C in a 5% CO_2 atmosphere. Later, the medium was replaced containing different concentrations of NPs in the range of 10-50 μg/ml. Then plates were placed at 37°C in a humidified 5% CO_2 incubator and after 24 h MTT-assay was performed.

For MTT assay, 10 μl of MTT (5 mg/ml) in DMEM was added to each well and incubated for 3 h under same conditions. After incubation, removal of MTT solution was done and DMSO (100 μl) was added to dissolve formazan crystals. The plates were kept on a shaker for 10 min and then absorbance was recorded at 490 nm using a micro plate reader (**Figure 3.10**). The absorbance was recorded in triplicate and cell viability was calculated from their average values.

Figure 3.10. Bio-Rad micro plate reader used for MTT assay (*Department of Cell Biology, CINVESTAV-IPN, Mexico city*)

3.8.3 Cell Labelling

Cells were incubated with different NPs to analyze the impact of viability caused by NPs. L6 and Hep2 were seeded on 13 mm glass coverslips positioned inside a 12-well culture plate with a seeding density of $1x10^3$ cells/coverslip. After 24 h, the adherent cells were washed with PBS then media was replaced and incubated for 24 h at 37°C. To remove the loosely bound and free NPs the cells were washed with PBS. Using 2% paraformaldehyde the cells are fixed. After washing, the cells are permeabilized with 500 µl of PBS-triton 0.1% and again washed with PBS. Then the cells are stained with 300 µl of Hoechst of 1:4000 dilution in 1x PBS. Later again stained with 300 µl of Phalloidin/Rhodamine dye. Finally after washing, vectashield was used to seal the coverslip on the glass slide to observe under confocal microscopy.

3.8.4 Confocal Imaging

Confocal microscopy was employed to visualize the cellular and nuclear morphology caused by NPs. Z-series confocal images were collected using Carl Zeiss LSCM 700 confocal microscope fitted with a 40x oil-immersion lens. Images were processed using Carl Zeiss ZEN 2.1 (black edition) software.

3.9 Software for data processing

In this thesis, origin software platform (OriginPro 8.5) was used to analyze and process the data for plotting various graph.

3.10 References

1. Ewald, P. *Fifty Years of X-ray Diffraction,* Springer 82–101, (1962).
2. R. F. Egerton. *Physical principles of electron microscopy*. *Materials Today* **8,** (2005).

3. Haider, M. *et al.* A spherical-aberration-corrected 200 kV transmission electron microscope. *Ultramicroscopy* **75,** 53–60 (1998).
4. Van Aert, S., Batenburg, K. J., Rossell, M. D., Erni, R. & Van Tendeloo, G. Three-dimensional atomic imaging of crystalline nanoparticles. *Nature* **470,** 374–377 (2011).
5. Li, Z. Y. *et al.* Three-dimensional atomic-scale structure of size-selected gold nanoclusters. *Nature* **451,** 46–48 (2008).
6. He, D. S., Li, Z. Y. & Yuan, J. Kinematic HAADF-STEM image simulation of small nanoparticles. *Micron* **74,** 47–53 (2015).
7. Baker, T. S. & Henderson, R. Electron cryomicroscopy. *Int. Tables Crystallogr. Vol. F* **F,** 451–463 (2001).
8. Stuart, B. Infrared Spectroscopy: Fundamentals and applications. *Methods* **8,** 224 (2004).
9. Petersen, John, Mohammad, A. A. Clinical and Forensic Applications of Capillary Electrophoresis - Basic Principles and Modes of Capillary Electrophoresis. *Springer* **39**, (2001).
10. Hofmann, S. *Auger and X-Ray Photoelectron Spectroscopy in Materials Science*. **49,** (2013).
11. Gabbott P., *Principles and Applications of Thermal Analysis* i–xviii (Blackwell Publishing Ltd), (2008).
12. Fagaly, R. L. *SQUID Instruments and Applications*. *Review of Scientific Instruments* (2005).
13. Owen, T. *Principles and applications of UV-visible spectroscopy*. Hewlett-Packard Company, **1**, 1-136, (1996).
14. Yeh, Y.C., Creran, B. & Rotello, V. M. Gold nanoparticles: preparation, properties, and applications in bionanotechnology. *Nanoscale*, **4**, 1871–1880 (2012).
15. Hua, S. Comparison of in vitro dialysis release methods of loperamide-encapsulated liposomal gel for topical drug delivery. *Int. J. Nanomedicine* **9,** 735–744 (2014).
16. Zhu, Y.J. & Chen, F. pH-Responsive Drug-Delivery Systems. *Chem.-An Asian J.* **10,** 284–305 (2015).
17. Costa, P. & Sousa Lobo, J. M. Modeling and comparison of dissolution profiles. *Eur. J. Pharm. Sci.* **13,** 123–133 (2001).
18. Siepmann, J. & Peppas, N. A. Modeling of drug release from delivery systems based on hydroxypropyl methylcellulose (HPMC). *Adv. Drug Deliv. Rev.* **48,** 139–157 (2001).
19. Costa, P. & Sousa Lobo, J. M. Modeling and comparison of dissolution profiles. *Eur. J. Pharm. Sci.* **13,** 123–133 (2001).
20. Siepmann, J. & Siepmann, F. Mathematical modeling of drug dissolution. *Int. J. Pharm.* **453,** 12–24 (2013).
21. Trujillo-Romero, C. J., Garcia-Jimeno, S., Vera, A., Leija, L. & Estelrich, J. Using Nanoparticles for Enhancing the Focusing Heating Effect of an External Waveguide Applicator for Oncology Hyper-Thermia: Evaluation in Muscle and Tumor Phantoms. *Prog. Electromagn. Res.* **121,** 343–363 (2011).
22. Franklin, W. A. *et al.* New anti-lung-cancer antibody cluster 12 reacts with human folate receptors present on adenocarcinoma. *Int. J. Cancer* **57,** 89–95 (1994).
23. Antony, A. C. The biological chemistry of folate receptors. *Blood* **79,** 2807–2820 (1992).
24. Rothberg, K. G., Ying, Y., Kolhouse, J. F., Kamen, B. A. & Anderson, R. G. W. The glycophospholipid-linked folate receptor internalizes folate without entering the clathrin-coated pit endocytic pathway. *J. Cell Biol.* **110,** 637–649 (1990).
25. Wang, S. & Low, P. S. Folate-mediated targeting of antineoplastic drugs, imaging agents, and nucleic acids to cancer cells. *J. Control. Release* **53,** 39–48 (1998).

26. Lee, R. J. & Low, P. S. Delivery of liposomes into cultured KB cells via folate receptor-mediated endocytosis. *J. Biol. Chem.* **269,** 3198–3204 (1994).
27. Stella, B. *et al.* Design of folic acid-conjugated nanoparticles for drug targeting. *J. Pharm. Sci.* **89,** 1452–1464 (2000).
28. Tacar, O., Sriamornsak, P. & Dass, C. R. Doxorubicin: An update on anticancer molecular action, toxicity and novel drug delivery systems. *J. Pharm. Pharmacol.* **65,** 157–170 (2013).
29. Hilmer, S. N., Cogger, V. C., Muller, M. & Couteur, D. G. Le. the Hepatic Pharmacokinetics of Doxorubicin and Liposomal Doxorubicin. *Drug Metab. Dispos.* **32,** 794–799 (2004).
30. Buchholz, T. A. *et al.* Global gene expression changes during neoadjuvant chemotherapy for human breast cancer. *Cancer J* **8,** 461–468 (2002).
31. Pandey, S. *et al.* Folic acid mediated synaphic delivery of doxorubicin using biogenic gold nanoparticles anchored to biological linkers. *J. Mater. Chem. B* **1,** 1361 (2013).
32. Sittampalam, G. S. *et al.* Assay Guidance Manual. *Eli Lilly Company and the National Center for Advancing Translational Sciences*, 261–263 (2016).

CHAPTER 4

Designing a nanocargo with Fe_3O_4@Au: A Tri-pronged mechanism for MR imaging, synaphic drug-delivery and apoptosis induction in Cancer cells

Table of contents

4.1 Introduction

Cancer, considered as a hallmark of diseases which is responsible for second most mortality and morbidity rates. The greatest discovery in the fundamental cancer biology has not been transformed into clinical therapeutics. There is a vast incongruity existing due to lack of translational medicine targeting towards the cancerous cells both temporally and spatially. Moreover, the drugs available possess a plethora of side-effects and are incapable of circumventing the biophysical barriers posed by tumor microphysiology. The two nano-vectors viz., drug-delivery and imaging have come to the rescue in such a debilitating condition of cancer therapeutics.

The recent upsurge of interest in medical nanotechnology has significantly expanded the breadth and depth of magnetic nanoparticle (**MNPs**) research. **MNPs** are exploited for various applications in biomedicine, such as Magnetic Resonance Imaging (MRI), drug-delivery and hyperthermia. But the biggest flaw in using **MNPs** is that they are highly reactive in nature, and moreover, they have the tendency to transform their oxidation states drastically. To circumvent this problem, there was a need of coating such particles with an inert transition metal i.e.gold (**GNPs**). This coating leads to stabilization of the particles, thus enhancing the biocompatibility as well as biodistribution in physiological conditions. Such a design of nanoparticles comprising of SPIONic core and gold shell can perform multi-functions

concomitantly such as imaging, drug-delivery and hyperthermia. Such a nanomedicinal model containing **MNPs** can perform two functions:

1) enhance proton relaxation of specific tissues,
2) serve as MR imaging contrast agents.

The nanoshell made up of **GNPs** is surface plasmon resonance (SPR) active substance, which can interact with a linker and then orchestrate anti-cancer drugs[1–6].

Such a targeted drug delivery cargo can be accrued within the tumor site by different mechanisms such as externally applied magnetic field[7], enhanced permeation and retention of small nanoparticles (NPs) due to the leaky vasculature[8] and folate receptor-based temporal and synaphic targeting. Once collated at the tumor site, such nanoflotillas are incorporated via receptor-mediated endocytosis and then release the active drug moiety in the intracellular compartment. This leads to induction of cellular apoptosis, thus reducing systemic side effects[9,10].

The most important criteria for any drug-delivery vehicle for *in vivo* applications are that, they must be stable to overcome the hydrodynamic fluid pressure as well as endothelial surface charges. These properties prevents undue accumulation and interaction with the physiological *milieu* which hinders the nanocargo to reach towards its destined cells. Nevertheless, these properties are important but they are not sufficient to exhibit antitumor action. The intracellular drug-delivery is possible only through various stimuli such as pH, temperature or ligand-receptor interaction[11–13]. For example, certain cancer cells overexpress folate receptors on their surface, hence using folic acid (**Fa**) moieties on the surface of the vehicle can help in synaphic delivery[14–16]. Moreover, **Fa** is non-toxic, non-immunogenic in nature and stable and finally imparts negative charge on the surface, thus leading to reduced agglomeration with endothelial cells which are also negatively charged[17,18]. Apart from **Fa**, large number of ligands can be exploited such as antibodies, peptides and aptamers[19–22].

In this research, we have reported a synthesis of gold coated magnetic NPs (**Fe@A**) for their applications in drug-delivery, MRI and microwave (MW) based hyperthermia (**Figure 4.1**). The cytotoxicity assays of such NPs were performed on both L6 and Hep2 cells. These particles were also used for the attachment of **Fa** & Doxorubicin (**Dox**) and the drug release studies were done at different pH 5.4, 6.8 and 7.4. The stability of these NPs were also studied using zeta (ζ) potential. MR Imaging and Hyperthermia studies of such particles were done and was analyzed in details.

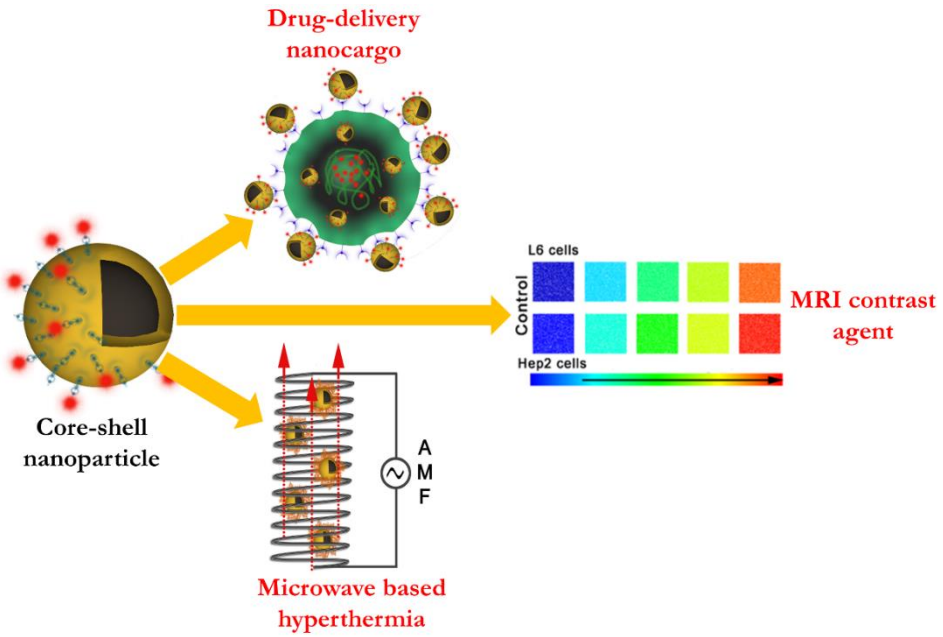

Figure 4.1. Schematic representation of **CSNPs** tri-pronged applications

4.2 Results and Discussions

4.2.1 Mechanism involved in the synthesis of core/shell nanoparticles (CSNPs)

MNPs synthesis (core) occurs when Fe^{3+} and Fe^{2+} reaches its critical supersaturation value causing short burst of nucleation. The reaction kinetics of such nuclei formation at 80°C is purely a temperature-dependent mechanism, in which the diffusion of ions takes place from the bulk phase to the surface of nuclei[23]. This growth step is followed by agglomeration due to Ostwald ripening which finally leads to reduction of overall energy of the system. Dimethyl sulfoxide (DMSO) stabilizes **MNPs** due to surface negative charge on them causing repulsion, thus preventing agglomeration of the particles[24]. To circumvent the problem of oxidation in air, an inert layer of Au nanoshell is encapsulated on the surface of **MNPs**. **MNPs** exhibit misalignment of spins on the surface. When gold interfacial layer is overlayed on such a disordered surface, there is further increment in the spin disorderness thus influencing the magnetic properties of **MNPs**[25].

The **CSNPs** synthesis involves a seed mediated approach constituting CTAB, Au ions and a mild reducing agent, AA. The reaction sequence involves metallomicelle formation by $AuCl_4^-$ with CTAB to form CTA^+AuBr_4, which is orange coloured solution. As $AuBr_4^-$ has lower potential as compared to $AuCl_4^-$ it is difficult for weak reducing agent such as AA to reduce $AuBr_4^-$ to form Au atoms. AA can only reduce $AuBr_4^-$ in the metallomicelle to form $AuBr_2^-$, which is light violet coloured solution. The first reduction reaction occurs in the

metallomicelles within the Au seed solution, while the second reduction reaction occurs on the surface of **MNPs**. At room temperature, the second reduction reaction cannot form a uniform shell on the surface of **MNPs** core hence a mild temperature of 80°C is required to form a uniform outer layer. Brown coloured magnetic particles became dark purplish when light violet coloured Au seed solution was mixed with it. The Au seeds supply large number of small randomly oriented crystalline domains along with particle mediated electron transfer, thus facilitating the Au shell on the surface of **MNPs**[26].

First Reduction: $\boldsymbol{Au^{3+} \rightarrow Au^{1+}}$

$$CTA - AuBr_4 + C_6H_8O_6 \rightarrow CTA - AuBr_2 + C_6H_6O_6 + 2H^+ + 2Br^- \ldots\ldots\ldots\ldots\ldots \textbf{(1)}$$

Second Reduction: $\boldsymbol{Au^{1+} \rightarrow Au^{0}}$

$$2CTA - AuBr_4 + C_6H_8O_6 \rightarrow 2Au + C_6H_6O_6 + 2CTA^+ + 2H^+ + 4Br^- \ldots\ldots\ldots\ldots\ldots \textbf{(2)}$$

4.2.2 Structural characterizations of CSNPs

XRD patterns of **CSNPs** is displayed in **Figure 4.2.** The characteristic peaks of pure **GNPs** (JCPDS file numbers: 004-0784) were compared with the **CSNPs**[27]. The XRD pattern demonstrated a strong peak at 2θ=38°, which is a signature marker for Au, which correspond to Miller Index (111) respectively. The Au peaks were dominant in XRD due to the heavy atom effect. Since Au is heavier than iron, all the other peaks of **MNPs** were suppressed[28–30]. From the XRD data, we also calculated the size of the NPs using the Scherrer formula[31]:

$$\boldsymbol{D_p} = {}^{0.94\lambda}/_{\beta_{1/2}Cos\theta} \ldots\ldots\ldots\ldots\ldots\ldots\ldots \textbf{(3)}$$

The average diameter of the NPs calculated using the above formula was estimated to be 14 nm, which was corroborated by TEM. In order to confirm the gold shell formation, the absorption spectra of SPR peak was monitored using UV-Vis spectroscopy. The deposition of Au seeds onto the metallic **Fe** core leads to a red-shift of the SPR peak to 581.5nm (**Figure 4.2**. inset) which proves the **CSNPs**[32].

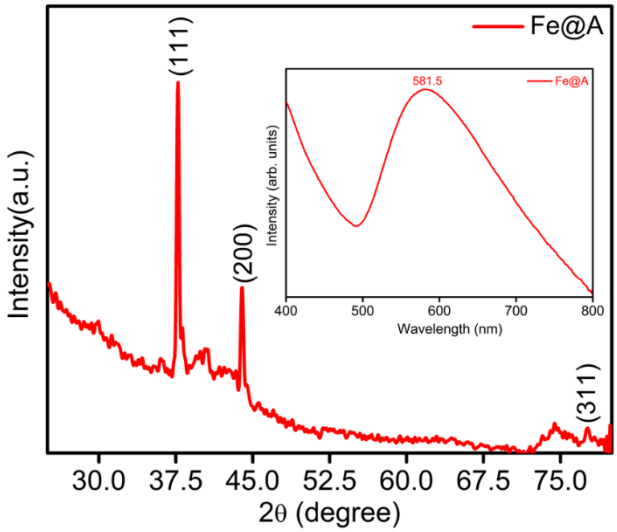

Figure 4.2. XRD pattern for the **CSNPs** showing characteristic peaks at (111), (200) and (311) for Au, inset represents the SPR peak of **CSNPs**

Transmission electron microscopy (TEM) of **Fe@A** demonstrated an average size of the particles in the range of 11 nm (**Figure 4.3a**, Histogram subset). The particles were nearly monodisperse and spherical. **CSNPs** typically exhibit no agglomerations due to very low free surface energy[33]. HRTEM of the **Fe@A CSNPs** revealed discrete separation between the Fe and Au phases, which is a clear indication of unique incorporation of Au shells on the surface of **MNPs**, as reported previously[34]. The diffusion of Au into Fe leads to the formation of metastable Au-Fe phase[35]. Due to the curvature effect, there is distortion in the crystal lattice on the surface of the NPs. The average diameter of **CSNPs** was increased to 11 nm from 6 nm of iron oxide seeds when gold chloride was reduced on its surface. Hence, the average thickness of the gold nano-shell was 5 nm, suggesting that the addition of Au on the surface of the NPs consequently increased the diameter of the NPs.

The number of shells of gold formed on iron oxide was calculated using the following formula:

$$\textbf{\textit{No. of shells formed}} = \frac{\textit{Thickness of Au shell}}{\textit{Atomic diameter of gold}} \quad \textbf{(4)}$$

$$= 5/0.2 = 25 \text{ shells}$$

Thus, around 25 shells of Au on average encapsulate each **MNPs**. These shells stabilized by CTAB confer a positive charge on the particles depicted from the Zeta potential values in **Table 4.2**.

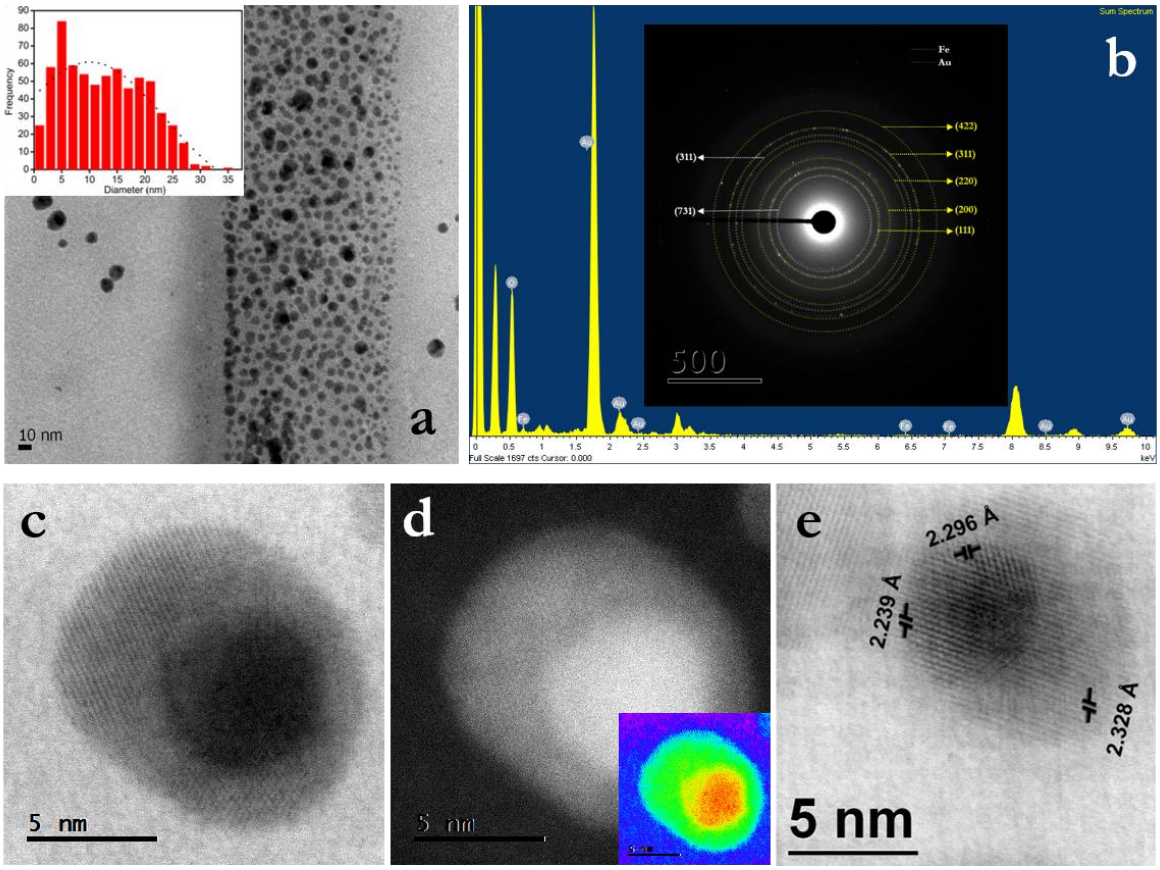

Figure 4.3. a) TEM micrograph of **CSNPs** exhibiting monodisperse NPs of size 5-20 nm (Histogram in subset), b) EDAX showing the presence of Au, Fe and O (Inset: SAED pattern from **CSNPs**, showing a superposition of Au and Fe lattices), c), d) HAADF imaging, maps the **CSNPs** Gold/Iron oxide NPs (Inset: RGB colour display clearly indicates the formation of **CSNPs** based on the difference in the colour contrast), e) measurement of the lattice distances

This leads to further enhancement of the stability of NPs due to the electrostatic force of repulsion existing between the particles. EDAX results shown in **Figure 4.3b** indicated particles comprised mainly three atoms: Fe (39.63%), Au (37.57%) and O (22.80%). **Figure 3b** inset represents the SAED pattern of **Fe@A** which is an overlapping of both Au and **Fe** lattices with distinguishable planes of majorly Au[36]. The HAADF imaging of **CSNPs** using STEM mode in **Figure 4.3c** and **d** demonstrated the intertwined MNPs, which were overlayed by Au nanoshells. The HAADF image was highly sensitive to the changes in the atomic number of atoms in the sample (Z-contrast images) due to very high angle, incoherently scattered electrons. The dark inner core as compared to lighter outer shell (**Figure 4.3c**) was due to the dominating mass contrast over diffraction contrast, thus making the shell lighter

even if Au had a higher electron density than **Fe**. The red-green-blue (RGB) colour display shown in **Figure 4.3d** inset clearly indicated the formation of **CSNPs** based on the difference in the colour contrast. The measurement of the lattice distances in **Figure 4.3e** revealed the evidence of the crystal plane (311) inside the core, thus indicating the presence of magnetite as well as planes (316) and (209), thus indicating the presence of maghemite. The presence of maghemite indicates that there is partial transformation of magnetite, resulting in the change in oxidation states of Fe. Furthermore, the shell constituted of (111) crystal plane which is a signature marker of Au. **Figure 4.4.** also shows line mapping of **CSNPs**, which confirmed the core of iron and shell of Au.

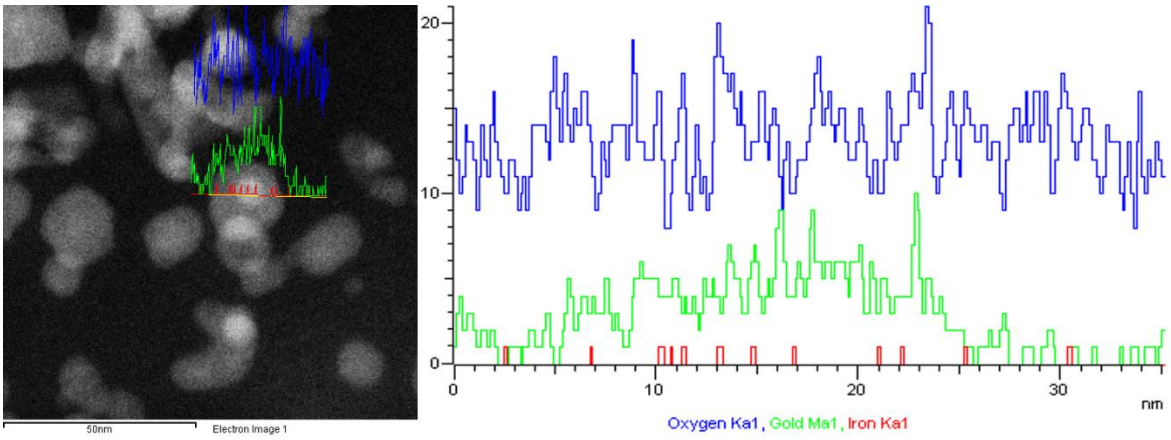

Figure 4.4. Line mapping of **CSNPs** indicating the core of iron and shell of gold

4.2.3 Magnetic characterizations

Figure 4.5. displays the plots of magnetization versus magnetic field at 5, 300 and 312 K for the **Fe@A CSNPs**. Saturation magnetization of **CSNPs** was 80.9 emu/g at 5 K and 53.2 emu/g at 312 K. These values were markedly lower than the saturation magnetization of bulk Fe NPs (92 emu/gm)[37,38]. The reduction in the saturation magnetization may be due to the decreased particle size[39]. The overall magnetism of the **CSNPs** displayed decreased saturation magnetization due to the incorporation of non-magnetic Au shell to the inner core. Furthermore, decrement in coercivity (Hc) also resulted due to the decrease in magnetic surface anisotropy as a consequence of Au shell formation[40].

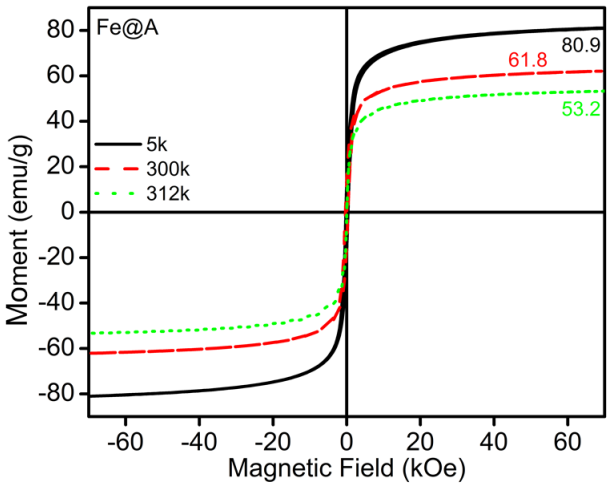

Figure 4.5. Magnetization of the **Fe@A** using SQUID at 5k, 300k & 312k

4.2.4 Surface composition of Fe@A

The important criteria for the synthesis of **CSNPs** is usually the completeness of shell onto the surface of core NPs[41]. Therefore, to confirm this criteria XPS was employed for evaluating the surface composition of **Fe@A** as shown in **Figure 4.6a***. Analysis of the individual elemental XPS spectrum confirmed the oxidation states of each elements in the solution. **Figure 4.6a** shows two dominant peaks at 710.8 eV and 724.5 eV which is a signature marker of Fe (2p3/2) and Fe (2p1/2), respectively. These two peaks consist of Fe^{2+} and Fe^{3+} of FeO and Fe_2O_3 peaks respectively of Fe_3O_4 NPs[42]. And the satellite peak at 718.9 eV was ascribed to Fe^{3+} ions. There is a minor blue-shift of Fe (2p3/2) peak from 711.2 to 710.8 eV which confirms a very strong electronic interface between Fe core and Au shell[43]. **Figure 4.6b** represents the XPS of Au spectra of the **CSNPs**. The two peaks at 83.99 eV and 87.65 eV relates to Au (4f7/2) and Au (4f5/2), respectively. These results confirms that the emission of 4f photoelectrons from Au^{0}[44], which suggest the presence of Au^{0} atoms on the Fe core NPs[45] also with the absence of Cl 2p ions (**Figure 4.6c**) confirming the deposition of Au onto the Fe NPs. Even after the coating of Au onto the Fe, detection of Fe atoms is possible it may be due to thin Au coating of 5-10 nm[46], or Fe atomic surface were exposed during the analysis[41]. The C 1s binding energy was used as an internal reference for the analysis (**Figure 4.6d**). The O 1s peaks is can be deconvoluted into two peaks at 530.1 and 532.7 eV which corresponds to O–Fe of **Fe**[47], and O–C of carboxyl group[48,49] (**Figure 4.6e**).

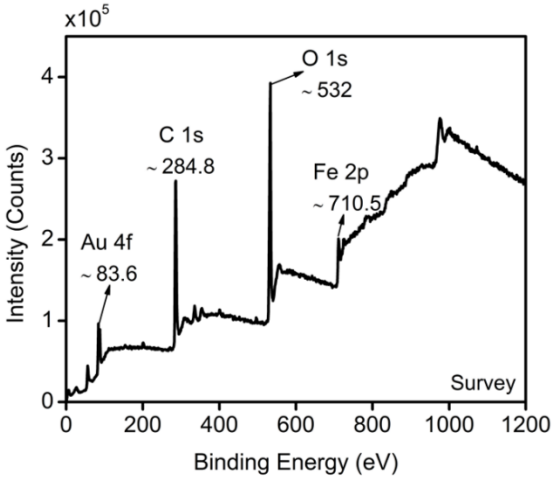

Figure 4.6a*. Scan survey of **Fe@A**

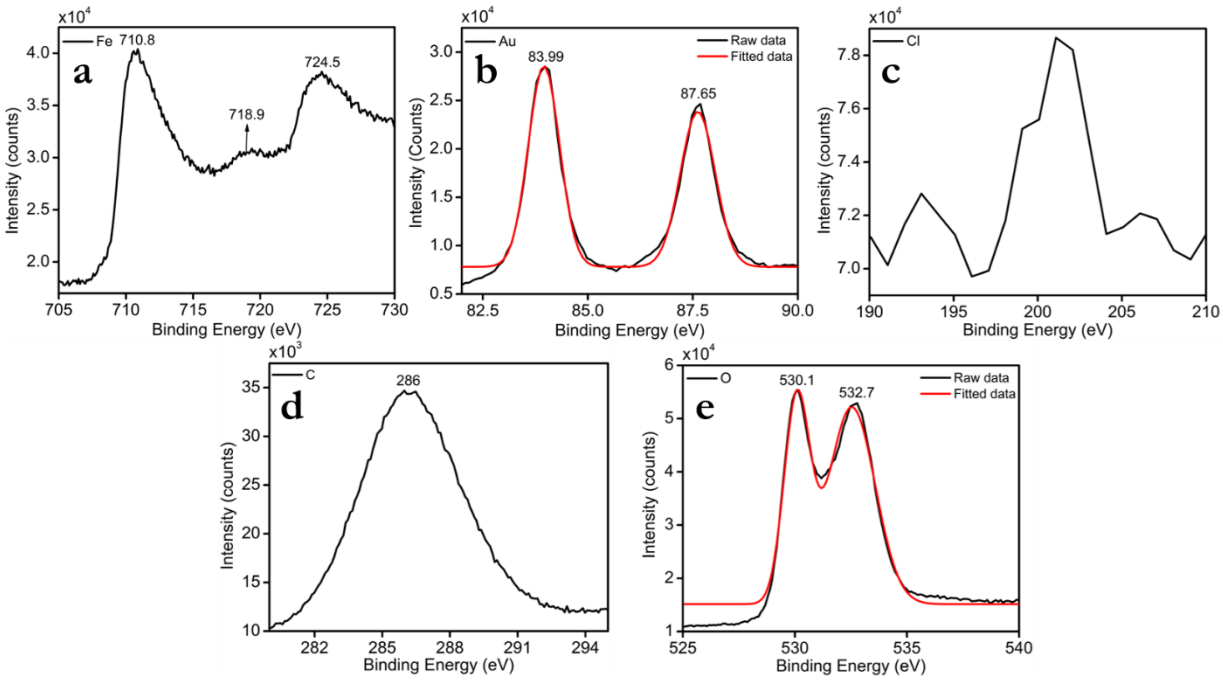

Figure 4.6. Elemental analysis of **Fe@A** by XPS which clearly shows the presence of elements such as a) Fe, b) Au, c) absence of Cl, d)C, and e) O

4.2.5 Surface modification using Fa and Dox onto the Fe@A surface

The efficiency of NPs based targeting or therapy depends on the efficacy of drug released in the specific target tissue which is purely based on the surface functionalization of NPs. These modifications aids in receptor mediated targeting which is a common strategy to increase the efficacy of drug[50,51]. The receptor mediated is majorly contributed by folic acid (**Fa**) to target cancer cells/tissue for specific delivery. **Fa** is a vitamin[52] which is very essential for the nucleoside synthesis[53,54]. So cancer cells overexpress the folate receptors[55], which has

high affinity towards **Fa** on the cell surface[56]. Additionally, these **Fa** is non-immunogenic, stable, and has small molecular size which can easily internalize the NPs through cellular membrane[57]. Thus we developed an efficient NPs-**Fa** conjugate complex for the following applications.

The UV-Vis absorption spectra of the **Fa-Fe@A** in aqueous solution is shown in **Figure 4.7a**. The SPR peak of the **Fe@A** and peak of **Fa** are observed. The absorption spectrum of **Fa-Fe@A** displayed the characteristic absorption peaks of the **Fa** (273.74 and 373.8 nm)[58], indicating the conjugation of **Fa** onto the surface of the Au shell. And due to SPR property the Au expresses the peak at 543.8 nm. This confirms the formation of **Fa** complex.

The attachment of Dox onto **Fa-Fe@A** was confirmed by UV-Vis spectra which is represented in **Figure 4.7b.** In this spectrum, the three major peaks are observed. In case of Fa, the weak hump is seen at 373.8 nm and the signature marker at 273.74 nm disappears because of the binding of **Dox**. For, **Fe@A** the absorption is seen at 546.4 nm showing minor red-shift from the previous spectrum and finally we have employed origin software to carry out the peak fitting (blue hexagon) for **Dox** which is observed at 494.5 nm with slight red-shift from 485 nm[59] due to the conjugation with **Fa** by amide bond[60] which is confirmed by FTIR. Therefore, this spectrum confirms the complex formation is successful which can be employed for further applications.

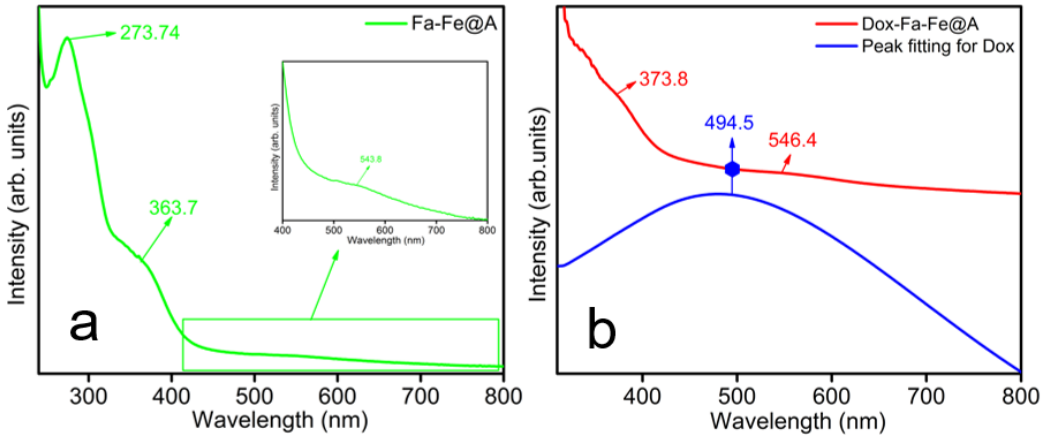

Figure 4.7. a) UV-Vis spectra of **Fa** functionalization and b) encapsulation of **Dox** onto **Fa-Fe@A**

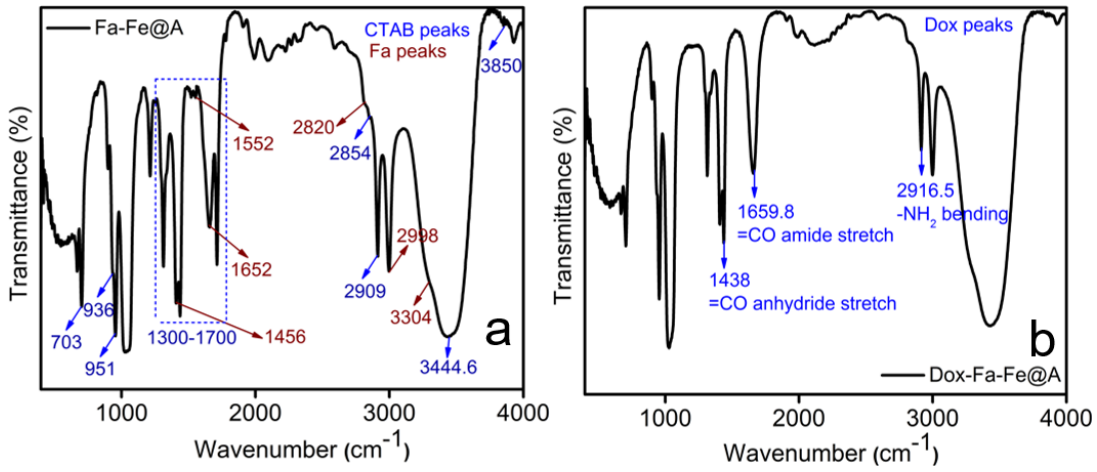

Figure 4.8. FTIR spectra showing the attachment of a) **Fa** and b) **Dox** onto **Fe@A**

Chemical structures of **Fa** and **Dox** attachment onto **Fe@A CSNPs** were investigated by FTIR spectroscopy. **Figure 4.8a** represents the FTIR bands of CTAB and **Fa** binding on the surface of **Fe@A**. The intensity of CTAB peaks are clearly shown because in most of the cases the peak intensities are purely depend on the metal NPs shape and size[61]. The peaks are shifted from the standard FTIR peaks of CTAB[62] which is compared in **Table 4.1**. This confirms that the CTAB aids in capping of Au NPs.

Table 4.1. FTIR peaks for CTAB (standard and observed) and its assignment

Assignment	CTAB peaks	
	Standard (cm^{-1})	Observed (cm^{-1})
CH_2 scissoring & O–H bending	1300-1680	1300-1700
C–H stretching	2846	2854
C–H anti-stretching	2932	2909
N–H stretching	3330–3460	3444.6
O–H stretching	3750	3850

The **Fa** attachment was confirmed by comparing with the characteristic peaks of pure **Fa**[63]. From the spectra, 5 major bands are obtained which is slightly shifted form the standard **Fa**. These proves that **Fa** has been successfully attached onto the surface of NPs forming a complex of **Fa-Fe@A**. In particular, the 3 significant peaks of **Fa** at 1456 ($–NH_2$), 1560 (–NH), and 1652 cm^{-1} (–CONH) were seen[64].

Figure 8b shows the FTIR spectra of **Dox** immobilization onto **Fa-Fe@A**. The spectra is plotted separately to avoid the overlapping of **Dox** peaks [1438 cm^{-1} (=CO anhydride stretch), 1659.8 cm^{-1} (=CO of amide stretching), 2916.5 cm^{-1} ($–NH_2$ bending)] with

the peaks of CTAB and **Fa**. It is inferred that the intensity of CTAB peaks has been reduced majorly proving that the exposure is less due to immobilization of more **Dox**. The **Dox** binds with **Fa** by means of –CONH bond by the conjugation between $–NH_2$ of **Fa** attached **Fe@A** and –COOH of **Dox**[65].

4.2.6 Stability and zeta potential studies of NPs

TGA was performed to confirm the thermal stability and step by step surface modification of the NPs under N_2 atmosphere is shown in **Figure 4.9a**. The NPs samples were heated upto 900°C, and the % weight loss of **Fe**, **Fe@A**, **Fa-Fe@A**, and **Dox-Fa-Fe@A** were 56%, 11.06%, 9.7%, and 0.9%, respectively. In TGA analysis, the curves are majorly divided into two segments: initial weight loss is due to dehydration, and later is produced by decomposition of organic/metal complexes[66]. From the thermograms figure, the initial weight loss for all samples of less than 200 °C is ascribed to water, precursors and solvent residues[67] from the particle synthesis are removed.

In case of **Fe**, a thermo-magnetometric study shows that at 270 °C maghemite is formed, and above 320 °C hematite is formed due to high temperature[68]. But the oxidation of **Fe** at higher temperature is prevented by coating with Au shell forming **Fe@A**. So eventually for **Fe@A**, initially all the water and unreacted precursors are degraded[69] and maintains a plateau until 760 °C and after that the surfactant (CTAB) and ascorbic acid (AA) are decomposed completely[70]. This proves that a large amount of CTAB and AA were employed in the reduction and protection of Au ions.

After the attachment of **Fa**, there is a drastic drop in the curve due to the loss of surface moisture and followed by a continuous decrement with a weight loss which could be assigned to **Fa** molecule loss on the surface[71]. Finally, the TGA curve of **Dox-Fa-Fe@A** shows a sudden drop from 50 to 106 °C which retains the same upto 785 °C and finally degraded completely. It is due to the complete organic nature of the NPs complex which is majorly exposed to **Fa** and **Dox** at high temperatures.

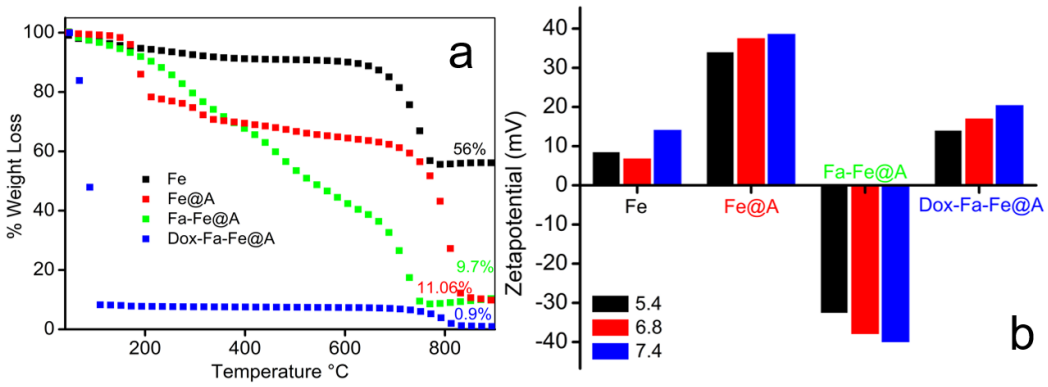

Figure 4.9. a) TGA analysis of all complexes to study the stability at higher temperatures, b) Zeta potential of **Fe**, **Fe@A**, **Fa** functionalized **Fe@A** and **Dox** encapsulated **Fa-Fe@A**

The zeta potential of the NPs were examined as because the stability and biocompatibility is purely depend on the NPs surface charges[72]. **Figure 4.9b** and **Table 4.2.** shows zeta potential measurements as a function of pH (5.4, 6.8 & 7.4) for the **Fe**, **Fe@A**, **Fa-Fe@A**, and **Dox-Fa-Fe@A.** The core **Fe** NPs synthesized by co-precipitation showed a ζ potential of +8.8 to +14.5 mV through DMSO modification; the S=O bond in DMSO forms a strong H bonds with H atoms of the NaOH (OH groups)[73,74]. In case of the Au coated Fe NPs, showed ζ potential value of +34.3 to +39 mV as the consequence of positive charge imposed by CTAB capping on AuNPs[75,76]. The **Fa-Fe@A** NPs expresses a negative charge (-32.9 to -40.4 mV) which is due to **Fa** –COOH groups deprotonation[77] on the NPs and the ζ potential value is more than -32.0 mV which indicates that the NPs are very stable. Finally, the ζ potential value of the **Dox-Fa-Fe@A** was noticed to be +14.3 to +20.8 mV as pH increases which is because of the inherent positive charge of **Dox**[78].

Table 4.2. Surface Zeta potential of NPs

Nanoparticles	Surface zeta potential (mV)		
	pH		
	5.4	**6.8**	**7.4**
Fe	+8.8	+7.2	+14.5
Fe@A	+34.3	+37.9	+39
Fa-Fe@A	-32.9	-38.3	-40.4
Dox-Fa-Fe@A	+14.3	+17.4	+20.8

4.2.7 Fa-Fe@A NPs internalization in cells

The **Fa** attached NPs has high affinity towards overexpressed folate receptors (FR) on the cancer cells[9]. Therefore, the trafficking of the **Fa-Fe@A** NPs inside the Hep2 cell lines was examined by cryoEM analysis by incubating NPs with the media (**Figure 4.10a & b**). The **Fa-Fe@A** complex entered the cells by receptor-mediated endocytosis pathway[79,80]. NPs cluster shown in **Figure 4.10b** which is high magnification cryoEM represents the internalization within the cell by vesicles formation in the cytoplasm. And also observed that there is no entry of NPs in the nuclei and cytoplasmic organelles was unaffected. This confirms that the Fa functionalized NPs are acting as an efficient nanocargo to deliver the drugs inside the cells.

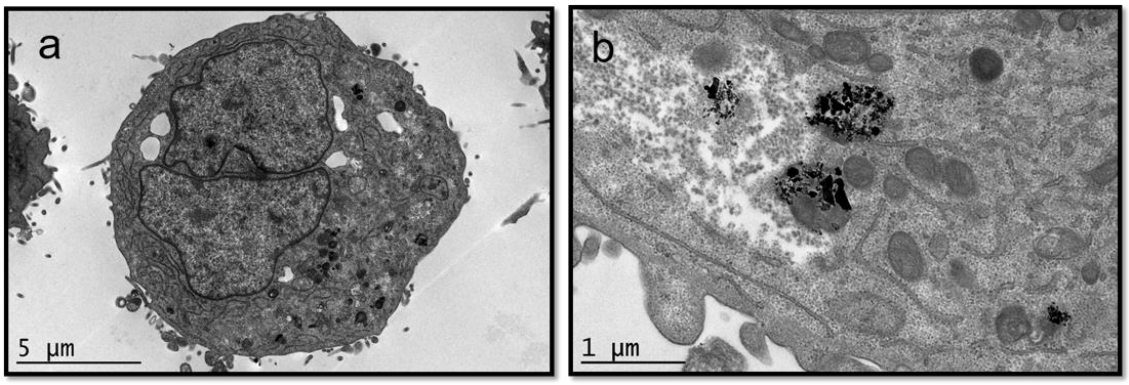

Figure 4.10. a) CryoEM image showing the entry of **Fe@A** and b) High magnification CryoEM image showing the cluster of **Fe@A** entry by the process of endocytosis

4.2.8 Evaluating cytocompatibility in L6 & Hep2 cells

The free drug - **Dox**, synthesized and functionalized NPs like **Fe**, **Fe@A**, **Fa-Fe@A**, and **Dox-Fa-Fe@A** were tested in a various range of concentrations (50-250 µg/ml) to evaluate their cytotoxic effects on the cell lines of L6 and Hep2 which is shown in **Figure 4.11a** & **b**. The cells were incubated with drug and NPs for a period of 24 h and then MTT assay was carried out to evaluate the cell viability. Both L6 and Hep2 exhibited more than 70% viability when exposed to **Fe**, **Fe@A**, **Fa-Fe@A** NPs showing minor toxicity even after exposure to high concentrations of NPs. This indicates that these NPs does not affect both the cell lines.

In case of free **Dox**, when exposed to L6 cells, shows minor killing but the same concentration of **Dox** with Hep2 cells showed 40% cell viability. And finally, the designed nanocargo **Dox-Fa-Fe@A** with L6 cells showing 25% of cell death and with Hep2 it carried

out its function by delivering the **Dox** effectively and killing the cancer cells upto 91% within 24 h. This proves that the nanocargo acts as an efficient system as an anti-cancer agent.

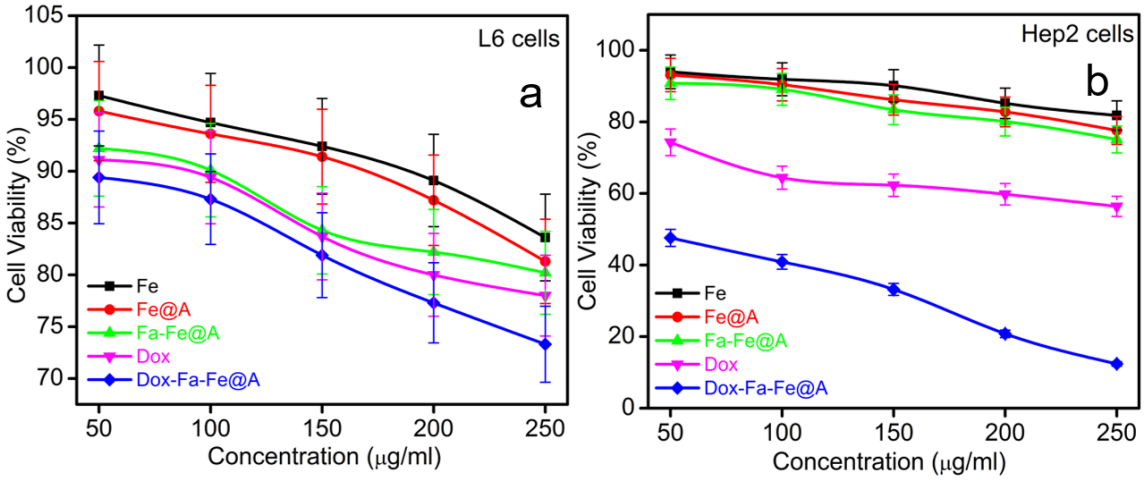

Figure 4.11. MTT assay of a) L6 cells with **Fe**, **Fe@A**, **Fa-Fe@A, Dox** and **Dox-Fa-Fe@A** showing no apoptosis at even at higher concentrations b) Hep2 cells with only **Dox** and **Dox-Fa-Fe@A** showing around 91% cell death at high conc.

After MTT testing, the morphological observation of both L6 and Hep2 cells were demonstrated. **Figure 11A** & **B** shows the confocal laser scanning microscopy (CLSM) of the cells incubated with **Fe**, **Fe@A**, **Fa-Fe@A,** and **Dox-Fa-Fe@A** for 24 h. The cellular uptake and cytotoxic effects of the NPs on the cells were studied.

L6 cells:

In case of L6 cells, the NPs complex does not shows any cytotoxic effect which can be seen by retaining the normal cytoplasmic and nuclear morphology (**Figure 4.12A-a, b & c**). While, the **Dox-Fa-Fe@A** treated cells show a minor nuclear disruption due to side-effects of drug **Dox** (**Figure 4.12A-d**). These results confirm that the NPs shows high permeability and biocompatibility so they are suitable as a nanocargos for cancer cell drug delivery.

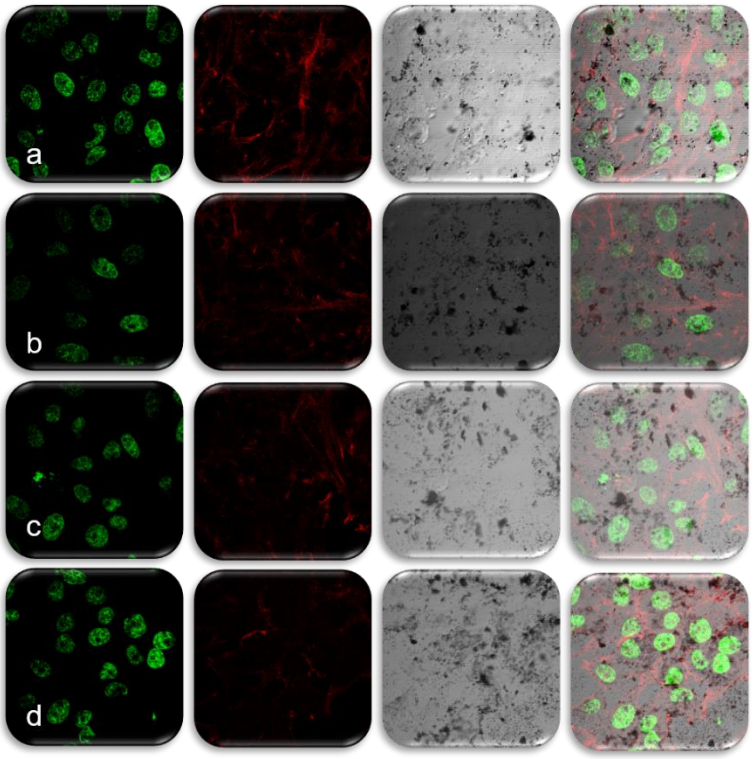

Figure 4.12A. L6 Cell morphology analysis by confocal microscopy study treated a) **Fe**, b) **Fe@A**, c) **Fa-Fe@A**, d) **Dox-Fa-Fe@A** (Scale bar is 20 μm)

Hep2 cells:

Meanwhile, with Hep2 cells there was major difference in the viability incubated with hybrid NPs confirmed by CLSM experiments. Similar results like L6 cells are seen that the **Fe**, **Fe@A**, and **Fa-Fe@A** (**Figure 4.12B-a, b & c**) does not affect the cells. But, the huge variation is seen with **Dox-Fa-Fe@A,** (**Figure 4.12B-d**) the Hep2 cells undergoes for apoptosis with the clear disruption of cellular and nuclear contents. This proves that the **Dox** is delivered in the nucleus and the drug does its function of initiating apoptosis and leading to cell death. Thus, the results obviously proves that the cargo can be a potential candidate for the drug delivery.

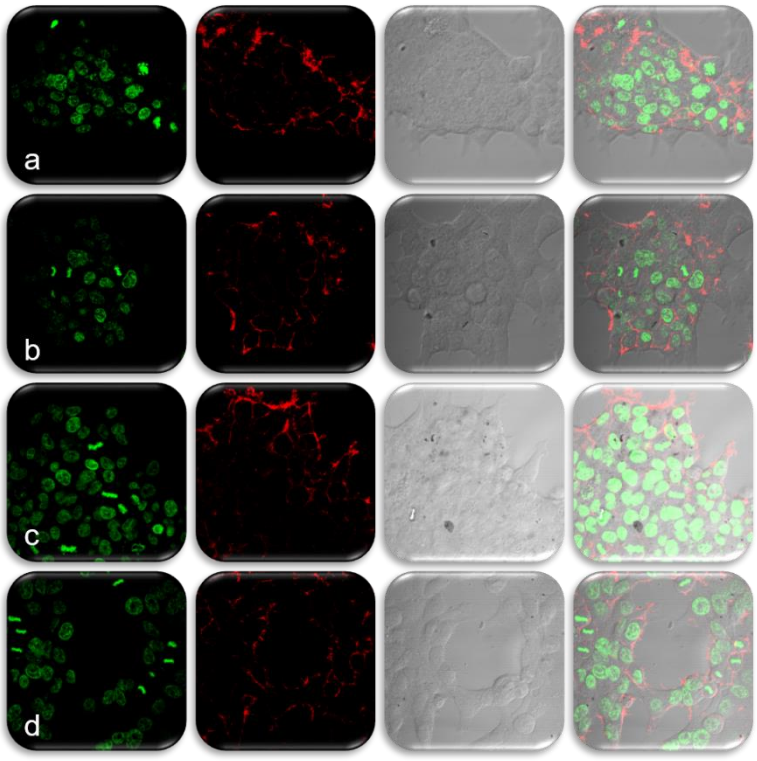

Figure 4.12B. Hep2 Cell morphology analysis by confocal microscopy study treated a) **Fe**, b) **Fe@A**, c) **Fa-Fe@A**, d) **Dox-Fa-Fe@A** (Scale bar is 20 μm)

4.3 Applications of Fe@A

There are many applications of the **Fe@A** complex, such as drug-delivery, MRI and hyperthermia. This multifunctional cargo can tether **Dox** and **Fa** making them more targeted and cancer cell cytotoxic. **MNPs** though in the core of the complex can exhibit T_2 contrast MR imaging. They are emerging as a nanoplatform for multimodal imaging. Such particles have finally led to diagnostic as well as therapeutics. Moreover, such **MNPs** also possess hyperthermal property. This has led to combination therapy, where the cytotoxicity of cells are due to both drug as well as heat generated by hyperthermia. This heat also enhances the drug release and furthermore causes enhanced killing.

4.3.1 Drug release and kinetics studies at different pH

Drug loading Efficiency:

Concentration of drug initially loaded= 0.079 mM

Concentration of unbound drug= 0.004 mM

[Concentration of drug is calculated using the standard calibration curve of **Dox** (Straight line equation: y=6.72x)]

$$\textbf{\textit{Concentration of drug loaded}} = concentration\ of\ drug\ intially\ loaded - concentration\ of\ unbound\ drug \quad \text{(1)}$$

= 0.079 mM – 0.004 mM = 0.0588 mM

$$\textbf{\textit{Drug loading efficieny}}\ (\%) = \frac{concentration\ of\ drug\ loaded\ finally}{concentartion\ of\ drug\ initially\ loaded} \times 100 \quad \text{(2)}$$

= 0.075/0.079*100 = 94.93 %

Tumor microenvironment possess lower pH as compared to the normal tissue *milieu*[81]. The normal physiological pH is 7.4, but due to anoxic microenvironment in tumor region, there is enhanced glucose uptake and its rapid breakdown into acid leads to the decrement of the pH of such regions to 6.8. A paradigm drug-delivery model needs to be designed in such a way that, there is maximal release at lower pH in comparison to physiological pH. Moreover, drugs like **Dox** becomes active in acidic environment, hence there must be maximum release in intracellular compartments, such as endosome, where pH becomes 5.4[82]. Keeping these points into consideration, the *in vitro* drug release of **Dox-Fa-Fe@A** was investigated by employing 3 PBS buffers at different pH (5.4, 6.8 & 7.4) at room temperature for 24 h. We determined that our NPs system is pH dependent. As the pH decreases in the cellular organelles thereby increasing the release of drugs. The **Dox** cumulative release at 3 different pH after 24 h was found to be 74.73% at pH 5.4, 71.74% at pH 6.8 and 59.99% at pH 7.4 (**Figure 4.13a**). At pH 5.4 it shows the maximum amount of drug release when compared to pH 6.8 & 7.4. This difference is due to pH decrement inside the endosomes which lead to detachment of drug by breaking the bond between the molecules. The obtained results were put into discrete drug kinetics model (**Figure 4.13b**) and realized that they followed first order rate kinetics from the high regression coefficient value ($\mathbf{R^2 = 0.9755}$).

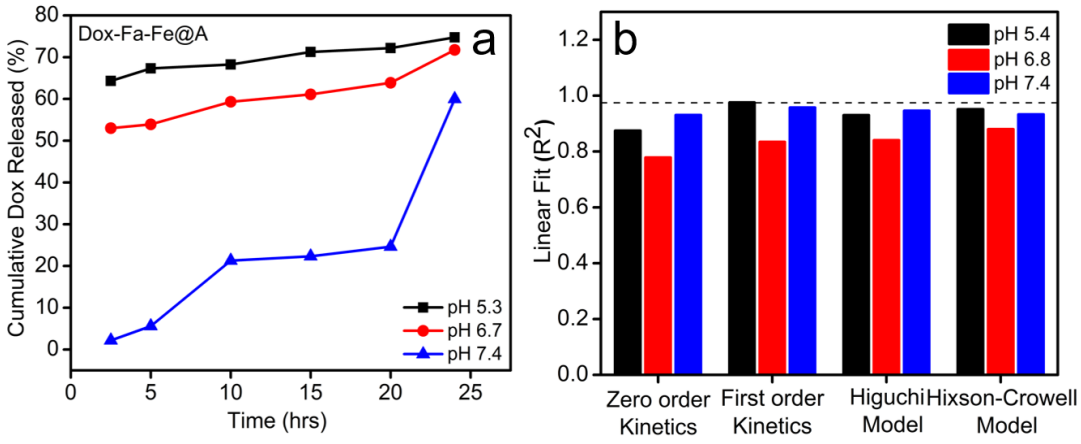

Figure 4.13. a) Cumulative release of **Dox** released at 3 different pH, b) plot representing various kinetic models of drug release kinetics

4.3.2 MR imaging using Fe@A in L6 & Hep2 cells

MR Imaging is a non-invasive method in which the active nuclei excited by radio-frequency pulse will be relaxing back to the initial ground state. This process is constituted of two components,

- longitudinal relaxation time (T_1), and
- transverse relaxation time (T_2),

which can be used to get an MR image[83]. This technique helps in diagnosis of pathologies based on the positive contrast enhancement as in T_1 or negative contrast enhancement as in T_2. **MNPs** become highly magnetized under magnetic field and possess induced magnetic fields that can lead to perturbation of the relaxation processes of the protons in the surrounding water molecules[84]. This causes shortening of the spin-spin relaxation time (T_2) of the proton, thus resulting in the darkening of the MR images. Such particles even after gold coating, do not lose their characteristics and exhibit T_2 contrast image, which is evident in the **Figure 4.14a**. As the concentration is increasing, the NPs show increased darkening of the images in both L6 and Hep2 cell lines as compared to the controls. Moreover, the relaxivity measurements showed r_2 higher than r_1 for both L6 and Hep2 (**Table 4.3**). The r_1 and r_2 values for L6 and Hep2 were represented in **Figure 4.14b** & **c.** The r_2 values are 130.13 $mM^{-1}s^{-1}$ and 182 $mM^{-1}s^{-1}$ respectively, while r_1 values were 6.94 $mM^{-1}s^{-1}$ and 8.81 $mM^{-1}s^{-1}$ respectively. The enhanced r_2 values confirmed that these NPs are an efficient T_2 contrast agents.

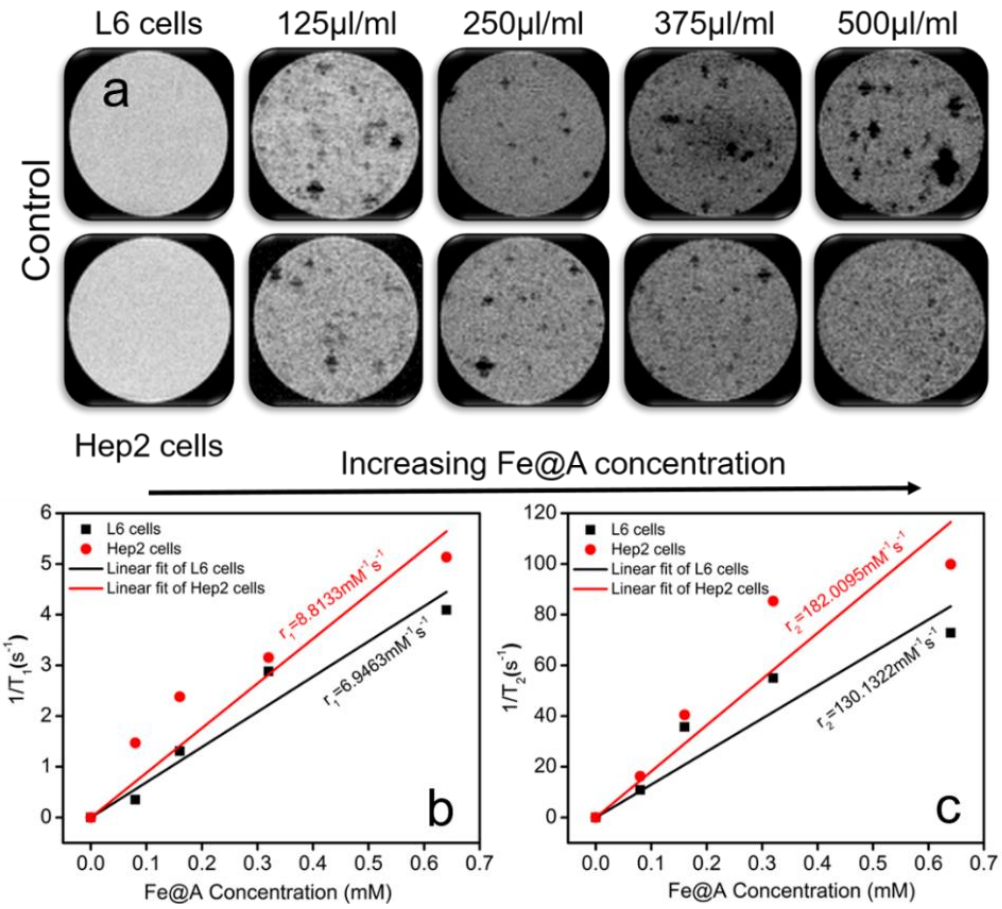

Figure 4.14. a) T_2 contrast image of **Fe@A** as the concentrations increases the darkening also increases b) r_1 relaxivity of **Fe@A** incubated with L6 and Hep2 cells c) r_2 relaxivity values of **Fe@A** incubated with L6 and Hep2 cells

Table 4.3. Relaxivity values calculation

Cells	Relaxivity values	
	r_1/r_2	r_2/r_1
L6	0.0533	18.73
Hep2	0.0484	20.65

4.3.3 Hyperthermal studies of Fe@A at 2.45GHz

In general, when the **MNPs** core diameter is less than 20 nm it behaves as a single domain and exhibit superparamagnetism nature[85,86]. These characteristics of NPs generates heating effect under alternating magnetic field (AMF) due to

- Brownian relaxation and/or

- Néel relaxation[87].

Therefore, the hyperthermic performance of **Fe@A CSNPs** at different concentrations (100-500 μg/ml) were scientifically studied under microwave (MW) at 2.45 GHz for a time span of 120 sec at 6W.

To conduct this studies, the **CSNPs** were suspended in an agar phantom and surrounded by a muscle equivalent phantom. The coaxial antenna was introduced at the agar phantom sphere center along with a temperature sensor and MW was irradiated. From the result it is inferred that the temperature to induce apoptosis in cancer cells (44-45°C)[88] was produced in around 42.7 sec and temperature responsible for causing necrosis (45-50°C)[89] was reached within 45-48 sec which is shown in (**Figure 4.15**). We believe that the rapid increment of temperature within a short span of time was purely dependent on the **GNPs** shell onto **Fe** core by retaining the superparamagnetic integrity of core intact within the gold shell.

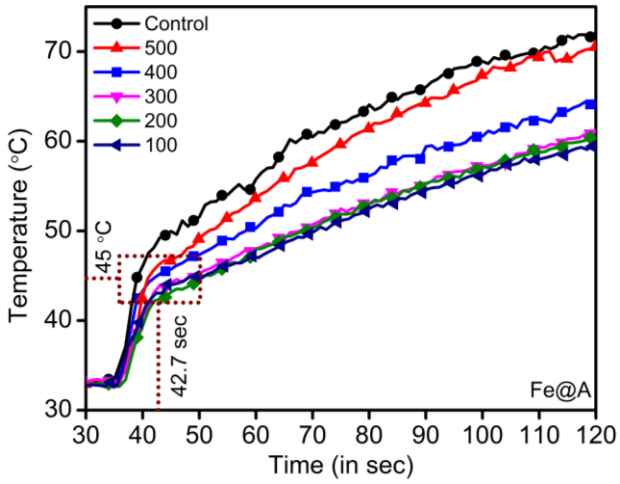

Figure 4.15. Plot showing increment of temperature as a function of time with the increased conc. of **Fe@A**

4.4 Conclusion

In summary, we have designed a synthetic route to obtain a gold coated magnetite core@shell (**Fe@A**) nanoparticles using seed-mediated technique along with functional linkers such as **Fa** and **Dox** (**Dox-Fa-Fe@A**). The bimetallic nature of the **CSNPs** was demonstrated using HRTEM and line-mapping techniques. The amalgamation of **Fe** core and the gold shell coating works in a collaborative approach by providing both magnetic properties and biocompatibility. The gold coating not only offers enough protection to **Fe** from oxidation and also the possibility of surface functionalizations.

Therefore, exploiting the core property and the surface capping we have employed it for 3 assorted applications. We inferred that the drug loading efficiency was 94.93% with the cumulative **Dox** release is around 74.73% at pH 5.4 due to acidic environment which simulated the cancer cell endosomic pH. And from the fitting, we found it pursued a first order rate kinetics with high $R^2 = 0.9755$ values. As these **CSNPs** were superparamagnetic, in MR imaging it expressed high r_2 values especially with Hep2 cells (182 $mM^{-1}s^{-1}$) due to **Fa** targeting and confirmed to be T_2 weighted contrast agents. Finally, under MW based hyperthermia, **CSNPs** produced suitable therapeutic temperature which is necessary to induce both apoptosis (42.7 sec) and necrosis (45-48 sec) rapidly with less concentrations. We confirm that the above versatile applications is solely on the multiple coating of gold layer by maintaining the core property and also providing enough platform for the surface functionalizations. From the above results, currently the **CSNPs** are further studied *in vivo* in our laboratory.

4.5 References

1. Wilhelm, C., Lavialle, F., Péchoux, C., Tatischeff, I. & Gazeau, F. Intracellular trafficking of magnetic nanoparticles to design multifunctional biovesicles. *Small* **4,** 577–582 (2008).
2. Cheng, F. Y. *et al.* Characterization of aqueous dispersions of Fe_3O_4 nanoparticles and their biomedical applications. *Biomaterials* **26,** 729–738 (2005).
3. Hergt, R. & Dutz, S. Magnetic particle hyperthermia-biophysical limitations of a visionary tumour therapy. *J. Magn. Magn. Mater.* **311,** 187–192 (2007).
4. Habib, A. H., Ondeck, C. L., Chaudhary, P., Bockstaller, M. R. & McHenry, M. E. Evaluation of iron-cobalt/ferrite core-shell nanoparticles for cancer thermotherapy. *J. Appl. Phys.* **103,** 07A307 (2008).
5. Lübbe, A. S. *et al.* Clinical experiences with magnetic drug targeting: a phase I study with 4'-epidoxorubicin in 14 patients with advanced solid tumors. *Cancer Res.* **56,** 4686–4693 (1996).
6. Alexiou, C. *et al.* Locoregional cancer treatment with magnetic drug targeting. *Cancer Res.* **60,** 6641–6648 (2000).
7. Widder, K. J., Senyei, A. E. & Scarpelli, D. G. Magnetic Microspheres: A Model System for Site Specific Drug Delivery in Vivo. *Exp. Biol. Med.* **158,** 141–146 (1978).
8. Maeda, H., Wu, J., Sawa, T., Matsumura, Y. & Hori, K. Tumor vascular permeability and the EPR effect in macromolecular therapeutics: A review. *J. Control. Release* **65,** 271–284 (2000).
9. Wang, S. & Low, P. S. Folate-mediated targeting of antineoplastic drugs, imaging agents, and nucleic acids to cancer cells. *J. Control. Release* **53,** 39–48 (1998).
10. Wang, Y., Wei, X., Zhang, C., Zhang, F. & Liang, W. Nanoparticle delivery strategies to target doxorubicin to tumor cells and reduce side effects. *Ther Deliv* **1,** 273–287 (2010).
11. Tang, X. & Pan, C. Y. Double hydrophilic block copolymers PEO-b-PGA: Synthesis,

application as potential drug carrier and drug release via pH-sensitive linkage. *J. Biomed. Mater. Res. - Part A* **86,** 428–438 (2008).
12. Rejinold, N. S., Chennazhi, K. P., Nair, S. V., Tamura, H. & Jayakumar, R. Biodegradable and thermo-sensitive chitosan-g-poly(N-vinylcaprolactam) nanoparticles as a 5-fluorouracil carrier. *Carbohydr. Polym.* **83,** 776–786 (2011).
13. Glangchai, L. C., Caldorera-Moore, M., Shi, L. & Roy, K. Nanoimprint lithography based fabrication of shape-specific, enzymatically-triggered smart nanoparticles. *J. Control. Release* **125,** 263–272 (2008).
14. Low, P. S. & Antony, A. C. Folate receptor-targeted drugs for cancer and inflammatory diseases. *Adv. Drug Deliv. Rev.* **56,** 1055–1058 (2004).
15. Guo, M. *et al.* Multifunctional superparamagnetic nanocarriers with folate-mediated and pH-responsive targeting properties for anticancer drug delivery. *Biomaterials* **32,** 185–194 (2011).
16. Sonvico, F. *et al.* Folate-conjugated iron oxide nanoparticles for solid tumor targeting as potential specific magnetic hyperthermia mediators: Synthesis, physicochemical characterization, and in vitro experiments. *Bioconjug. Chem.* **16,** 1181–1188 (2005).
17. Wang, Y., Wang, Y., Xiang, J. & Yao, K. Target-specific cellular uptake of taxol-loaded heparin-PEG-folate nanoparticles. *Biomacromolecules* **11,** 3531–3538 (2010).
18. Sun, C., Sze, R. & Zhang, M. Folic acid-PEG conjugated superparamagnetic nanoparticles for targeted cellular uptake and detection by MRI. *J. Biomed. Mater. Res. - Part A* **78,** 550–557 (2006).
19. Cirstoiu-Hapca, A., Bossy-Nobs, L., Buchegger, F., Gurny, R. & Delie, F. Differential tumor cell targeting of anti-HER2 (Herceptin®) and anti-CD20 (Mabthera®) coupled nanoparticles. *Int. J. Pharm.* **331,** 190–196 (2007).
20. Leuschner, C. *et al.* LHRH-conjugated magnetic iron oxide nanoparticles for detection of breast cancer metastases. *Breast Cancer Res. Treat.* **99,** 163–176 (2006).
21. Veiseh, O. *et al.* Inhibition of tumor-cell invasion with chlorotoxin-bound superparamagnetic nanoparticles. *Small* **5,** 256–264 (2009).
22. Yigit, M. V., Mazumdar, D. & Lu, Y. MRI detection of thrombin with aptamer functionalized superparamagnetic iron oxide nanoparticles. *Bioconjug. Chem.* **19,** 412–417 (2008).
23. Peterson, A. W., Wolf, L. K. & Georgiadis, R. M. Hybridization of mismatched or partially matched DNA at surfaces. *J. Am. Chem. Soc.* **124,** 14601–14607 (2002).
24. Vijayendran, R. A. & Leckband, D. E. A quantitative assessment of heterogeneity for surface-immobilized proteins. *Anal. Chem.* **73,** 471–480 (2001).
25. Van Dijk, M. A. *et al.* Absorption and scattering microscopy of single metal nanoparticles. *Phys. Chem. Chem. Phys.* **8,** 3486–95 (2006).
26. Robinson, I., Tung, L. D., Maenosono, S., Wälti, C. & Thanh, N. T. K. Synthesis of core-shell gold coated magnetic nanoparticles and their interaction with thiolated DNA. *Nanoscale* **2,** 2624–2630 (2010).
27. Karaagac, O., Kockar, H., Beyaz, S. & Tanrisever, T. A simple way to synthesize superparamagnetic iron oxide nanoparticles in air atmosphere: Iron ion concentration effect. *IEEE Trans. Magn.* **46,** 3978–3983 (2010).
28. Yu, F., Yao, D. & Knoll, W. Oligonucleotide hybridization studied by a surface plasmon diffraction sensor (SPDS). *Nucleic Acids Res.* **32,** e75 (2004).
29. Okahata, Y. *et al.* Kinetic Measurements of DNA Hybridization on an Oligonucleotide-Immobilized 27-MHz Quartz Crystal Microbalance. *Anal. Chem.* **70,** 1288–1296 (1998).
30. Fan, A., Lau, C. & Lu, J. Magnetic bead-based chemiluminescent metal immunoassay

with a colloidal gold label. *Anal. Chem.* **77,** 3238–3242 (2005).
31. Schroder, L., Lowery, T. J., Hilty, C., Wemmer, D. E. & Pines, A. Molecular imaging using a targeted magnetic resonance hyperpolarized biosensor. *Science (80-.).* **314,** 446 (2006).
32. Xu, Z., Hou, Y. & Sun, S. Magnetic core/shell Fe_3O_4/Au and Fe_3O_4/Au/Ag nanoparticles with tunable plasmonic properties. *J. Am. Chem. Soc.* **129,** 8698–8699 (2007).
33. Thaxton, C. S., Mirkin, C. A. & Nam, J. Nanoparticle-Based Bio – Bar Codes for the Ultrasensitive Detection of Proteins. *Science (80-.).* **301,** 1884–1886 (2003).
34. Aslan, K., Lakowicz, J. R. & Geddes, C. D. Plasmon light scattering in biology and medicine: New sensing approaches, visions and perspectives. *Curr. Opin. Chem. Biol.* **9,** 538–544 (2005).
35. Thanh, N. T. K. & Green, L. A. W. Functionalisation of nanoparticles for biomedical applications. *Nano Today* **5,** 213–230 (2010).
36. Huang, C., Jiang, J., Muangphat, C., Sun, X. & Hao, Y. Trapping Iron Oxide into Hollow Gold Nanoparticles. *Nanoscale Res. Lett.* **6,** 1–5 (2011).
37. Tiller, W. A. *The Science of Crystallization*. (Cambridge University Press, 1991). doi:10.1017/CBO9780511623158
38. Rao, C. N. R., Müller, A. & Cheetham, A. K. *Nanomaterials Chemistry: Recent Developments and New Directions*. *Nanomaterials Chemistry: Recent Developments and New Directions* (Wiley-VCH Verlag GmbH & Co. KGaA, 2007). doi:10.1002/9783527611362
39. Luzar, A. & Chandler, D. Structure and hydrogen bond dynamics of water–dimethyl sulfoxide mixtures by computer simulations. *J. Chem. Phys.* **98,** 8160–8173 (1993).
40. Murphy, C. J. *et al.* The many faces of gold nanorods. *J. Phys. Chem. Lett.* **1,** 2867–2875 (2010).
41. Goon, I. Y. *et al.* Fabrication and dispersion of gold-shell-protected magnetite nanoparticles: Systematic control using polyethyleneimine. *Chem. Mater.* **21,** 673–681 (2009).
42. Barr, T. L. An ESCA study of the termination of the passivation of elemental metals. *J. Phys. Chem.* **82,** 1801–1810 (1978).
43. Wang, F. *Quantitative Methods and Applications in GIS*. (CRC Press, 2006). doi:10.1201/9781420004281
44. Jaramillo, T. F., Baeck, S. H., Cuenya, B. R. & McFarland, E. W. Catalytic activity of supported Au nanoparticles deposited from block copolymer micelles. *J. Am. Chem. Soc.* **125,** 7148–7149 (2003).
45. Lo, C. K. *et al.* Homocysteine-protected gold-coated magnetic nanoparticles: synthesis and characterisation. *J. Mater. Chem.* **17,** 2418 (2007).
46. Siegbahn, K. Electron Spectroscopy for Chemical Analysis (E.S.C.A.). *Philos. Trans. R. Soc. London A Math. Phys. Eng. Sci.* **268,** (1970).
47. Liu, H., Jiang, E. Y., Zheng, R. K. & Bai, H. L. Structure and magnetic properties of polycrystalline Fe_3O_4 films deposited by reactive sputtering at room temperature. *Phys. status solidi* **201,** 739–744 (2004).
48. Vogelson, C. T. *et al.* Molecular coupling layers formed by reactions of epoxy resins with self-assembled carboxylate monolayers grown on the native oxide of aluminium. *J. Mater. Chem.* **13,** 291–296 (2003).
49. Mohapatra, S. & Pramanik, P. Synthesis and stability of functionalized iron oxide nanoparticles using organophosphorus coupling agents. *Colloids Surfaces A Physicochem. Eng. Asp.* **339,** 35–42 (2009).

50. Říhová, B. Receptor-mediated targeted drug or toxin delivery. *Adv. Drug Deliv. Rev.* **29,** 273–289 (1998).
51. Swaan, P. W. Recent Advances in Intestinal Macromolecular Drug Delivery via Receptor-Mediated Transport Pathways. *Pharm. Res.* **15,** 826–834 (1998).
52. Cezar, G. G. *et al.* Identification of small molecules from human embryonic stem cells using metabolomics. *Stem Cells Dev.* **16,** 869–882 (2007).
53. Weitman, S. D. *et al.* Distribution of the folate receptor GP38 in normal and malignant cell lines and tissues. *Cancer Res.* **52,** 3396–401 (1992).
54. Ross, J. F., Chaudhuri, P. K. & Ratnam, M. Differential regulation of folate receptor isoforms in normal and malignant tissues in vivo and in established cell lines. Physiologic and clinical implications. *Cancer* **73,** 2432–43 (1994).
55. Gabizon, A. *et al.* Targeting folate receptor with folate linked to extremities of poly(ethylene glycol)-grafted liposomes: In vitro studies. *Bioconjug. Chem.* **10,** 289–298 (1999).
56. Lu, Y. & Low, P. S. Folate-mediated delivery of macromolecular anticancer therapeutic agents. *Adv. Drug Deliv. Rev.* **54,** 675–693 (2002).
57. Stella, B. *et al.* Design of folic acid-conjugated nanoparticles for drug targeting. *J. Pharm. Sci.* **89,** 1452–1464 (2000).
58. Dántola, M. L. *et al.* Mechanism of photooxidation of folic acid sensitized by unconjugated pterins. *Photochem. Photobiol. Sci.* **9,** 1604–1612 (2010).
59. Chen, X., Tang, Y., Cai, B. & Fan, H. 'One-pot' synthesis of multifunctional GSH-CdTe quantum dots for targeted drug delivery. *Nanotechnology* **25,** 235101 (2014).
60. Ravichandran, M. *et al.* Plasmonic/Magnetic Multifunctional nanoplatform for Cancer Theranostics. *Sci. Rep.* **6,** 34874 (2016).
61. Honary, S., Barabadi, H., Gharaei-Fathabad, E. & Naghibi, F. Green Synthesis of Silver Nanoparticles Induced by the Fungus Penicillium citrinum. *Trop. J. Pharm. Res.* **12,** 7–11 (2013).
62. Ede, S. R., Nithiyanantham, U. & Kundu, S. Enhanced catalytic and SERS activities of CTAB stabilized interconnected osmium nanoclusters. *Phys. Chem. Chem. Phys.* **16,** 22723–22734 (2014).
63. Zhang, J., Rana, S., Srivastava, R. S. & Misra, R. D. K. On the chemical synthesis and drug delivery response of folate receptor-activated, polyethylene glycol-functionalized magnetite nanoparticles. *Acta Biomater.* **4,** 40–48 (2008).
64. Yuan, Q., Hein, S. & Misra, R. D. K. New generation of chitosan-encapsulated ZnO quantum dots loaded with drug: Synthesis, characterization and in vitro drug delivery response. *Acta Biomater.* **6,** 2732–2739 (2010).
65. Pandey, S. *et al.* Folic acid mediated synaphic delivery of doxorubicin using biogenic gold nanoparticles anchored to biological linkers. *J. Mater. Chem. B* **1,** 1361 (2013).
66. Huang, J., Su, P., Zhao, B. & Yang, Y. Facile one-pot synthesis of β-cyclodextrin-polymer-modified Fe 3 O 4 microspheres for stereoselective absorption of amino acid compounds. *Anal. Methods* **7,** 2754–2761 (2015).
67. Chen, J., Wang, Y., Ding, X., Huang, Y. & Xu, K. Analytical Methods on hydroxy functional ionic liquid-modi fi ed magnetic nanoparticles. *Anal. Methods* **6,** 8358–8367 (2014).
68. Sanders, J. P. & Gallagher, P. K. Thermomagnetometric evidence of γ-Fe_2O_3 as an intermediate in the oxidation of magnetite. *Thermochim. Acta* **406,** 241–243 (2003).
69. Rai, A., Prabhune, A. & Perry, C. C. Antibiotic mediated synthesis of gold nanoparticles

with potent antimicrobial activity and their application in antimicrobial coatings. *J. Mater. Chem.* **20,** 6789 (2010).
70. Basavegowda, N., Idhayadhulla, A. & Lee, Y. R. Phyto-synthesis of gold nanoparticles using fruit extract of Hovenia dulcis and their biological activities. *Ind. Crops Prod.* **52,** 745–751 (2014).
71. Sahoo, B. *et al.* Facile preparation of multifunctional hollow silica nanoparticles and their cancer specific targeting effect. *Biomater. Sci.* **1,** 647 (2013).
72. Jin, H. *et al.* Folate-Chitosan Nanoparticles Loaded with Ursolic Acid Confer Anti-Breast Cancer Activities in vitro and in vivo. *Sci. Rep.* **6,** 30782 (2016).
73. Shenderova, O., Hens, S. & McGuire, G. Seeding slurries based on detonation nanodiamond in DMSO. *Diam. Relat. Mater.* **19,** 260–267 (2010).
74. Zhang, W., Patel, K., Schexnider, A., Banu, S. & Radadia, A. D. Nanostructuring of biosensing electrodes with nanodiamonds for antibody immobilization. *ACS Nano* **8,** 1419–28 (2014).
75. Wang, L. *et al.* Surface chemistry of gold nanorods: origin of cell membrane damage and cytotoxicity. *Nanoscale* **5,** 8384 (2013).
76. Ricles, L. M., Nam, S. Y., Treviño, E. A., Emelianov, S. Y. & Suggs, L. J. A dual gold nanoparticle system for mesenchymal stem cell tracking. *J. Mater. Chem. B* **2,** 8220–8230 (2014).
77. Das, M., Mishra, D., Maiti, T. K., Basak, a & Pramanik, P. Bio-functionalization of magnetite nanoparticles using an aminophosphonic acid coupling agent: new, ultradispersed, iron-oxide folate nanoconjugates for cancer-specific targeting. *Nanotechnology* **19,** 415101 (2008).
78. Pandey, S. *et al.* Carbon dots functionalized gold nanorod mediated delivery of doxorubicin: tri-functional nano-worms for drug delivery, photothermal therapy and bioimaging. *J. Mater. Chem. B* **1,** 4972 (2013).
79. Kamen, B. A. & Capdevila, A. Receptor-mediated folate accumulation is regulated by the cellular folate content (5-methyltetrahydro[3Hlfolate binding/folate-binding factor). *Cell Biol.* **83,** 5983–5987 (1986).
80. Leamon, C. P. & Low, P. S. Delivery of macromolecules into living cells: a method that exploits folate receptor endocytosis. *Proc. Natl. Acad. Sci. U. S. A.* **88,** 5572–6 (1991).
81. Estrella, V. *et al.* Acidity generated by the tumor microenvironment drives local invasion. *Cancer Res.* **73,** 1524–1535 (2013).
82. Rybak, S. L. & Murphy, R. F. Primary cell cultures from murine kidney and heart differ in endosomal pH. *J. Cell. Physiol.* **176,** 216–222 (1998).
83. Scherzinger, A. L. & Hendee, W. R. Basic principles of magnetic resonance imaging--an update. *West. J. Med.* **143,** 782–92 (1985).
84. Pooley, R. A. Fundamental Physics of MR Imaging. *RadioGraphics* **25,** 1087–1099 (2005).
85. Krishnan, K. M. Advances in Magnetics Biomedical Nanomagnetics: A Spin Through Possibilities in Imaging , Diagnostics , and Therapy. **46,** 2523–2558 (2010).
86. B. D. Cullity, C. D. G., Cullity, B. D. & Graham, C. D. Introduction to magnetic materials. 550 (2011).
87. Néel, L. Théorie du traînage magnétique des substances massives dans le domaine de Rayleigh. *J. Phys. le Radium* **11,** 49–61 (1950).
88. Bettaieb, A. & Averill-Bates, D. A. Thermotolerance induced at a fever temperature of 40 degrees C protects cells against hyperthermia-induced apoptosis mediated by death receptor signalling. *Biochem. Cell Biol.* **86,** 521–538 (2008).

89. Meenach, S. A., Hilt, J. Z. & Anderson, K. W. Poly(ethylene glycol)-based magnetic hydrogel nanocomposites for hyperthermia cancer therapy. *Acta Biomater.* **6,** 1039–1046 (2010).

CHAPTER 5

Multiple Iterative Seeding of Surface plasmon enhanced Cobalt-Iron Oxide Nanokernels for Cancer Theranostics

Table of Contents

5.1 Introduction

Cancer is the second leading disease which causes major mortality and morbidity worldwide[1]. In cancer therapy, it is crucial to increase the drug specificity and drug efficacy to minimise or completely eradicate significant side-effects on patients[2]. Cancer nanotherapeutics overcome many serious drawbacks of chemotherapy such as non-specific targeting, lower

efficacy, insolubility of drug moieties in water and oral bioavailability[3]. Accordingly, Superparamagnetic Iron Oxide Nanoparticles (**SPIONs**) are exploited as an important nanomaterial for cancer detection as well as therapeutics[4]. Such magnetic nanoparticles (**NPs**) gained its momentum because of their single-domain ordering along with their large surface to volume ratio (providing large surface area for attachment of biological entities). Hence, this property makes them a suitable candidate as a contrast agent, drug-carrying cargo and hyperthermal agent[5]. The doping of **SPIONs** with cobalt ions further enhances their magnetic property, thus forming $CoFe_2O_4$ nanokernels (**Nks**). These spinel ferrite **Nks** possess ca.20-30 times higher magneto-crystalline anisotropy as compared to **SPIONs**; this increases the performance of materials for biomedical applications[6–8]. Specifically, these **Nks** are mostly used in biomedicine than any other spinel structure because of their enhanced magnetic property and large anisotropy[9]. The increased superparamagnetism makes them an efficient system for theranostics[10–12].

Such superparamagnetic **Nks** are reactive and toxic to cells; hence, gold **NPs** are used for creating a shell on the magnetic core. This architecture is biocompatible and chemically inert in the physiological system[13]. The core-shell nanoparticles (**CSNPs**) possesses unique optical and magnetic properties, thus creating an efficient platform for nanomedicine[14]. The significant benefit of the gold nanoshell is to provide complete protection to the inner magnetic core from a plethora of environmental factors[15]. This coat also acts as an excellent platform for surface modifications,[16,17] real-time imaging and drug carrying cargos[18,19].

The major hurdle in synthesising **CSNPs** is that there is no uniform coating of gold shell on the surface of the iron oxide core, even though the ratio between iron and gold is 1:7[20,21]. Therefore, gold iteration is a method that improves the formation of **CSNPs** and controls precisely the thickness of Au shell[22,23] on the magnetic core. Even though iron oxide and gold **CSNPs** have been explored extensively[24,25] for more than two decades, there are very few reports about $CoFe_2O_4$@Au nanoparticles[21,26].

Doxorubicin **(Dox)** is one of the potential and most widely used anti-cancer agents for various types of cancers. This drug has shown inimical side effects on healthy cells such as cardiotoxicity, mucositis and myelosuppression[27–29]. These adverse effects are minimised by targeted drug delivery which uses specific molecules such as folic acid **(FA)** since cancerous

cells overexpress folate receptors on their surface[30]. Apart from synaphic delivery of drugs, the most crucial parameter is its actual release for killing the cancerous cells. The effective release is dependent on different types of stimuli such as internal (alterations in pH, temperature, redox condition as well as the enzyme activities) or external (such as a magnetic field, radiations and ultrasound)[31].

Hyperthermia induced by external magnetic field is the most celebrated mechanism that enhances drug release efficiency of the system and are easiest to be used[32]. The synergistic action of hyperthermia and chemotherapy induces apoptosis as well as necrosis in the cancer cells followed by an enhanced immune response. There is a huge impact of hyperthermia-combined chemotherapy on the immune system of hosts since they induce both adaptive as well as innate immunity. Hence, thermo-chemosensitization is considered as the future of clinical research[33].

This work reports multiple iterative gold seed coated cobalt iron oxide nanokernels (**Nk@A**) as a tri-pronged cancer theranostic agent. The attachment of **FA** on the surface of **Nk@A** was used for tethering folate receptors present on cancerous cells[30]. Furthermore, **Dox** moieties orchestrated on **FA** attached **Nk@A** were responsible for their anti-cancer activity. Hence, these nanocargos act as proficient drug delivery missiles that targets cancer cells. The drug release profiles were studied using release kinetic models. Moreover, these **Nk@A** also served as a T_2 contrast agent for MR imaging. Finally, such a complex nanocargo was exploited for microwave based localized hyperthermia of cancer cells.

5.2 Results and Discussions

5.2.1 Characterization of Plasmonic/Magnetic NPs

5.2.1.1 XRD measurement

XRD analysis was carried out to detect the purity and phase crystallinity of the synthesized **Nk** and **Nk@A** (**Figure 5.1**). XRD pattern of **Nk** cubic spinel phase exhibited well-defined diffraction peaks that match with the $CoFe_2O_4$ structures (JCPDS card no.22-1086)[34]. XRD pattern of **Nk@A** showed reflections that corelated well with the FCC ordering of Au (JCPDS card no.04-0784), thus confirming the formation of a nanoshell onto **Nk**. In this case, only Au diffraction peaks were observed due to the heavy metal atom effect of Au[18,32]. The average particle sizes (D_{xrd}) of **Nk** and **Nk@A** were calculated by considering the

most intense peaks [**Nk** (220), (311), (440) and **Nk@A** (111)]. According to Scherrer equation, the average crystalline size calculated for **Nk** was 9.68 nm and for **Nk@A,** 16.69 nm. The particle sizes obtained were well corroborated with corresponding TEM images.

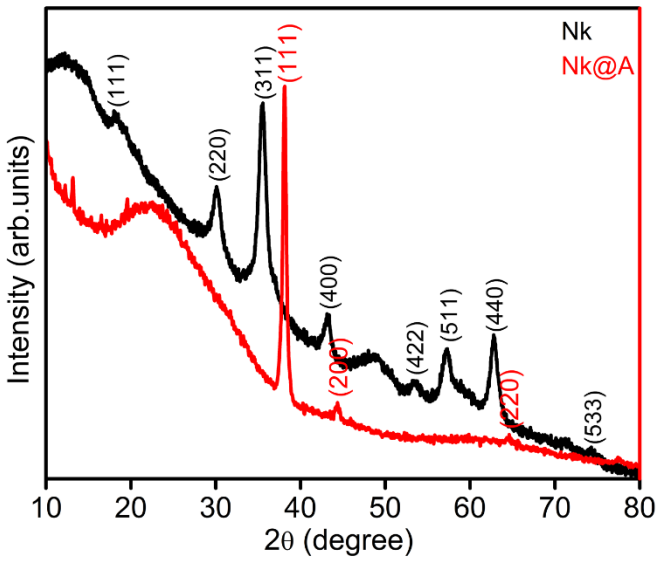

Figure 5.1. XRD spectrum representing the formation of **Nk** and **Nk@A**

5.2.1.2 Morphological analysis by TEM

Figure 5.2a-d† shows TEM, HR-TEM, HAADF-STEM images and line scan of **Nk** and **Nk@A** (1st, 3rd & 5th iterations). TEM image of **Nks** were spherical in shape with the size range of 11-14 nm exhibiting high crystallinity with aggregation which is illustrated in **Figure 5.2a & a***. The crystal lattice structure of **Nks** were distorted on the surface due to the curvature effect. Hence, the gold shell could grow epitaxially on the surface of **Nks** due to a large lattice mismatch. This leads to the formation of **Nk** as a core and gold as a shell. As iteration increased, the size of the core-shell is also increased five times from 1st to 5th iteration with Au nanoshell. This increment was due to the continued conjugation of nanogold onto the surface of the core **Nk**, which lead to the formation of **Nk@A**. HAADF-STEM analysis clearly demonstrated the discrimination between the core and the shell. This is because this contrast is directly proportional to atomic number (Z). In the 1st iterative step, the **Nk** was coated with Au nanoshell of around 1-1.5 nm (**Figure 5.2b & b***) without any aggregation. This proves that the Au iterations not only forms a shell but also stabilizes the nanoparticles. However, in order to enhance the **SPR** property, the iteration was continued; thus leading to

the formation of a nanoflower, that constituted of the collective core made of **Nk** encapsulated by a thick Au shell. The nanocluster showed jagged-like morphology due to non-homogeneously aggregated **Nk**, which leads to highly asymmetric coating of Au layer (**Figure 5.2c & c***)[35]. The thick gold nanoshell formation after multiple iterations in the **Nk@A** solution could be inferred from the colour change (**Figure 5.3a**). **Figure 5.2c†** illustrates the line scan analysis of 3rd iterated nanoflowers showing the elemental distribution of Co, Fe and Au in a single nanoparticle. The line scan confirms that Au signal is seen on the surface of **Nks** and Co, Fe signals are enriched in the inner core of the **Nks**. But as the iterations (5th iterations) continued, the Au seeds started to fill in the empty space of the knobby structures[22]. This resulted in the formation of separated spherical **Nk@A** and consecutively the shell size increased to 5-6 nm (**Figure 5.2d & d***). Similar kind of **NPs** were obtained for Au@Fe_3O_4, which had a thin shell of Au[36]. **Figure 5.2d†** represents the corresponding line scan, which clearly shows the Co K, Fe K edges in the core and Au L edges in the shell similar to that of 3rd iterated particles. Additionally to the line scan intensities illustrated in **Figure 5.2c† & d†**, it is interesting to define the stoichiometry represented by the Au Lα, whose ratio is higher than the core elements such as Co and Fe Kα. This proves that the Au signal is exhibited strongly than the signal from the core. Therefore, these results suggest that the formation of **CSNPs** expressing typical elemental composition of high Au content than the core elements, is well corroborated from XRD spectra. The colour mapping shown in **Figure 5.2a*, b*, c* & d*** proves that the nanostructures are made up of two different metals depending on the electronic density of the atoms. This colour mapping was carried out using the Digital Micrograph 3.7.0 by Gatan software. EDS spectra was carried out to determine the composition of **CSNPs** for the 1st, 3rd and 5th iterations (**Figure 5.3b, c & d**) showing the signal of Au, Co & Fe[37]. The spectra clearly distinguishes the different Au iterations from 1 to 5 just by increasing order of Au signal intensity.

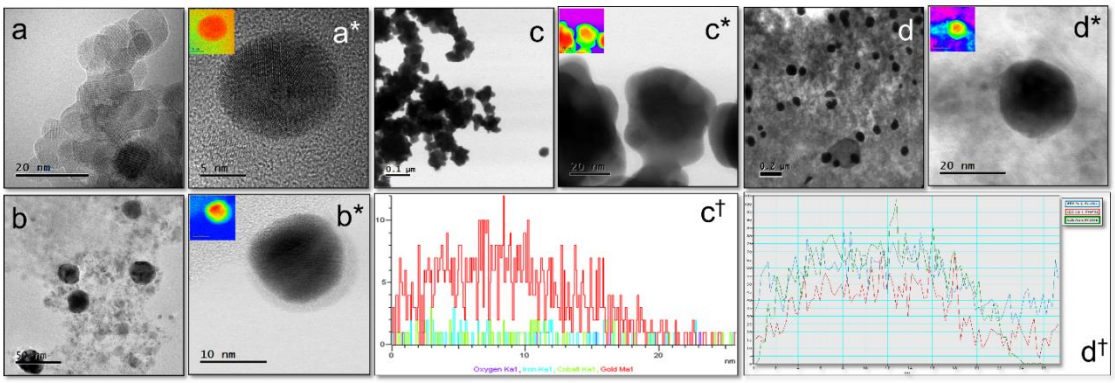

Figure 5.2. a & a*) TEM, HRTEM image of **Nk,** TEM and HAADF-STEM image of: b & b*) 1st iteration consisting of very thin Au shell and depicting 2 different contrast which proves the formation of core-shell nanoparticles along CTAB layer, c & c*) 3rd iteration showing nanoflower formation, d & d*) 5th iterative **Nk@A** with thick Au shell around 6-7 nm (Inset representing the colour mapping of corresponding images), c† & d†) Line scan analysis showing the distribution of Fe, Co and Au elements from a single nanoparticle.

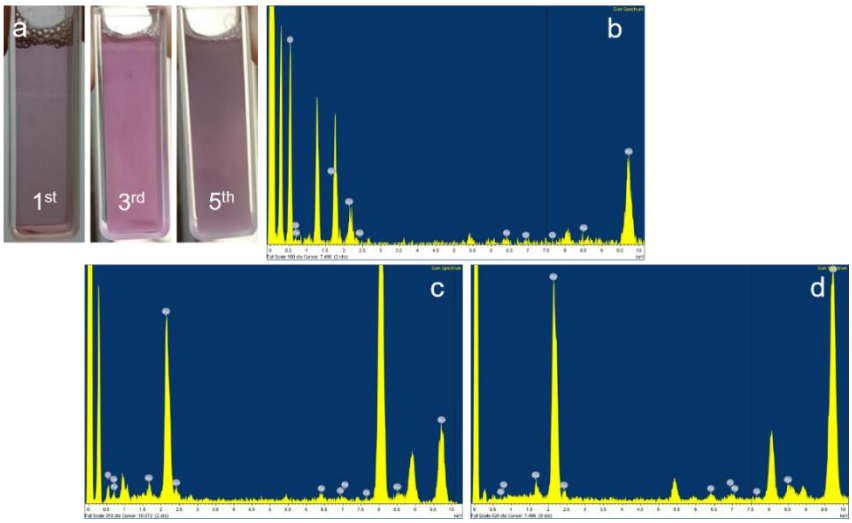

Figure 5.3. a) Colour of the **Nk@A** solution at 1st iteration, 3rd iteration and 5th iteration which changes from light purple to dark purple, EDS analysis of various Au iterations such as a) 1st iteration, b) 3rd iteration, c)5th iteration

5.2.1.3 Magnetic measurements by SQUID

The magnetic property of **Nk@A** is imperative to have an effective penetration in the cancer cell[38]. SQUID analysis (**Figure 5.4**) shows a decrement in magnetic saturation (MS)

from 74 to 45 emu/g, along with the diminishing hysteretic features. As temperature increased from 5 to 312 K, coercivity (HC) and remanence (Mr) decreased from 146 to 32 Oe and from 8 to 2 emu/g, respectively (**Table 5.1**).

This magnetic behaviour was attributed to the thermal relaxation of the magnetic moments of the **Nk@A**. This behaviour was also ascribed to the re-orientation of the magnetic moments of **NPs** caused by the thermal energy once it surpassed the magnetic energy imposed by the applied field. Thus, the magnetic characteristics of the **Nk@A** can be ascribed to those expected from a soft ferromagnetic material, even at 312 K. This kind of ferromagnetic character can be understood from MR imaging which showed high relaxivity values without the interference of Au nanoshell. Moreover, in the case of hyperthermia, the **Nk@A** showed increased heat dissipation under microwave irradiation in a short span of time.

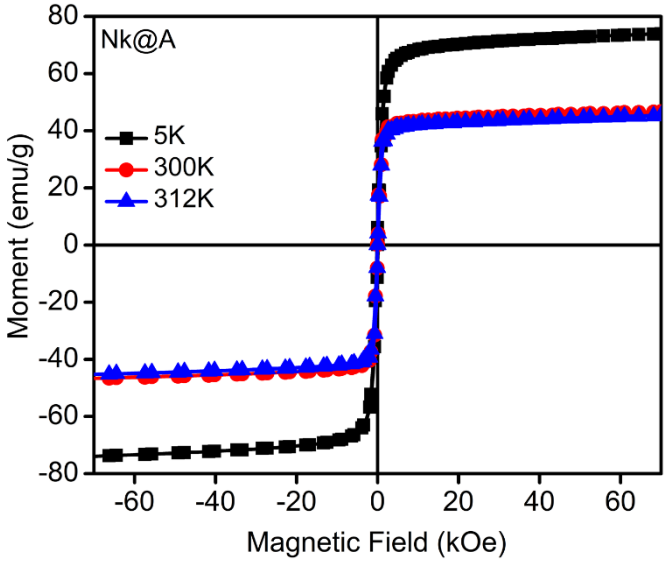

Figure 5.4. Magnetic measurements for **Nk@A** using SQUID at 5k, 300k & 312k

Table 5.1. SQUID measurements of **Nk@A** showing Hc, Mr & Ms at 5K, 300K & 312K.

Nk@A	Hc (Oe)	Mr (emu/g)	Ms (emu/g)
5K	-145.84	7.53	74.03
300K	-7.42	0.39	46.72
312K	-25.38	0.24	45.39

5.2.1.4 Elemental analysis by XPS

XPS measurements determined the binding energies and composition of **Nk@A**. The elements viz., Au, Co, Fe, C and O existed within the range from 0 to ≈1300 eV. Core level spectra were recorded and represented in **Figure 5.5**. Fe2p3/2 and 2p1/2 peaks from **Figure 5.6a** situated at around 711.7 and 725 eV respectively, were broadened due to the presence of Fe^{3+} ions in tetrahedral sites[39,40]. There is also a satellite peak of Fe^{3+} at 719.6 eV, which confirms the presence of Fe^{3+}[41]. The orbitals of Co (**Figure 5.6b**) showed that Co2p3/2 electrons exhibited binding energies at 781.2 eV, which corresponds to ions. This may be due to the substitution of Fe^{3+} ions with Co^{2+} in the tetrahedral site. There is also the existence of a peak at 786.6 eV, which again confirms the presence of Co^{2+}. This is in accordance with the XRD data, which proves that there are no mixed phases of CoO or Fe_2O_3 in the **Nk** samples[41]. **Figure 5.6c** shows Au binding energies with doublet peaks at 83.8 and 87.4 eV thus denoting the Au state of Au4f7/2 and Au4f5/2, respectively. This shows that gold ions are completely converted into metallic Au^0, leading to the formation of **CSNPs**. Interestingly, the spectrum did not show any detectable Cl2p signal[42] which further proved the complete reduction of Au onto the surface of **Nk** (**Figure 5.6d**). The O1s peak showed in **Figure 5.6e** confirmed the presence of oxygen atoms[43]. The C1s signature markers of carbon atom binding energy at 284.7 eV were taken as a reference (**Figure 5.6f**)[43]. Therefore, XPS pattern was in good agreement with XRD data, TEM-EDS and line scanning results.

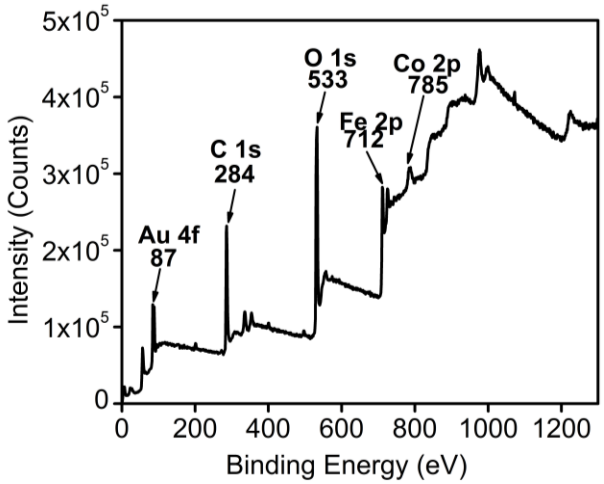

Figure 5.5. Scan survey of XPS showing the presence of all the elements

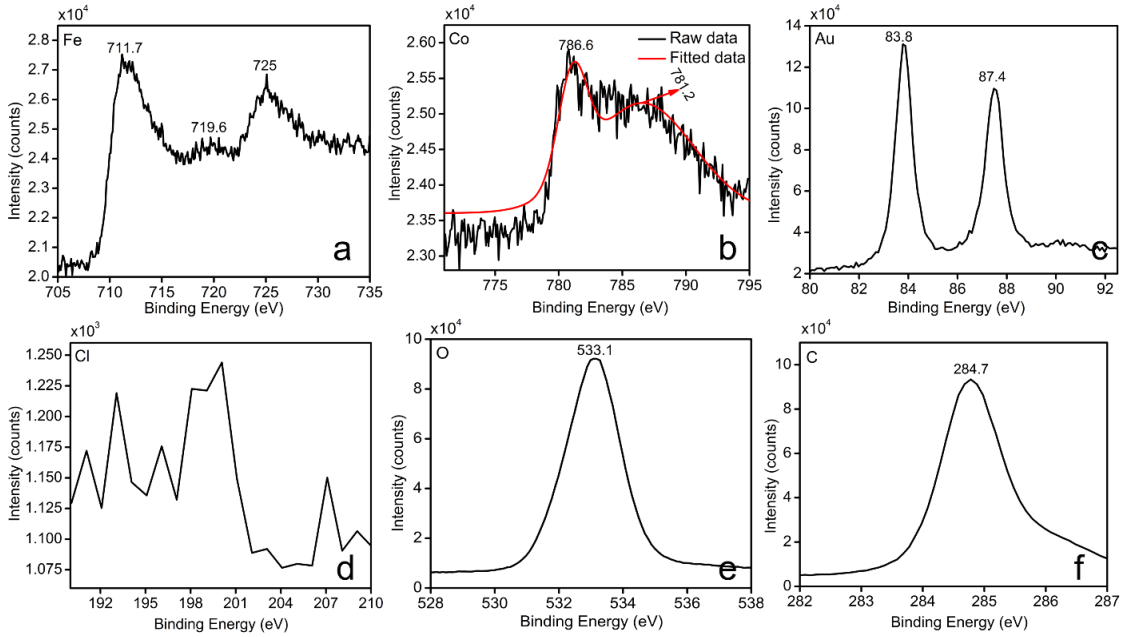

Figure 5.6. Elemental analysis of **Nk@A** by XPS which clearly shows the presence of elements such as Fe, Co, Au, C, O and absence of Cl

5.2.2 Tethering folic acid linker and Doxorubicin molecules on Nk@A

5.2.2.1 UV-Vis spectroscopy to confirm Nk@A formation, FA attachment & Dox binding

UV-Visible absorption spectra of different iterations of **Nk@A** were performed as seen in **Figure 5.7a**. As the number of gold iterations on **Nk** increased from one to three, there was a bathochromic shift of surface plasmon resonance peak (**SPR**) from 541 to 546 nm. In addition, as the iteration increased from three to five, this **SPR** peak further shifted from 546 to 551 nm. This bathochromic shift in the **SPR** peak was related to the increment in the thickness of gold shells on the surface of the magnetic core[18]. Moreover, as iterations increased, the charge density and the amplitude of the free electron oscillation inside the particles also increased. This may be due to the increased surface coating of CTAB, thus causing enhanced plasmonic absorption[44]. The spectra of **Nk** and Au seeds are also shown in **Figure 5.8**. UV-Visible spectra of **FA** attached **Nk@A** (**Figure 5.7b**) shows distinct peaks at 280.8 and 375.2 nm, which are signature markers of **FA**. Accordingly, there was a bathochromic shift in the **SPR** peak after **FA** attachment which showed a peak at 562.4 nm; this shift confirmed that **FA** formed a complex with **Nk@A**[45]. **Dox** attachment was

confirmed from the peak (inset) at 490.7 nm with minor red-shift of **Nk@A** peak (538.9 nm) and slight blue-shift of the **FA** attachment (268.7 & 375.2 nm). These shifts ensured the formation of the **Dox-FA-Nk@A** complex, which is shown in **Figure 5.7c**.

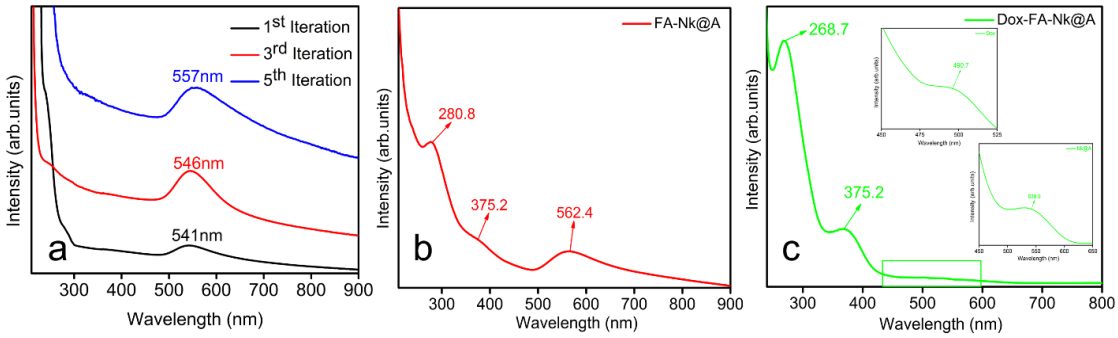

Figure 5.7. a) UV-Visible absorption spectra showing different iterations from 1-5 with the red shift of Au peak representing the increment of nanoshell, UV-Vis spectra of b) **FA** functionalization, c) binding of **Dox** onto **FA-Nk@A**

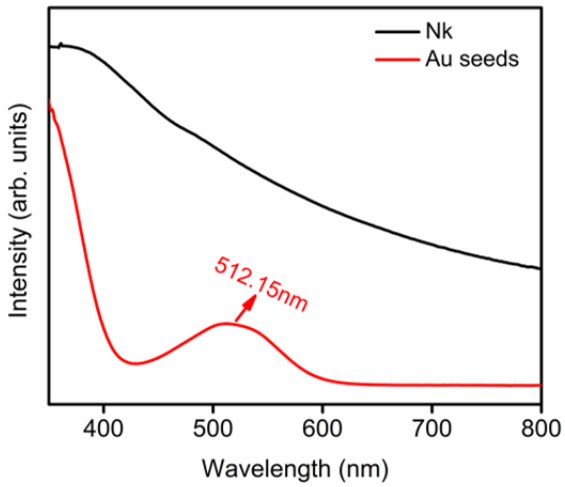

Figure 5.8. UV-Vis spectra of **Nk** and Au seeds solution which is a combination of Au precursor, CTAB and AA exhibiting a **SPR** peak at 512.15 nm

5.2.2.2 FTIR spectroscopy for CTAB removal, FA attachment and Dox binding onto Nk@A

FTIR spectra of functional organic markers on the surface of **Nk@A** is shown in **Figure 5.9a**. Spectra A represented only CTAB peaks (**Table 5.2**),[46] which proved that there was an excess amount of CTAB in the solution. However, spectra B which was analyzed after repeated centrifugation and washing the **Nk@A** solution, showed a minor peak of CTAB

which stabilizes the Au shell (**Table 5.2**). This was also demonstrated from its cytocompatibility towards L6 cells, which was evident from MTT assay and confocal microscopy studies.

Figure 5.9b shows FTIR spectra of **FA-Nk@A** and **Dox-FA-Nk@A**. Spectra A represents both activated **FA**, which show bands at 1640.7 cm^{-1} and 1718 cm^{-1} expressing –CH stretch and –NH stretch, respectively. **FA** conjugation to **Nk@A** was confirmed from –NH and –CH stretch; while the asymmetric stretching of primary amines –NH and bending vibrations of –CO confirmed the formation of amide linkage between **FA** and **Nk@A** at 1585.2 cm^{-1}[147]. Spectra B represents the attachment of **Dox** moieties onto **FA-Nk@A**. The interaction between these molecules was via amide linkage, which involved –NH amino group of FA and –COOH carboxylic group of **Dox**. Bands representing these attachments were 1436.8 cm^{-1} that represents anhydride =CO stretch and 1651.4 cm^{-1} denotes amide stretch of =CO. The peak at 2915 cm^{-1} was a classic peak of secondary –NH2 bending, and peak at 3000.68 cm^{-1} corresponded to primary $–NH_2$ bending[47].

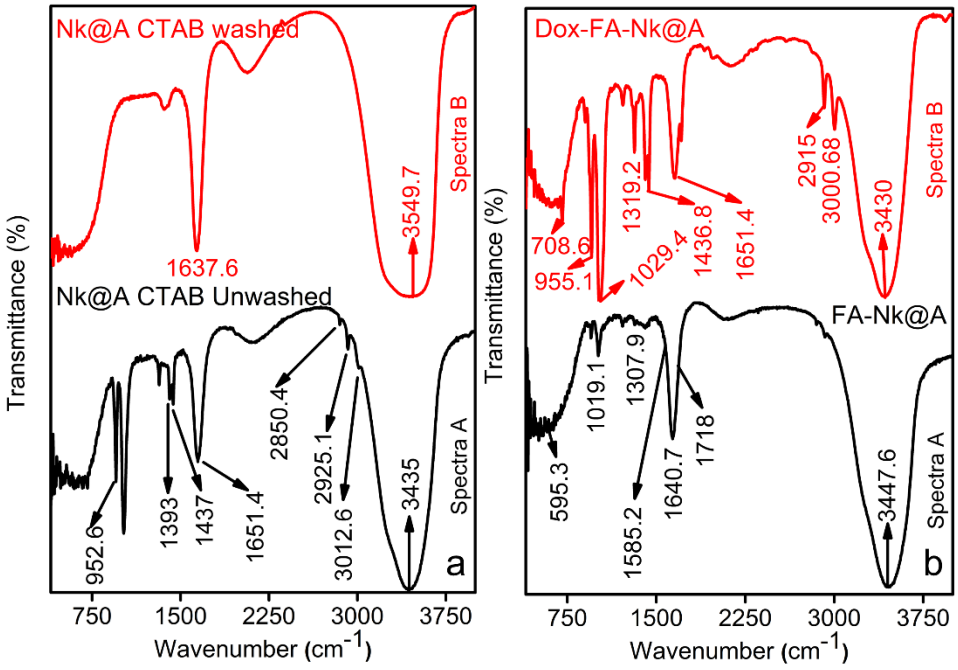

Figure 5.9. FTIR spectra of a) **Nk@A** with CTAB before and after washing, b) The attachment of **FA** and **Dox** onto **Nk@A**

Table 5.2. FTIR peaks of **Nk@A** with CTAB before and after washing

Sample	Peak(cm^{-1})	Functional groups
Nk@A sample unwashed (Spectra A)	952.6	N–H bending mode
	1651.4, 1437, 1393	deformation of –CH and –CH2 groups
	3012.6, 2925.1, 2850.4	stretching vibrations of –CH3 and –CH2 groups
	3435	N–H stretching vibration
Nk@A sample washed (Spectra B)	1637.6	scissor bending vibration of H_2O molecules
	3549.7	O–H stretching in H-bonded water

5.2.2.3 TGA Analysis to confirm the stability of NPs

TGA analysis was carried out for all samples in the temperature range of 30-900°C under N_2 flow atmosphere and any change in % weight loss was recorded. TGA graph (**Figure 5.10**) shows **Nk**, **Nk@A**, **FA-Nk@A**, **Dox-FA-Nk@A**, activated **FA** and **Dox**. Initially, activated **FA** and **Dox** showed a gradual weight loss from 30 to 100°C. The degradation of these moieties was rapid because they are completely organic in nature. **Nk** showed a rapid degradation at 122°C, which was due to the complete evaporation of water molecules. Then, there was a solid plot up to 555°C and a drop at 728°C followed by a slow degradation of bound chlorides and hydroxides. In the case of **Nk@A**, the initial weight loss from 30 to 288°C was due to the complete desorption of water and CTAB molecules from the surface[48]. The second degradation, from 289 to 595°C, was a result of the covalent interaction of CTA^+ ions; the final degradation at a higher temperature, from 596 to 900°C was most likely due to the electrostatic interaction of the ammonium group from CTAB attached to the Au **NP**s surface[49]. In **FA-Nk@A** complex, the weight loss in the range of 30-100°C was due to desorption of intercrystalline water molecules. The second degradation, in the range of 101-750°C, was due to **FA** covalent attachment, which was seemingly induced by the disintegration of groups like hydroxyl, carboxyl and amino groups present in **FA**[50]. **Dox-FA-Nk@A** complex initially showed degradation of water moieties and weak surface interactions of hydrogen with the **Nk@A**. The second decomposition from 96 to 740°C, was due to the decomposition of **FA** and **Dox** from the **NPs** complex and the decomposition from 741 to 900°C is due to slow degradation of **Nk@A**[51].

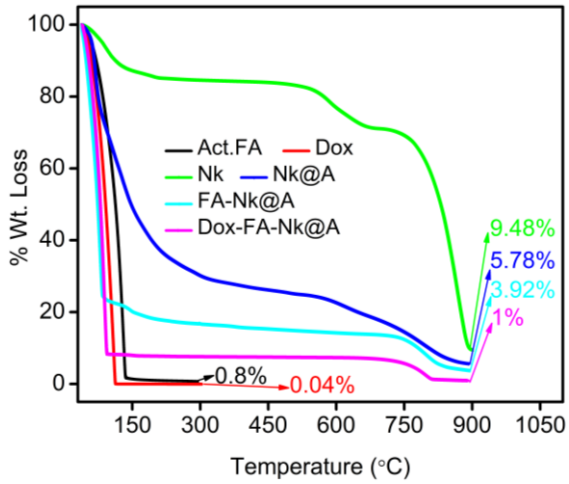

Figure 5.10. TGA analysis of all complexes to study the stability

5.2.3 Internalization and Stability studies

5.2.3.1 CryoEM & Zeta potential analysis

CryoEM analysis confirmed **Nk@A** internalization and endocytic cavities that contained **NPs** (**Figure 5.11a & b**) with aggregation, as the pH was acidic. This observation gave an insight towards the mechansim of receptor-mediated endocytosis of **Nk@A**, which can be attributed to **FA** and folate receptor interactions[52]. Moreover, the cellular uptake of **NPs** is also dependent on the surface charge. Zeta potential (ζ) values for **Nk, Nk@A, FA-Nk@A** and **Dox-FA-Nk@A** complex were in the range of +11.9 to +12.1 mV, +33.4 to +37.7 mV, -35.9 to -38.4 mV, +16.8 to +19.4 mV, respectively (**Figure 5.12**)[53–55]. This charge dependency is due to the stability of the complex, which conciliates the harsh physiological milieu, such as in the bloodstream or inside the cell. The mechanism of cellular uptake for positively charged nanoparticles is interaction of the positive moieties with the negatively charged cell surface[56]. Rotello and coworkers studied the effect of surface charge on the stability of amine functionalized gold nanoparticles. It was found that net positive charge caused more displacement of ligands in extracellular[57] and intracellular environments[58].

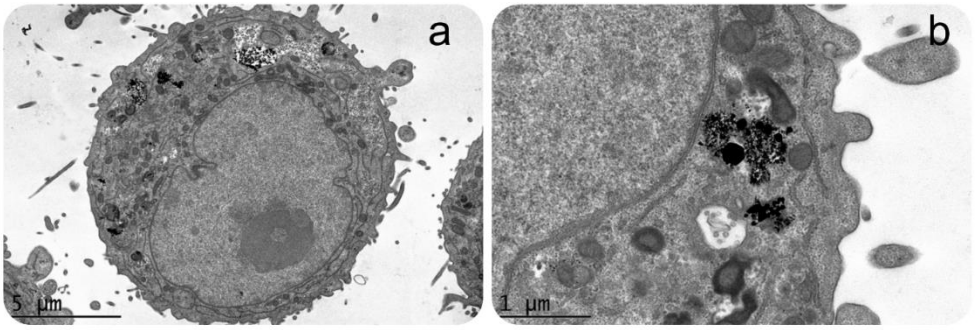

Figure 5.11. *In-vitro* cellular uptake of **Nk@A** a) CryoTEM image showing the uptake of **Nk@A** by Hep2 cells, b) magnified view of vesicles showing the cluster of **Nk@A** entry by the process of endocytosis

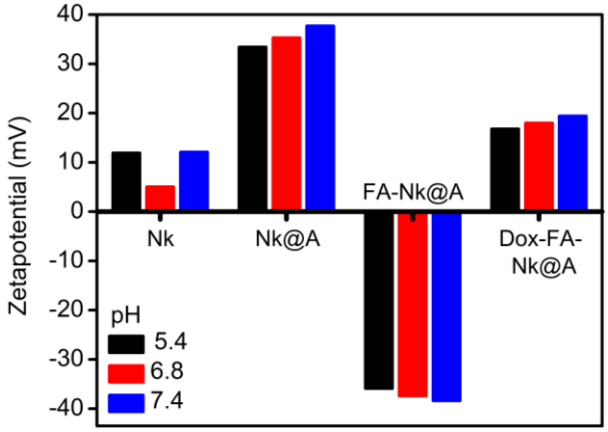

Figure 5.12. Zeta potential of **Nk**, **Nk@A**, **FA** functionalized **Nk@A** and **Dox** bounding onto **FA-Nk@A**

5.2.3.2 Intracellular localization of Dox & Dox-FA-Nk@A by confocal microscopy

The tracking of **Dox-FA-Nk@A** inside the cells was performed using confocal microscopy. Hep2 cell lines were incubated only with **Dox** (without any fluorescent dye, since **Dox** itself is a good bioimaging agent) and it showed the internalization. Initially, **Dox** was distributed all over the cytoplasm (**Figure 5.13a**) and cellular membrane, but after 24 h of incubation, the **Dox** signal in nucleus was very high due to the migration of **Dox** to this compartment and its release promoted by internal pH changes (**Figure 5.13b**). This confirmed that the binding of **Dox** molecules to the nuclei by intercalating into DNA leads to inhibition of macromolecular biosynthesis[59].

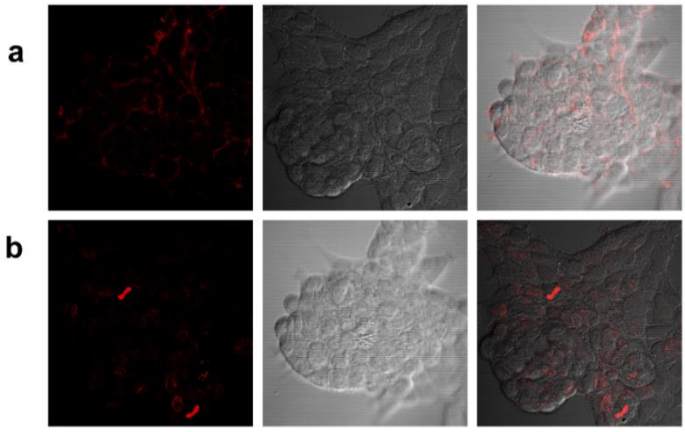

Figure 5.13. Confocal microscopy image representing the internalization of **Dox** moieties at various time periods a) initial (0 h), b) final (24 h)

5.2.3.3 Cell viability by MTT assay

In order to assess the cell viability, MTT assay was carried out by incubating L6 and Hep2 cells with **Nk**, **Nk@A**, **FA-Nk@A** and **Dox-FA-Nk@A** for 24 h in the concentration range of 10-50 µg/mL (**Figure 5.14a & b**). Even though the concentrations of all the above complexes increased to 50 µg/ml, there was not much cytotoxicity observed for L6 cells. Similarly, Hep2 cells also showed less cytotoxicity when exposed to **Nk**, **Nk@A** and **FA-Nk@A** at concentrations as high as 50 µg/ml. However, the Hep2 cell viability started decreasing rapidly when the concentration of **Dox-FA-Nk@A** was increased from 10 to 50 µg/ml. This may be due to the overexpression of folate receptors on the surface of Hep2 cells, which increases receptor mediated endocytosis and overall cellular uptake[60].

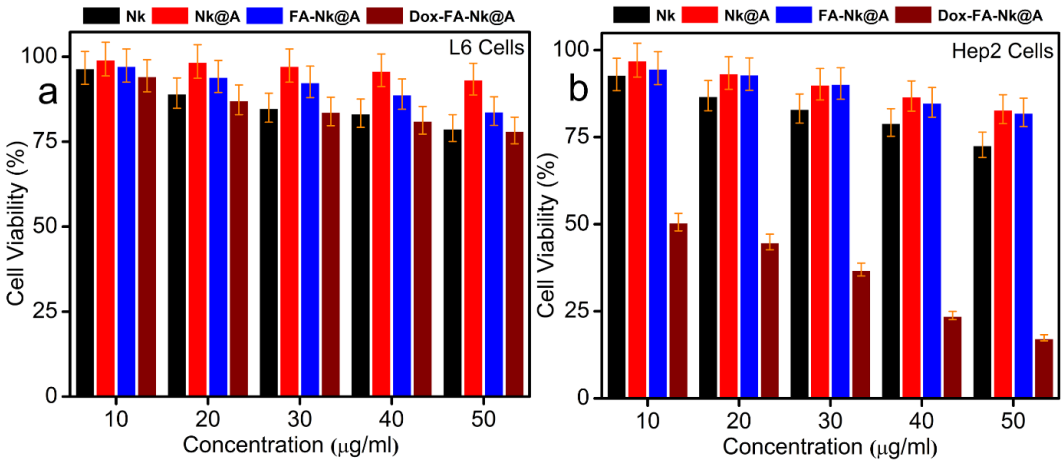

Figure 5.14. MTT assay of a) L6 cells, b) Hep2 cells with **Nk**, **Nk@A**, **FA-Nk@A** showing no apoptosis even at higher concentrations but **Dox-FA-Nk@A** treated L6 cells showing very negligible cell death and Hep2 cells showing more than 80% cell death at high concentrations

5.2.3.4 Cell viability visualized by confocal morphology

In order to evaluate the cellular and nuclear morphology of L6 and Hep2 cells on incubation with **Nk**, **Nk@A**, **FA-Nk@A** and **Dox-FA-Nk@A,** the cells were examined using confocal microscopy (**Figure 5.15a & b**). The morphology of cells treated with **Nk**, **Nk@A** and **FA-Nk@A** did not show any noticeable change in both L6 and Hep2 cells. The activity of **Dox-FA-Nk@A**, illustrated in **Figure 5.15a** (d), showed no effect on L6 cells, while Hep2 cells [**Figure 5.15b** (d)] exhibited major apoptosis caused by disruption of nuclear membrane, which leads to total cell damage. This proved that the **Dox-FA-Nk@A** acted as an efficient nanocargo in delivering the **Dox**, which finally causes cell death. The increased cytotoxicity of **Dox-FA-Nk@A** can be due to the active transport of **Dox** by receptor-mediated endocytosis mechanism as compared to the passive diffusion of free **Dox** into the cells[61].

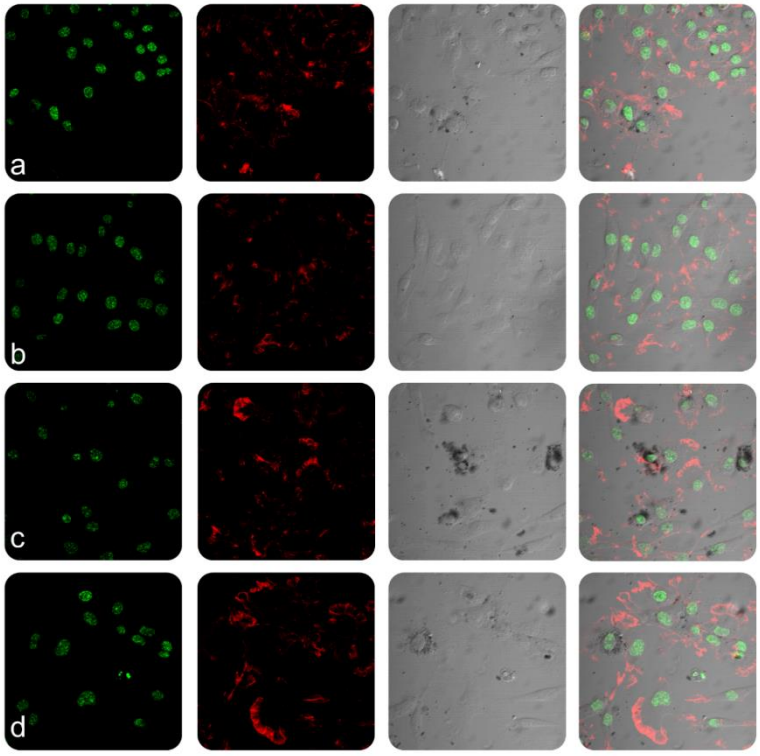

Figure 5.15a. Confocal microscopy study representing the morphology of L6 cells treated with nanoparticles for 24 h a) **Nk**, b) **Nk@A**, c) **FA-Nk@A,** d) **Dox-FA-Nk@A** which shows no cell death even at higher concentration of nanoparticles (Scale bar-20 μm)

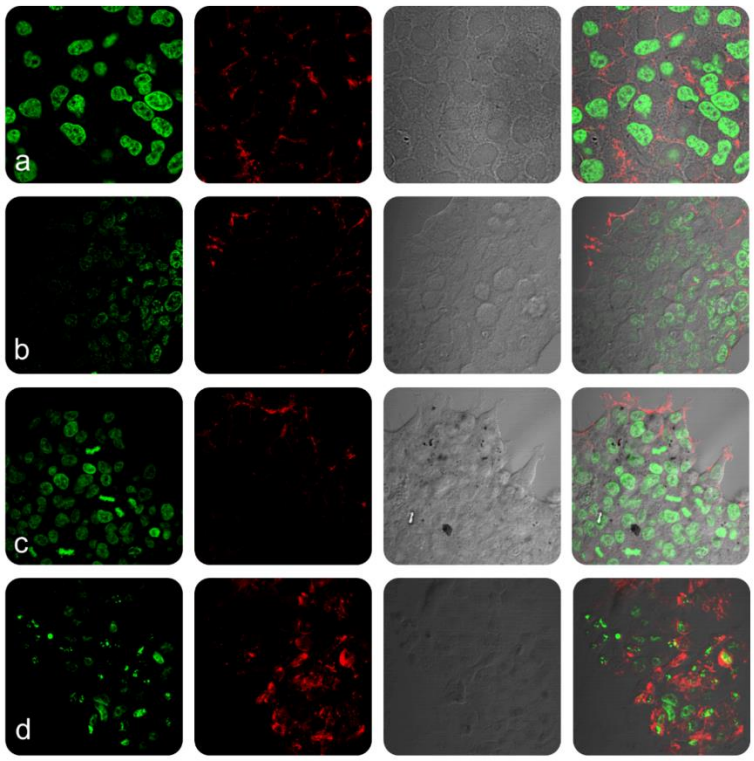

Figure 5.15b. Confocal microscopy study representing the morphology of Hep2 cells treated with nanoparticles for 24 h a) **Nk**, b) **Nk@A**, c) **FA-Nk@A** which shows negligible cell death but d) **Dox-FA-Nk@A** clearly shows the increased cell death at higher concentration of nanoparticles (Scale bar-20 μm)

5.3 Applications of Nk@A

5.3.1 *In-vitro* Dox release kinetics

The *in-vitro* drug release behavior of **Dox-FA-Nk@A** was assessed by using 3 different pH of PBS buffers (5.4, 6.8 & 7.4) for 24h and drug loading efficiency was calculated which is as follows:

Dox *loading efficiency calculation:*

Concentration of drug initially loaded = 1.4285mM

Concentration of unbound drug = 0.0705mM (Abs-0.474)

[Concentration of drug is calculated using the standard calibration curve of **Dox** (Straight line equation: y = 6.721x)]

Concentration of drug loaded = Concentration of drug initially loaded – Concentration of drug of unbound drug

=1.4285mM – 0.0705mM

= 1.358mM

Drug Loading Efficiency (%) = (Concentration of drug finally loaded / Concentration of drug initially loaded)*100

= 1.358/1.428*100

= 95.09%

We determined that the **NPs** system was both pH dependent and site-specific; which made it as a unique drug delivery system for cancer therapy. As pH decreased in the cellular organelles, thereby increasing the release of drugs as seen in **Figure 5.16a**. The cumulative release of **Dox** at 3 different pH after 24 h was 77.9% at pH 5.4, 74.6% at pH 6.8, and 33.6% at pH 7.4, thus confirming pH-dependent release mechanism. The pH 7.4 mimics normal physiological pH; hence, drug release is minimum. Moreover, the tumor microenvironment exhibits a pH of 6.8[62,63] where drug release is comparatively more, which occurs due to the partial dissociation of the amide bonds between **FA** and **Dox** molecules. The complex showed maximum amount of drug release at pH 5.4. This pH is a signature marker of endosomal acidic pH consequently leading to the dissociation of the drug from the complex by breaking the amide bond between **FA** and **Dox** molecules. Moreover, **Dox** becomes highly water-soluble as well as hydrophilic at lower pH as compared to neutral pH. Hence, **Dox** is in its inactive form in normal tissues at neutral pH, while it gains its activity in cancerous tissue at lower pH[64].

These results were fitted to different drug kinetic models such as zero order kinetics, first order kinetics, Higuchi model and Hixon-Crowell model (**Figure 5.16b**). The drug release followed first order rate kinetics model which was attributed to the high regression coefficient value (**R^2=0.9865**). This confirms that the drug release is pH as well as concentration dependent mechanism.

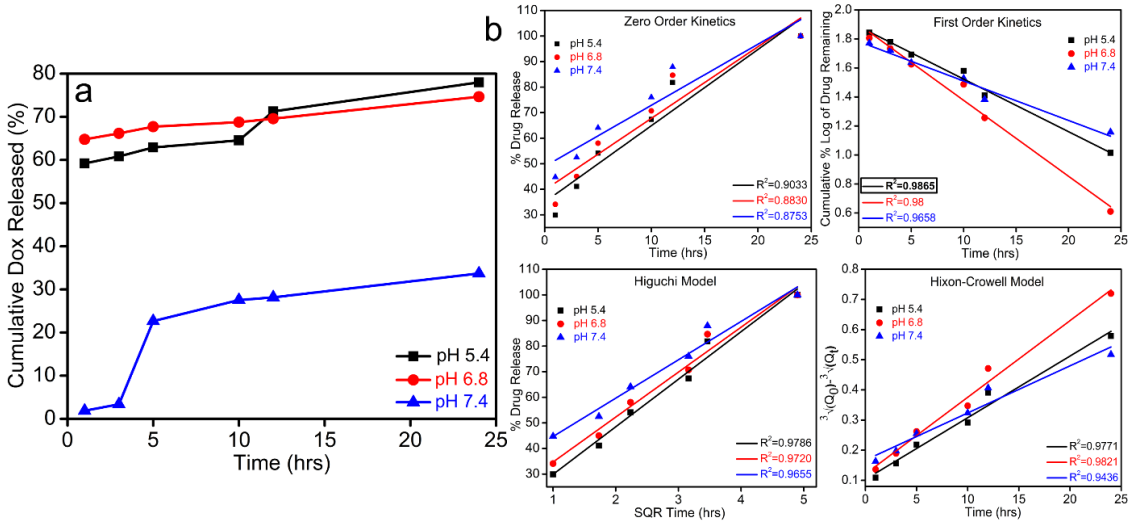

Figure 5.16. a) Cumulative release of **Dox** at 3 different pH, b) Various plots representing different fitting in kinetic models of drug release

5.3.2 Magnetic Resonance Imaging in normal and cancerous cells

Nk@A was employed as an efficient MR imaging contrast agent. **It was** cultured with both L6 and Hep2 cells. The cells were harvested and then resuspended in PBS with agar gel. These agar phantoms were used to evaluate the T_1 and T_2-weighted images shown in **Figure 5.17a** (only T_2-weighted images). As the concentration increased from 0.08-0.64 mM of **Nk@A**, there was an increment in T_2-weighed image, which became darker with both cells. The linear relationship was calculated in order to obtain the longitudinal relaxivity r_1 and transverse relaxivity r_2 of both L6 and Hep2 cells incubated with **Nk@A** (**Figure 5.17b & c**). The r_1/r_2 and r_2/r_1 values were calculated and are shown in **Table 5.3**. We found that the r_2/r_1value of L6 was 83.15 and for Hep2 it was 120.68. This was much higher than r_1/r_2 of both, which confirmed that **Nk@A** were efficient T_2 contrast agent as compared to T_1. But in the previous report for $CoFe_2O_4$@Au, r_2/r_1value was around 33[21]. So, we concluded that the increment in the r_2/r_1 value was mainly due to Au iterations.

The r_2 value of **Nk@A** with L6 was 118.08 $mM^{-1}s^{-1}$ and Hep2 was 217.24 $mM^{-1}s^{-1}$. This is highly comparable to the clinically used MRI contrast agent such as Feridex 105 $mM^{-1}s^{-1}$[165], which shows noticeable changes after injecting iron oxide **NPs**[66]. Therefore this confirmed that the Au nanoshell around **Nk** did not play a role in **Nk** core spin[67]. But the r_2 value with Hep2 cells showed significant increment when compared to L6 cells because of gold iterations.

The other reason might be the uptake of gold coated magnetic **NPs** by cancerous cells was higher than that of normal cells[68] because the electrostatic interactions of surface charge from gold coating cause more interaction with the cell[69]. Finally, we demonstrated that the **Nk@A** can be effectively used as an efficient T_2 contrast agent.

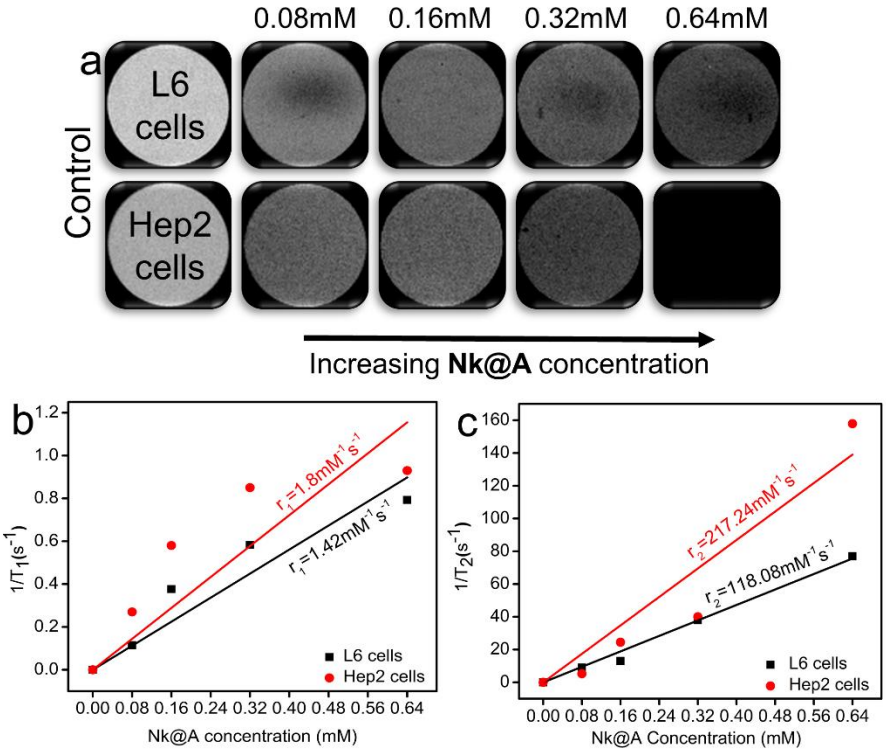

Figure 5.17. a) T_2 contrast image of **Nk@A** as the concentration increases the darkening effect also increases depending upon the type of cells, b) r_1, c) r_2 relaxivity values of **Nk@A** incubated with L6 and Hep2 cells

Table 5.3. Calculation of relaxivity values

Nk@A incubated with	L6 cells	Hep2 cells
r_1/r_2	0.0120	0.0143
r_2/r_1	83.15	120.68

5.3.3 Microwave based Hyperthermia therapy

Hyperthermia therapy involves increase in the temperature of tissues or cells, so that they become more susceptible to anti-cancer drugs. **Nk@A** nanoparticles were tested as a hyperthermal agent under microwave (**Mw**) irradiation by using a microcoaxial double slot antenna as an applicator. The increment of temperature as a function of time was measured

under ISM (Industrial, Scientific and Medical) approved frequency of 2.45 GHz in order to induce localized hyperthermia. The applicator was inserted in the phosphate buffered saline (PBS) containing **Nk@A** of various concentrations (10-125 μg/ml) and the increment of temperature was measured by using noninterfering fiber optic probes. The **Mw** was irradiated using a home-made setup[70] for 150 sec at 6 W. Interestingly, the temperature increment was very rapid and reached 45°C in around 75 sec, which was enough to kill cancer cells; the temperature raised upto 50-60°C within 150 sec for **Nk@A** (**Figure 5.18a**).

The PBS was used as a control which showed maximum rise in temperature as water has the highest absorption of **Mw**[71]. This temperature increment was purely based on the Au iterations on **Nks**. Au nanoshell as well as superparamagnetic core led to energy increment which may be due to magnetic anisotropy[72] as compared to **Nks** in xylene at 2.45 GHz[73]. The temperature increment was much higher when compared with Au@γ-Fe_2O_3, which was around 38°C at 2.45 GHz in water, for 10 mins at a power of 120 W[74].

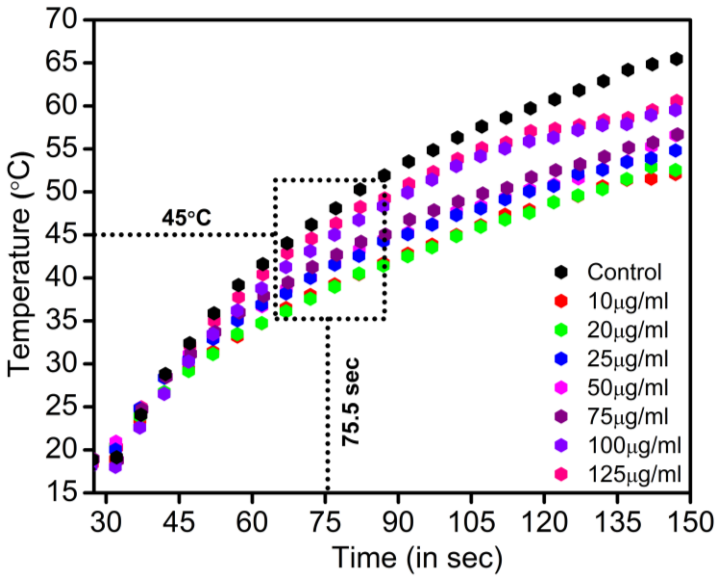

Figure 5.18a. Plot showing increment of temperature as a function of time with the increased conc. of **Nk@A** as a potential hyperthermal agent

5.3.3.1 In-vitro Hyperthermia and Chemo-Hyperthermia therapy

Chemo-hyperthermal effect or thermo-chemosensitization is quantified by the interaction of anti-cancer drugs with cells at elevated temperature. The thermal enhancement ratio (TER) for **Dox** is 1 at two different temperatures (41.5°C versus 43.5°C, respectively)[75].

There is a relationship between drug-heat interactions on cell cytotoxicity. This pharmacodynamics is responsible for enhanced killing of cells. The mechanism of thermal enhancement for drug cytotoxicity includes enhanced drug uptake as well as DNA damage and retardation of DNA repair[33]. There are previous studies, which reported the thermal enhancement of cellular cytotoxicity when drug interaction with cells takes place at higher temperatures[76]. In this report, an increase in **Nk@A** concentration shows an increased cell mortality in addition to **Mw** radiation exposure for 50 sec. The cells interacting with increased **Nk@A** concentration, but without any exposure to **Mw** irradiation (**Figure 5.18b**), showed comparatively lesser mortality than the exposed ones. Both Au shell and superparamagnetic core absorb **Mw**, due to which hyperthermia is induced in the cells, thus consequently leading to cell death. The viability of Hep2 cells was suppressed more by **Dox-FA-Nk@A** when exposed to microwave as compared to unexposed ones (**Figure 5.18c**). The **Dox** concentration was considered based on its half-maximal inhibitory concentration (IC50) value of 12.5 μg. Hence, here the **Dox** tethered **Nk@A** concentration was in the range of 2-14 μg/ml. The IC50 value of **Dox-FA-Nk@A-MW** was 8 μg as compared to the IC50 value of **Dox-FA-Nk@A**, which is 12 μg. This clearly shows thermal enhancement of **Dox** cytotoxicity at lower IC50 values in comparison with **Dox** alone. Hence, **Dox** orchestrated **Nk@A** efficiently inhibited the cell viability at elevated temperatures and very low concentrations of **Dox**, thus improving the therapeutic proficiency along with minimum side-effects. Concurrently, this combined therapy shows efficient synergism, thus exhibiting inimical effect on Hep2 cells.

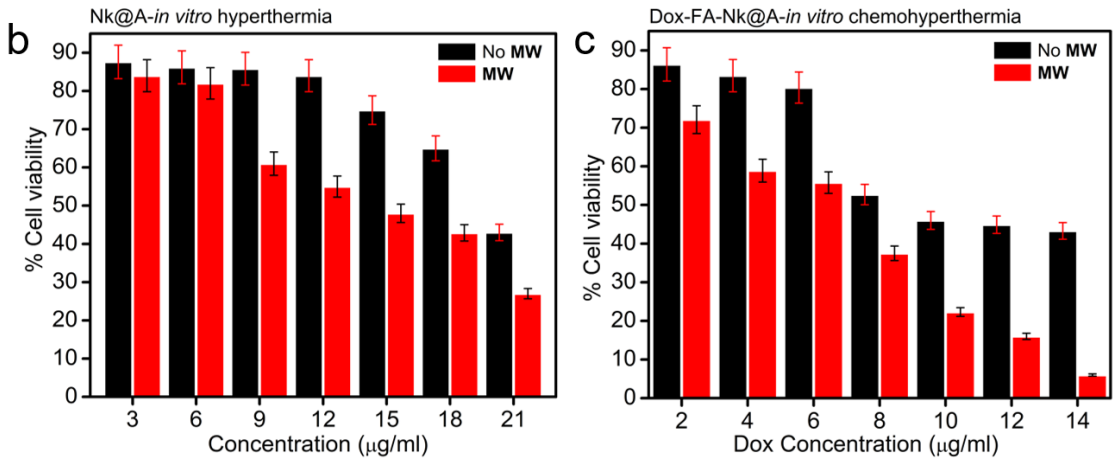

Figure 5.18. b) *in-vitro* hyperthermia where cells treated with **Nk@A** which represents the killing of cells as the concentration increases by producing enough heat, c) *in-vitro* chemohyperthermia where cells treated with **Dox-FA-Nk@A** which represents the killing as the concentration increases by producing heat and also release of **Dox**

5.4 Summary

In summary, we have developed **SPR** enhanced **Nk@A** by multiple iterative method, which proved to be a promising nanomaterial with multifunctional properties specifically in the field of cancer nanotheranostics. These multiple iterations provided a new platform for high surface functionalization. This helped in the efficient delivery of drugs, following first order rate kinetics. This **Nk@A** was also used as a competent MRI contrast agent and proved to be an effective T_2 agent with high relaxivity values in the presence of both L6 and Hep2 cells. Finally, **Nk@A** was used as a hyperthermal agent. In an *in-vitro* study using Hep2 cells, both **Nk@A** and **Dox-FA-Nk@A** on exposure to microwave irradiation using 2.45GHz for 50sec showed cell mortality. It was found that there is an enhancement of cell mortality when **MW** based hyperthermia collates with Chemotherapy. With this efficiency, **Nk@A** can be used for potential applications as a single nanomaterial for 3 different uses, from tracking, diagnosing to therapeutics.

5.5 References

1. Jemal, A., Bray, F. & Ferlay, J. Global Cancer Statistics: 2011. *CA Cancer J Clin* **49,** 1,33-64 (1999).
2. Lévy, M. *et al.* Magnetically induced hyperthermia: size-dependent heating power of γ-Fe_2O_3 nanoparticles. *J. Phys. Condens. Matter* **20,** 204133 (2008).
3. Cho, K., Wang, X., Nie, S., Chen, Z. G. & Shin, D. M. Therapeutic nanoparticles for drug delivery in cancer. *Clin. Cancer Res.* **14,** 1310–6 (2008).
4. Shah, J. *et al.* Photoacoustic imaging and temperature measurement for photothermal cancer therapy. *J. Biomed. Opt.* **13,** 34024 (2008).
5. Zhang, L., Dong, W.F. & Sun, H.B. Multifunctional superparamagnetic iron oxide nanoparticles: design, synthesis and biomedical photonic applications. *Nanoscale* **5,** 7664–84 (2013).
6. Beji, Z. *et al.* Magnetic properties of Zn-substituted $MnFe_2O_4$ nanoparticles synthesized in polyol as potential heating agents for hyperthermia. Evaluation of their toxicity on endothelial cells. *Chem. Mater.* **22,** 5420–5429 (2010).
7. Yang, H. *et al.* Water-soluble superparamagnetic manganese ferrite nanoparticles for magnetic resonance imaging. *Biomaterials* **31,** 3667–3673 (2010).
8. Giri, J. *et al.* Synthesis and characterizations of water-based ferrofluids of substituted ferrites [$Fe1\text{-}xBxFe_2O_4$, B=Mn,Co(x=0-1)] for biomedical applications. *J. Magn. Magn.*

Mater. **320,** 724–730 (2008).
9. Tung, L. D. *et al.* Magnetic properties of ultrafine cobalt ferrite particles. *J. Appl. Phys.* **93,** 7486–7488 (2003).
10. Ekreem, N. B., Olabi, A. G., Prescott, T., Rafferty, A. & Hashmi, M. S. J. An overview of magnetostriction, its use and methods to measure these properties. *J. Mater. Process. Technol.* **191,** 96–101 (2007).
11. Baldi, G. *et al.* Synthesis and Coating of Cobalt Ferrite Nanoparticles: A First Step toward the Obtainment of New Magnetic Nanocarriers. *Langmuir* **23,** 4026–4028 (2007).
12. Pita, M. *et al.* Synthesis of cobalt ferrite core/metallic shell nanoparticles for the development of a specific PNA/DNA biosensor. *J. Colloid Interface Sci.* **321,** 484–492 (2008).
13. Goon, I. Y. *et al.* Fabrication and dispersion of gold-shell-protected magnetite nanoparticles: Systematic control using polyethyleneimine. *Chem. Mater.* **21,** 673–681 (2009).
14. Zhang, Y. *et al.* Facile one-step synthesis of plasmonic/magnetic core/shell nanostructures and their multifunctionality. *J. Mater. Chem.* **22,** 10779 (2012).
15. Wang, L. *et al.* Monodispersed Core-shell Fe_3O_4@Au Nanoparticles. 21593–21601 (2005).
16. Daniel, M. C. M. & Astruc, D. Gold Nanoparticles: Assembly, Supramolecular Chemistry, Quantum-Size Related Properties and Applications toward Biology, Catalysis and Nanotechnology,. *Chem. Rev.* **104,** 293–346 (2004).
17. Xia, Y., Gates, B., Yin, Y. & Lu, Y. Monodispersed colloidal spheres: Old materials with new applications. *Adv. Mater.* **12,** 693–713 (2000).
18. Wang, L. *et al.* Iron oxide-gold core-shell nanoparticles and thin film assembly. *J. Mater. Chem.* **15,** 1821–1832 (2005).
19. Hormes, J., Modrow, H., Bönnemann, H. & Kumar, C. S. S. R. The influence of various coatings on the electronic, magnetic, and geometric properties of cobalt nanoparticles (invited). *J. Appl. Phys.* **97,** (2005).
20. Alonso-Cristobal, P., Laurenti, M., Lopez-Cabarcos, E. & Rubio-Retama, J. Efficient synthesis of core@shell Fe_3O_4@Au nanoparticles. *Mater. Res. Express* **2,** 75002 (2015).
21. Gallo, J., García, I., Padro, D., Arnáiz, B. & Penadés, S. Water-soluble magnetic glyconanoparticles based on metal-doped ferrites coated with gold: Synthesis and characterization. *J. Mater. Chem.* **20,** 10010 (2010).
22. Lyon, J. L., Fleming, D. A., Stone, M. B., Schiffer, P. & Williams, M. E. Synthesis of Fe oxide Core/Au shell nanoparticles by iterative hydroxylamine seeding. *Nano Lett.* **4,** 719–723 (2004).
23. Zhang, Q. *et al.* Tailored synthesis of superparamagnetic gold nanoshells with tunable optical properties. *Adv. Mater.* **22,** 1905–1909 (2010).
24. Caruntu, D., Cushing, B. L., Caruntu, G. & O'Connor, C. J. Attachment of gold nanograins onto colloidal magnetite nanocrystals. *Chem. Mater.* **17,** 3398–3402 (2005).
25. Oliva, B. L., Pradhan, A., Caruntu, D., O'Connor, C. J. & Tarr, M. a. Formation of gold-coated magnetic nanoparticles using TiO_2 as a bridging material. *J. Mater. Res.* **21,** 1312–1316 (2006).
26. Banchelli, M. *et al.* Magnetic nanoparticle clusters as actuators of ssDNA release. *Phys.*

Chem. Chem. Phys. **16,** 10023 (2014).
27. Kang, Y. M. *et al.* In vivo efficacy of an intratumorally injected in situ-forming doxorubicin/poly(ethylene glycol)-b-polycaprolactone diblock copolymer. *Biomaterials* **32,** 4556–4564 (2011).
28. Octavia, Y. *et al.* Doxorubicin-induced cardiomyopathy: From molecular mechanisms to therapeutic strategies. *J. Mol. Cell. Cardiol.* **52,** 1213–1225 (2012).
29. Molyneux, G. *et al.* Haemotoxicity of busulphan, doxorubicin, cisplatin and cyclophosphamide in the female BALB/c mouse using a brief regimen of drug administration. *Cell Biol. Toxicol.* **27,** 13–40 (2011).
30. Zwicke, G. L., Mansoori, G. A. & Jeffery, C. J. Targeting of Cancer Nanotherapeutics. *Nano Rev.* **1,** 1–11 (2012).
31. Torchilin, V. P. Nanoparticulate pharmaceutical drug delivery systems (NDDSs) are widely used in pharmaceutical research and in clinical settings to enhance the effectiveness of diagnostic agents and drugs, including anticancer, antimicrobial and antiviral drugs. *Nat. Publ. Gr.* **13,** (2014).
32. Dobson, J. Magnetic nanoparticles for drug delivery. *Drug Dev. Res.* **67,** 55–60 (2006).
33. Issels, R. D. Hyperthermia adds to chemotherapy. (2008). doi:10.1016/j.ejca.2008.07.038
34. Bohara, R. a., Thorat, N. D., Yadav, H. M. & Pawar, S. H. One-step synthesis of uniform and biocompatible amine functionalized cobalt ferrite nanoparticles: a potential carrier for biomedical applications. *New J. Chem.* **38,** 2979 (2014).
35. Ma, L. L. *et al.* Growth of textured thin Au coatings on iron oxide nanoparticles with near infrared absorbance. *Nanotechnology* **24,** 25606 (2013).
36. Jain, P. K., Xiao, Y., Walsworth, R. & Cohen, A. E. Surface plasmon resonance enhanced magneto-optics (SuPREMO): Faraday rotation enhancement in gold-coated iron oxide nanocrystals. *Nano Lett.* **9,** 1644–1650 (2009).
37. Carlà, F. *et al.* Electrochemical characterization of core@shell $CoFe_2O_4$/Au composite. *J. Nanoparticle Res.* **15,** 1813 (2013).
38. Kong, S. D. *et al.* Magnetically Vectored Nanocapsules for Tumor Penetration and Remotely Switchable On-Demand Drug Release. *Nano Lett.* **10,** 5088–5092 (2010).
39. Li, P., Jiang, E. Y. & Bai, H. L. Fabrication of ultrathin epitaxial γ-Fe_2O_3 films by reactive sputtering. *J. Phys. D. Appl. Phys.* **44,** 75003 (2011).
40. Barbieri, A., Weiss, W., Van Hove, M. A. & Somorjai, G. A. Magnetite Fe_3O_4(111): surface structure by LEED crystallography and energetics. *Surf. Sci.* **302,** 259–279 (1994).
41. Mosivand, S. & Kazeminezhad, I. Synthesis of electrocrystallized cobalt ferrite nanopowders by tuning the cobalt salt concentration. *RSC Adv.* **5,** 14796–14803 (2015).
42. Shi, Y. *et al.* Selective decoration of Au nanoparticles on monolayer MoS_2 single crystals. *Sci. Rep.* **3,** 1839 (2013).
43. Liu, B. *et al.* Synthesis of patterned nanogold and mesoporous $CoFe_2O_4$ nanoparticle assemblies and their application in clinical immunoassays. *Nanoscale* **3,** 2220–2226 (2011).
44. Xu, Z., Hou, Y. & Sun, S. Magnetic Core/Shell Fe_3O_4/Au and Fe_3O_4/Au/Ag Nanoparticles with Tunable Plasmonic Properties. *J. Am. Chem. Soc* **129,** 8698–8699 (2007).

45. Shi, X., Thomas, T. P., Myc, L. A, Kotlyar, A. & Baker, J. R. Synthesis, characterization, and intracellular uptake of carboxyl-terminated poly(amidoamine) dendrimer-stabilized iron oxide nanoparticles. *Phys. Chem. Chem. Phys.* **9,** 5712–5720 (2007).
46. Baruah, B. & Kiambuthi, M. Facile synthesis of silver and bimetallic silver–gold nanoparticles and their applications in surface-enhanced Raman scattering. *RSC Adv.* **4,** 64860–64870 (2014).
47. Pandey, S. *et al.* Folic acid mediated synaphic delivery of doxorubicin using biogenic gold nanoparticles anchored to biological linkers. *J. Mater. Chem. B* **1,** 1361 (2013).
48. Gordel, M. *et al.* Post-synthesis reshaping of gold nanorods using a femtosecond laser. *Phys. Chem. Chem. Phys.* **16,** 71–8 (2014).
49. Rai, A., Prabhune, A. & Perry, C. C. Antibiotic mediated synthesis of gold nanoparticles with potent antimicrobial activity and their application in antimicrobial coatings. *J. Mater. Chem.* **20,** 6789 (2010).
50. Wortmann, L. *et al.* Bioconjugated iron oxide nanocubes: synthesis, functionalization, and vectorization. *ACS Appl. Mater. Interfaces* **6,** 16631–16642 (2014).
51. Mewada, A., Pandey, S., Thakur, M., Jadhav, D. & Sharon, M. Swarming carbon dots for folic acid mediated delivery of doxorubicin and biological imaging. *J. Mater. Chem. B* **2,** 698–705 (2014).
52. Mellman, I. Endocytosis and Molecular Sorting. *Annu. Rev. Cell Dev. Biol.* **12,** 575–625 (1996).
53. Chen, H. *et al.* Drug loaded multilayered gold nanorods for combined photothermal and chemotherapy. *Biomater. Sci.* **2,** 996 (2014).
54. Wang, X. *et al.* Folate receptor-targeted aggregation-enhanced near-IR emitting silica nanoprobe for one-photon in vivo and two-photon ex vivo fluorescence bioimaging. *Bioconjug. Chem.* **22,** 1438–1450 (2011).
55. Sharon, M. Surface Orchestration of Gold Nanoparticles Using Cysteamine as Linker and Folate as Navigating Molecule for Synaphic Delivery of Doxorubicin. *J. Nanomedicine Res.* **1,** (2014).
56. Sandhu, K. K., McIntosh, C. M., Simard, J. M., Smith, S. W. & Rotello, V. M. Gold nanoparticle-mediated transfection of mammalian cells. *Bioconjug. Chem.* **13,** 3–6 (2002).
57. Chompoosor, A., Han, G. & Rotello, V. M. Charge dependence of ligand release and monolayer stability of gold nanoparticles by biogenic thiols. *Bioconjug. Chem.* **19,** 1342–1345 (2008).
58. Rosi, N. L. Oligonucleotide-Modified Gold Nanoparticles for Intracellular Gene Regulation. *Science* **312,** 1027–1030 (2006).
59. Denard, B., Lee, C. & Ye, J. Doxorubicin blocks proliferation of cancer cells through proteolytic activation of CREB3L1. *Elife* **2012,** 1–14 (2012).
60. Xie, M. *et al.* Expression of folate receptors in nasopharyngeal and laryngeal carcinoma and folate receptor-mediated endocytosis by molecular targeted nanomedicine. *Int. J. Nanomedicine* **8,** 2443–2451 (2013).
61. Yoo, H. S., Lee, K. H., Oh, J. E. & Park, T. G. In vitro and in vivo anti-tumor activities of nanoparticles based on doxorubicin-PLGA conjugates. *J. Control. Release* **68,** 419–431 (2000).
62. Estrella, V. *et al.* Acidity generated by the tumor microenvironment drives local invasion. *Cancer Res.* **73,** 1524–1535 (2013).

63. Som, A., Bloch, S., Ippolito, J. E. & Achilefu, S. Acidic extracellular pH of tumors induces octamer-binding transcription factor 4 expression in murine fibroblasts in vitro and in vivo. *Sci. Rep.* **6,** 27803 (2016).
64. Gurav, D. D., Kulkarni, A. S., Khan, A. & Shinde, V. S. pH-responsive targeted and controlled doxorubicin delivery using hyaluronic acid nanocarriers. *Colloids Surfaces B Biointerfaces* **143,** 352–358 (2016).
65. Rohrer, M., Bauer, H., Mintorovitch, J., Requardt, M. & Weinmann, H.J. Comparison of magnetic properties of MRI contrast media solutions at different magnetic field strengths. *Invest. Radiol.* **40,** 715–724 (2005).
66. Reimer, P. & Balzer, T. Ferucarbotran (Resovist): a new clinically approved RES-specific contrast agent for contrast-enhanced MRI of the liver: properties, clinical development, and applications. *European radiology* **13,** (2003).
67. Malyutin, A. G. *et al.* Virus like Nanoparticles with Maghemite Cores Allow for Enhanced MRI Contrast Agents. *Chem. Mater.* **27,** 327–335 (2015).
68. Kodiha, M. *et al.* Gold nanoparticles induce nuclear damage in breast cancer cells, which is further amplified by hyperthermia. *Cell. Mol. Life Sci.* **71,** 4259–73 (2014).
69. Cho, E. C., Xie, J., Wurm, P. A. & Xia, Y. Understanding the role of surface charges in cellular adsorption versus internalization by selectively removing gold nanoparticles on the cell surface with a I2/KI etchant. *Nano Lett.* **9,** 1080–1084 (2009).
70. Trujillo-Romero, C. J., Garcia-Jimeno, S., Vera, A., Leija, L. & Estelrich, J. Using Nanoparticles for Enhancing the Focusing Heating Effect of an External Waveguide Applicator for Oncology Hyper-Thermia: Evaluation in Muscle and Tumor Phantoms. *Prog. Electromagn. Res.* **121,** 343–363 (2011).
71. Kim, D. K. *et al.* Energy absorption of superparamagnetic iron oxide nanoparticles by microwave irradiation. *J. Appl. Phys.* **97,** 10J510-10J510-3 (2005).
72. Mohammad, F., Balaji, G., Weber, A., Uppu, R. M. & Kumar, C. S. S. R. Influence of Gold Nanoshell on Hyperthermia of Super Paramagnetic Iron Oxide Nanoparticles (SPIONs). *J. Phys. Chem. C. Nanomater. Interfaces* **114,** 19194–19201 (2010).
73. Holzwarth, A., Lou, J., Hatton, T. A. & Laibinis, P. E. Enhanced Microwave Heating of Nonpolar Solvents by Dispersed Magnetic Nanoparticles. *Ind. Eng. Chem. Res.* **37,** 2701–2706 (1998).
74. Pearce, J. A., Cook, J. R. & Emelianov, S. Y. Ferrimagnetic nanoparticles enhance microwave heating for tumor hyperthermia therapy. *2010 Annu. Int. Conf. IEEE Eng. Med. Biol. Soc. EMBC'10* 2751–2754 (2010). doi:10.1109/IEMBS.2010.5626583
75. Urano, M., Kuroda, M. & Nishimura, Y. For the clinical application of thermochemotherapy given at mild temperatures. *Int. J. Hyperth.* **15,** 79–107 (1999).
76. Ramachandra Kurup Sasikala, A. *et al.* Multifunctional Nanocarpets for Cancer Theranostics: Remotely Controlled Graphene Nanoheaters for Thermo-Chemosensitisation and Magnetic Resonance Imaging. *Sci. Rep.* **6,** 20543 (2016).

CHAPTER 6

Nano-Flotillas $MnFe_2O_4$@Au core-shell nanoparticles: An efficient MRI contrast agent, magneto-hyperthermal and drug-delivery armada for cancer

Table of Contents

6.1 Introduction

In the recent years, Nanomedicine research drive to the designing of multifunctional nanoparticles for various biomedical applications in the field of diagnosis, treatment, and therapy. In particular, the functionalized magnetic nanoparticles (MNPs) have been widely exploited for several advantages which opens up many opportunities in the biomedicine and biotechnology field[1]. It is due to their uncommon chemical and physical features such as magnetic, electronic, and optical properties. And also, MNPs size, shape, surface modification, water dispersity, biocompatibility plays a major role in various applications. Some of the MNPs based applications are magnetic resonance imaging (MRI), hyperthermia, and drug delivery[2–8]. The extensive studies has been carried out using iron oxides, but among ferrites manganese ferrite (**Mf**) is prominently used for various biomedical applications which is due to their property such as superparamagnetism, stability, high magnetization etc. These properties have attracted the researchers to develop the **Mf** into a multifunctional nanoparticles by various strategies such as core-shell (**CSNPs**) formation/bimetallic nanoparticles, surface modifications.

Among the various **CSNPs**, MNP (core) and GNP (shell) based are always created a niche in the field of biomedicine due to their excellent magnetic and optical properties[9]. The

formation of **CSNPs** are usually carried out using noble metals like gold (Au) or silver. Some of the **CSNPs** are Fe_3O_4@Au/Ag, and $MnFe_2O_4$@Ag[10–13]. Because these coatings offers a very less reactivity, avoiding aggregation of nanoparticles, high stability from the biological environment, less cytotoxic, increasing the chances of surface functionalization with various moieties such as drugs, targeting ligands/markers, and biomolecules (DNA, RNA, Proteins) and finally making the nanoparticles water-dispersible which is one of the important characteristics for biomedical applications[14–16]. These opportunities exposed the advantages of **CSNPs** and using various techniques, the **CSNPs** are synthesized by layer-by-layer electrostatic deposition, chemical reduction, and reverse micelle method etc[17–19].

CSNPs with various surface modifications acts as a multi-tasker for various applications. For example, in case of cancer theranostics the surface modified **CSNPs** can be an excellent drug delivery cargo, MR imaging agent, hyperthermal agent, photothermal agent etc[20]. Even though, MNP based **CSNPs** are widely explored for the past two decades, there are very less reports on the **Mf** based Au **CSNPs** for biomedical applications[2,20–23].

Based on these advantages, we have designed an **Mf** coated with GNP along with surface modifications using folic acid (**Fa**) and doxorubicin (**Dox**) for the intention to use for biomedical applications especially in the field of cancer. The main purpose of **Fa** is because it acts as a steering molecule towards the folate receptor expressing cancer cells and enters the cell to deliver the drugs by means of endocytosis[24,25]. And the objective of **Dox** is acting as an anticancer-agent which can be released by **CSNPs** and affects the cancer cell by two important possible mechanisms either by intercalating with DNA and disrupting topoisomerase-II-mediated DNA repair or by free radical generation leading to collapse of cellular membranes and other biomolecules[26].

Therefore, we present a novel strategy method to synthesize Au coated $MnFe_2O_4$ multifunctional NPs (**Mf@A**) using seed mediated technique to form a **CSNPs** is demonstrated. We have characterized this **CSNPs** to analyze the various properties like optical, structural, chemical, magnetic and also the biocompatibility by a combination of UV-Vis spectroscopy, X-ray diffraction, X-ray photoelectron spectroscopy, HRTEM analysis, SQUID measurements. After various confirmations the NPs are subjected to surface treatment using activated **Fa** and finally with the **Dox** moieties. The binding between **Fa** and **Dox** was confirmed by using FTIR, TGA and zeta potential. Later, the toxicity of various complexes were tested by MTT assay and visually analyzed the cellular and nuclear

morphologies by confocal microscopy. The above characterizations and testing gave a strong instinct to use it as a nanocargo for drug-delivery study which was carried out at 3 different pH, and employed the **CSNPs** as an efficient MR imaging contrast agent and finally, the magnetic property of **Mf** was taken advantage for the hyperthermal agent under microwave (**Mw**).

6.2 Results and Discussions of Optimization and characterization of CTAB stabilized $MnFe_2O_4$@Au core/shell nanoparticles

Formation mechanism of Core/shell nanoparticles

A novel seed mediated approach for CTAB stabilized **Mf@A CSNPs** involves gold seed particles, which constitutes a surfactant (CTAB), gold ions and a mild reducing agent Ascorbic acid (AA). Each constituent plays critical role in determining the surface chemistry of the particles. CTAB is comprised of two head groups: one interacts with the gold anionic surface electrostatically by its quaternary ammonium (cationic) head groups, while the other, which possesses the surfactant head group, interacts with the aqueous solution. There are three distinct interfaces formed that are energetically favourable:

- the gold nuclei-CTAB interface,
- CTAB bilayer,
- outer leaflet of CTAB exposed to the aqueous solution.

The role of CTAB in the formation of **CSNPs** is as follows. Firstly, it forms a staunch complex with $HAuCl_4$, diminishing its reduction. Secondly, it acts like a protection barrier for gold ions by forming a metallomicellar complex. Thirdly, it adsorbs on the surface of the magnetic core and allows slow reduction of the gold complex to form a shell. When the molar ratio of AA and $HAuCl_4$ exceeds 1.2, the reduction rate is enhanced and a uniform shell layer forms on the surface of the inner **Mf** core. At room temperature, there was no uniform shell formation on the surface of core; hence, a mild temperature of 80 °C is very important to form a uniform layer of the outer shell. **CSNPs** is thermodynamically and potentially very favourable, since the shell metal, $[AuBr_2]^-$, has a higher reduction potential (+0.962 V) as compared to the core metal (-0.447 V).This leads to a reduction-transmetalation reaction, forming a thin gold shell on the surface of the core. Black-coloured **Mf** NPs became dark-purple in colour when the light violet-coloured gold seed solution was mixed with the **Mf** seed solution. Gold seeds supply a large number of small randomly oriented crystalline domains,

leading to seed-mediated growth of the Au shell. The gold seeds initially formed on core, increase in diameter until a continuous shell is formed on the iron oxide surface, followed by outward growth of the shell. Particle-mediated electron transfer occurs and facilitates the formation of the shell.

6.2.1 Structural & Magnetic Characterization of Mf@A NPs

XRD analysis was carried out to detect the purity and phase crystallinity of the synthesized **Mf** and **Mf@A**. **Figure 6.1.** depicts the XRD pattern of **Mf** cubic spinel phase (JCPDS card no.01-074-2403) exhibiting diffraction peaks with well-defined lattice planes of (311), (400), (422), (511), (440) and (622) respectively[27,28]. The XRD pattern of **Mf@A**, having diffraction peaks at 2θ 38.15°, 44.32°, 65°, and 77.6° which was indexed to (111), (200), (220) and (311) planes of Au (JCPDS card no.004-0784) leading to the formation of **CSNPs**[20]. But the Au peaks are dominant which is due to heavy metal atom effect[29] due to the formation of **Mf@A CSNPs**. The presence of only one **Mf** peak denotes that there is a complete layer of Au is formed on the oxide core which can be further proved by our TEM data. Furthermore, the average crystalline size of **Mf** and **Mf@A** were calculated by considering FWHM using the Scherrer equation which was found to be about 11.3 and 14.9 nm, respectively, coinciding with those of TEM images.

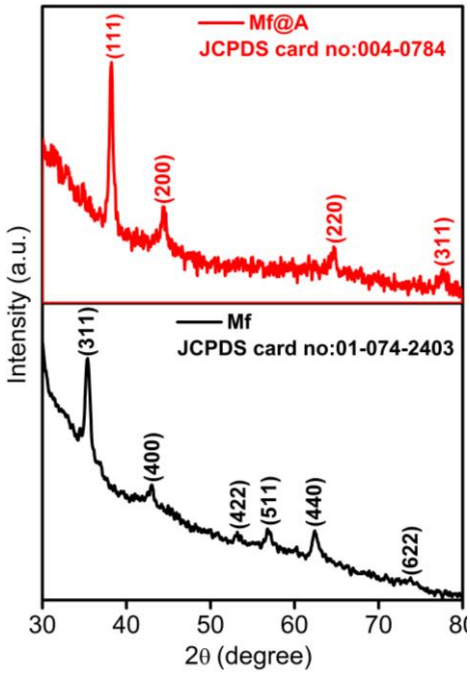

Figure 6.1. XRD spectrum representing the formation of **Mf** and **Mf@A**

TEM observations of the **Mf** and **Mf@A** are shown in the **Figure 6.2** & **6.3**. **Figure 6.2.** depicts that the **Mf** are spherical in shape and the size ranges from 13-24 nm with high aggregation due to magnetic nature of core NPs. And the **Mf@A** size is increased ≈1.25 fold from the diameter of the core particle because of the conjugation on nanogold onto the surface of the core NPs leading to the formation of **CSNPs**. HAADF-STEM analysis (**Figure 6.3b**) clearly distinguish the core and the shell. Due to thick Au shell formation continuously onto the surface of core NPs which makes it stable by enhancing steric stabilization and avoiding aggregation of particles.

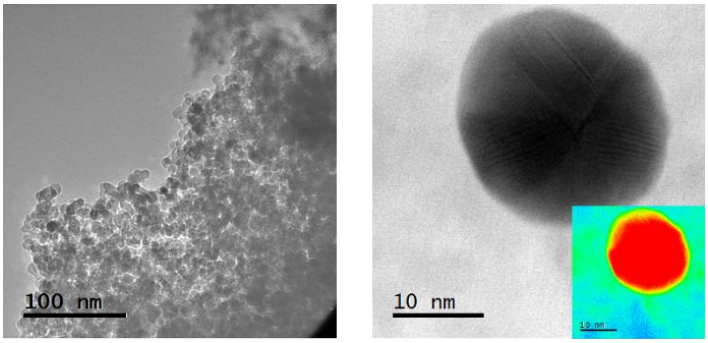

Figure 6.2. TEM image of core (Size: 13-24 nm), HRTEM image and colour mapping of **Mf**

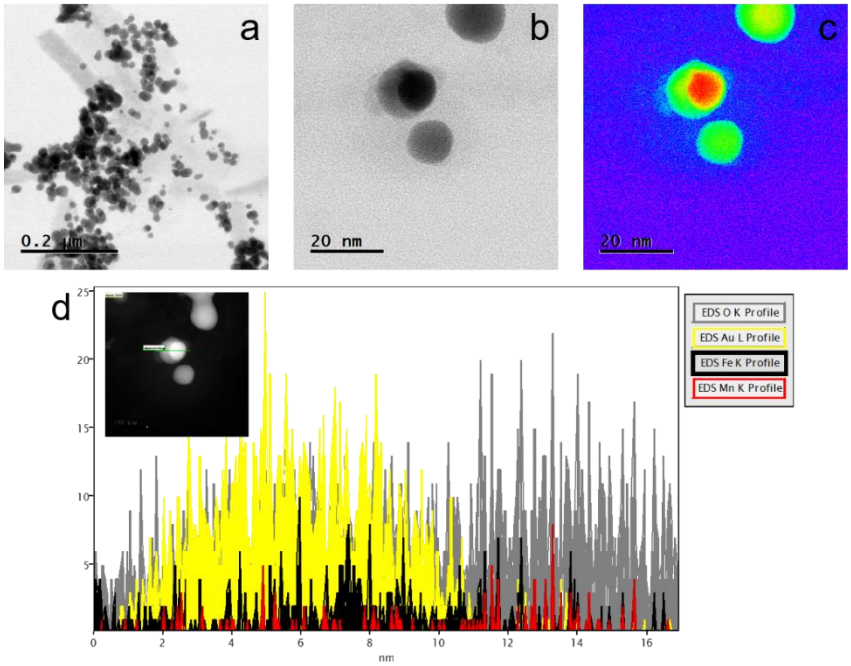

Figure 6.3. a) TEM of **Mf@A** (size: 16-38 nm), b) HRTEM of **Mf@A** which consists of very thin Au shell (3-4 nm), c) corresponding colour mapping showing 2 different contrast

which proves the formation of **Mf@A**, d) Core-shell confirmation by line mapping showing the presence of all elements

Line scanning for a single **CSNPs** was collected to determine the composition and distribution of elements. **Figure 6.3d.** shows the line scan of **Mf@A** NPs which confirms that Fe and Mn ions are concentrated in the core and Au shell signal is exhibited from the outside of the NPs forming a complex. From the spectra it is interfered that the intensities of the Au was dominated when it is compared with **Mf** peaks which clearly indicates that the particles are coated with thick layer of Au by correlating with the obtained molar ratios of Au^0 to **Mf**.

6.2.2 Elemental composition of Mf@A NPs

Binding energies and composition of **Mf@A** nanostructure were detected by using XPS measurements. **Figure 6.4a.** represents the wide-scan of XPS spectrum demonstrating the existence of Mn, Fe, Au, C and O elements with the range from 0 to ≈1300 eV of binding energies. **Figure 6.4b.** represents the high resolution core level spectra of individual elements. The oxidation states of Mn ions are observed which is present in the states of Mn2p3/2 and Mn2p1/2 electrons show binding energies at 641.1 and 652.7 eV[30]. Additionally, there are two more strong peaks observed at 645.33 and 658 eV. These binding energies represent to Mn^{3+}, but due to oxygen, Mn^{2+} is formed because of oxidation process[31,32]. Fe 2p3/2 and 2p1/2 peaks from Fe^{3+} ions are situated at around 710.63 and 724.24 eV which are broadened, and a small weak-up were observed at 719.1 eV[33]. The 2p peaks of Mn and Fe is due to the spin-orbit coupling and electrostatic interactions between their core 2p and also because of their unpaired 3d electrons[30,34]. Au binding energies were deconvoluted in two prominent peaks at 83.97 and 87.65 eV which directly denoted the Au state of Au4f7/2 and Au4f5/2 bands respectively with no doublets at 86.8 and 90.5 eV. Interestingly, the spectrum does not show any detectable Cl signal which usually within the bonding energy ranges from 196 eV to 204 eV. Thus it proves that there is a complete reduction of Au (III) to Au (0) onto **Mf** which is very well confirmed from TEM analysis[35–38]. The O1s peak (531.9 eV) can be seen which corresponds to the surface component oxygen atoms. In this case of XPS analysis, C1s peak of carbon atom binding energy was taken as a reference which is 284.82 eV. Therefore, from the XPS pattern it is very well in good agreement with XRD data and TEM results which reveals the formation of **Mf@A** CSNPs.

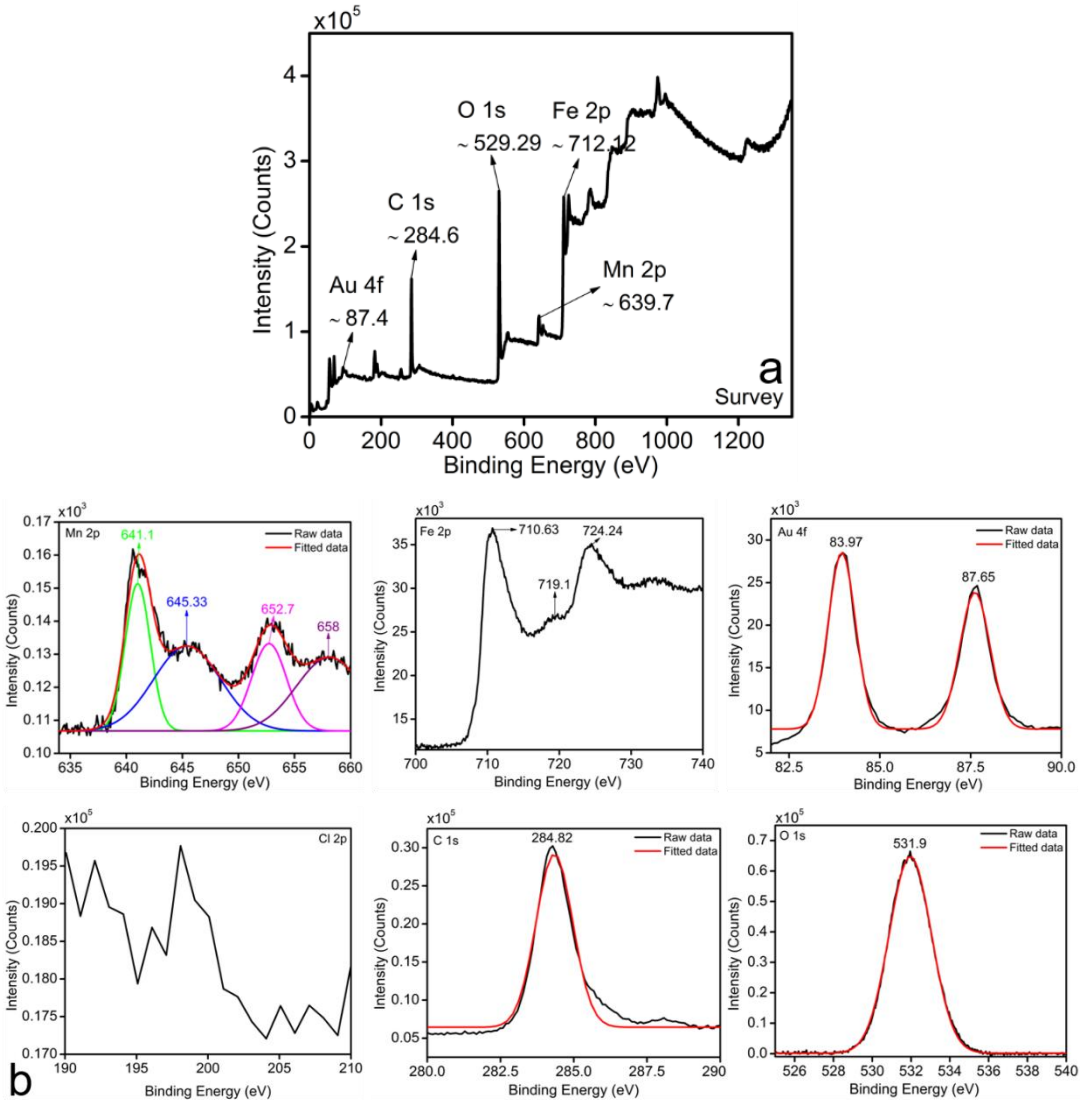

Figure 6.4. a) Scan survey & b) Elemental analysis of **Mf@A** by XPS which clearly shows the presence of elements such as Mn, Fe, Au, C, O and absence of Cl

The magnetic properties of **Mf@A** were evaluated at various temperatures. **Figure 6.5.** shows the magnetization field-dependent [M(H)] curves of **Mf@A** obtained at 5, 300 and 312 K showing the superparamagnetism which is absence of "magnetic memory", even at room temperature by retaining the magnetic property of **Mf** cores. Here it can be noticed a decrease on magnetic saturation (MS), from 81.3 to 61.1 emu/g from 5 to 312 K which is due to Au shell. Even though the MS value is decreased, but it is still high enough to be manipulated under external magnetic field for the applications of MR imaging and hyperthermia.

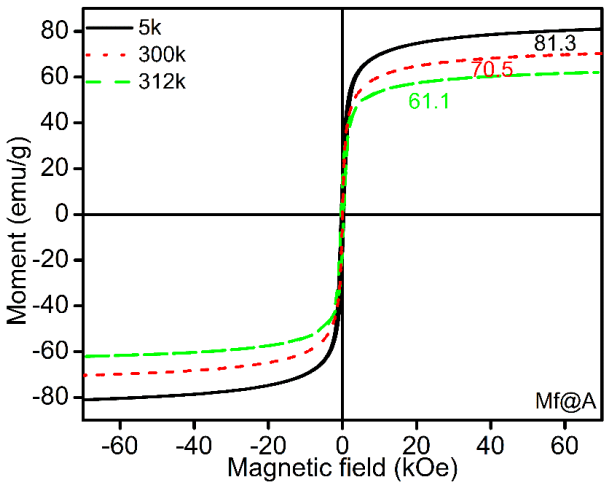

Figure 6.5. Magnetic measurements for **Mf@A** using SQUID at 5 k, 300 k & 312 k

6.2.3 Bioconjugation of folic acid linker and Doxorubicin molecules on Mf@A

6.2.3.1 Optical analysis

The SPR property of **CSNPs** provides the initial confirmation of formation of **Mf@A**. **Figure 6.6a*, a & b.** shows the UV-Vis absorption spectra measured for **Mf@A**, **Fa** functionalized **Mf@A** and **Dox** coated **Fa** functionalized **Mf@A** NPs. The synthesized **Mf@A** shows prominent optical plasmon absorption band at λmax = 546.6 nm (**Figure 6.6a***) which was red-shifted from GNPs values because of the Au nanoshell formation onto the **Mf** cores. **Mf@A CSNPs** are functionalized with **Fa** onto the surface to enhance the target specificity of NPs to the laryngeal carcinoma cells which express high folate receptors[39]. **Fa** functionalization on **Mf@A** NPs (**Figure 6.6a**) were confirmed from optical analysis which shows a peak at 273.9 nm and 357.8 nm which is **Fa** signature marker absorption wavelength[40] with minor blue-shift due to Au shell. And the distinct intensity of **Mf@A** NPs were seen at 533.5 nm which proves the **Fa-Mf@A** complex formation. Finally, **Dox** attachment were confirmed from the peak (inset) at 450.2 nm and **Mf@A** peak at 576.2 nm and **Fa** attachment from the 2 clear peaks at 274.8 nm a slight blue-shift and 358.7 nm which ensure the formation of **Dox-Fa-Mf@A** NPs complex (**Figure 6.6b**).

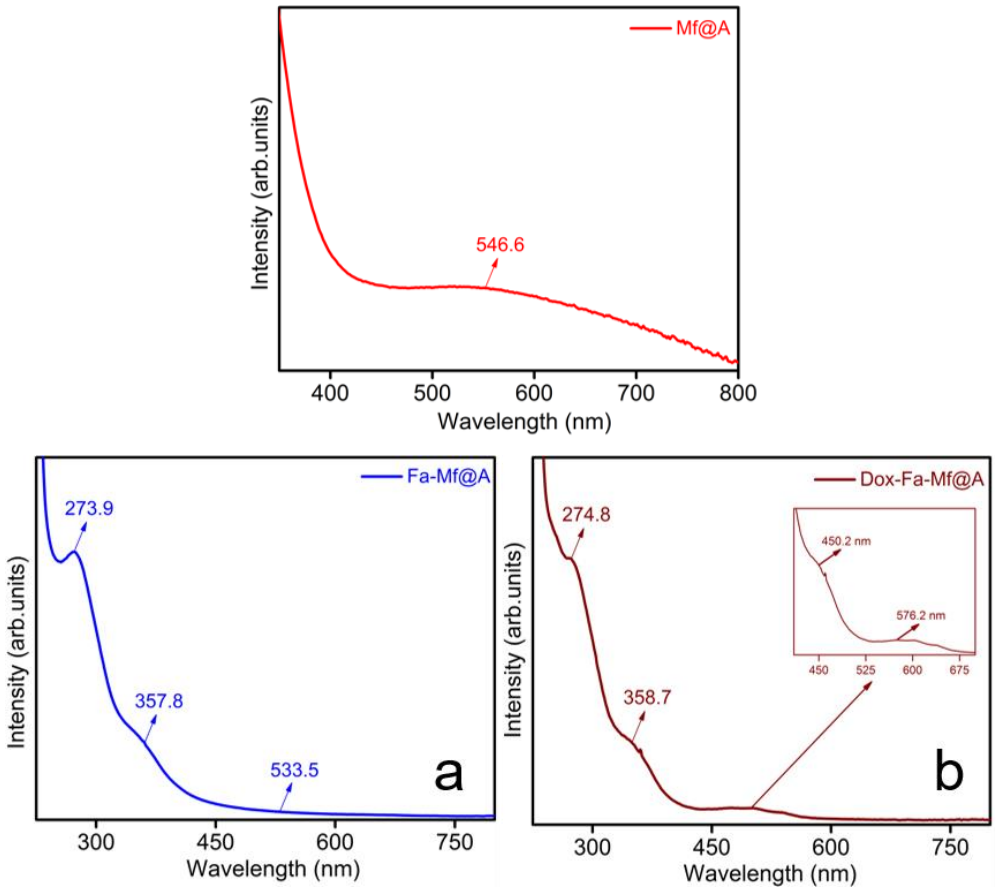

Figure 6.6. UV-Vis spectra of a*) SPR peak of **Mf@A** at 546.6 nm, a) **Fa** functionalization, b) Immobilization of **Dox** onto **Fa-Mf@A**

6.2.3.2 Spectroscopy analysis

FTIR spectra has been carried out for the samples to confirm the chemical design and attachment of organic molecules onto the NPs surface at frequency 400-4000 cm^{-1}. After the removal of excess CTAB from the **Mf@A CSNPs** surface it is bioconjugated with **Fa** and encapsulated with **Dox** (**Figure 6.7.**). Spectra A depicts the peaks of activated **Fa** showing bands at 1639.8 and 1723 cm^{-1} of –CH and –NH stretch respectively. **Fa** conjugation to **Mf@A** NPs is by asymmetric stretching of primary amines –NH and bending vibrations of –CO confirming the formation of amide linkage between **Fa** and **Mf@A** NPs at 1583.9 cm^{-1}. Spectra B represents the immobilization of **Dox** moieties to **Fa-Mf@A** NPs. The interaction between these moieties are purely based on –NH amide group and –COOH carboxylic groups of **Fa** and **Dox** respectively. Bands representing the attachments are 1430.5 cm^{-1} anhydride and 1650.8 cm^{-1} amide stretching of =CO. The peaks at 2905.6 cm^{-1} is of secondary and 3005.3 cm^{-1} of secondary and primary $–NH_2$ bending respectively[41].

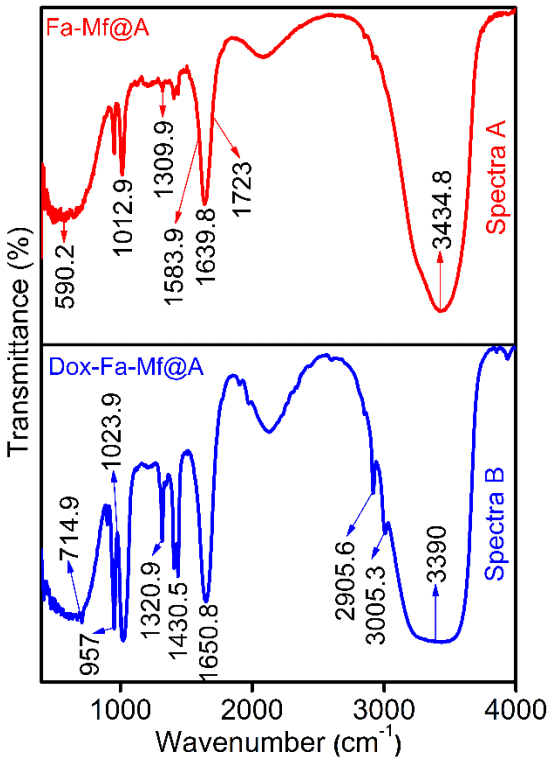

Figure 6.7. FTIR spectra showing the attachment of spectra A) **Fa** and spectra B) **Dox** onto **Mf@A**

6.2.4 Zeta potential, cytotoxicity studies of nanoparticle complexes

Figure 6.8. depicts zeta (ζ) potential measurements as a function of pH for bare **Mf**, **Mf@A**, **Fa** functionalized **Mf@A** and **Dox** coated **Fa** functionalized **Mf@A** NPs. All these NPs pH are adjusted to 5.4, 6.8 and 7.4 as the drug delivery study is mainly carried out in these ranges and the measurements are recorded after 24 h. In case of bare **Mf** NPs it is inferred that in all 3 different pH the ζ potential value lies in the range of positive, due to heavy aggregation because of superparamagnetic behaviour which is already confirmed by means of SQUID analysis (+10.8 to +12.5 mV). But, interestingly after the Au coating the ζ value is increased to positive range by stabilizing the NPs ranging from +32 to +37 mV which is due to the presence of CTA^+ ions on the surface of **CSNPs**. The functionalization of **Fa** increases the ζ value in the negative mV depicting that the protein moieties attachment changes the surface charge which confirms the stabilization of **Fa-Mf@A** complex. Finally, **Dox-Fa-Mf@A** complex also shows the ζ value to be in the positive range of +16 to +19.8 mV because of **Dox** attachment which is inherent with positive charge which provides the perfect stability

and avoiding aggregation of NPs complex by electrostatic repulsion[41]. So, this favors the use of these complex as a drug delivery vehicle.

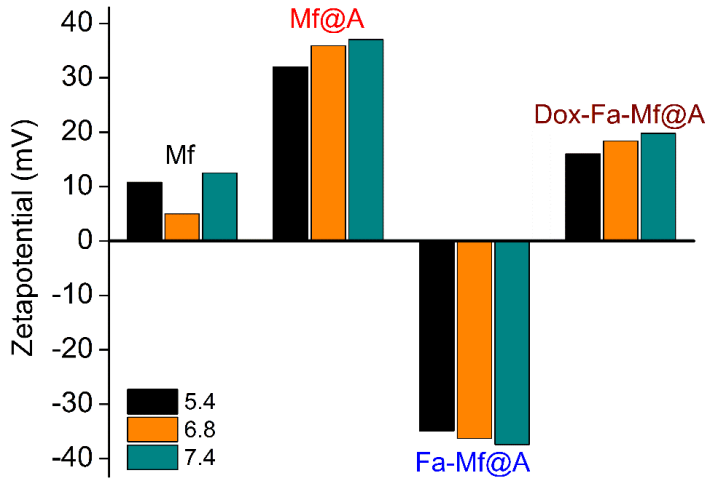

Figure 6.8. Zeta potential of **Mf**, **Mf@A**, **Fa** functionalized **Mf@A** and **Dox** immobilized **Fa-Mf@A**

MTT assay was carried out to assess the cell viability by incubating L6 and Hep2 cells with bare **Mf** and **Mf@A** NPs for a period of 24 h in the concentration range of 10-50 µg/mL. **Figure 6.9.** shows viability of cells which is more than 85% even at relatively higher dose of NPs. Therefore it is well proven that these NPs are highly biocompatible for biomedical applications. But as expected there is negligible cell death in case of **Fa** functionalized **Mf@A** nanocluster. The cell viability was evaluated by inoculating free **Dox** and **Dox** coated **Fa** functionalized **Mf@A** in both L6 and Hep2 cells. **Figure 6.10a.** depicts that free **Dox** shows minor cell death which confirms the side-effect of **Dox** to normal cells and negligible cell death with **Dox-Fa-Mf@A** complex. But **Figure 6.10b.** clearly proves the purpose of **Dox** in the Hep2 cancer cell line by killing them and the activity of **Dox** is increased in case of **Dox-Fa-Mf@A** complex by showing apoptosis of 12%. This proves that the entry of **Dox** inside the nucleus is higher which induces DNA damage causing cell death by efficient **Fa** functionalized **Mf@A** nanocargos.

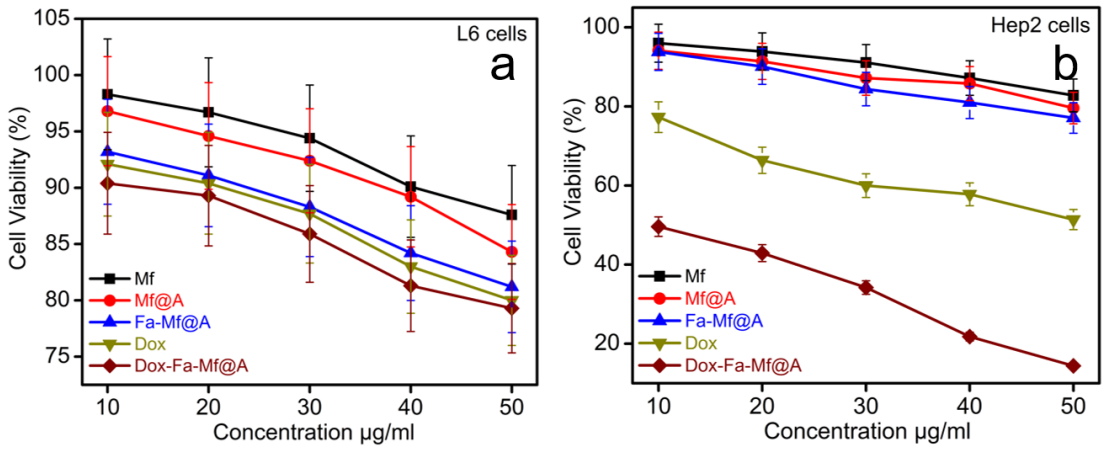

Figure 6.9. MTT assay of a) L6 cells with **Mf**, **Mf@A**, **Fa-Mf@A**, **Dox** and **Dox-Fa-Mf@A** showing no apoptosis at even at higher concentrations, b) Hep2 cells with only **Dox** and **Dox-Fa-Mf@A** showing around 88% cell death at high concentration

6.2.5 Nanoparticles internalization studies

Further cryoEM analysis has been carried out to confirm NPs internalization inside the cell instead of just interaction onto the cytoplasm shown in **Figure 6.11a**. This entry of NPs is based on a mechanism as follows[42]:

i. Initially the NPs attach onto the surface of the cell which causes intussusception of plasma membrane,

ii. Then forming endocytic cavities,

iii. Finally internalized into the cell.

Figure 6.10b. shows the high-magnification image of NPs clumping inside the lysosomes. This is because in the tumor region the pH is acidic (pH 4-6) causing aggregation of NPs. This proves that **Fa-Mf@A** NPs passed through the cellular membrane by process of an endocytic mechanism[43,44].

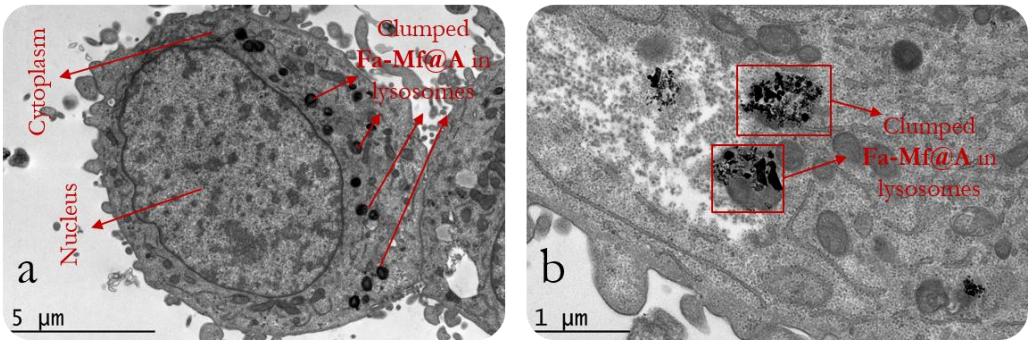

Figure 6.10. a) CryoEM image showing the **Fa-Mf@A** clusters, b) High resolution CryoEM image showing the engulfed cluster of **Fa-Mf@A** inside the lysosome by the process of endocytosis

6.2.6 Dox Intracellular distribution

From the cryoEM studies, we confirmed the entry of **Fa** attached NPs. So, furthermore to evaluate the process of **Dox** internalization inside the Hep2 cells were studied by incubating **Dox-Fa-Mf@A** NPs and exploiting the fluorescent character of **Dox** moieties at various time intervals by confocal microscopy which is shown in **Figure 6.11**.

0 h: Initially, after incubation of NPs, a lot of fluorescent spots were observed around the cellular membrane with no florescence seen in the nucleus,

6 h: After 6 h, the weak signal of **Dox** is seen from the cytoplasm which confirms the endocytosis pathway of NPs internalization,

12 h: The fluorescent intensity of **Dox** is increased all over the cell and the intensity difference is seen very clearly from the 0 h and 12 h,

24 h: After prolonged incubation of 24 h, **Dox** florescence in nuclei became very strong, with no signal from the cytoplasm. This is due to change in pH which cleaves the bond between the **Fa** and **Dox** moieties.

These results indicated that **Dox** attached NPs complex showed **Mf@A** acts a potential nanocargo and specifically targets the Hep2 cells.

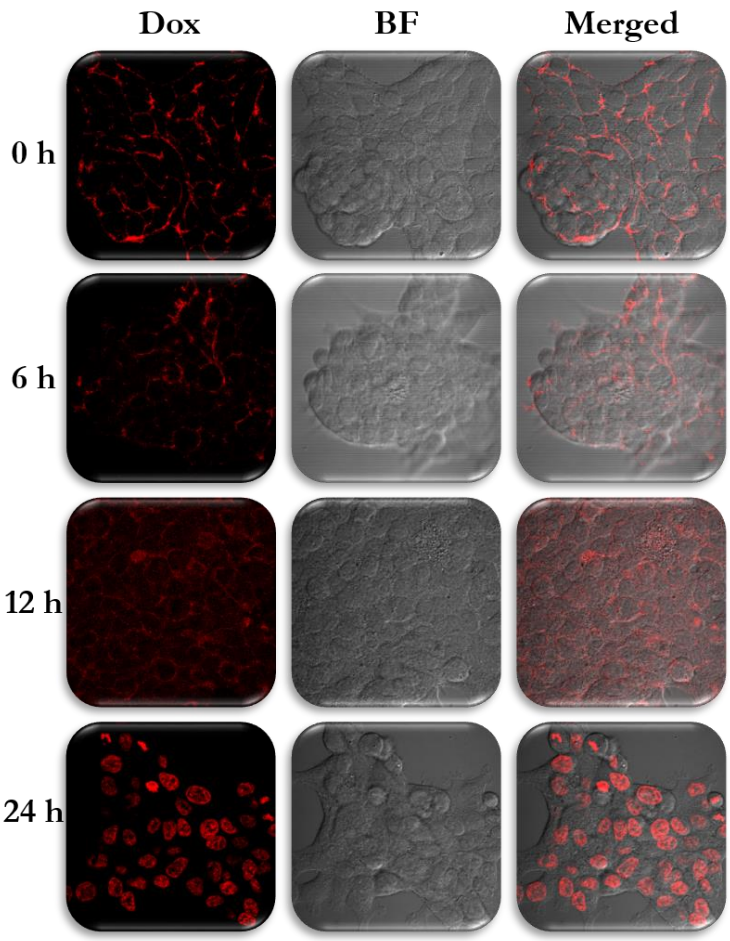

Figure 6.11. Confocal microscopy images of Hep2 cells incubated with **Dox-Fa-Mf@A** NPs for 0, 6, 12, and 24 h (BF: Bright Field, Scale bar: 25 μm)

6.2.6 Cellular and nuclear morphology studies

To evaluate the cellular and nuclear morphology of L6 and Hep2 cells incubated with **Mf**, **Mf@A**, **Fa-Mf@A** and also **Dox-Fa-Mf@A** potential application it was visualized under confocal microscopy. **Figure 6.12.** shows the morphologies treated with **Mf**, **Mf@A** and **Fa-Mf@A** which does not show any noticeable changes in both the type of cell lines. But the activity of **Dox-Fa-Mf@A** were shown in **Figure 6.12.** in which L6 cells is not been affected much but the Hep2 cells shows major apoptosis by disruption of nuclear membrane and the whole cell damage (**Figure 6.13.**). This proves that the **Dox-Fa-Mf@A** acts as an efficient nanocargo in delivering the **Dox** which causes cell death.

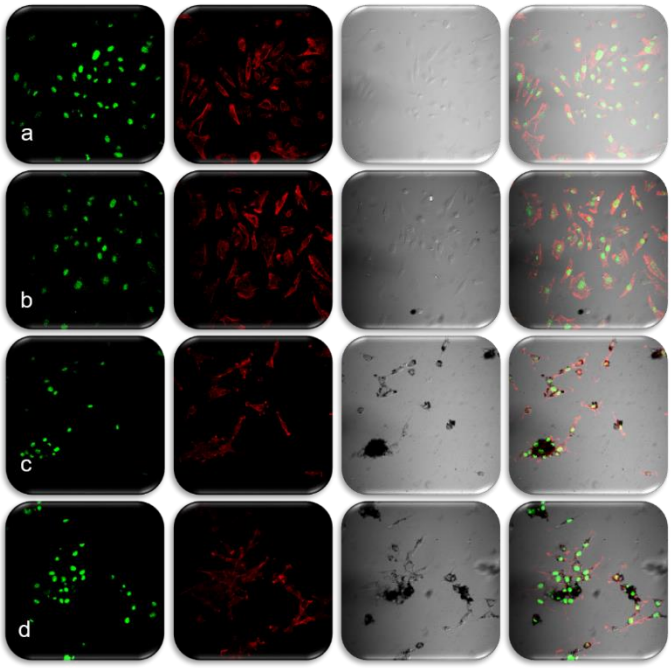

Figure 6.12. L6 Cell morphology analysis by confocal microscopy study treated a) **Mf**, b) **Mf@A**, c) **Fa-Mf@A**, d) **Dox-Fa-Mf@A** (Scale bar: 50 μm)

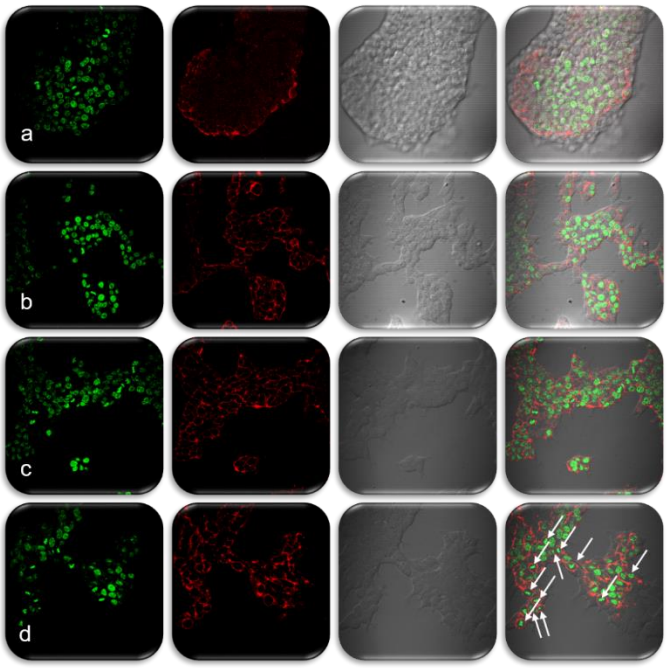

Figure 6.13. Hep2 Cell morphology analysis by confocal microscopy study treated a) **Mf**, b) **Mf@A**, c) **Fa-Mf@A**, d) **Dox-Fa-Mf@A** (Scale bar: 50 μm)

6.3 Applications of MF@A

6.3.1 *In-vitro* Dox release and its kinetics

Calculation for Drug loading Efficiency

Concentration of drug initially loaded = 1.2095 mM

Concentration of unbound drug = 0.03 mM (Abs-0.474)

[Concentration of drug is calculated using the standard calibration curve of **Dox** (Straight line equation: y= 6.721x)]

$$\textbf{\textit{Concentration of drug loaded}} = \textit{concentration of drug intially loaded} - \textit{concentration of unbound drug} \ldots\ldots\ldots\ldots\ldots\ldots\ldots\ldots\ldots \textbf{(1)}$$

=1.2095 mM – 0.03 mM

= 1.1795 mM

$$\textbf{\textit{Drug loading efficieny}}\ (\%) = \frac{\textit{concentration of drug loaded finally}}{\textit{concentartion of drug initially loaded}} \times 100 \ldots\ldots\ldots\ldots \textbf{(2)}$$

= 1.1795/1.2095*100

= 97.5 %

The drug loading efficiency (%) was calculated before initiating the drug release studies which was found to be 97.5%. Then, the *in-vitro* drug release performance of **Dox-Fa-Mf@A** NPs was investigated by employing at 3 different pH of PBS buffers (5.4, 6.8 & 7.4) at room temperature for 24 h. The pH based studies was evaluated, because cancer cells shows lower pH profile when compared to normal cells due to formation of lactic acid because of a lesser amount of blood flow which decreases both the oxygen and nutrients content which is known as Warburg effect[45]. We determined that our NPs system is pH sensitive which makes it a distinctive drug delivery system. Therefore, as the pH decreases in the cellular organelles thereby increasing the release of drugs which is shown in **Figure 6.14a.** The major benefits of pH depend drug delivery system is that, the early release of drug moieties inside the cell can be avoided, increased drug loading and release rate and finally dosage[46,47]. The **Dox** cumulative release at 3 different pH after 24 h was found to be 79.6% at pH 5.4, 76.9% at pH 6.8 and 37.6% at pH 7.4. At pH 5.4 shows the maximum amount of drug release when compared to pH 6.8 & 7.4. This difference is due to pH decrement inside the cell organelle (acidic pH) which lead to dissociation of drug from the complex by the breaking the amide bond between **Fa** and **Dox** molecules[48].

By obtaining the above *in-vitro* release elucidation, these results were analyzed with different mathematical drug kinetics models such as zero order, first order, Higuchi and Hixon-Crowell model to predict the drug release rates and diffusion characteristics (**Table 6.1.**) by calculating the R^2 (coefficient of determination) values for each model. Usually the various kinetic models denotes the amount of dissolved drug corresponding to the function of time[49]. From the calculations, it is found that the first order rate kinetics expressed very high regression coefficient value of **R^2 = 0.9742**. Thus, this model is considered to be a best model for this NPs based drug release of **Dox** which clearly signifies that the drug release rate is depend on its concentration. So, this proves **Dox-Fa-Mf@A** NPs system is more efficient as a nanocargo for drug delivery.

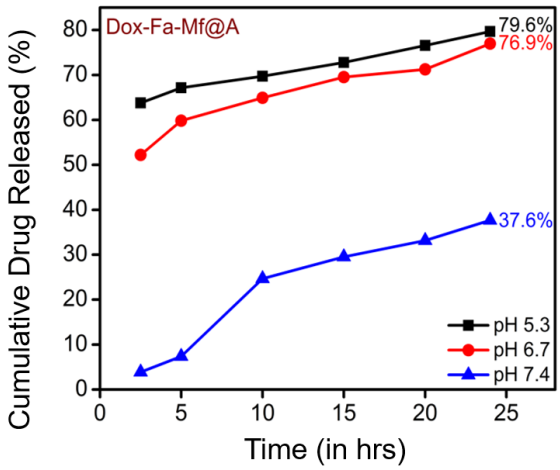

Figure 6.14. Cumulative release of **Dox** released at 3 different pH,

Table 6.1. Tabulation representing various kinetic models of drug release kinetics and its **R^2** values

	Drug release Kinetic Models											
	Zero order (% drug release)			First order (% drug remaining to release)			Higuchi (% drug release)			Hixon-Crowell (Cube root initial Q_0- Cube root Q_t)		
	pH											
	5.4	6.8	7.4	5.4	6.8	7.4	5.4	6.8	7.4	5.4	6.8	7.4
R^2	0.9226	0.9065	0.9003	**0.9742**	0.9138	0.8641	0.9036	0.8912	0.8848	0.9431	0.9054	0.89

6.3.2 Microwave ablation therapy

Mf@A particles were tested as a hyperthermal agent under microwave (**Mw**) irradiation. The choice of **Mw** was because the higher temperature produced by electromagnetic field leads to complete annihilation of tissues by causing irretrievable cell injury by the mechanism of apoptosis and necrosis. The increment of temperature is produced

by the concept of rotating dipoles or dielectric hysteresis[50]. So, the increment of temperature as a function of time has been carried out at a frequency of 2.45 GHz to induce localized hyperthermia by employing interstitial antenna which acts as a source from the generator power to the NPs sample. The **Mf@A** were dispersed in PBS and the applicator was inserted with the temperature probe and **Mw** was irradiated using home-made setup for 120 sec at 6 W. It is observed that the temperature increment was very rapid and reached 45±1°C around 70 sec and temperature raised up to 51±1.5°C within 120 sec for **Mf@A** which is shown in **Figure.6.15**. Here water was used as a control which shows the maximum absorption of **Mw**[51] and the temperature increment was maximum. This temperature is completely depend on the Au iteration on **Mf** particles. The Au coating on the core surface retains the superparamagnetic behaviour of **Mf** NPs which leads to increment of energy by magnetic anisotropy within the Au nanoshell[52]. The obtained result is compared with gold coated maghemite CSNPs where the temperature increment was 38°C (10 mins, 120 W) at 2.45 GHz in water.[53]

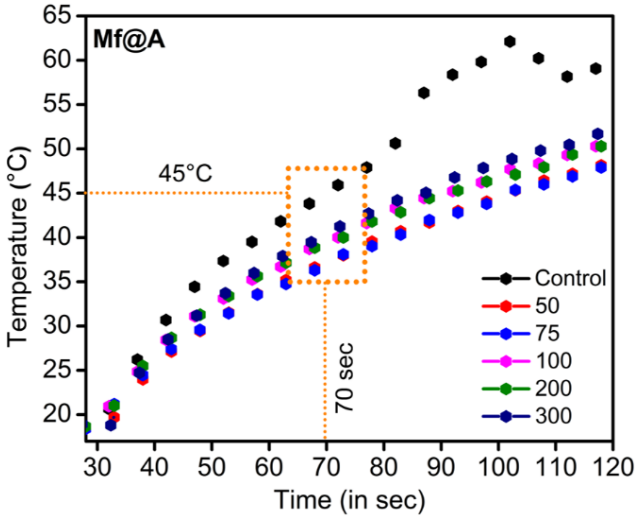

Figure 6.15. Plot showing increment of temperature as a function of time with the increased concentration of **Mf@A**

6.4 Summary

In the present work, a biomedical platform of **Mf@A** comprised of an inorganic core NPs and a biocompatible surface coating was engineering which can provide enough stabilization under physiological conditions to perform multiple functions simultaneously, such as in multimodal imaging, drug delivery and real-time monitoring, as well as combined therapeutic approaches.

Therefore, **Mf@A CSNPs** were used as able paraphernalia for the docking of anti-cancer drug such as **Dox** using **Fa** as a linker for the attachment. The attachment could be monitored using UV-visible spectroscopy. HAADF-STEM and line mapping confirms the formation of **CSNPs** structure. SQUID confirms the **CSNPs** are highly superparamagnetic. The stability of **Mf@A** NPs was scrutinized by measuring the zeta potential measurements. The amalgamation of the drug along with activated **Fa** as a navigational molecule is the critical phase for targeted drug delivery. Attachments were verified using FTIR which confirmed the formation of non-covalent interactions. **Mf@A-Fa-Dox** complex was found to be non-toxic for normal cells and considerably toxic for Hep2 cells detected by confocal microscopy and MTT assay. Then the complex was employed for drug delivery and hyperthermia studies. The drug loading capacity was found to be more than 90%. Drug-release was carried out at 3 different pH like 5.4, 6.8 & 7.4 and found that at pH 5.4 & 6.8 the release is maximum which is favourable for cancer cell treatment. The mathematical modelling studies shows it follows the first order rate kinetics with high R^2 values. Finally, under microwave the **CSNPs** produced enough heat to cause both apoptosis and necrosis in a shot span of time. This proves the designed **CSNPs** can be a potential candidate for various biological applications especially in the field of cancer theranostics.

6.5 References

1. Reddy, L. H., Arias, J. L., Nicolas, J. & Couvreur, P. Magnetic nanoparticles: design and characterization, toxicity and biocompatibility, pharmaceutical and biomedical applications. *Chem. Rev.* **112,** 5818–78 (2012).
2. Oh, Y., Lee, N., Kang, H. W. & Oh, J. *In vitro* study on apoptotic cell death by effective magnetic hyperthermia with chitosan-coated $MnFe_2O_4$. *Nanotechnology* **27,** 115101 (2016).
3. Wang, G., Chen, G., Wei, Z., Dong, X. & Qi, M. Multifunctional Fe_3O_4/graphene oxide nanocomposites for magnetic resonance imaging and drug delivery. *Mater. Chem. Phys.* **141,** 997–1004 (2013).
4. Wang, G. *et al.* Preparation and characterization of PVPI-coated Fe_3O_4 nanoparticles as an MRI contrast agent. *J. Magn. Magn. Mater.* **340,** 57–60 (2013).
5. Chalkidou, A. *et al. In-vitro* application of Fe/MgO nanoparticles as magnetically mediated hyperthermia agents for cancer treatment. *J. Magn. Magn. Mater.* **323,** 775–780 (2011).
6. Laurent, S., Dutz, S., Häfeli, U. O. & Mahmoudi, M. Magnetic fluid hyperthermia: Focus on superparamagnetic iron oxide nanoparticles. *Adv. Colloid Interface Sci.* **166,** 8–23 (2011).
7. Majeed, M. I. *et al.* Highly water-soluble magnetic iron oxide (Fe_3O_4) nanoparticles for drug delivery : enhanced in vitro therapeutic efficacy of doxorubicin and MION conjugates. *J. Mater. Chem. B* **1,** 2874–2884 (2013).

8. Chomoucka, J. *et al.* Magnetic nanoparticles and targeted drug delivering. *Pharmacol. Res.* **62,** 144–149 (2010).
9. Oza, G., Ravichandran, M., Jagadale, P. & Velumani, S. in *Engineering of Nanobiomaterials* 429–483 (Elsevier Inc., 2016). doi:http://dx.doi.org/10.1016/B978-0-323-41532-3.00014-2
10. Ye, M. *et al.* Fast assembling microarrays of superparamagnetic Fe_3O_4@Au nanoparticle clusters as reproducible substrates for surface-enhanced Raman scattering. *Nanoscale* **7,** 13427–13437 (2015).
11. Wang, C. *et al.* Polyethylenimine-interlayered silver-shell magnetic-core microspheres as multifunctional SERS substrates. *J. Mater. Chem. C* **3,** 8684–8693 (2015).
12. Kouassi, G. K. & Irudayaraj, J. Magnetic and gold-coated magnetic nanoparticles as a DNA sensor. *Anal. Chem.* **78,** 3234–3241 (2006).
13. Wang, J. *et al.* Magnetically Assisted Surface-Enhanced Raman Spectroscopy for the Detection of *Staphylococcus aureus* Based on Aptamer Recognition. *ACS Appl. Mater. Interfaces* **7,** 20919–20929 (2015).
14. Sun, Z. *et al.* Multifunctional Fe_3O_4@SiO_2–Au Satellite Structured SERS Probe for Charge Selective Detection of Food Dyes. *ACS Appl. Mater. Interfaces* **8,** 3056–3062 (2016).
15. Serhiy Malynych, Igor Luzinov, & Chumanov, G. Poly(Vinyl Pyridine) as a Universal Surface Modifier for Immobilization of Nanoparticles. (2002). doi:10.1021/JP013236D
16. Arvizo, R. R. *et al.* Intrinsic therapeutic applications of noble metal nanoparticles: past, present and future. *Chem Soc Rev* **41,** 2943–2970 (2012).
17. Spasova, M. *et al.* Magnetic and optical tunable microspheres with a magnetite/gold nanoparticle shell. *J. Mater. Chem.* **15,** 2095 (2005).
18. Sung-Jin Cho, *et al.* Magnetic and Mössbauer Spectral Study of Core/Shell Structured Fe/Au Nanoparticles. (2006). doi:10.1021/CM0522073
19. Wang, L. *et al.* Monodispersed core-shell Fe_3O_4@Au nanoparticles. *J. Phys. Chem. B* **109,** 21593–21601 (2005).
20. Wang, J. *et al.* Facile Synthesis of Au-Coated Magnetic Nanoparticles and Their Application in Bacteria Detection via a SERS Method. *ACS Appl. Mater. Interfaces* **8,** 19958–19967 (2016).
21. Pal, M., Rakshit, R. & Mandal, K. Surface modification of $MnFe_2O_4$ nanoparticles to impart intrinsic multiple fluorescence and novel photocatalytic properties. *ACS Appl. Mater. Interfaces* **6,** 4903–4910 (2014).
22. Ahmad, T. *et al.* Relaxivities of hydrogen protons in aqueous solutions of gold-coated manganese ferrite nanoparticles. *J. Korean Phys. Soc.* **62,** 1696–1701 (2013).
23. Gallo, J., García, I., Padro, D., Arnáiz, B. & Penadés, S. Water-soluble magnetic glyconanoparticles based on metal-doped ferrites coated with gold: Synthesis and characterization. *J. Mater. Chem.* **20,** 10010 (2010).
24. Pandey, S. *et al.* Folic acid mediated synaphic delivery of doxorubicin using biogenic gold nanoparticles anchored to biological linkers. *J. Mater. Chem. B* **1,** 1361 (2013).
25. Kamen, B. A. & Capdevila, A. Receptor-mediated folate accumulation is regulated by the cellular folate content (5-methyltetrahydro[3Hlfolate binding/folate-binding factor). *Cell Biol.* **83,** 5983–5987 (1986).
26. Gewirtz, D. A. A critical evaluation of the mechanisms of action proposed for the antitumor effects of the anthracycline antibiotics adriamycin and daunorubicin. *Biochem. Pharmacol.* **57,** 727–741 (1999).
27. Stolyarchuk, I. L., Dolgikh, L. Y., Vasilenko, I. V., Pyatnitskii, Y. I. & Strizhak, P. E.

Catalysis of steam reforming of ethanol by nanosized manganese ferrite for hydrogen production. *Theor. Exp. Chem.* **48,** 129–134 (2012).

28. Kardar, Z. S., Beyki, M. H. & Shemirani, F. Takovite-aluminosilicate@$MnFe_2O_4$ nanocomposite, a novel magnetic adsorbent for efficient preconcentration of lead ions in food samples. *Food Chem.* **209,** 241–247 (2016).
29. Teng, X., Black, D., Watkins, N. J., Gao, Y. & Yang, H. Platinum-maghemite core-shell nanoparticles using a sequential synthesis. *Nano Lett.* **3,** 261–264 (2003).
30. Nesbitt, H. W. & Banerjee, D. Interpretation of XPS Mn(2p) spectra of Mn oxyhydroxides and constraints on the mechanism of MnO_2 precipitation. *Am. Mineral.* **83,** 305–315 (1998).
31. Huang, C. C., Khu, N. H. & Yeh, C. S. The characteristics of sub 10nm manganese oxide T1 contrast agents of different nanostructured morphologies. *Biomaterials* **31,** 4073–4078 (2010).
32. Kim, T. *et al.* Urchin-shaped manganese oxide nanoparticles as pH-responsive activatable T_1 contrast agents for magnetic resonance imaging. *Angew. Chem. Int. Ed. Engl.* **50,** 10589–93 (2011).
33. Li, Z. *et al.* Ultrasmall Manganese Ferrite Nanoparticles as Positive Contrast Agent for Magnetic Resonance Imaging. *Adv. Healthc. Mater.* **2,** 958–964 (2013).
34. Grosvenor, A. P., Kobe, B. A., Biesinger, M. C. & McIntyre, N. S. Investigation of multiplet splitting of Fe 2p XPS spectra and bonding in iron compounds. *Surf. Interface Anal.* **36,** 1564–1574 (2004).
35. Li, X. *et al.* Programmed synthesis of magnetic mesoporous silica nanotubes with tiny Au nanoparticles: a highly novel catalyst system. *J. Mater. Chem. A* **2,** 10485 (2014).
36. Zhu, Y. *et al.* Multifunctional Magnetic Composite Microspheres with in Situ Growth Au Nanoparticles: A Highly Efficient Catalyst System. *J. Phys. Chem. C* **115,** 1614–1619 (2011).
37. Xiong, R., Wang, Y., Zhang, X., Lu, C. & Lan, L. In situ growth of gold nanoparticles on magnetic γ-Fe_2O_3@cellulose nanocomposites: a highly active and recyclable catalyst for reduction of 4-nitrophenol. *RSC Adv.* **4,** 6454 (2014).
38. Fernandes, C., Pereira, C., Guedes, A., Rebelo, S. L. H. & Freire, C. Gold nanoparticles decorated on bingel-thiol functionalized Multiwall carbon nanotubes as an efficient and robust catalyst. *Appl. Catal. A Gen.* **486,** 150–158 (2014).
39. Xie, M. *et al.* Expression of folate receptors in nasopharyngeal and laryngeal carcinoma and folate receptor-mediated endocytosis by molecular targeted nanomedicine. *Int. J. Nanomedicine* **8,** 2443–2451 (2013).
40. Dántola, M. L. *et al.* Mechanism of photooxidation of folic acid sensitized by unconjugated pterins. *Photochem. Photobiol. Sci.* **9,** 1604–1612 (2010).
41. Ravichandran, M. *et al.* Plasmonic/Magnetic Multifunctional nanoplatform for Cancer Theranostics. *Sci. Rep.* **6,** 34874 (2016).
42. Zhang, C. *et al.* Silica- and alkoxysilane-coated ultrasmall superparamagnetic iron oxide particles: A promising tool to label cells for magnetic resonance imaging. *Langmuir* **23,** 1427–1434 (2007).
43. Mellman, I. Endocytosis and Molecular Sorting. *Annu. Rev. Cell Dev. Biol.* **12,** 575–625 (1996).
44. Dausend, J. *et al.* Uptake mechanism of oppositely charged fluorescent nanoparticles in Hela cells. *Macromol. Biosci.* **8,** 1135–1143 (2008).
45. Karimi, M. *et al. Smart micro/nanoparticles in stimulus-responsive drug/gene delivery systems. Chem. Soc. Rev.* **45,** (Royal Society of Chemistry, 2016).

46. Rasouli, S., Davaran, S., Rasouli, F., Mahkam, M. & Salehi, R. Synthesis, characterization and pH-controllable methotrexate release from biocompatible polymer/silica nanocomposite for anticancer drug delivery. *Drug Deliv.* **21,** 155–163 (2014).
47. Wang, Y. *et al.* PEG–PCL based micelle hydrogels as oral docetaxel delivery systems for breast cancer therapy. *Biomaterials* **35,** 6972–6985 (2014).
48. Yong S.Cho, H. D. G. and V. R. W. A. *Encyclopedia of Nanoscience and Nanotechnology*. *Ceramic Nanopowders* **1,** (American Scientific Publishers, 2004).
49. Shaikh, H. K., Kshirsagar, R. V & Patil, S. G. Mathematical Models for Drug Release Characterization : a Review. *World J. Pharm. Pharm. Sci.* **4,** 324–338 (2015).
50. Chu, K. F. & Dupuy, D. E. Thermal ablation of tumours: biological mechanisms and advances in therapy. *Nat. Rev. Cancer* **14,** 199–208 (2014).
51. Kim, D. K. *et al.* Energy absorption of superparamagnetic iron oxide nanoparticles by microwave irradiation. *J. Appl. Phys.* **97,** 10J510-10J510-3 (2005).
52. Mohammad, F., Balaji, G., Weber, A., Uppu, R. M. & Kumar, C. S. S. R. Influence of Gold Nanoshell on Hyperthermia of Super Paramagnetic Iron Oxide Nanoparticles (SPIONs). *J. Phys. Chem. C. Nanomater. Interfaces* **114,** 19194–19201 (2010).
53. Pearce, J. A., Cook, J. R. & Emelianov, S. Y. Ferrimagnetic nanoparticles enhance microwave heating for tumor hyperthermia therapy. *2010 Annu. Int. Conf. IEEE Eng. Med. Biol. Soc. EMBC'10* 2751–2754 (2010). doi:10.1109/IEMBS.2010.5626583

CHAPTER 7

Concluding remarks & Future prospects

Table of Contents

7.1 Concluding remarks

The work presented in this thesis, aims to downgrade the side effects provoked by old-fashioned chemotherapy, by designing a versatile nanoparticle and demonstrating its capability of targeted delivery for a chemotherapeutic agent. Specifically, we have designed a multifunctional nanoparticle by employing iron oxide XFe_2O_4 (X=Fe/Mn/Co) (core)/gold (shell) based magneto/plasmonic core-shell nanoparticles using multiple gold iterations by seed-mediated method and used for cancer theranostic approaches such as

- drug delivery,
- magnetic resonance imaging agent,
- hyperthermal agent.

Firstly, we have synthesized magnetic cores (Fe_3O_4, $CoFe_2O_4$, $MnFe_2O_4$) using co-precipitation route using respective precursors and sodium hydroxide as a reducing agent. Then the post-treated core nanoparticles was coated with a multiple layers of inorganic gold shell employing CTAB as surfactant and ascorbic acid as a reducing agent in the search of complementary properties for the final core-shell nanoparticles: basically

- chemical stability,
- biocompatibility,
- surface functionalization of biomolecules,
- Applications.

We have exploited the gold coating for the surface functionalization of folic acid and doxorubicin. Activated folic acid was used as an anchoring agent to specifically target the cancer cells using the strategy of overexpressed folate receptors onto the cancer cells. And doxorubicin was used as an anti-cancer drug by inducing apoptosis which was confirmed by MTT assay and confocal microscopy studies. The attachment between folic acid and doxorubicin was an amide linkage which was confirmed by FTIR studies.

Finally, these complexes were used for doxorubicin drug delivery, MR imaging agent and microwave induced hyperthermia. All the applications are carried out in *in vitro* experiments.

To conclude, we have developed core-shell nanoparticles by multiple iterative method, which proved to be a promising nanomaterial with multifunctional properties specifically in the field of cancer nanotheranostics. These multiple iterations provided a new platform for high surface functionalization. This helped in the efficient delivery of drugs, following first order rate kinetics. And also used as a competent MRI contrast agent and proved to be an effective T_2 agent with high relaxivity values. Finally, used as a hyperthermal agent on exposure to microwave irradiation using 2.45 GHz showed increased heat generation within a short span of time (**Table 7.1.**). With this efficiency, these nanoparticles can be used for potential applications as a single nanomaterial for 3 different uses, from

Tracking, Diagnosing & Therapeutics

Table 7.1. Brief tabulation of all results including characterization techniques and applications of 3 different **CSNPs**

<table>
<tr><td rowspan="2">Characterizations</td><td>Fe_3O_4@Au NPs (Fe@A)</td><td>$CoFe_2O_4$@Au NPs (Nk@A)</td><td>$MnFe_2O_4$@Au NPs (Mf@A)</td></tr>
<tr><td colspan="3">Attached with activated
Folic acid (FA/Fa) & Doxorubicin (DOX/Dox)</td></tr>
<tr><td colspan="4">Characterization of Nanoparticles</td></tr>
<tr><td>XRD - 2θ° (10-80)</td><td colspan="3">Au diffraction peaks with minor core peaks were observed due to the heavy metal atom effect of gold</td></tr>
<tr><td>Morphology analysis</td><td colspan="3">TEM (spherical shape)
<table><tr><td>Nanoparticles</td><td>Particle size (in nm)</td></tr><tr><td>Fe@A</td><td>16-32</td></tr><tr><td>Nk@A</td><td>18-32</td></tr><tr><td>Mf@A</td><td>16-38</td></tr></table>Line mapping confirms the CSNPs formation</td></tr>
<tr><td>SQUID - 5, 300 & 312 K</td><td colspan="3">Exhibited Superparamagnetic behaviour
<table><tr><td>Temperature (K)</td><td>Fe@A</td><td>Nk@A</td><td>Mf@A</td></tr><tr><td>5</td><td>80.9</td><td>74.03</td><td>81.3</td></tr><tr><td>300</td><td>61.8</td><td>46.72</td><td>70.5</td></tr><tr><td>312</td><td>53.2</td><td>45.39</td><td>61.1</td></tr></table></td></tr>
</table>

<table>
<tr><td rowspan="2">XPS - 0 to ≈1300 eV</td><td>Presence of Au, Fe, C & O</td><td>Presence of Au, Co, Fe, C & O</td><td>Presence of Au, Mn, Fe, C & O</td></tr>
<tr><td colspan="3">Absence of Cl signal which proved the complete reduction of Au onto the core surface</td></tr>
<tr><td>UV-Visible Spectroscopy</td><td colspan="3">Confirmed Au coating by SPR peak, the attachment of FA/Fa & DOX/Dox was confirmed with minor shifts from their signature marker
<table>
<tr><td rowspan="2">SPR peak (in nm)</td><td>Fe@A</td><td>Nk@A</td><td>Mf@A</td></tr>
<tr><td>581.5</td><td>535.6</td><td>546.6</td></tr>
</table></td></tr>
<tr><td>FTIR – 400 to 4000 cm^{-1}</td><td colspan="3">Confirmed the attachment of FA/Fa and DOX/Dox onto the CSNPs, (Interaction between FA/Fa and DOX/Dox molecules was via amide linkage, which involved –NH amino group of FA/Fa and –COOH carboxylic group of DOX/Dox)</td></tr>
<tr><td>TGA - 30 to 900°C</td><td colspan="3">% weight loss of core, CSNPs, FA/Fa-CSNPs, & DOX/Dox-FA/Fa-CSNPs, curves are majorly divided into 2 segments: weight loss due to dehydration, and decomposition of organic/metal complexes</td></tr>
<tr><td>CryoEM</td><td colspan="3">Analysis confirmed CSNPs internalization by receptor-mediated endocytosis</td></tr>
<tr><td>Zeta potential analysis</td><td colspan="3">Except core NPs, all other NPs complex proved it to be highly stable at all 3 pH</td></tr>
<tr><td colspan="4">Cytocompatibility studies</td></tr>
<tr><td>Cytotoxicity Assay - L6 & Hep2 cells</td><td colspan="3">MTT assay of core, CSNPs, FA/Fa-CSNPs expressed no toxicity to both the cell lines, DOX/Dox-FA/Fa-CSNPs showed minor toxicity with L6 cells and major apoptosis with Hep2 cells</td></tr>
<tr><td>Confocal Imaging - L6 & Hep2 cells</td><td colspan="3">Imaging of core, CSNPs, FA/Fa-CSNPs did not show any noticeable change in both L6 and Hep2 cells, the activity of DOX/Dox-FA/Fa-CSNPs, showed no effect on L6 cells, while Hep2 cells exhibited major apoptosis by disruption of nuclear membrane, which leads to total cell damage</td></tr>
</table>

<table>
<tr><th colspan="2">Applications of Nanoparticles</th></tr>
<tr><td>In-vitro drug release studies – pH 5.4, 6.8 & 7.4 for 24 h</td><td>NPs system was both pH dependent and site-specific; drug release is comparatively more at pH 6.8 due to the dissociation of the amide bonds between FA/Fa and DOX/Dox molecules</td></tr>
<tr><td>Drug kinetics models – 0 & 1st order kinetics, Higuchi & Hixon-Crowell model</td><td>The drug release followed first order rate kinetics which was attributed to the high regression coefficient value [Fe@A-R^2=0.9755, Nk@A-R^2 =0.9865, Mf@A-R^2=0.9742)] confirming that the drug release is pH as well as concentration dependent mechanism</td></tr>
<tr><td>MR Imaging experiments – 7 T</td><td>Proved to be an efficient T_2 contrast agent as compared to T_1
<table>
<tr><th rowspan="2">Nanoparticles</th><th colspan="2">R_2 values ($mM^{-1}s^{-1}$)</th></tr>
<tr><th>L6 cells</th><th>Hep2 cells</th></tr>
<tr><td>Fe@A</td><td>130.13</td><td>182</td></tr>
<tr><td>Nk@A</td><td>118.08</td><td>217.24</td></tr>
<tr><td>Mf@A</td><td>-</td><td>-</td></tr>
</table></td></tr>
<tr><td>Mw based hyperthermia experiment - 2.45 GHz</td><td>Temperature enough to kill cancer cells (45 °C): Fe@A-42.7 sec, Nk@A-75 sec, Mf@A-70 sec</td></tr>
</table>

From the comparison of results of all 3 core-shell nanoparticles it is inferred that the nanoparticles are highly stable, minimally cytotoxic to normal cells and causing heavy damage to cancerous cells by delivering drugs, producing enough heat which can be tracked via., MR imaging, MTT assay and confocal imaging. These proves that all 3 core-shell nanoparticles can be a potential candidate for biomedical applications.

7.2 Future prospects

With the promising outcomes obtained from the above investigations, the future work is aimed to assess these nanoparticle systems *in vivo* and to scrutinize the effects and applications would be interesting. In order to achieve this, it would be ideal to synthesize monodispersed nanoparticles to reduce the degree of aggregation under physiological conditions and also can be administered intravascularly for sustained circulation in the blood

stream. So, the aim of future prospects is to synthesize monodispersed core-shell nanoparticles encapsulated with liposome along with various surface modifications to enhance the efficiency of various biomedical applications in the field of theranostics.

- Monodispersed core magnetic nanoparticles will be synthesized with the optimized thermal decomposition protocol excluding toxic surfactants and solvents (**Figure 7.1**).

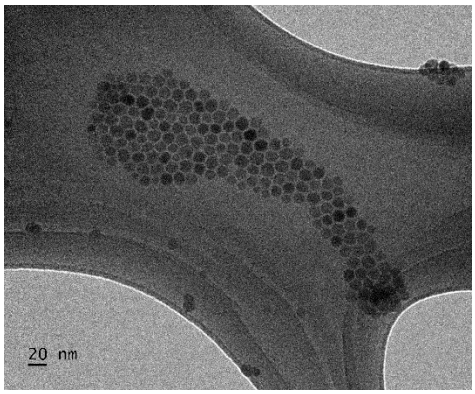

Figure 7.1 TEM image of core nanoparticles depicting the average particle size of 20.3 nm

- The gold shell coating is achieved by optimized seed-mediated approach with homogeneous distribution.
- The as-synthesized core-shell nanoparticles can be attached with specific antibody and drug moieties.
- Thus the whole complex can be encapsulated with liposome to enhance the retention time in the blood stream.
- Finally these complex is injected into mice model to study the cytotoxic effects and various *in vivo* applications.

7.3 Appendix

Publications

Book chapter:

1. Goldie Oza, **M. Ravichandran**, Pravin Jagadale, S. Velumani, January 2016, Engineering of Nanobiomaterials, 1st Edition, Volume 2, Applications of Nanobiomaterials, Edited by A. Grumezescu,

Chapter 14: Inorganic nanoflotillas as engineered particles for drug and gene delivery, pages 429-483; 01/**2016**, Elsevier, ISBN: 9780323415323. Doi: http://dx.doi.org/10.1016/B978-0-323-41532-3.00014-2

Publications in peer-reviewed journals:

1. **M. Ravichandran**, Goldie Oza, S. Velumani, Jose Tapia Ramirez, Francisco Garcia Sierra, Norma Barragán Andrade, Marco A. Garza-Navarro, Domingo I. Garcia-Gutierrez, R. Asomoza,
   One-dimensional ordered growth of magneto-crystalline and biocompatible cobalt ferrite nano-needles, - Materials Letters, 135 (**2014**) 67. Doi:10.1016/j.matlet.2014.07.154 *(IF: 2.437)*
2. **M. Ravichandran**, Goldie Oza, S.Velumani, Jose Tapia Ramirez, Francisco Garcia-Sierra, Norma Barragán Andrade, Marco A.Garza-Navarro, Domingo I.Garcia-Gutierrez, Rafael Lara Estrada, Emilio Sacristán-Rock and Junsin Yi,
   Cobalt Ferrite Nanowhiskers as T_2 MRI Contrast agent, - RSC Adv., 5 (**2015**) 17223. Doi: 10.1039/c4ra11934g *(IF: 3.289)*
3. Goldie Oza, **M. Ravichandran**, Victor-Ishrayelu Merupo, Sachin Shinde, Ashmi Mewada, Jose Tapia Ramirez, S. Velumani, Madhuri Sharon & Maheshwar Sharon,
   Camphor-mediated synthesis of carbon nanoparticles, graphitic shell encapsulated carbon nanocubes and carbon dots for bioimaging, - Sci. Rep., 6 (**2016**) 21286. Doi: 10.1038/srep21286 *(IF: 5.228)*
4. **M. Ravichandran**, Goldie Oza, S. Velumani, Jose Tapia Ramirez, Francisco Garcia-Sierra, Norma Barragan Andrade, A. Vera, L. Leija and Marco A. Garza-Navarro,
   Plasmonic/Magnetic Multifunctional nanoplatform for Cancer Theranostics, - Sci. Rep., 6 (**2016**) 34874. Doi: 10.1038/srep34874 *(IF: 5.228)*
5. **M. Ravichandran**, S. Velumani, Jose Tapia Ramirez,
   Water-dispersible magnetite nanoparticles as T_2 MR imaging contrast agent, - Biomed. Phys. Eng. Express, 3 (**2017**) 015011. Doi: 10.1088/2057-1976/aa59bf

Article under revision

1. **M. Ravichandran[#]**, Goldie Oza[#], S. Velumani, Jose Tapia Ramirez, A. Vera, & L. Leija,
   Multifunctional magneto-plasmonic nanocarrier for the treatment of cancer

Article under preparation

1. Goldie Oza, **M. Ravichandran**, Kaligotla Krishnajyothi, S. Velumani, Jose Tapia Ramirez, Pedro Chavez Olmos, Efrain Garrido Guerrero, Juan Manuel Gutierrez Salgado, M. Sridharan,

Electrochemical-Plasmonic-Fluorescence based detection of point mutations using Au-Fe_3O_4 Core/shell nanoparticles

2. **M. Ravichandran**, Goldie Oza, S.Velumani, Jose Tapia Ramirez,
   Facile synthesis of superparamagnetic nanoferrite for biomedical applications,
3. **M. Ravichandran**, Goldie Oza, S.Velumani, Jose Tapia Ramirez,
   Nano-Flotillas $MnFe_2O_4$@Au core-shell nanoparticles: An efficient MRI contrast agent, magneto-hyperthermal and drug-delivery armada for cancer

Conferences

Oral & Poster Presentation:

1. K. K. Jyothi, I.G. Becerril, S.Velumani, M. Sridharan, J. Tapia Ramirez, J. Romero Ibarra, A. Angeles Pascual, **M. R. Chandran**, A. Ramirez, G. Oza,
   Gold-coated Magnetite Nanoparticles: Synthesis and Characterization, 4th Mexican Workshop on Nanostructured Materials **2013**, March 19-22, Benemerita Universidad Autonoma de Puebla, Mexico.
2. **Ravichandran Manisekaran**, Goldie Oza, Jose Tapia Ramirez, Velumani Subramaniam, *Engineering iron oxide nanoparticles (Fe_3O_4) with cobalt and manganese for efficient enhancement of superparamagnetic behaviour*, symposium 7D, Advances In Functional Semiconducting Materials, XXII International Materials Research Congress, IMRC-**2013**, August 11 - 15, Cancún, México.
3. Goldie Oza, **Ravichandran Manisekaran**, Jose Tapia Ramirez, Velumani Subramaniam, *Synaphic delivery of Doxorubicin using Au-Fe_3O_4 core-shell as a nano-vehicle for folic acid & cysteamine mediated targeted therapy*, symposium 2A, Biomaterials for medical applications, XXII International Materials Research Congress, IMRC-**2013**, August 11 - 15, Cancún, México.
4. Goldie oza, **M. Ravichandran**, S. Velumani, R. Asomoza,
   Biological synthesis of metal sulfide semi-conducting nanocrystals, symposium 7A, Advances In Functional Semiconducting Materials, XXIII International Materials Research Congress, IMRC-**2014**, August 17 - 21, Cancún, México.
5. **M. Ravichandran**, Goldie Oza, S. Velumani, Jose Tapia, Francisco Sierra-Garcia, Norma Barragan Andrade, R. Asomoza,
   Biological Synthesis of Semiconductor Zinc Sulfide Nanoparticles, symposium 7A, Advances In Functional Semiconducting Materials, XXIII International Materials Research Congress, IMRC-**2014**, August 17 - 21, Cancún, México.

6. **M. Ravichandran**, Goldie Oza, S. Velumani, Jose Tapia, Francisco Sierra-Garcia, Norma Barragan Andrade, R. Asomoza,
   Core/Shell Nanoclusters of Doxorubicin Functionalized Au-M(Co, Mn)Fe_2O_4: A Theranostic approach for Cancer Therapeutics, symposium 2C, Biomaterials for medical applications, XXIII International Materials Research Congress, IMRC-2014, August 17 - 21, Cancún, México.
7. Goldie oza, **R. Manisekaran**, S. Velumani, Jose Tapia, Francisco Sierra-Garcia, Norma Barragán Andrade, R. Asomoza,
   Designing a drug-delivery vehicle with Au-Fe_3O_4-Graphene Quantum dots: A Tri-pronged mechanism for Bioimaging, synaphic delivery and apoptosis induction in Cancer cells, symposium 2C, Biomaterials for medical applications, XXIII International Materials Research Congress, IMRC-**2014**, August 17 - 21, Cancún, México.
8. **M. Ravichandran**, Goldie Oza, Jose Tapia Ramirez, Francisco Garcia-Sierra, Norma Barragán Andrade, S. Velumani,
   Core-Shell (Au-$MnFe_2O_4$) nano-flotillas as cargos for drug delivery in larynx carcinoma cells, Symposium 2B, Biomaterials for medical applications, XXIV International Materials Research Congress, IMRC-**2015**, August 16 - 20, Cancún, México.
9. Goldie oza, **M. Ravichandran**, Jose Tapia Ramirez, Francisco Sierra-Garcia, Norma Barragán Andrade, S. Velumani,
   Au-Fe_3O_4-carbon dots as nanoarmadas for bioimaging and drug delivery, Symposium 2B, Biomaterials for medical applications, XXIV International Materials Research Congress, IMRC-**2015**, August 16 - 20, Cancún, México.
10. Goldie Oza, Victor-Ishrayelu Merupo, **M. Ravichandran**, A. Kassiba, S. Velumani,
    Biological Synthesis of Semiconducting Bismuth Vanadate ($BiVO_4$) Photocatalysts, Symposium 7A Advances in Functional Semiconducting Materials, XXIV International Materials Research Congress, IMRC-**2015**, August 16 - 20, Cancún, México.
11. **M. Ravichandran**, Goldie Oza, Jose Tapia Ramirez, S. Velumani,
    Green Synthesis of Metal Sulfide Semi-Conducting Nanocrystals, Symposium 7A Advances in Functional Semiconducting Materials, XXIV International Materials Research Congress, IMRC-**2015**, August 16 - 20, Cancún, México.
12. **M. Ravichandran**, Goldie Oza, Jose Tapia Ramirez, Francisco Garcia-Sierra, Norma Barragan Andrade, Sirenia gonzalez posos, Rafael Lara-Estrada, Emilio Sacristan-Rock Abdel-Hadi Kassiba and S. Velumani,

Au@$CoFe_2O_4$ yolk-shell nanoparticles: An efficient MRI contrast agent, Magneto-Hyperthermal and drug-delivery armada for cancer Theranostics, 4th Nano Today Conference, December 6-10, **2015**, Dubai, UAE.

13. Goldie Oza, **M. Ravichandran**, Victor Ishrayelu Merupo, Jose Tapia Ramirez, Francisco Garcia-Sierra, Norma Barragan Andrade, Francisco Manuel Sánchez Arévalo, Abdel-Hadi Kassiba and S. Velumani,
    Au-Fe_3O_4-Graphene Quantum dots as a Magneto-Plasmonic-Luminescent Trojan horse, 4th Nano Today Conference, December 6-10, **2015**, Dubai, UAE.
14. Goldie Oza, **M. Ravichandran**, Jose Tapia Ramirez, Francisco Garcia-Sierra, Norma Barragan Andrade, Abdel-Hadi Kassiba and S. Velumani,
    HDL orchestrated plasmonic copper nanoparticles as synaphic nano-flotilla: a combinatorial cancer therapeutic approach, 4th Nano Today Conference, December 6-10, **2015**, Dubai, UAE.
15. **M. Ravichandran**, Goldie Oza, S. Velumani & Jose Tapia Ramirez,
    Au@$CoFe_2O_4$ yolk-shell nanoparticles: An efficient MRI contrast agent, Magneto-Hyperthermal and drug-delivery armada for Cancer Theranostics, 11th International Conference on the Scientific and Clinical Applications of Magnetic Carriers, May 31-June 4, **2016**, Vancouver, Canada.
16. Goldie Oza, **M. Ravichandran**, S. Velumani, Jose Tapia Ramirez,
    Au-Fe_3O_4 core-shell nanoparticles orchestrated carbon dots as nanoflotillas for bioimaging and drug delivery, 6th Mexican Workshop on Nanostructured Materials, October 12-14, **2016**, Puebla, Mexico.